

**Photodissociation dynamics of vibrationally excited hydrogen molecules
examined with reaction microscopy in kinematically complete VUV + NIR
experiments**

by

Spenser Burrows

A dissertation submitted to the Graduate Faculty of
Auburn University
in partial fulfillment of the
requirements for the Degree of
Doctor of Philosophy

Auburn, Alabama
December 9, 2023

Keywords: COLTRIMS, Laser, Electron Retroaction, LICI, Hydrogen Molecule, Photo
Dissociation, Vibrational Excitation, VUV-NIR Pump-Probe

Copyright 2023 by Spenser Burrows

Approved by

Guillaume Laurent, Professor of Physics
Thorsten Weber, Principle Investigator
Allen Landers, Professor of Physics
Stuart Loch, Professor of Physics
Minseo Park, Professor of Physics

Hans-Werner van Wyk, Associate Professor of Mathematics and Statistics
George Flowers, Dean of the Graduate School and Professor of Mechanical Engineering

Abstract

Using the Cold Target Recoil Ion Momentum Spectroscopy (COLTRIMS) technique, we investigated the dissociation of vibrationally excited H_2 and D_2 molecules after two-color vacuum ultraviolet (VUV) + near-infrared (NIR) absorption. The Advanced Light Source synchrotron provided horizontally polarized VUV radiation to photoionize H_2 (or D_2), leaving H_2^+ (or D_2^+) ions in specific vibrational states. A synchronized 1030-nm NIR, horizontally polarized, 12 ps-long laser pulse with an intensity of $\approx 3 \times 10^{11} W/cm^2$ then dissociated these ions at a time delay that was controlled with picosecond-scale precision. We report on electron emission in the molecular frame, retrieved from the recoil ion lab-frame momentum. For some vibrational states, we observed an asymmetric photoelectron angular distribution that depends on the VUV/NIR time delay. We observed dissociation of lower energy vibrational states that should be forbidden. We also investigate the dependence of this asymmetry on the angle between the molecular axis and the polarization direction of the synchrotron radiation for one-color VUV-only dissociation, and the dependence of dissociation on the angle between the molecular axis and the polarization directions of the synchrotron and laser radiation for the two-color dissociation. We believe this asymmetry might be related to photoelectron retroaction with the dissociating ion in both the one-color and two-color dissociation, and that the dissociation of lower energy vibrational states could be due to a dressed potential energy surface with a light induced conical intersection.

Acknowledgments

First, I would like to thank my advisors, Dr. Guillaume Laurent at Auburn and Dr. Thorsten Weber at LBNL, for their guidance and support during my PhD.

I'd like to thank Dr. Allen Landers, Dr. Stuart Loch, Dr. Minseo Park, and Dr. Hans-Werner van Wyk, my PhD committee.

I would like to thank my collaborators from the multiple institutions whose contributions made the two-color experiment at the core of this manuscript possible. Dr. Elio Champenois, Dr. Averell Gatton, Dr. Wael Iskandar, Dr. Kirk Larsen, Dr. Niranjana Shivaram, and Dr. Dan Slaughter from the LBNL experimental group helped take and analyze the data. Dr. C. William McCurdy, Dr. Jan Dvořák, Dr. Robert Lucchese, and Dr. Tom Rescigno from the LBNL theory group provided invaluable theory support to help interpret the results. I'd also like to thank Dr. Reinhard Dörner, Dr. Miriam Weller, and Dr. Hendrik Sann from Frankfurt, Dr. Itzik Ben-Itzhak, Dr. Ben Berry, and Dr. Travis Severt from Kansas State University, and Dr. Joshua Williams from the University of Nevada at Reno for all of their contributions to the two-color experiment.

I'd like to thank Dr. Till Jahnke and Dr. Achim Czasch for their help with the LMF2Root program used for the analysis of this data.

I'd like to thank Dr. Ricky Strom, Dr. John Vaughan, Trevor Olsson, Swapneal Jain, Scott Chumley, Jody Davis, Courtney Wicklund, Brady Unzicker, Geoffrey Harrison, Davis Arthur, and Bree Tatum, my fellow students in the experimental AMO physics group at Auburn.

I'd like to thank Dave Patrick, Rick Stringer, Mary Prater, Jennifer Morris, Freddie Killian, and Glenda Stroud, the staff of the Auburn Physics Department.

I'd like to thank my parents, my sister Landry, and my brother-in-law Greg for their love and support.

I'd like to thank my mentors Robert Neidig, Pam Neidig, Charles Avila, Lea Stage, Dr. Charles Rogers, Dr. Tobin Munsat, Dr. Mihaly Horanyi, and Dr. Andrew Collette who have positively impacted my life and put me on a path to accomplish this goal.

Finally, I'd like to thank my friends Dr. Stephen Williams, Dr. Spencer LeBlanc, Robert Merritt, Rhiannon Ellifritz, Dr. Michael Tanksalvala, Dr. Nic Kuon, Maggie Abeyta, Dr. Lori McCabe, Dr. Ivan Arnold, Dr. Peter Traverso, Nic Allen, Dr. Curtis Johnson, Ali Fisher, Dr. Omar Lopez, Dr. Jalaan Avritte, Daphanie Stacks, Bernard Sellers, Thomas Hicks, Matt Lord, Jon Huber, Hillary Ondrla, Sophie Vor, Lydia Love, Weston Love, Oliver Goodenough, Alison Vice, Michael Simmons, Faith Walker, Caid Wingo, and SO many others that have helped me stay sane and have made this journey one that I will look back upon fondly for the rest of my life.

Table of Contents

Abstract	ii
Acknowledgments	iii
List of Figures	viii
List of Tables	xxi
1 Introduction	1
1.1 The hydrogen molecule	1
1.2 Electron retroaction effect	5
1.3 Light induced conical intersections	10
1.4 Motivation for a two-color experiment	13
2 Experimental setups	18
2.1 Vacuum ultraviolet light sources	18
2.2 High Harmonic Generation process	19
2.3 The Auburn Source of Attosecond Pulses	22
2.3.1 VUV spectrometer	23
2.3.2 HHG and the two-color electron retroaction experiment	27
2.4 Synchrotron radiation	27
2.5 The Advanced Light Source (ALS)	28
2.5.1 Beamline 10	29
2.5.2 Synchrolocked near-infrared laser	30
2.6 Cold Target Recoil Ion Momentum Spectroscopy (COLTRIMS)	31
2.6.1 Microchannel Plate/Delay Line Anode detector	33
2.7 COLTRIMS endstation	36
3 General COLTRIMS analysis using LMF2Root	41

3.1	LMF2Root 3.42 overview	41
3.2	Data flow	41
3.3	Installation	42
3.4	Compiling	42
3.5	LMF2Root configuration file (Config.txt)	43
3.6	Detector electronics calibration	45
3.7	Hit reconstruction	49
3.8	Time-of-flight using a bunchmarker signal	52
3.9	Momentum calculation	52
3.10	ColAHell configuration file (ColAHell.cfg)	53
3.11	Excel COLTRIMS simulation	55
3.12	Time offset calibration procedure	56
3.13	Magnetic and electric field calibration procedure	57
3.14	Detector rotation procedure	59
3.15	Determination of magnetic field direction	61
3.16	Gas jet calibration procedure	62
3.17	Generating custom plots in LMF2Root	63
4	Detailed analysis of the two-color experiment	66
4.1	Fine momentum calibration procedure	66
4.1.1	Momentum sphere and calibration angles	67
4.1.2	Momentum shift and stretch operations	70
4.1.3	Momentum skew operations	72
4.2	Contamination removal	75
4.3	Molecular Frame Photoelectron Angular Distribution (MFPAD)	80
4.4	Asymmetry parameter	82
4.4.1	Uncertainty in asymmetry parameter	84
4.5	Legendre polynomial fit parameters	85

4.6	Classical retroaction model	86
4.7	Lab-frame photoelectron angular distribution	87
4.8	Detector homogeneity	90
5	Experimental results	93
5.1	Data overview	93
5.2	One-color channel	96
5.2.1	Angular dependence on polarization for dissociation via the one-color channel	97
5.2.2	Parallel and perpendicular one-color channel dissociation MFPADs at different electron energies	101
5.2.3	Energy-dependent perpendicular side lobes	111
5.3	Two-color channel	116
5.3.1	18.54 eV D_2 dataset	119
5.3.2	18.54 eV H_2 dataset	128
5.3.3	18.34 eV H_2 dataset	133
5.3.4	17.9 eV H_2 dataset	138
6	Conclusion	148
	References	150
	Appendices	153
A	Isolation of the vibrational archipelago in the two-color channel	153
B	Two-color calibration spectra	156
C	One-dimensional MFPADs	163
D	Recoil ion θ_z distributions	169
E	Recoil ion θ_z vs MFPAD plots	175
F	17.9 eV vibrational state $\nu=6$	181

List of Figures

1.1	Linear Combinations of Atomic Orbitals.	2
1.2	Energy curves for the lowest electronic states in H_2^+ that can be used to calculate vibrational states.	3
1.3	Overlap (shown in red) between the ground vibrational state of neutral H_2 (shown in orange) and an excited vibrational state of H_2^+ (shown in blue). The Franck-Condon region is bounded by the classical turning points of the initial state, which are shown in magenta.	4
1.4	Electron retroaction energy diagram. The direct dissociation pathway involves transitioning from the ground state neutral hydrogen wavefunction χH_2 (shown in red) to a continuum energy level E_K , shown in blue. The retroaction pathway, shown in green, involves first a transition to a bound vibrational state of the H_2^+ $1s\sigma_g$ electronic state, followed by a transition to a $2p\sigma_u$ state. Figure taken from [6].	7
1.5	Superposition of gerade and ungerade wavefunctions.	8
1.6	Simple cartoon visualization of the electron retroaction effect.	9
1.7	Potential energy surface of H_2^+ showing LICIs. LICIs occur when the angle θ between the molecular axis and the polarization axis is equal to $\pm\pi/2$, taken from[11].	11

1.8	Potential energy curves of H_2^+ shown at $\theta = \pi/2$ (black and blue curves) and $\theta = 0$ (red curves). Taken from[11].	12
1.9	Quantum electronic and vibrational states involved in the two-color experiment.	16
2.1	Electromagnetic spectrum from 10^{-1} m to 10^4 m.	18
2.2	Three-step model diagram of HHG in a gas cell irradiated by an intense laser, taken from the PhD thesis of John Vaughan[15]. In step 1, an electron tunnels through the potential barrier weakened by the laser. In step 2, the electron accelerates back towards the parent atom as the electric field of the laser oscillates and gains energy. In step 3, the electron recombines with the parent atom, and a photon with a frequency that is a multiple of the original laser frequency is emitted.	20
2.3	ASAP beamline diagram.	23
2.4	Flat Field Grating geometry[20].	24
2.5	VUV spectrometer CAD model.	26
2.6	The completed ASAP VUV spectrometer.	26
2.7	The Advanced Light Source (ALS).	28
2.8	ALS beamline map.	29
2.9	Beamline 10.0.1 layout[25].	30
2.10	COLTRIMS animation, taken from [29].	33
2.11	Microchannel plate.	34
2.12	Delay line anode wire timing.	35

2.13 Quad delay line detector and hexanode wiring[32].	36
2.14 AMOS COLTRIMS chamber.	37
2.15 AMOS COLTRIMS Spectrometer.	38
2.16 Constant Fraction Discriminator.	38
2.17 AMOS COLTRIMS chamber vacuum setup.	39
2.18 Experimental coordinate system.	40
3.1 Compiling LMF2Root in Visual Studio 2017.	43
3.2 Filehandling in Config.txt.	44
3.3 Zeroed recoil ion and electron time sums and centered position plots.	47
3.4 Recoil ion and electron run times.	48
3.5 Recoil ion and electron auto-calibration.	49
3.6 Example ColAHeLL.cfg file.	54
3.7 COLTRIMS5d Excel file.	56
3.8 Raw wiggles plot and time offset fit.	57
3.9 Simulated and actual wiggles runs.	58
3.10 Properly rotated recoil detector hit position plot.	59
3.11 Properly rotated electron detector hit position plot.	60
3.12 Electron momentum vs recoil ion momentum plots with incorrect upside-down detector rotation.	60

3.13	Electron momentum vs recoil ion momentum plots with correct detector rotation.	61
3.14	Electron momentum vs recoil ion momentum plots with incorrect B field direction.	61
3.15	Recoil ion momentum plots before (a) and after (b) correction for gas jet velocity.	62
3.16	Histograms in user_analysis.cpp.	63
4.1	Electron energy vs KER with course calibration.	66
4.2	Uncorrected recoil ion and electron momentum sphere projections.	67
4.3	Uncorrected recoil ion and electron θ and ϕ angles.	69
4.4	Shifted and stretched recoil ion and electron θ and ϕ angles.	71
4.5	Electron energy vs KER with shifts and stretches.	72
4.6	Momentum plots showing skewed momentum sphere.	73
4.7	Skewed recoil ion and electron θ and ϕ angles.	74
4.8	Electron energy vs KER with sheer mapping operations.	75
4.9	Jet dot contamination.	76
4.10	Contamination signature.	77
4.11	Contamination isolation.	78
4.12	Removed contamination.	79
4.13	Energy maps after contamination removal.	80
4.14	Polar representation of a Molecular Frame Photoelectron Angular Distribution.	81

4.15	MFPADs of events dissociating with molecular axis parallel to polarization axis.	83
4.16	MFPADs of events dissociating with molecular axis perpendicular to polarization axis.	83
4.17	Legendre polynomial MFPAD C_h and C_p fits.	86
4.18	Angular slice for photoelectron azimuthal angular distribution in a lab frame plane. Events within $\pm 15^\circ$ are added to the distribution by finding their azimuthal angular projection upon the plane.	89
4.19	A set of planes that are all parallel to the lab frame Z axis. The red planes represent the YZ and XZ planes in the lab frame. The green planes are rotated 30° from the lab frame YZ and XZ planes. The blue planes are rotated 60° from the lab frame YZ and XZ planes.	89
4.20	A set of acceptance regions that are all parallel to the lab frame Z axis. The red regions are within $\pm 15^\circ$ of the YZ and XZ planes in the lab frame. The green regions are within $\pm 15^\circ$ of planes that are rotated 30° from the lab frame YZ and XZ planes. The blue regions are within $\pm 15^\circ$ of planes that are rotated 60° from the lab frame YZ and XZ planes. All events inside those regions are projected onto the nearest plane to generate a planar lab frame PAD.	90
4.21	Hit positions of C_h and C_p events with positive recoil ion Z momentum.	91
4.22	Hit positions of C_h and C_p events with negative recoil ion Z momentum.	91
5.1	Overlapping and non-overlapping VUV and NIR pulses.	94
5.2	Two-color datasets taken during the 2017 two bunch beamtime at the ALS. . .	95
5.3	Isolation of the one-color dissociative channel in 18.54 eV H_2^+	96

5.4	45° Asymmetry parameter δ vs electron energy for the dissociation of H_2^+ via the one-color channel in a VUV-only experiment. Data points represent δ parameter values, and lines represent classical β parameter fits. VUV energies of 18.16 eV, 18.3 eV, 18.5. and 19.8 are indicated in red, green, blue, and black respectively. Taken from [8].	97
5.5	MFPAD energy dependence for events that dissociate via the one-color channel in 18.54 eV H_2^+ (short delay dataset) without any gating dependent on the angle between the molecular axis and the polarization axis.	98
5.6	H_2^+ Lab-frame photoelectron angular distributions of events that dissociate via the one-color channel at a VUV energy of 18.54 eV and electron energy between .00 eV and .10 eV.	99
5.7	H_2^+ lab-frame photoelectron angular distributions of events that dissociate via the one-color channel at a VUV energy of 18.54 eV and electron energy between .30 eV and .40 eV.	100
5.8	Recoil ion θ_z vs one-color dissociation MFPAD plot for 18.54 eV H_2^+ (long delay dataset).	101
5.9	Parallel and perpendicular dissociation via the one-color channel gating shown using recoil θ_z vs MFPAD plot for 18.54 eV H_2^+ (long delay dataset).	102
5.10	Parallel one-color dissociation MFPAD energy dependence in 18.54 eV H_2^+ (short delay dataset).	103
5.11	δ asymmetry parameters and β fit lines for events dissociating via the one-color channel while the molecular axis and polarization axis are parallel.	104

5.12	Asymmetry parameter δ (defined in section 4.4) vs electron energy for events dissociating via the one-color channel while the molecular axis and polarization axis are parallel.	105
5.13	Legendre polynomial fit asymmetry parameter $\delta\sigma$ (defined in Section 4.4) vs electron energy for events dissociating via the one-color channel while the molecular axis and polarization axis are parallel.	106
5.14	Perpendicular one-color dissociation MFPAD energy dependence in 18.54 eV H_2^+ (short delay dataset).	107
5.15	δ asymmetry parameters and β fit lines for events dissociating via the one-color channel while the molecular axis and polarization axis are perpendicular.	109
5.16	Asymmetry parameter δ vs electron energy for events with perpendicular dissociation via the one-color channel.	110
5.17	Legendre polynomial fit asymmetry parameter $\delta\sigma$ vs electron energy for events with perpendicular dissociation via the one-color channel.	111
5.18	MFPAD vs recoil ion θ_z plot showing narrow acceptance window to select events with a molecular axis that is at an angle of between 89° and 91° to the polarization vector that dissociate via the one-color channel (18.54 eV H_2^+ short delay dataset).112	
5.19	Perpendicular one-color dissociation MFPADs showing side lobes (18.54 eV H_2^+ short delay dataset).	113
5.20	Energy diagram showing 33 eV experiment to access Q_1 and Q_2 states. The Q_1 energy curve is shown in red, and the Q_2 curve is shown in blue. Figure adapted from [5].	114

5.21	Calculated and experimental angular distributions showing sidelobes at KER values of .02 eV and 6.3 eV in the dissociative ionization of D_2 . The ion is shown in blue, and the neutral atom is shown in green. The polarization vector is shown as a black vertical arrow, and is perpendicular to the molecular axis. Figure adapted from [5].	115
5.22	Isolation of the two-color dissociative channel in 18.54 eV H_2^+	116
5.23	Lab-frame photoelectron angular distributions in the two-color channel ($\nu = 10$ 18.54 eV H_2^+ , long delay dataset).	117
5.24	Recoil θ_z vs MFPAD plot for 18.54 eV H_2^+ long delay dataset.	118
5.25	D_2^+ energy map.	119
5.26	D_2^+ vibrational islands.	120
5.27	D_2^+ electron energy vibrational spectrum.	121
5.28	D_2^+ experimental vibrational peaks vs theoretical peaks calculated using Franck–Condon factors by Jan Dvořák.	122
5.29	D_2^+ $\nu=16$ vibrational and continuum wavefunctions used to calculate the Franck–Condon factor for dissociation. Figure courtesy of Jan Dvořák.	124
5.30	VUV/NIR time delay for D_2 dataset.	125
5.31	δ vs ν for 18.54 eV D_2^+ with 30 ps delay.	125
5.32	Legendre polynomial fit asymmetry Parameter $\delta\sigma$ vs ν for 18.54 eV D_2^+ with 30 ps delay.	126
5.33	VUV/NIR time delays for 18.54 eV H_2 datasets.	128

5.34	18.54 eV H_2^+ energy maps.	129
5.35	18.54 eV H_2^+ vibrational islands.	129
5.36	18.54 eV H_2^+ electron energy vibrational spectrum.	130
5.37	18.54 eV H_2^+ experimental vibrational peaks vs theoretical peaks calculated using Franck–Condon factors. Figure courtesy of Jan Dvořák.	131
5.38	δ vs ν for 18.54 eV H_2^+	132
5.39	Legendre polynomial fit asymmetry parameter $\delta\sigma$ vs ν for 18.54 eV H_2^+	132
5.40	VUV/NIR time delay for 18.34 eV H_2 dataset.	134
5.41	18.34 eV H_2^+ energy map.	134
5.42	18.34 eV H_2^+ vibrational islands.	135
5.43	18.34 eV H_2^+ electron energy vibrational spectrum.	135
5.44	18.34 eV H_2^+ experimental vibrational peaks vs theoretical peaks calculated using Franck–Condon factors. Figure courtesy of Jan Dvořák.	136
5.45	δ vs ν for 18.34 eV H_2^+ with 180 ps delay.	137
5.46	Legendre polynomial fit asymmetry parameter $\delta\sigma$ vs ν for 18.34 eV H_2^+ with 180 ps delay.	137
5.47	VUV/NIR time delays for 17.9 eV H_2 datasets.	138
5.48	17.9 eV H_2^+ energy maps.	139
5.49	17.9 eV H_2^+ vibrational islands.	140

5.50	17.9 eV H_2^+ electron energy vibrational spectrum.	141
5.51	17.9 eV H_2^+ experimental vibrational peaks vs theoretical peaks calculated using Franck–Condon factors. Figure courtesy of Jan Dvořák.	142
5.52	δ vs ν for states $\nu = 9$, $\nu = 10$, $\nu = 11$, and $\nu = 12$ for 17.9 eV H_2^+	143
5.53	δ vs ν for all states for 17.9 eV H_2^+	143
5.54	Legendre polynomial fit asymmetry parameter $\delta\sigma$ vs ν for 17.9 eV H_2^+	144
5.55	Recoil ion θ_z vs MFPAD plots for states $\nu = 7$ and $\nu = 8$ in 17.9 eV H_2^+	145
5.56	Potential energy curves of H_2^+ shown at $\theta = \pi/2$ (green and blue curves) and $\theta = 0$ (orange and violet curves). Figure courtesy of Jan Dvořák.	146
A.1	Full vibrational archipelago of events dissociating via the two-color channel in the short-delay 18.54 eV H_2 dataset.	153
A.2	Full vibrational archipelago of events dissociating via the two-color channel in the long-delay 18.54 eV H_2 dataset.	154
A.3	Full vibrational archipelago of events dissociating via the two-color channel in the 18.54 eV D_2 dataset.	154
A.4	Full vibrational archipelago of events dissociating via the two-color channel in the 18.34 eV H_2 dataset.	155
A.5	Full vibrational archipelago of events dissociating via the two-color channel in the short-delay 17.9 eV H_2 dataset.	155
A.6	Full vibrational archipelago of events dissociating via the two-color channel in the long-delay 17.9 eV H_2 dataset.	156

B.1	Recoil ion and electron θ and ϕ calibration plots for the 18.54 eV short delay H_2 dataset.	157
B.2	Recoil ion and electron θ and ϕ calibration plots for the 18.54 eV long delay H_2 dataset.	158
B.3	Recoil ion and electron θ and ϕ calibration plots for the 18.54 eV D_2 dataset.	159
B.4	Recoil ion and electron θ and ϕ calibration plots for the 18.34 eV H_2 dataset.	160
B.5	Recoil ion and electron θ and ϕ calibration plots for the 17.9 eV long delay H_2 dataset.	161
B.6	Recoil ion and electron θ and ϕ calibration plots for the 17.9 eV short delay H_2 dataset.	162
C.1	One-dimensional MFPADs for states dissociating via the two-color channel for the short delay 18.54 eV H_2 dataset.	163
C.2	One-dimensional MFPADs for states dissociating via the two-color channel for the long delay 18.54 eV H_2 dataset.	164
C.3	One-dimensional MFPADs for states dissociating via the two-color channel for the 18.54 eV D_2 dataset.	165
C.4	One-dimensional MFPADs for states dissociating via the two-color channel for the 18.34 eV H_2 dataset.	166
C.5	One-dimensional MFPADs for states dissociating via the two-color channel for the short delay 17.9 eV H_2 dataset.	167
C.6	One-dimensional MFPADs for states dissociating via the two-color channel for the long delay 17.9 eV H_2 dataset.	168

D.1	Recoil ion θ_z distributions for states dissociating via the two-color channel for the short delay 18.54 eV H_2 dataset.	169
D.2	Recoil ion θ_z distributions for states dissociating via the two-color channel for the long delay 18.54 eV H_2 dataset.	170
D.3	Recoil ion θ_z distributions for states dissociating via the two-color channel for the 18.54 eV D_2 dataset.	171
D.4	Recoil ion θ_z distributions for states dissociating via the two-color channel for the 18.34 eV H_2 dataset.	172
D.5	Recoil ion θ_z distributions for states dissociating via the two-color channel for the short delay 17.9 eV H_2 dataset.	173
D.6	Recoil ion θ_z distributions for states dissociating via the two-color channel for the long delay 17.9 eV H_2 dataset.	174
E.1	Recoil ion θ_z vs MFPAD plots for states dissociating via the two-color channel for the short delay 18.54 eV H_2 dataset.	175
E.2	Recoil ion θ_z vs MFPAD plots for states dissociating via the two-color channel for the long delay 18.54 eV H_2 dataset.	176
E.3	Recoil ion θ_z vs MFPAD plots for states dissociating via the two-color channel for the 18.54 eV D_2 dataset.	177
E.4	Recoil ion θ_z vs MFPAD plots for states dissociating via the two-color channel for the 18.34 eV H_2 dataset.	178
E.5	Recoil ion θ_z vs MFPAD plots for states dissociating via the two-color channel for the short delay 17.9 eV H_2 dataset.	179

E.6	Recoil ion θ_z vs MFPAD plots for states dissociating via the two-color channel for the long delay 17.9 eV H_2 dataset.	180
F.1	Zoomed-in vibrational archipelago displaying states $\nu=6$, $\nu=7$, and $\nu=8$ for 17.9 eV H_2^+	181
F.2	Isolation of vibrational state $\nu=6$ for 17.9 eV H_2^+	182
F.3	Recoil θ_z vs MFPAD plots for vibrational state $\nu=6$ for 17.9 eV H_2^+	182
F.4	Recoil θ_z distributions for vibrational state $\nu=6$ for 17.9 eV H_2^+	183
F.5	One-dimensional MFPADs for vibrational state $\nu=6$ for 17.9 eV H_2^+	183

List of Tables

3.1	TDC channels and the source of their signals.	45
3.2	Typical conversion factors.	46
3.3	Reconstruction methods and number of input signals from each TDC source that are required for the method to be used.	51
3.4	Important ColAHelL commands.	64
3.5	Important vector operations.	65
5.1	COLTRIMS spectrometer settings for the two-color experiment.	95
5.2	Summary of two-color D_2^+ data.	126
5.3	Summary of two-color 18.54 eV H_2^+ short delay data.	133
5.4	Summary of two-color 18.54 eV H_2^+ long delay data.	133
5.5	Summary of two-color 18.34 eV H_2^+ data.	138
5.6	Summary of two-color 17.9 eV H_2^+ short delay data.	144
5.7	Summary of two-color 17.9 eV H_2^+ long delay data.	144

Chapter 1

Introduction

1.1 The hydrogen molecule

The idea of the wave-particle duality of matter, one of the key cornerstones of quantum mechanics, was proposed by Louis de Broglie in 1924[1]. Quantum theory is almost a century old at the time of this writing in 2023, and in that time, it has greatly expanded the boundaries of human knowledge about how the building blocks of the world around us work. The advancements in understanding of how light and matter interact have changed the world dramatically. The science of chemistry and our understanding of atoms and molecules has been completely revolutionized. However, despite the incredible progress that has been made, there are still unanswered questions about even the simplest molecular systems.

Hydrogen is the most common element in the universe by far. The hydrogen molecular ion, H_2^+ , is the simplest possible molecule in the universe. Quantum mechanics can provide a closed form analytical model for the hydrogen atom[2], but even the simplest possible molecule poses a problem that cannot be solved in an analytically closed form. Physicists studying diatomic molecules have had to devise increasingly intricate tools to model these systems with increasing accuracy.

Electronic states can be found using Molecular Orbital theory[3], which approximates the electronic states of molecules using linear combinations of atomic orbitals. As a simple example, if we let ψ_a equal the ground electronic state of one atom in a diatomic molecule, and we let ψ_b be the ground electronic state of the other in the molecule, and let N represent a normalization factor, we can write the combined wavefunction as a linear combination of the two:

$$\psi_{\pm} = N(\psi_a \pm \psi_b) \quad (1.1)$$

This leads to two molecular orbitals, one of even and one of odd parity. In this example, the even parity (also known as gerade or g) orbital has a region of constructive interference of the contributing wavefunctions ψ_a and ψ_b between the two nuclei. The odd parity (also known as ungerade or u) orbital has a region of destructive interference of the contributing wavefunctions ψ_a and ψ_b between the two nuclei. When the probability density is determined from the combined wavefunction, the gerade orbital acts as a bonding orbital, with electron probability between the two nuclei, and the ungerade orbital acts as an antibonding orbital, with no electron probability between the two nuclei, as seen in Figure 1.1.

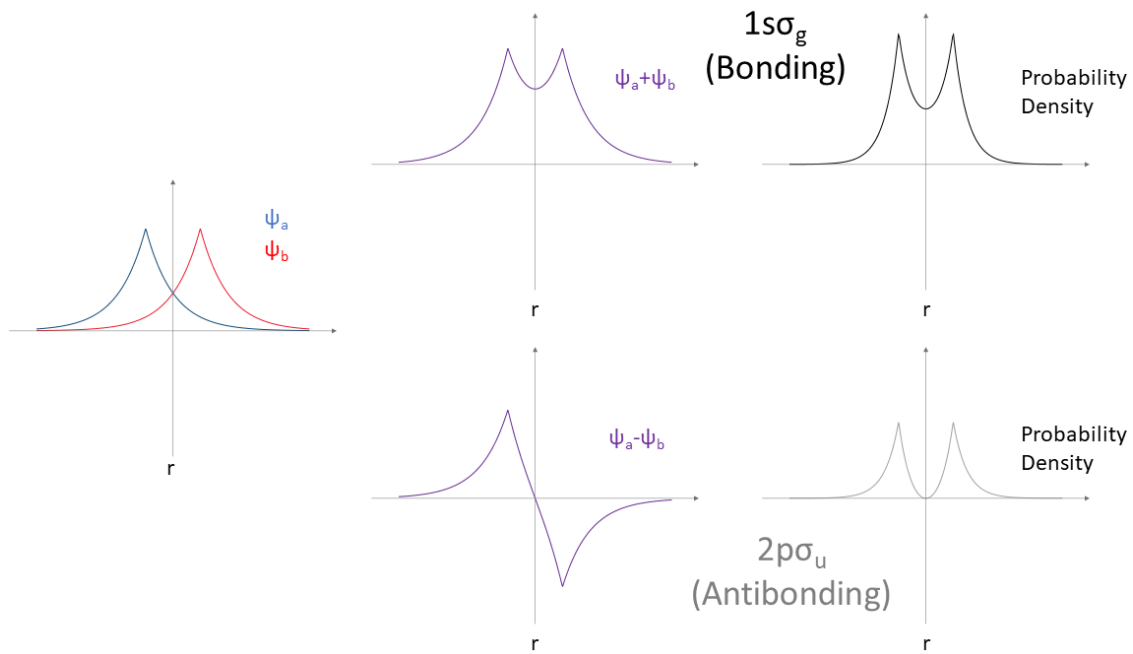


Figure 1.1: Linear Combinations of Atomic Orbitals.

The Born-Oppenheimer approximation, which treats the heavy nuclei as stationary compared to the light and fast-moving electrons, was first proposed in 1927[4]. This allows the electronic states to be calculated for multiple values of the internuclear separation, and allows for the quantum vibrational states of the nuclei to be calculated using the potential

from the electronic states. This approximation is a fundamental tool in calculating stationary states in molecules.

When the energy of these wavefunctions is determined as a function of internuclear distance, there is an energy splitting between the g and u orbitals. The bonding gerade orbital is lower in energy, and the antibonding ungerade orbital is higher, as seen in Figure 1.2.

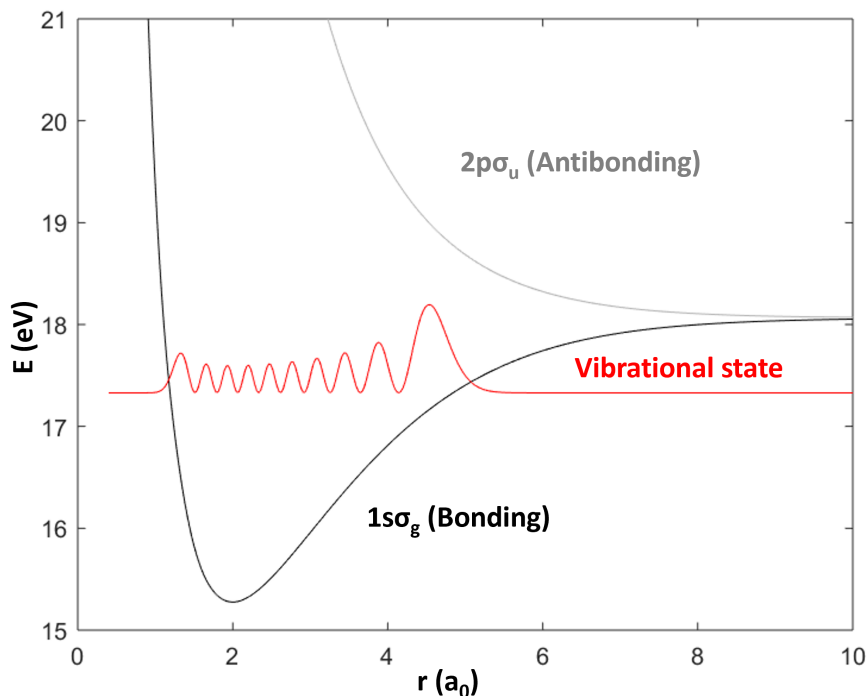


Figure 1.2: Energy curves for the lowest electronic states in H_2^+ that can be used to calculate vibrational states.

This energy difference between the two orbitals determines how much energy is required to break the molecule's chemical bond once it has been formed.

Similar arguments to those underlying the Born-Oppenheimer approximation also carry over to transitions between different electronic quantum states. The Franck-Condon principle, proposed around the same time, states that as electrons are far lighter and faster than nuclei, transitions between one electronic state and another occur while the nuclei are stationary. This leads to a higher probability of electronic transitions near classical turning points of the nuclei, and states that the probability of these vertical transitions between electronic

states is proportional to the overlap of the initial wavefunction and the final wavefunction, as shown in Figure 1.3.

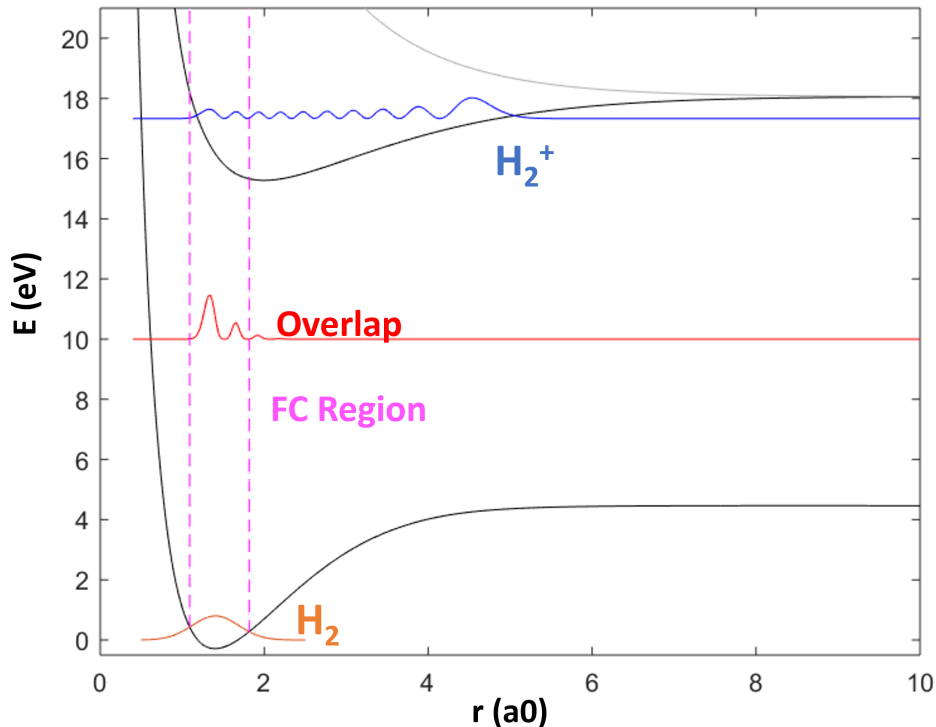


Figure 1.3: Overlap (shown in red) between the ground vibrational state of neutral H_2 (shown in orange) and an excited vibrational state of H_2^+ (shown in blue). The Franck-Condon region is bounded by the classical turning points of the initial state, which are shown in magenta.

This can be derived from the transition dipole moment μ_{fi} . If we separate a molecule with n electrons and N nuclei into electronic states $|\epsilon\rangle$ and vibrational states $|\nu\rangle$, the transition dipole moment can be written as[3]:

$$\mu_{fi} = \langle \epsilon_f \nu_f | \{ -e \sum_n r_n + e \sum_N Z_N R_N \} \epsilon_i \nu_i \rangle \quad (1.2)$$

Exploiting the orthogonality of the electronic states, to eliminate the sum over N , this expression can be further evaluated to yield:

$$\mu_{fi} = -e \sum_n \langle \epsilon_f | r_n | \epsilon_i \rangle \langle \nu_f | \nu_i \rangle \quad (1.3)$$

This can be further simplified to:

$$\mu_{fi} = \mu_{\epsilon_f \epsilon_i} P_f^i \quad (1.4)$$

where $\mu_{\epsilon_f \epsilon_i} = -e \sum_n \langle \epsilon_f | r_n | \epsilon_i \rangle$, the electronic transition dipole moment, and $P_f^i = \langle \nu_f | \nu_i \rangle$ is known as a Franck–Condon factor. These Franck–Condon factors are widely used tools to understand transitions between electronic states, and help to determine spectroscopic properties of molecules.

From the earliest days of quantum chemistry in the 1920s to today, incredible strides in understanding have been made. However, there are still many unanswered questions, especially when simple approximations begin to falter.

1.2 Electron retroaction effect

One simple system with dynamics that can require going beyond simple models to fully understand is the dissociative photoionization of hydrogen. When a neutral hydrogen molecule is irradiated with sufficient energy, an electron can be removed, leading to the following reaction:



If the energy is high enough (above a level known as the dissociation threshold), there is also a probability of a molecular breakup involving the H_2^+ molecular ion. In this case, the ion dissociates into a proton and a neutral hydrogen atom, leading to the following overall net reaction:



The lowest lying electronic states in H_2^+ are $1s\sigma_g$ and $2p\sigma_u$. Therefore, we can also write the previous reactions as follows:



The result of the transition from H_2 to $H_2^+(2p\sigma_u)$ will always be a dissociation, with an equal probability of either nuclear center of the molecular ion ending as the neutral hydrogen and equal probability of either nuclear center ending as the leaving proton. The transition from H_2 to $H_2^+(1s\sigma_g)$ can result in either a bound vibrational ion, or a direct transition to the vibrational continuum. In this dissociative case, there is an equal probability of either nuclear center of the molecular ion ending as the neutral hydrogen and equal probability of either nuclear center ending as the leaving proton. Either of these direct dissociative paths leads to a completely symmetric dissociation, where the proton has an equal probability of being emitted towards or away from the photoelectron.

However, this reaction, one of the simplest possible, experimentally does not always have the symmetry it would be expected to have. Processes that involve autoionization from doubly excited Q states are a known mechanism to break this symmetry[5], but this requires enough energy to excite electrons into these excited states. Asymmetry in dissociative photoionization in the presence of relatively low energy radiation that is incapable of reaching these excited Q states needs to happen via a different mechanism.

Such a mechanism was proposed in 2014 by Serov and Kheifets[6]. This mechanism, dubbed electron retroaction, notes that the Coulomb field of the leaving photoelectron can interact with the molecular ion. At low incident radiation energies, the nuclei of the molecular ion are in bound vibrational states of the $1s\sigma_g$ electronic potential. If the leaving photoelectron is going slowly enough, this interaction between the field of the photoelectron

and the molecular ion can lead to a coupling of the $1s\sigma_g$ and $2p\sigma_u$ states while the nuclei are near the outer turning point of their bound vibrational state. An energy diagram showing this retroaction mechanism and the direct dissociative pathway is shown in Figure 1.4.

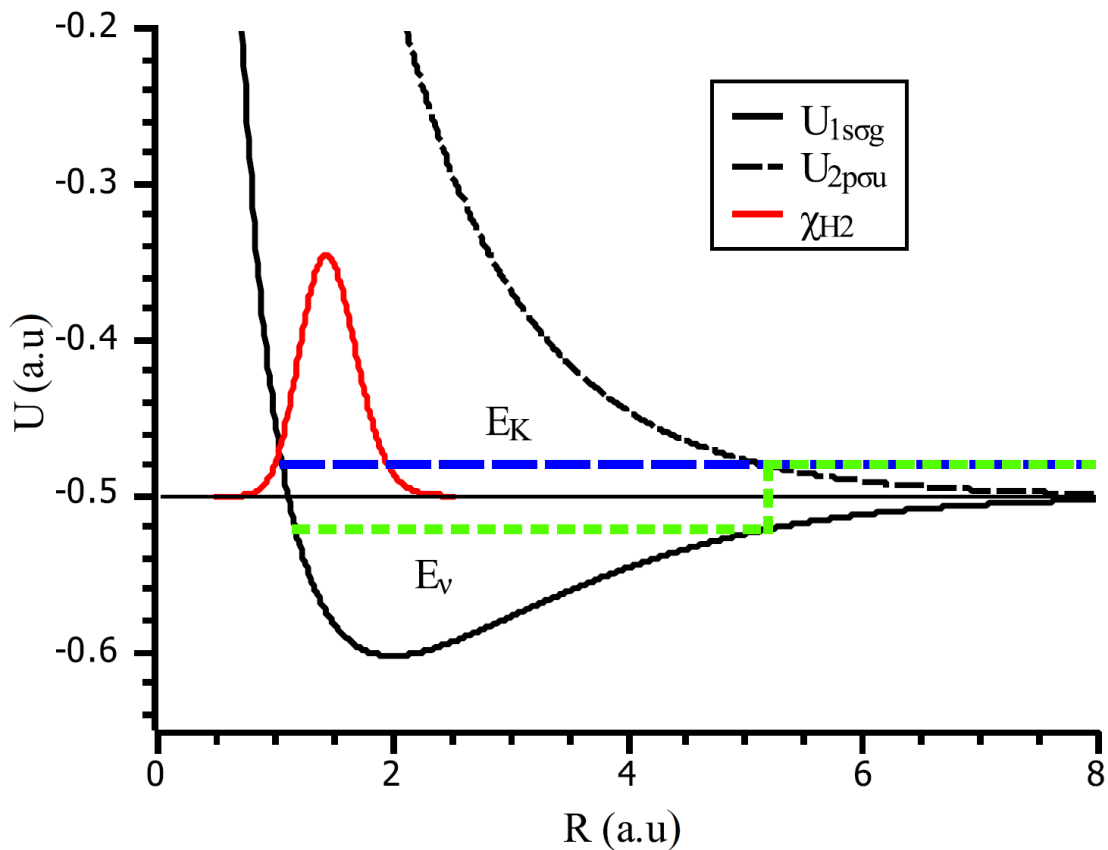


Figure 1.4: Electron retroaction energy diagram. The direct dissociation pathway involves transitioning from the ground state neutral hydrogen wavefunction χ_{H_2} (shown in red) to a continuum energy level E_K , shown in blue. The retroaction pathway, shown in green, involves first a transition to a bound vibrational state of the H_2^+ $1s\sigma_g$ electronic state, followed by a transition to a $2p\sigma_u$ state. Figure taken from [6].

Superpositions of the gerade and ungerade states result in an asymmetric state, as seen in Figure 1.5.

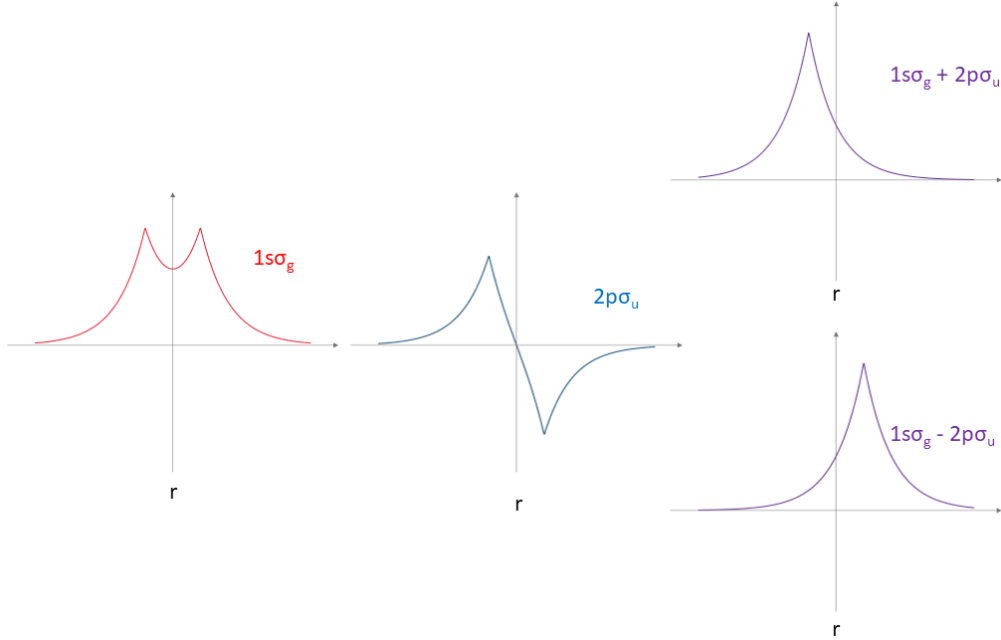


Figure 1.5: Superposition of gerade and ungerade wavefunctions.

These superpositions can be expressed as right and left states, as shown below:

$$|l\rangle = (|1s\sigma_g\rangle + |2p\sigma_u\rangle) / \sqrt{2} \quad (1.9)$$

$$|r\rangle = (|1s\sigma_g\rangle - |2p\sigma_u\rangle) / \sqrt{2} \quad (1.10)$$

These states will experience a different potential due to the leaving photoelectron, as one is closer to the electron and one is further away. This potential difference can be expressed as $2d(R)/r_e^2$, where $d(R)$ is the dipole matrix element and r_e is the distance to the ejected electron[6]. This potential difference is therefore inversely proportional to the photoelectron's energy and the amount of time since the photoelectron was ejected. For slow photoelectrons ejected to the right side of the molecule that have had little time to escape the area, the potential for the state at the right side of the molecule is higher, leading to preferential localization of the bound electron on the left side of the molecule. This means that in the dissociation, a proton will preferentially be emitted in the direction of the photoelectron.

Interference between the retroaction pathway and the direct dissociative pathway leads to asymmetry in the observed proton emission.

A simpler cartoon way of thinking about retroaction process is to imagine the bound electron cloud being repulsed by the leaving photoelectron. If the photoelectron leaves quickly, the repulsion is minor and the cloud can return to its equilibrium once the photoelectron has moved far enough away. However, if the photoelectron leaves slowly, the cloud has more time to feel the repulsion, and can be pushed far enough away to allow a proton to escape, as shown in Figure 1.6.

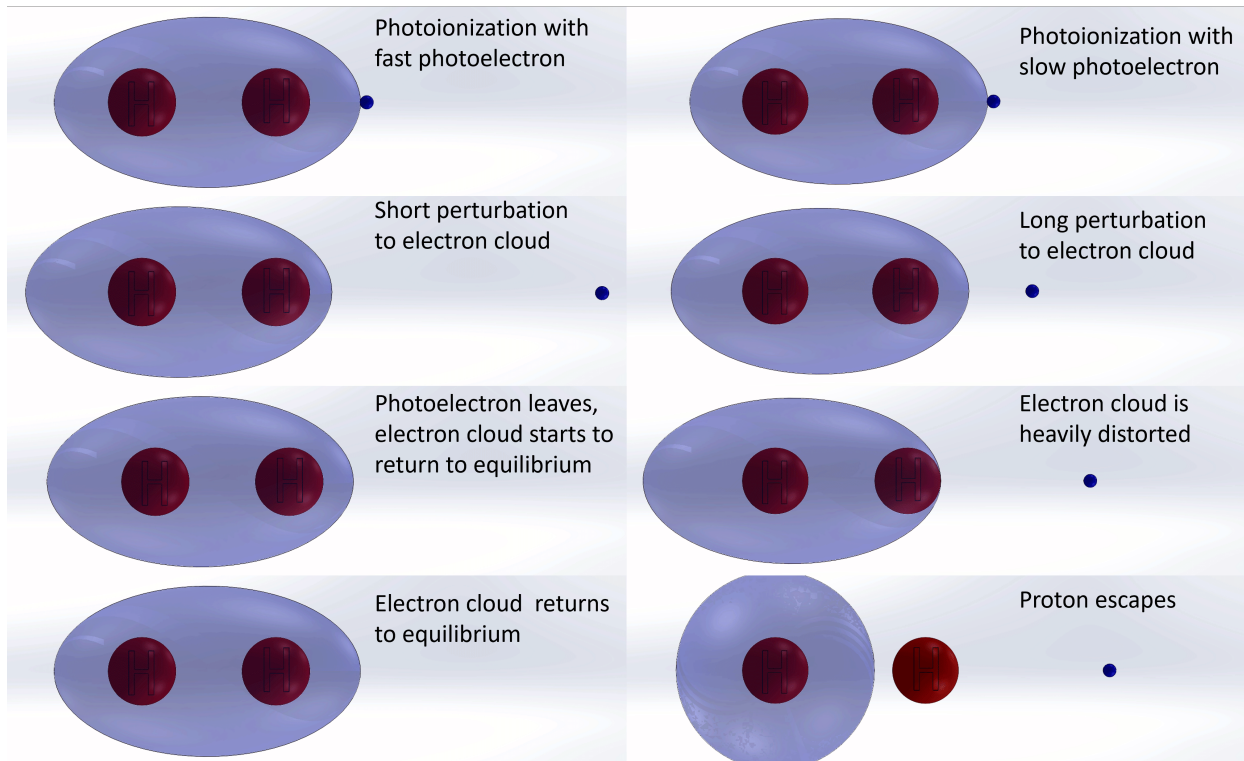


Figure 1.6: Simple cartoon visualization of the electron retroaction effect.

After being theoretically proposed in 2014, experiments published in 2016[7] and 2019[8] have reported on the effect. The expected asymmetry trend, with preferential proton emission in the direction of the photoelectron, the expected dependence of that asymmetry on photoelectron energy, where asymmetry decreases with increasing photoelectron energy, and

the expected dependence of the asymmetry on kinetic energy release, where asymmetry increases with decreasing kinetic energy release, were all observed experimentally.

1.3 Light induced conical intersections

Another subject of interest in the study of interactions between molecules and light is the angular relationship between molecules and polarized light that is low in energy, with wavelengths in the near-infrared region.

As stated earlier, in the Born-Oppenheimer approximation nuclear vibrational states are dependent upon the electronic potential energy. The potential energy surface for a homonuclear diatomic molecule like H_2 or D_2 is one-dimensional, where the potential energy depends on the internuclear separation, the only internal degree of freedom[9]. However, in the presence of a sufficiently intense polarized external field, the polarization of the field represents a second internal degree of freedom and allows for a 2-dimensional potential energy surface. This 2-dimensional surface results in a variety of physically interesting phenomena. One of the most important is a state crossing, also known as a conical intersection. These conical intersections, which usually only exist in polyatomic molecules because they require multiple degrees of freedom, allow for electronic decays that are key to the stability of important molecules such as DNA[10]. At the conical intersection, nonadiabatic processes dominate. Away from the conical intersection in the angular dimension, the potential energy surface is also modified, effectively pinching the potential energy curves closer together in the energy dimension than they would be in the absence of the light. Adiabatic dynamics dominate in this region, which can serve to soften chemical bonds.

A three-dimensional representation of the potential energy surface of H_2^+ with so-called Light Induced Conical Intersections (LICI) due to the overlapping NIR field from a laser is shown in Figure 1.7.

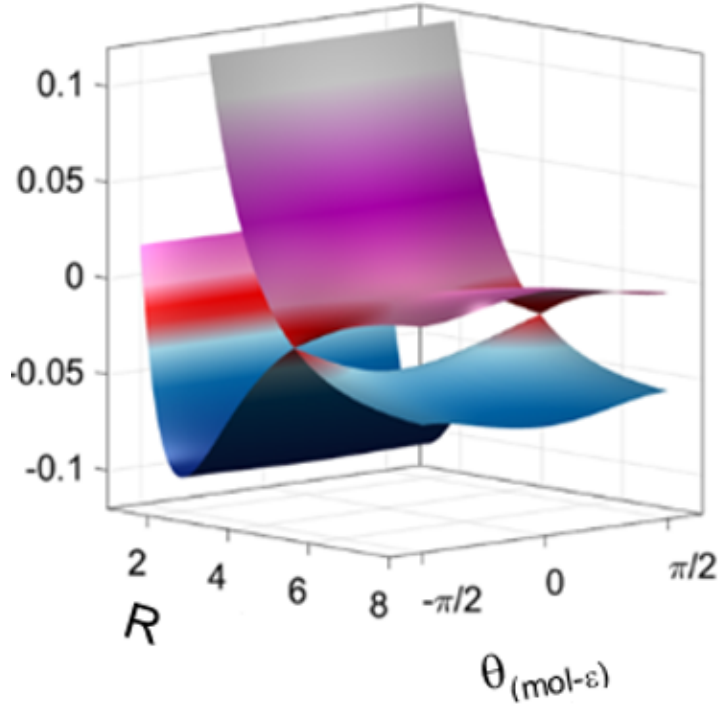


Figure 1.7: Potential energy surface of H_2^+ showing LICIs. LICIs occur when the angle θ between the molecular axis and the polarization axis is equal to $\pm\pi/2$, taken from[11].

This can be derived using the Floquet approximation[12], which involves using a basis set of periodic states to solve time-dependent problems. The time-evolution of a state $|\psi(t)\rangle$ with a time-dependent Hamiltonian $H(t)$ can be expanded into a number of time-independent coefficients a_n and periodic eigenstates $|n\rangle$, allowing the time-dependent problem to be treated as if it were time-independent. In this approximation, the Floquet Hamiltonian for the LICIs in H_2^+ can be written as:

$$H = T_N + \begin{pmatrix} V_g(R) & \frac{\epsilon}{2}d(R)\cos\theta \\ \frac{\epsilon}{2}d(R)\cos\theta & V_u(R) - \hbar\omega \end{pmatrix} \quad (1.11)$$

where V_g and V_u are the potential curves for the $1s\sigma_g$ and $2p\sigma_u$ states, $d(R)$ is the transition dipole moment, $\hbar\omega$ is the energy of the light, ϵ is the intensity of the light, θ is the angle

between the molecular axis and the polarization of the light, and T_N is the fixed nuclei Hamiltonian.

The energy surfaces can be found by diagonalizing the potential energy matrix. For H_2^+ , the shape of these potential energy surfaces means that the chemical bond holding the molecular ion together is stronger when the molecule is perpendicular to the polarization ($\theta = \pi/2$), and weaker when parallel to the polarization ($\theta = 0$). This would imply much stronger dissociation parallel to polarization, a prediction that has been supported by experimental results[11].

A two-dimensional plot showing the parallel and perpendicular cases for H_2^+ is shown in Figure 1.8.

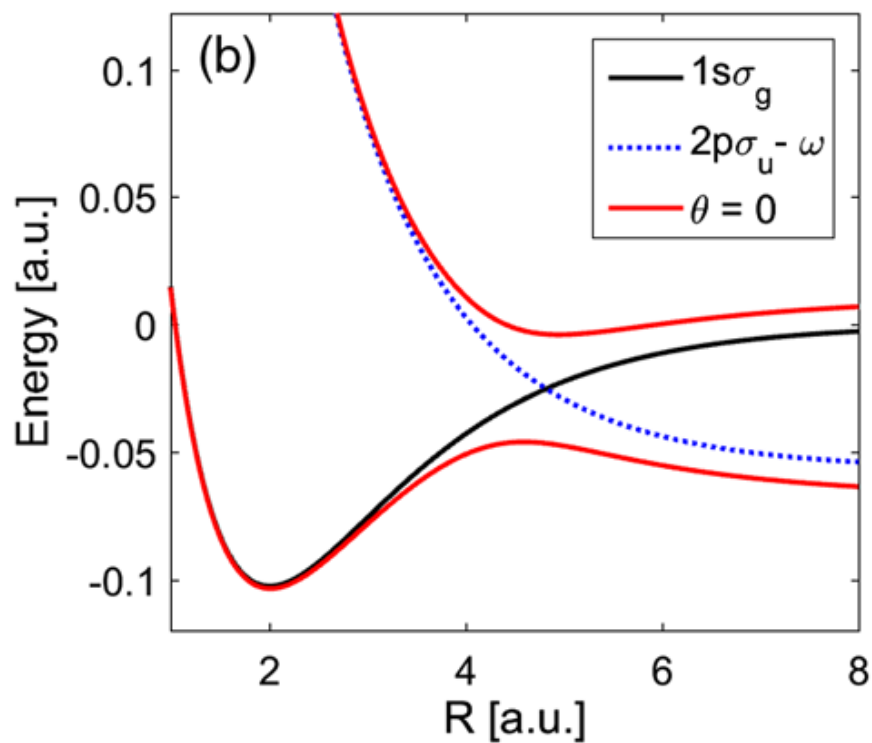


Figure 1.8: Potential energy curves of H_2^+ shown at $\theta = \pi/2$ (black and blue curves) and $\theta = 0$ (red curves). Taken from[11].

1.4 Motivation for a two-color experiment

Armed with the above knowledge, the idea for a two-color experiment that can explore the interactions between both effects begins to take shape. If an experiment were conducted using radiation with an energy near the dissociation threshold to photoionize H_2 to H_2^+ , resulting in very low energy photoelectrons, AND with NIR laser radiation to dissociate the resulting molecular ions that end up in bound vibrational states, the electron retroaction effect in the presence of a dressed potential energy surface with LICIs could be explored experimentally.

Doing this yields three distinct reaction channels. The first is photoionization of H_2 to H_2^+ :



This channel will have a distinct electron energy and ion time of flight signature, and can be easily separated from the other two.

The second channel is one-color dissociation of the bound H_2^+ ion, and is only available if the energy is above the dissociation threshold:



This is the channel where the retroaction effect has been observed with photoelectrons ranging from ≈ 20 meV to 3 eV. Events in this channel will follow an energy sum relation, as shown below:

$$E_{sum} = KER + E_e = h\nu_{UV} - E_{diss} \quad (1.14)$$

where E_e is the photoelectron energy, $h\nu$ is the energy of the ionizing photon, E_{diss} is the dissociation energy, and KER is the kinetic energy release of the reaction. In this case, the

kinetic energy release is equal to the sum of the kinetic energy of the proton and the neutral hydrogen atom:

$$KER = E_{H^+} + E_H \quad (1.15)$$

For a two body breakup, the momenta of the proton and the neutral hydrogen atom sum to zero:

$$\vec{v}_{H^+}m_{H^+} + \vec{v}_Hm_H = 0 \quad (1.16)$$

This means that the energy of the hydrogen atom can be expressed as:

$$E_H = \frac{m_{H^+}}{m_H} E_{H^+} \quad (1.17)$$

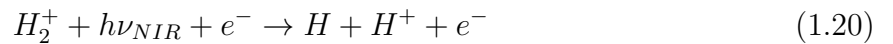
With this, the KER can be rewritten in terms of the ion energy:

$$KER = E_{H^+} + \frac{m_{H^+}}{m_H} E_{H^+} \quad (1.18)$$

Finally, this can be simplified using the reduced mass $\mu = \frac{m_{H^+}m_H}{m_{H^+}+m_H}$ and the ion momentum, as shown below:

$$KER = \frac{P_{H^+}^2}{2\mu} \quad (1.19)$$

The third channel, which is novel to this experiment, is two-color dissociation. In this channel, bound vibrational states of the H_2^+ ion dissociate in the presence of NIR laser radiation:



This reaction can occur because a population of H_2^+ created in the initial photoionization of H_2 exists in bound vibrational states. The transition of ground state neutral hydrogen to each vibrational state $|\chi_\nu\rangle$ of H_2^+ can be estimated using a Franck-Condon factor as shown below:

$$P_\nu^0 = |\langle \chi_\nu | \chi_0^0 \rangle|^2 \quad (1.21)$$

Bound vibrational states that are not able to dissociate via the one-color dissociation channel can dissociate in the two-color channel if their vibrational energy level is closer to the dissociation energy than the NIR photon energy. Because of this, the two-color channel will follow an energy sum relation that includes the energy of the NIR photon, as shown below:

$$E_{sum} = KER + E_e = h\nu_{VUV} + h\nu_{NIR} - E_{diss} \quad (1.22)$$

The strength of this dissociation can be estimated using another Franck-Condon factor, this time for the transition from a bound vibrational state χ_ν to a continuum vibrational state χ_ϵ :

$$P_\nu = |\langle \chi_\epsilon | \mu | \chi_\nu \rangle|^2 \quad (1.23)$$

An energy diagram of this process, showing photoionization and the promotion from ground state hydrogen to vibrationally excited bound H_2^+ , and the subsequent NIR induced promotion from vibrationally excited bound H_2^+ to a continuum vibrational state is shown in Figure 1.9.

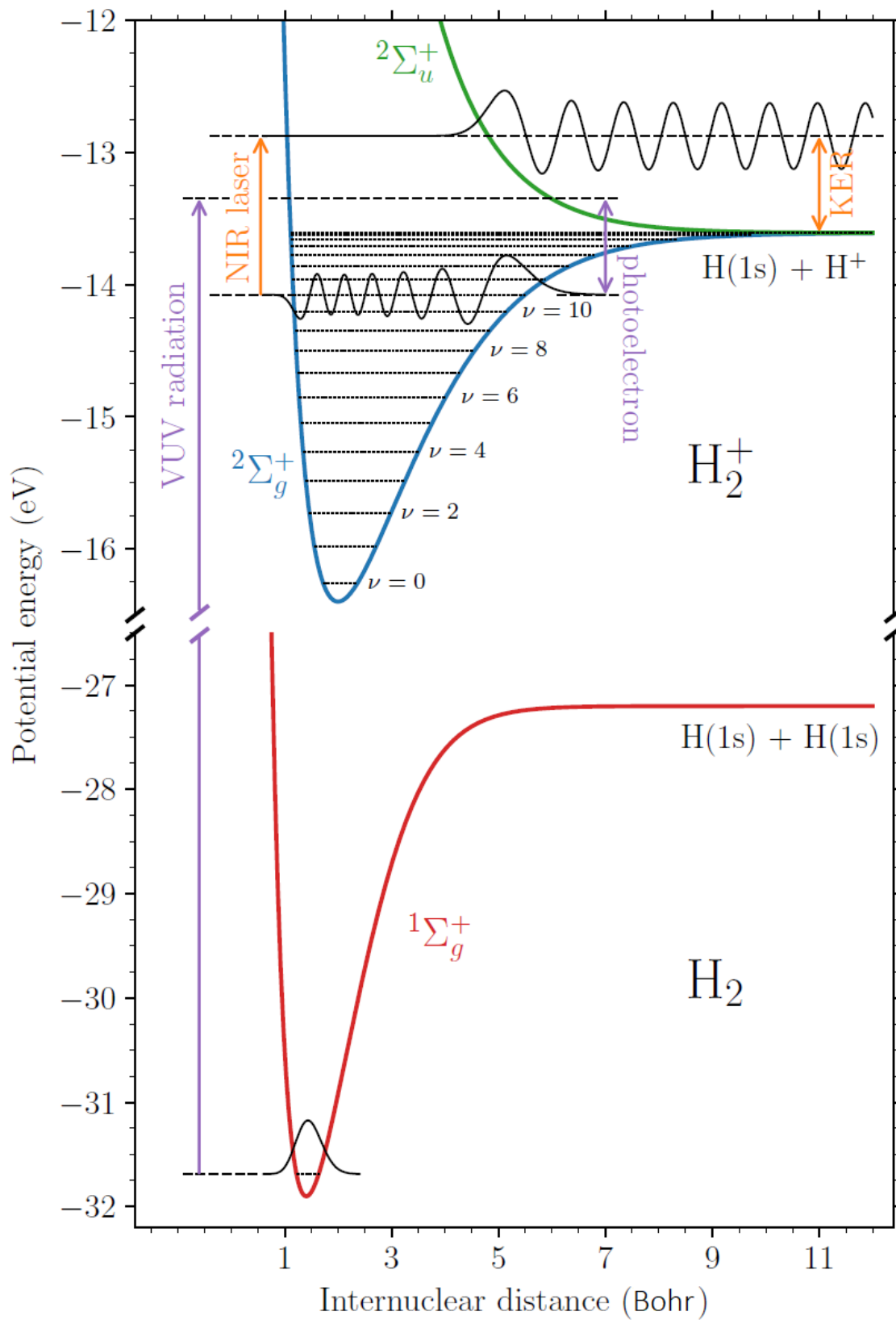


Figure 1.9: Quantum electronic and vibrational states involved in the two-color experiment.

This two-color channel also opens up an avenue of controlling when dissociation happens by controlling the time delay between the photoionizing pulse and the NIR laser pulse.

If we treat the photoelectron as a classical particle, its velocity can be expressed as $v = \sqrt{\frac{2E_e}{m_e}}$. Using this relation, a photoelectron with a kinetic energy of .1 eV would have a velocity of 3.544 Bohr per femtosecond. After 1000 femtoseconds (1 picosecond), the photoelectron has traveled 3544 Bohr.

The bond length for H_2^+ is 1.9972 Bohr[13]. After a delay of around a picosecond, the electron has traveled far from the vicinity of the remaining bound ion. The atomic unit for electric fields is $5.14 \times 10^9 V/cm$. After a picosecond and now at a distance of 3544 Bohr, the Coulomb field strength of the .1 eV photoelectron is $409 V/cm$, or 7.964×10^{-8} atomic units, a value that is small enough that it should have no effect on the remaining molecular ion.

This implies that if there is a sufficient delay between the photoionization of H_2 and a NIR pulse that induces dissociation of the resulting H_2^+ ion from a bound vibrational state, the electron will have had time to leave the area and the electron retroaction effect should no longer be observed.

The asymmetry in proton emission from retroaction effect should be detectable in this channel if it is present and survives the interaction with the NIR field. Additionally, a light-induced conical intersection, if present, should lead to a dependence on the angle between the polarization axis and the molecular axis for dissociation. This could also lead to an increased dissociation probability by allowing dissociation via tunneling to the continuum.

In Chapter 2, the experimental setup that was used to carry out this investigation will be described. Chapters 3 and 4 will describe the data analysis that was carried out. Chapter 5 will contain the results extracted, and Chapter 6 will serve as a conclusion.

Chapter 2

Experimental setups

2.1 Vacuum ultraviolet light sources

In order to study the photoionization phenomena of interest, light sources that can provide radiation in the desired energy region of the electromagnetic spectrum are needed. The dissociation threshold for H_2 is 18.075 eV, and the first ionization energy for H_2 is 13.6 eV. These energies lie in the vacuum ultraviolet or VUV region of the EM spectrum. The VUV region can be defined in wavelength as being between approximately 200nm and 10nm, which corresponds to approximately 6.2 eV to 124 eV in energy, as shown in Figure 2.1.

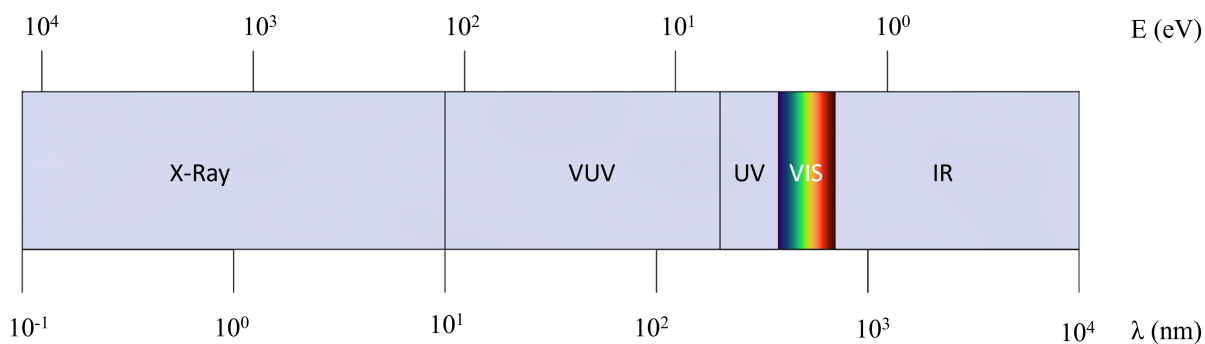


Figure 2.1: Electromagnetic spectrum from 10^{-1} m to 10^4 m.

There are several ways of generating VUV light pulses. One method is to use a tabletop High Harmonic Generation (HHG) setup. This yields a pulse with a very narrow temporal profile comprised of many different wavelengths of light. Another way to generate VUV light pulses is to use a synchrotron light source. Synchrotron light sources are user facilities that use synchrotron radiation given off by relativistically accelerated electrons to generate light pulses that have a narrower energy width but with a wider temporal profile than HHG pulses.

The advantages and drawbacks of each method of creating VUV light determines which is optimal for a given experiment.

2.2 High Harmonic Generation process

The first method to discuss is High Harmonic Generation (HHG). HHG is performed by taking a laser and irradiating a target (usually a noble gas) at a high intensity of between $10^{11}W/cm^2$ and $10^{14}W/cm^2$.

At this intensity, the electric field of the laser is similar in strength to the electric field inside the atom. At this field strength, a high harmonic generation process described using a semi-classical three-step model first proposed in the 90s[14], can take place.

In the first step, an electron in one of the atoms making up the gas target experiences a modified potential due to the laser. This electron can quantum tunnel out of its bound potential due to the field of the laser. In the second step, the laser electric field oscillates and changes direction. This causes the electron to accelerate and gain energy. In the final step, the energetic electron finally recombines with the parent ion. The extra energy gained by the electron during this acceleration is given off as a photon. These photons have energies that are integer multiples of the original laser energy, as shown below:

$$E = n\hbar\omega \tag{2.1}$$

This leads to generation of a number of higher harmonics of the original frequency of the photons in the laser (also known as the fundamental frequency). A diagram of this three-step process is shown in Figure 2.2.

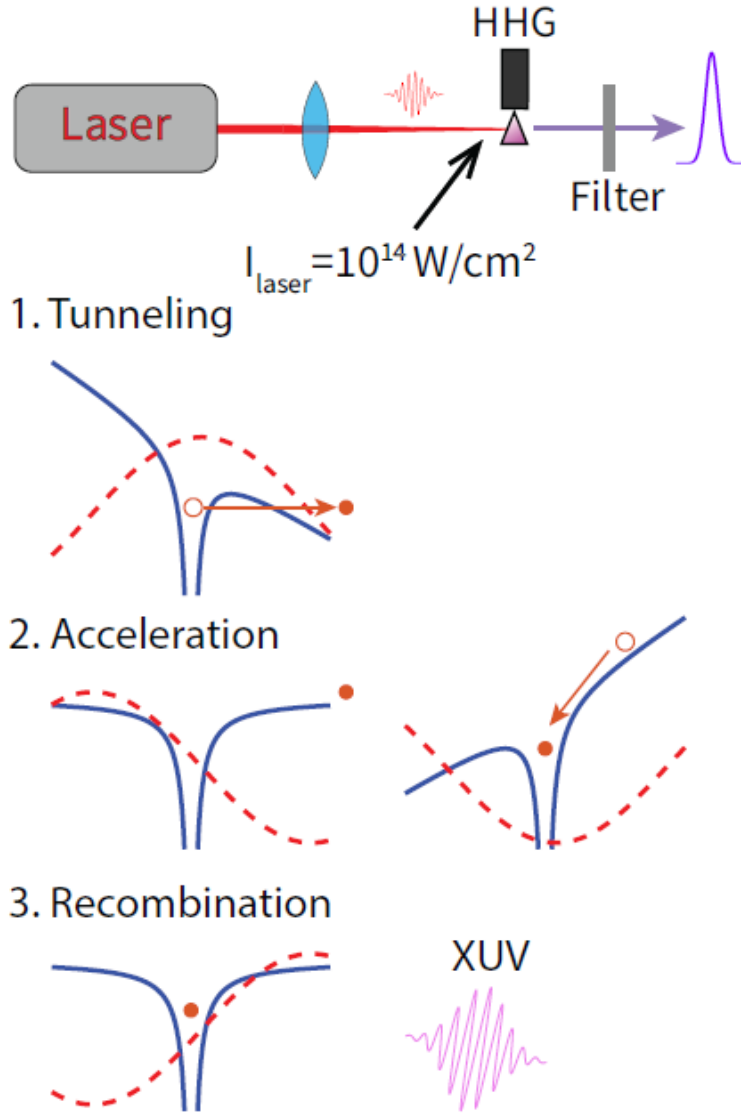


Figure 2.2: Three-step model diagram of HHG in a gas cell irradiated by an intense laser, taken from the PhD thesis of John Vaughan[15]. In step 1, an electron tunnels through the potential barrier weakened by the laser. In step 2, the electron accelerates back towards the parent atom as the electric field of the laser oscillates and gains energy. In step 3, the electron recombines with the parent atom, and a photon with a frequency that is a multiple of the original laser frequency is emitted.

The excess energy released when an electron recombines can be written as:

$$\Omega = I_p + 2U_p \sin^2(\omega_L t) \quad (2.2)$$

In this expression I_p is the ionization potential of the HHG target, ω_L is the fundamental frequency of the laser, and U_p is the cycle-averaged kinetic energy of the electron in the laser field, also known as the ponderomotive energy. This ponderomotive energy is related to the electric field strength of the laser E_L , and can be expressed as[15]:

$$U_p = \frac{e^2 E_L^2}{4m_e \omega_L^2} \quad (2.3)$$

where e and m_e are the charge and mass of an electron respectively. This ponderomotive energy is also an important parameter in that it can be used to determine the maximum photon energy that can be generated in an HHG process. The maximum harmonic photon energy, also known as the cutoff energy, can be expressed as[15]:

$$E_{\Omega max} = I_p + 3.17U_p \quad (2.4)$$

The above expressions can be combined, and the maximum photon energy achievable in an HHG process can be written as an explicit function of the laser parameters:

$$E_{\Omega max} = I_p + 3.17 \frac{e^2 E_L^2}{4m_e \omega_L^2} \quad (2.5)$$

Each time a photon is absorbed or emitted, it produces a change in angular momentum of $\Delta l = \pm 1$. This leads to only odd numbers of transitions and therefore only odd harmonics of the fundamental frequency. However, if a second color is added by using a frequency doubling β Barium Borate (BBO) crystal and several other optical elements to correct for the delay caused by the crystal[16], even harmonics of the original fundamental frequency can also be generated.

These higher harmonic frequencies of the fundamental frequency then add together to create very short light pulses that contain VUV radiation. These pulses are very sharp in the time domain, and have pulse lengths in the attosecond ($10^{-18}s$) timescale, but they are also wide in the frequency domain, containing many harmonics.

Generating these extremely short HHG pulses requires a complex tabletop setup and specific conditions to operate. Auburn University’s HHG beamline serves as one such experimental tool.

2.3 The Auburn Source of Attosecond Pulses

The Auburn Source of Attosecond Pulses (ASAP) laboratory has a HHG beamline that is set up to conduct pump-probe measurements by varying the time delay between an attosecond-timescale VUV pulse and a femtosecond-timescale NIR pulse.

A commercial Ti:Sapphire Vitara-S laser manufactured by Coherent is the heart of the system. This laser generates 1.5mJ, 35fs, 800nm NIR pulses. These pulses travel through a beamsplitter that bifurcates the beam into two separate optical paths in a Mach-Zehnder interferometer arrangement.

One path goes through an argon gas cell to create the HHG attosecond pulse. This is then sent through an aluminum filter that screens out the remaining 800nm IR radiation. A toroidal mirror is used to focus the remaining light.

The other path goes through an optical system with mirrors on piezoelectric stages. This pathlength can be controlled at nm precision, and is stabilized by a novel stabilization system using the interference pattern between the femtosecond NIR pulse laser and a coaxial CW laser that is capable of maintaining a stable time delay on the order of 10 attoseconds over several hours of runtime[17]. This allows for extremely fine control of the time delay between the attosecond VUV pulse and the femtosecond NIR pulse.

Light from both optical paths is directed to a recombination mirror, which then directs it to a molecular spectrometer. After the molecular spectrometer, the light finally then travels to and terminates in an inline VUV spectrometer.

A diagram of this setup is shown in Figure 2.3.

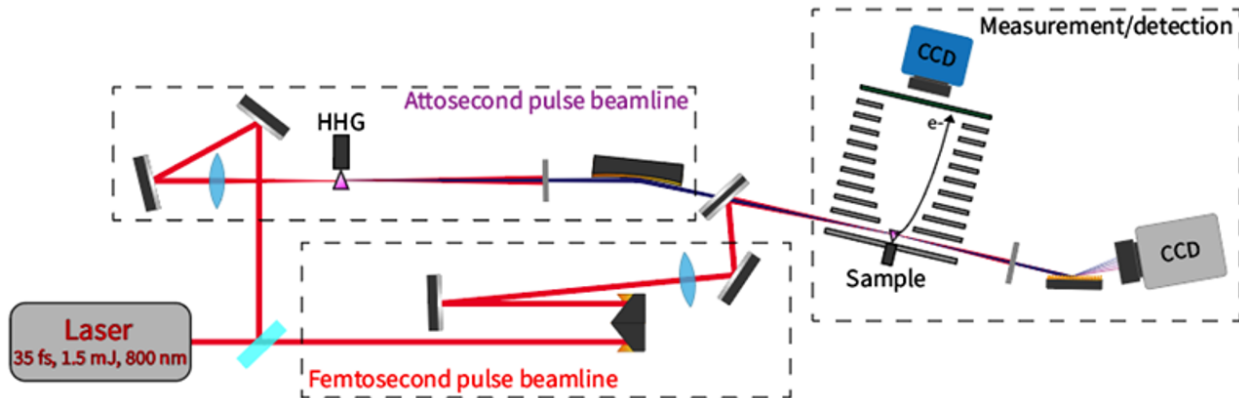


Figure 2.3: ASAP beamline diagram.

2.3.1 VUV spectrometer

In order to properly tune the high harmonic generation process, the spectral content of the HHG pulses needs to be known in real time. Gas density, laser power, and laser focus are all parameters that can be adjusted to optimize the HHG process to yield the desired attosecond VUV pulse, and this is done using information from the pulse's spectral content.

In order to do this, an VUV spectrometer is required. At the simplest level, this instrument consists of a diffraction grating that spreads out the different wavelengths of light that make up the pulse and a detector that can record the spatially separated spectrum. Commercial off-the-shelf VUV spectrometers are available, but in order to tailor to exact requirements, a custom instrument was designed and built for the Auburn ASAP lab.

The first step in design of this instrument was to select a diffraction grating. A design requirement was to look at VUV light in the 20-80nm wavelength range. Transmission gratings with a line density high enough to be suitable for this regime are available. State-of-the-art ultra high line density transmission gratings can be produced using ultraviolet based nano imprint lithography (UV-NIL) with a line density of 10,000 lines per mm[18]. These gratings would allow a very simple and convenient in-line geometry to be used. The angular separation of the light as a function of wavelength for such an optical arrangement can be expressed with a very simple grating equation:

$$\alpha = \arcsin\left(\frac{m\lambda}{d}\right) \quad (2.6)$$

where d is the line period, λ is the wavelength, α is the diffraction angle, and m is the diffraction order.

Unfortunately, at the time of the design of this instrument and of this writing, the ultra high line density UV-NIL transmission grating remains a very novel and extremely expensive solution, and was not within the economic scope of the project.

A more economical and technologically mature solution is to use a grazing incidence flat field grating. These gratings are concave, and use a grazing angle of incidence to focus a spatially resolved spectrum at a specific point in space. Here, the angular relationship is given by:

$$\beta = \arcsin(Nm\lambda - \sin(\alpha)) \quad (2.7)$$

where N is the groove density, λ is the wavelength, α is the angle of incidence, and m is the diffraction order[19]. The optimal geometry, including the proper angular and spatial positions to focus the longest and shortest wavelengths intended for the grating, is shown in Figure 2.4.

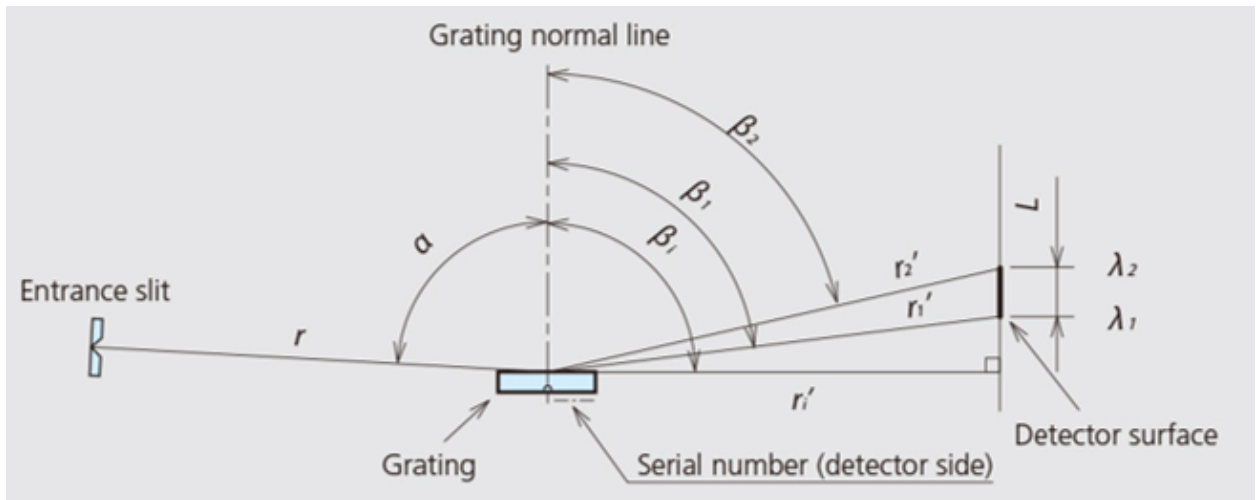


Figure 2.4: Flat Field Grating geometry[20].

A Shimadzu 30-006 Laminar-type Replica Diffraction Grating was selected for use in this spectrometer. This flat field grating has a groove density at the center of 300 grooves per mm, is optimized for wavelengths between 20nm and 80nm, and focuses these wavelengths on a 25.3mm long detector surface[20]. The location of this detector surface relative to the grating, and the location of the grating relative to the incident light, are all specified precisely by the design of the grating. This necessitated fabrication of a custom edge-welded flexible bellows to allow precise positioning of the detector element.

A direct-detection CCD camera was decided upon for the detector element. This type of camera is optimized to directly record incident photons in the desired wavelength range.

An Andor Newton SO DO940P BEN direct detection CCD camera was selected as the detector. This camera has a 2048 x 512 pixel resolution, and has a 27.6mm x 6.9mm back-illuminated detector area[21]. An aluminium filter eliminates the NIR light from the incident pulses to prevent camera saturation.

The camera interfaces with a Windows PC using a USB connection, and Andor provided a LABVIEW software development kit as part of the camera tender. This LABVIEW SDK was used to write a control VI that operates the camera and allows it to save spectra and allows the user to conveniently identify specific harmonics of the 800nm laser.

The entire VUV spectrometer assembly is mounted to an optical breadboard that is secured to the optical table at the end of the ASAP AMO beamline, and is pumped down to high vacuum through a pair of flexible bellows connecting it to the molecular spectrometer and its turbopump positioned upstream.

The CAD model for the VUV spectrometer is shown in Figure 2.5, and the completed operational instrument is shown in Figure 2.6.

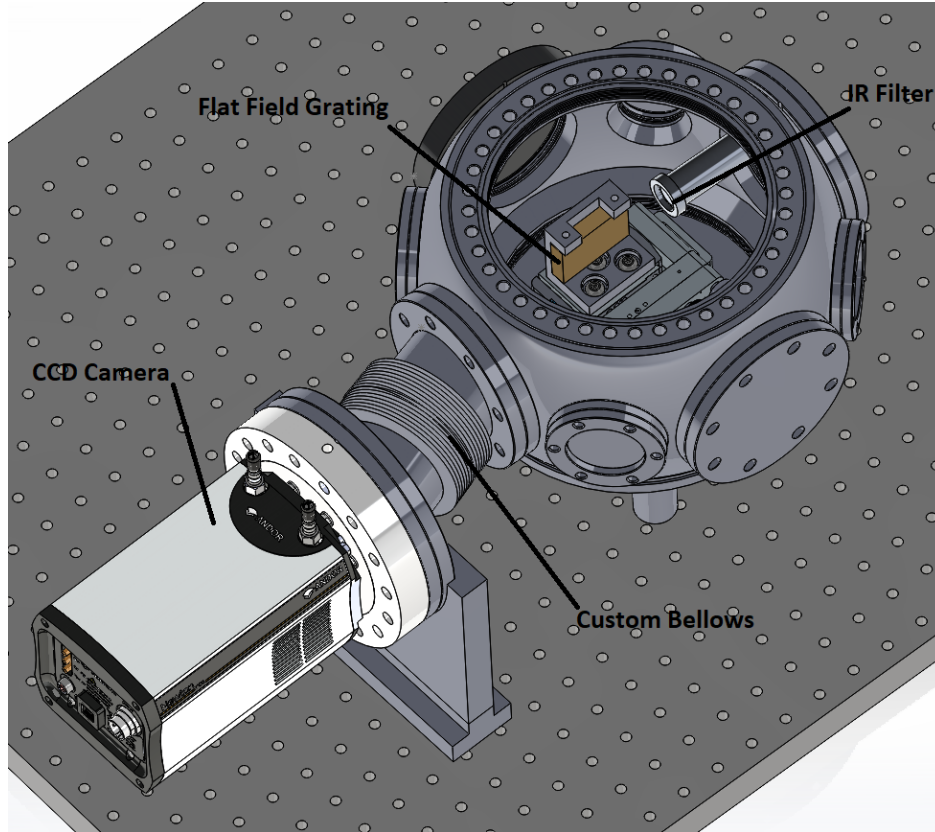
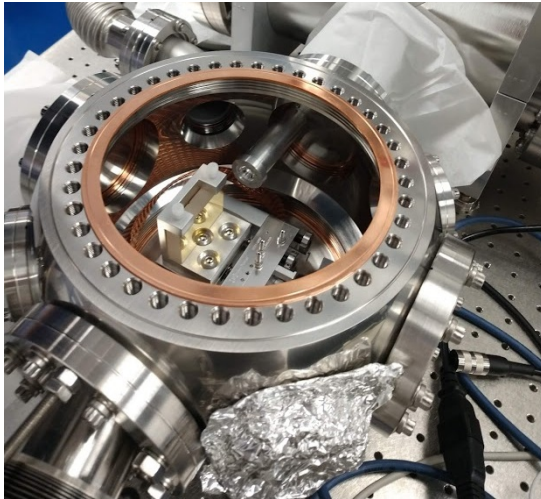
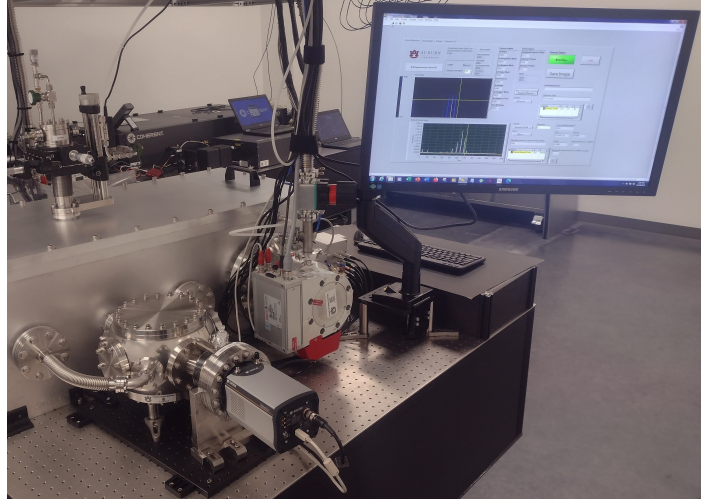


Figure 2.5: VUV spectrometer CAD model.



(a) VUV spectrometer interior.



(b) VUV spectrometer exterior.

Figure 2.6: The completed ASAP VUV spectrometer.

The spectrometer came online in 2019, and currently allows the ASAP beamline to precisely control the HHG process in real time.

2.3.2 HHG and the two-color electron retroaction experiment

The ASAP HHG beamline can generate the desired VUV pulses in the desired energy range, and can provide NIR radiation at a precisely controlled time delay. However, while the temporal width of the attosecond HHG pulses is extremely narrow, the spectral width is very wide. More optics to pick out specific wavelengths would need to be installed to precisely control the ionization of the initial neutral diatomic molecules. The energies would also be limited to the specific harmonics of the 800nm laser.

Unfortunately, while it would be convenient to use a relatively inexpensive tabletop HHG like the one located at Auburn, such a system is not a feasible option for this experiment.

2.4 Synchrotron radiation

When a charged particle is accelerated, energy is radiated. When this acceleration is perpendicular to the velocity of a relativistic charged particle, the power radiated by the particle can be described by the relativistic Larmor formula[22]:

$$P_{\perp} = \frac{q^2}{6\pi\epsilon_0 c^3} \gamma^4 a^2 \quad (2.8)$$

Synchrotrons are particle accelerators that use fields that are adjusted as the particles accelerate to keep them in a circular path[23]. These devices are able to accelerate charged particles to relativistic velocities, and the energy the particles emit by synchrotron radiation can be used as a light source. This radiation can be produced in the VUV region, and while the temporal profile of the synchrotron light pulses is far broader than what can be achieved with HHG pulses, the spectral width is far narrower. A 600 as single attosecond pulse from an HHG source has an energy bandwidth of 3.042 eV[15], while the resolution available at a synchrotron light source can be on the order of .01 eV.

Synchrotron light sources are large and expensive user facilities. While beamtime at these facilities is limited and in high demand, a synchrotron light source is the best option for the VUV needed to carry out this experiment.

2.5 The Advanced Light Source (ALS)

The Advanced Light Source (ALS) is a 3rd generation synchrotron light source located at the Lawrence Berkeley National Laboratory (LBNL) in Berkeley, California, shown in Figure 2.7.



Figure 2.7: The Advanced Light Source (ALS).

The ALS can accelerate electrons up to 99.999996% the speed of light[24]. Under normal operating conditions, there are multiple bunches leading to almost continuous illumination. However, in order to enable certain measurements such as those that require time of flight information, there are periodic beamtimes where only two electron bunches, spaced 328 ns apart, are in the accelerator. This allows the ALS to provide pulsed light, with each pulse being 80 picoseconds long. One of these two-bunch beamtimes at the ALS was used to take the data for this experiment.

2.5.1 Beamline 10

The ALS features multiple beamlines arranged around the storage ring like spokes on a wheel. Each beamline has specialized equipment to meet specific user requirements and provide different ranges of soft X-ray energy light. A map of the ALS beamlines is shown Figure 2.8.

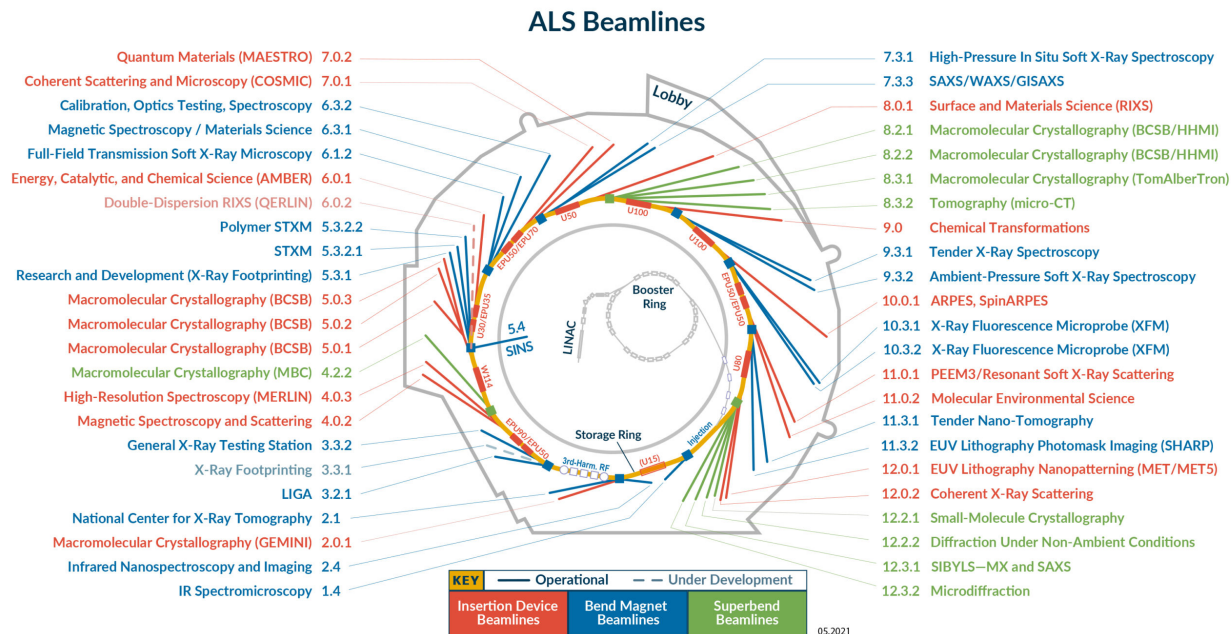


Figure 2.8: ALS beamline map.

As a 3rd generation synchrotron, the ALS also has undulator magnets that wiggle the beam along its circular path to provide more intense and tuned radiation. This greatly increases the intensity of the radiation given off compared to what would be given off by only bending the beam using the storage ring bending magnets. The undulator for the beamline also works in concert with an optical monochromator to allow users to select a very precise energy of synchrotron radiation for their experiments.

This experiment was carried out at beamline 10.0.1. This beamline is equipped with a very high-resolution monochromator featuring 3 diffraction gratings, allowing for selection of particular energy light from 17eV to 340eV [25]. A diagram of the beamline optics for beamline 10 is shown in Figure 2.9.

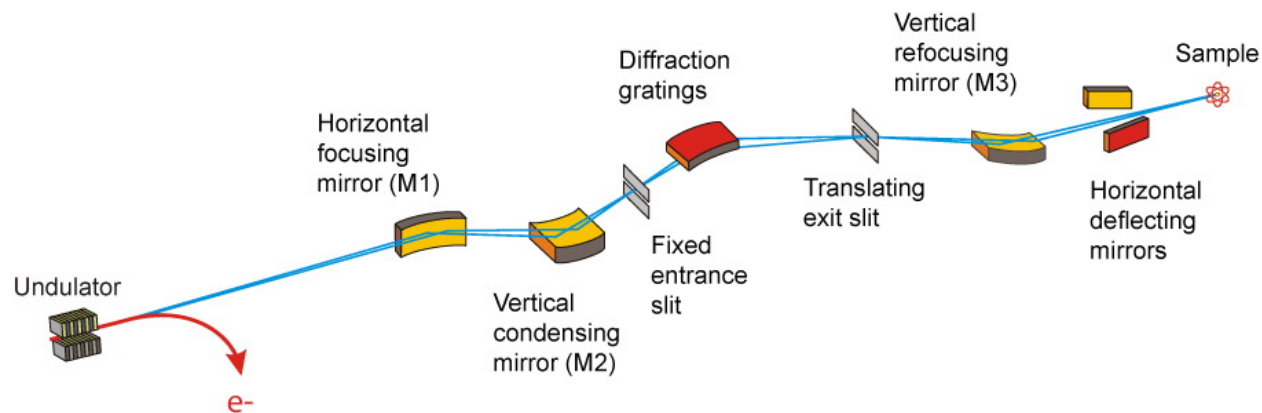


Figure 2.9: Beamline 10.0.1 layout[25].

The horizontally polarized light from the ALS and beamline 10.0.1 allows for extremely precise irradiation of molecules with exactly the energy of VUV radiation desired, at a high repetition rate of one 80ps pulse every 328.28ns.

2.5.2 Synchrolocked near-infrared laser

The ALS provides an excellent VUV source, but in order to carry out a two-color experiment with NIR, another light source is needed for the NIR. A Q-Peak Yb:YAG NIR laser was used for this experiment. The laser has a wavelength of 1030nm and an average power of 100W.

This laser can provide horizontally polarized, 1.2 eV, 12ps NIR pulses every 656.56ns (a duty cycle of 2 compared to the ALS). These pulses have an intensity on the order of $10^{11}W/cm^2$, which is high enough to probe the existence of predicted LICl phenomena. However, a major technical challenge existed in synchronizing the ALS and the Q-peak NIR laser.

A large feature of interest for this experiment is examining what happens at different VUV/IR pulse time delays. This requires precise and consistent control of the delay between the VUV pulse from the ALS and the NIR pulse from the laser. A complex synchrolock system that actively stabilized the two pulse trains was developed, and is described in great depth in the PhD thesis of A. Gatton[26].

In short, this system records both pulse trains and adjusts the laser pulse train to maintain a set time delay. The ALS beamline provides a bunchmarker signal that indicates when an electron bunch is traveling past that will deliver a pulse of synchrotron radiation. The laser signal is captured by a photodiode. The laser and bunchmarker signals are then compared and synchronized using the custom synchrolock system that had been developed, which uses an analog mixer, an analog delay line, and a proportional–integral–derivative controller to directly adjust piezoelectric elements in the laser to control the time delay.

This system, while complex and temperamental, allowed the level of temporal control required to undertake this experiment.

2.6 Cold Target Recoil Ion Momentum Spectroscopy (COLTRIMS)

With the required light, a two-color breakup involving the electron retroaction effect in the presence of an NIR field can take place. The remaining technical hurdle is to actually measure the reaction.

Experimental investigation of these phenomena is challenging to say the least. The goal is no less than a kinematically complete measurement of the breakup of a single molecule in a two-color VUV/NIR experiment. An energy spectrum, as can be provided by techniques such as Velocity Map Imaging, would not be able to see the asymmetry signature of the retroaction effect, as it cannot record ions and electrons in coincidence[27].

Cold Target Recoil Ion Momentum Spectroscopy, or COLTRIMS, is a technique that allows a kinematically complete, full 4π solid angle measurement of a breakup that results in charged fragments [28].

In COLTRIMS photoionization experiments, a neutral gas is fed into a vacuum chamber through a nozzle. As the gas expands adiabatically into the vacuum, it cools. The gas passes through a skimmer with a 0.3mm diameter and an aperture with a 0.5mm diameter, and forms a two-stage supersonic gas jet. This internally cold (≈ 80 K) gas jet, containing

unexcited atoms or molecules in the ground state, is then irradiated (Figure 2.10a), causing a breakup (Figure 2.10b).

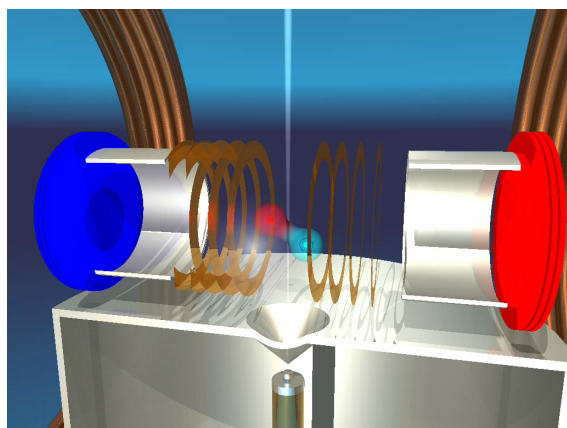
The COLTRIMS spectrometer has a series of copper plates that are connected in series with 500 k Ω resistors to provide a uniform electric field, and a Helmholtz coil is used to provide a uniform magnetic field. The momentum vectors of these charged fragments can be oriented anywhere in space, but the field strengths are set high enough to confine a full 4π solid angle of fragments.

The charged fragments follow paths defined by the Lorentz force law, where the force on a charged particle can be described as:

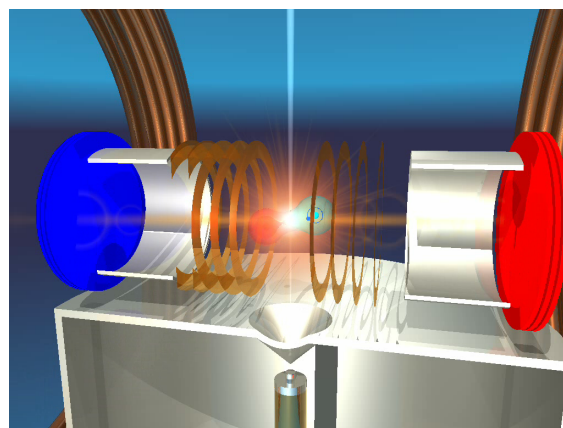
$$\vec{F} = q \left(\vec{E} + \vec{v} \times \vec{B} \right) \quad (2.9)$$

The trajectories of the far more massive recoil ions experience negligible deflection due to the magnetic fields, but the fields serve to confine the lighter and faster electrons to helical trajectories that terminate at the detectors.

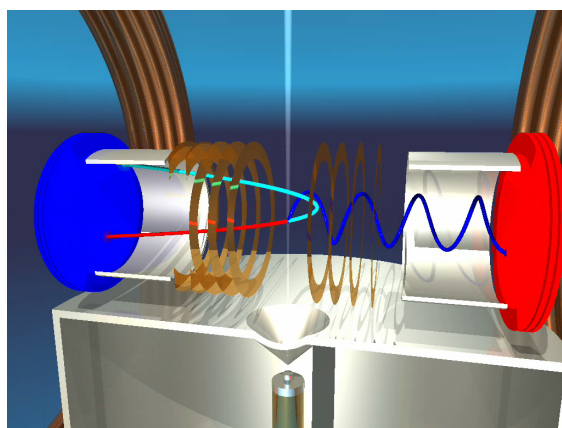
Finally, the charged fragments hit detectors (Figure 2.10c). These detectors record the hit position and the impact time.



(a) A gas jet of neutral molecules gas jet is irradiated



(b) A molecular breakup occurs



(c) Charged fragments are confined and drawn towards detectors

Figure 2.10: COLTRIMS animation, taken from [29].

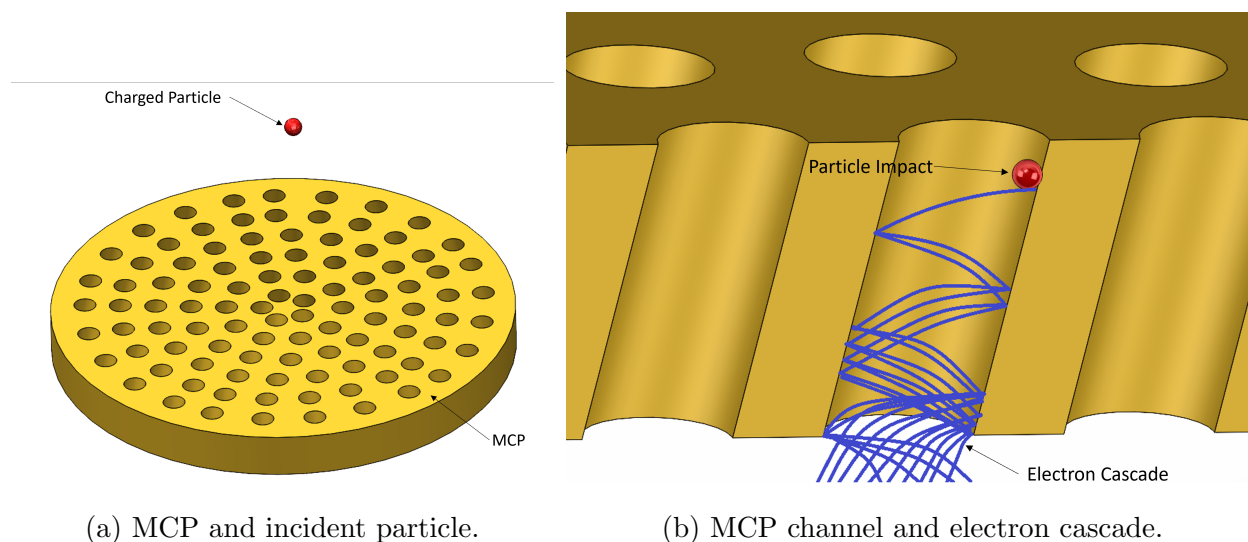
The impact time and the bunchmarker time can be used to determine the time of flight, and with the time of flight and the impact position, the initial momentum vectors of the fragments can be determined.

2.6.1 Microchannel Plate/Delay Line Anode detector

The detector elements of a COLTRIMS spectrometer, MicroChannel Plates (MCPs) and Delay Line Anodes (DLAs), are intended to provide a precise measurement of the arrival time and hit position of the charged particle, respectively.

A microchannel plate is a device that features a large number of parallel electron-multiplying tubes through a lead glass material[30]. Each channel is slightly angled, so an incident particle has a higher chance of hitting the wall of the channel. MCPs operate under vacuum, using high voltage power supplies to apply a large voltage (around 1000 V per plate) to the material.

When an incident particle hits the side of one of the channels in the MCP, an electron is freed. This electron also hits the wall, and frees another, and another, leading to an electron cascade as seen in Figure 2.11.



(a) MCP and incident particle.

(b) MCP channel and electron cascade.

Figure 2.11: Microchannel plate.

MCPs can also be used in a chevron configuration, where two plates are stacked so the angled channels form a chevron to improve the amplification factor to around 10^6 . Using this scheme, a million electrons are created in the cascade for each charged particle that hits the plate.

MCPs allow for extremely good spatial ($< .15\text{mm}$) and temporal ($< 1\text{ns}$) resolution, but the spatial position of the electron cascade still needs to be recorded. MCPs in detectors are often paired with a phosphor element and a CCD to record the location of the electron cascade signal. For COLTRIMS, however, phosphor/CCD stacks have limitations that make them undesirable, particularly in terms of how rapidly data can be read out [31].

COLTRIMS spectrometers use devices known as delay line detectors to record the signals from the MCP hits. Conceptually, delay line anode detectors are very simple. An electron cascade induces an electrical signal in a wire. The electrical signal moves at a constant speed towards both ends of the wire, and the readout times of both signals is recorded, as shown in Figure 2.12.

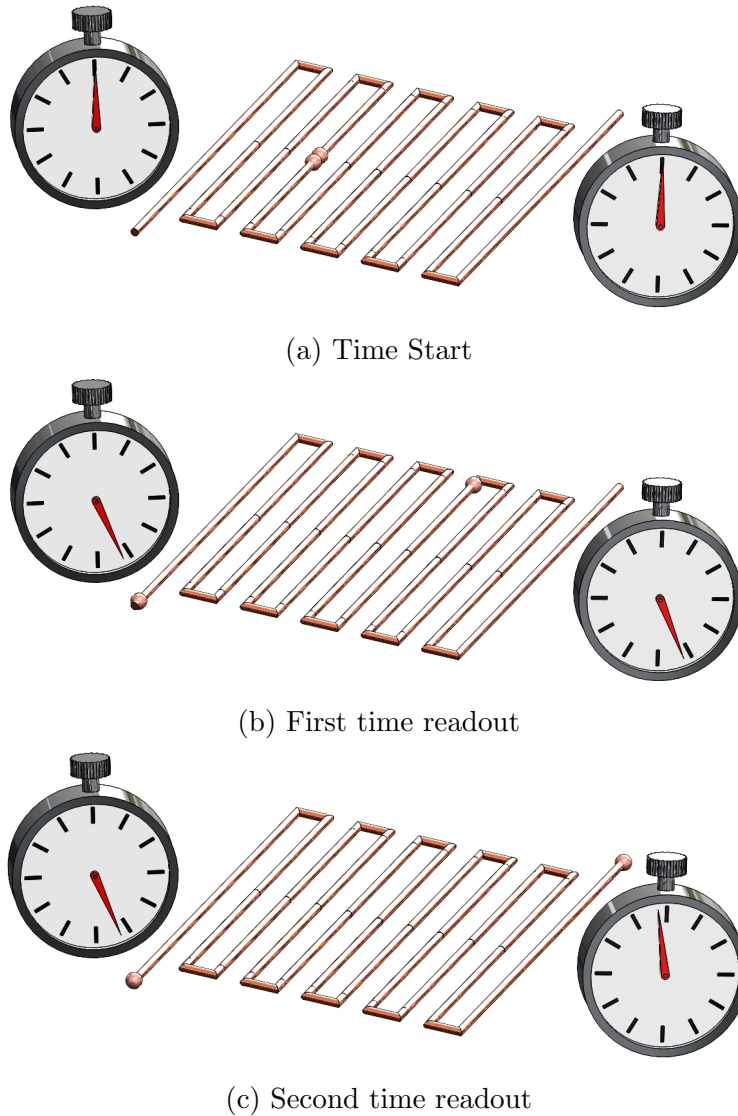


Figure 2.12: Delay line anode wire timing.

If we measure the difference in times between both ends of the wire, the exact position of the signal's origin can be found. At least one wire is needed to record the hit coordinate

in each spatial dimension. More layers can be added to improve the accuracy and reduce the multi-hit deadtime before another hit can be recorded. Since delay line anodes used in COLTRIMS spectrometers have very long wires, parallel wire pairs are employed to prevent dispersion of the signal pulses.

Delay line anodes offer extremely fast and precise readouts ideal for single particle detection. COLTRIMS spectrometers typically use four-readout quad delay line anodes for ion detection, and a six-readout hexanode detector for electrons to increase the accuracy for the harder-to-detect electrons. A schematic of the wiring for these detectors is shown in Figure 2.13.

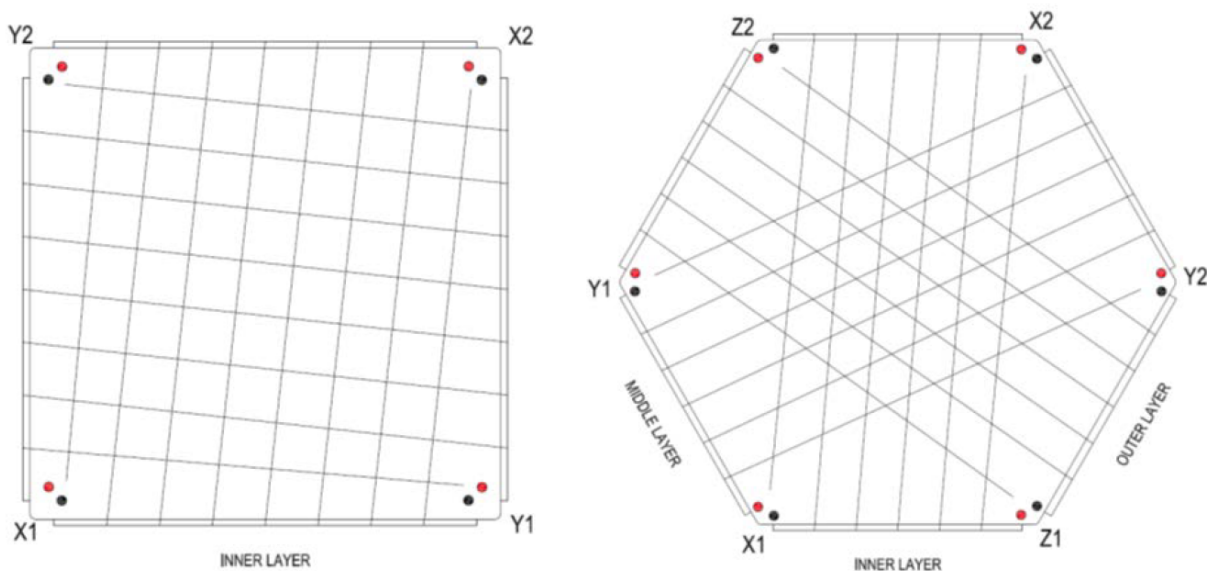


Figure 2.13: Quad delay line detector and hexanode wiring[32].

2.7 COLTRIMS endstation

The Lawrence Berkeley National Laboratory Atomic Molecular Optical Science (AMOS) group's COLTRIMS apparatus was used in this experiment. This chamber, shown in Figure 2.14, is a mobile unit that is rolled up to the beamline for experiments. It is aligned to the beamline using a telescope, and the associated electronics and vacuum equipment are assembled in position at the beamline before the beamtime starts.

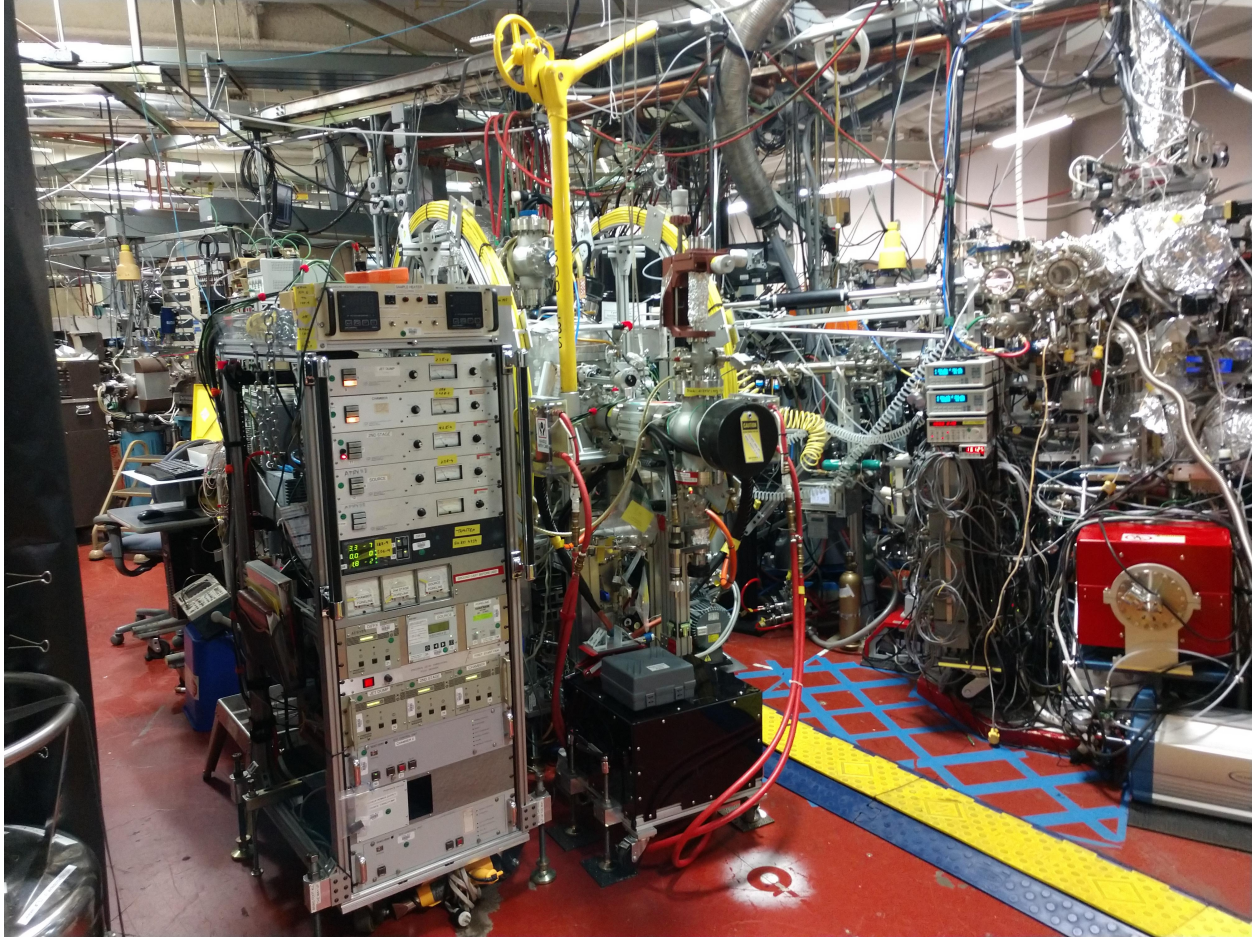


Figure 2.14: AMOS COLTRIMS chamber.

The recoil ion side of the COLTRIMS spectrometer features a 44.0mm acceleration region and a 22.0mm booster region. The booster region is used to reduce the fringe field of the ion MCP in the extraction region by providing a high field region to ensure that the ions are caught by the detector, even though the detector is placed further from the interaction point. A RoentDek DLD120 quad delay line detector with a 120mm diameter MCP is used to detect ions.

The electron side of the spectrometer has a 68.65mm acceleration region and a 139.13mm drift region. This drift region is field free, and allows for improved temporal resolution by focusing the spread of the electrons in the time-of-flight direction into a smaller time interval [33]. A RoentDek HEX80 hexanode detector with an 80mm MCP is used to detect electrons. The assembled spectrometer is shown in Figure 2.15.

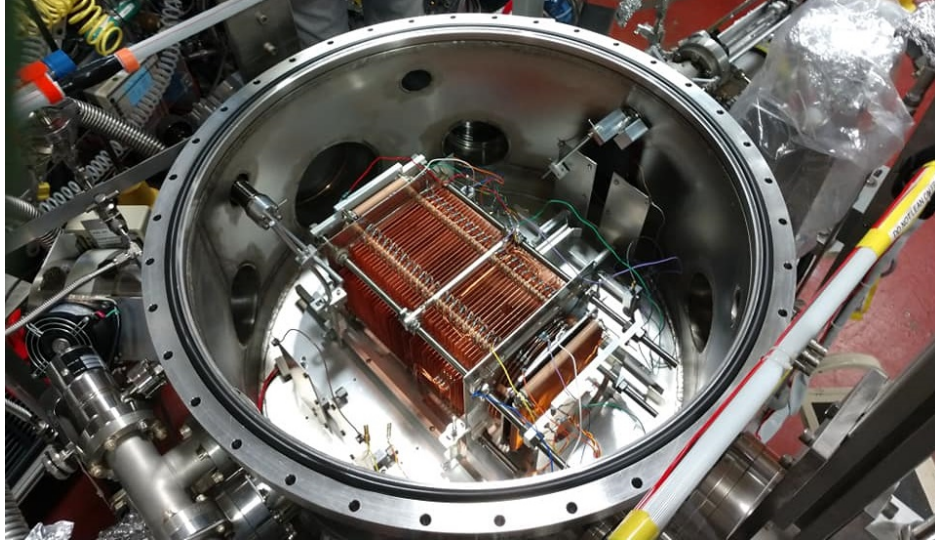


Figure 2.15: AMOS COLTRIMS Spectrometer.

Time signals from the DLD120 and HEX80 are sent to an amplifier, and then to a constant fraction discriminator (CFD). CFDs work by splitting an incoming pulse into two signals. One signal is inverted, and the other is delayed slightly. The signals are then added, leading to a zero crossing that can be used to trigger a time recording that is independent of the height of any individual pulse, as shown in Figure 2.16.

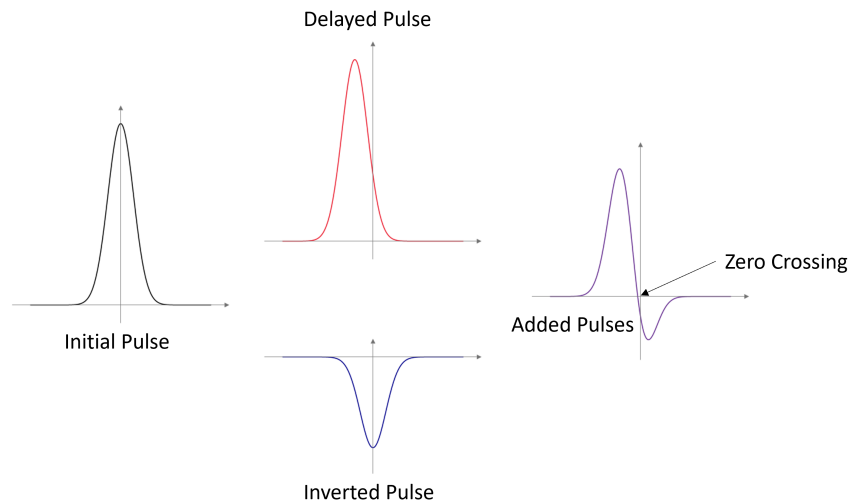


Figure 2.16: Constant Fraction Discriminator.

This scheme for triggering results in better timing resolution, which in turn leads to better performance of the detectors.

After going through CFDs, time signals are delivered to a RoentDek TDC8HP time-to-digital converter (TDC) card that digitizes the signals. For this experiment, signals were digitized and recorded if the ion detector was triggered. Bunchmarker signals from the beamline without an associated hit are not recorded, and triggering is done using the ion detector because the ion signals suffer from less background noise, and therefore have the cleanest and lowest trigger rate.

The chamber has a relatively large internal volume, which is pumped down to a vacuum on the order of 10^{-8} millibar using multiple turbopumps and a liquid nitrogen cold trap. This LN₂ cold trap needs to be regularly topped off by the personnel monitoring the chamber during the beamtime, but greatly increases the vacuum quality by a factor of 3 to 5. The vacuum setup is shown in Figure 2.17.

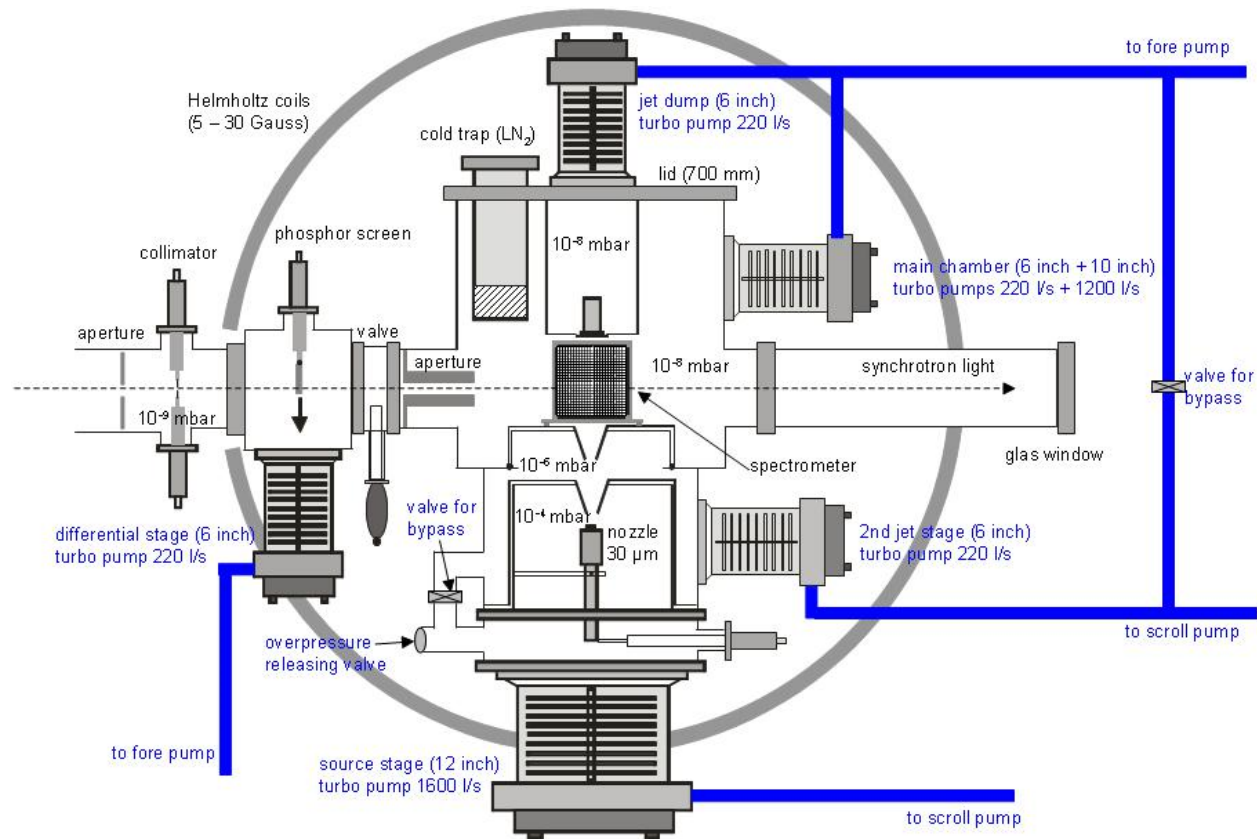


Figure 2.17: AMOS COLTRIMS chamber vacuum setup.

Finally, for the purposes of this experiment, a right-handed coordinate system can be defined. The ALS propagation direction defines the X coordinate, the gas jet defines the Y coordinate, and the spectrometer time of flight axis defines the Z coordinate. This coordinate system will be used for the rest of this work, and a diagram of this is shown in Figure 2.18.

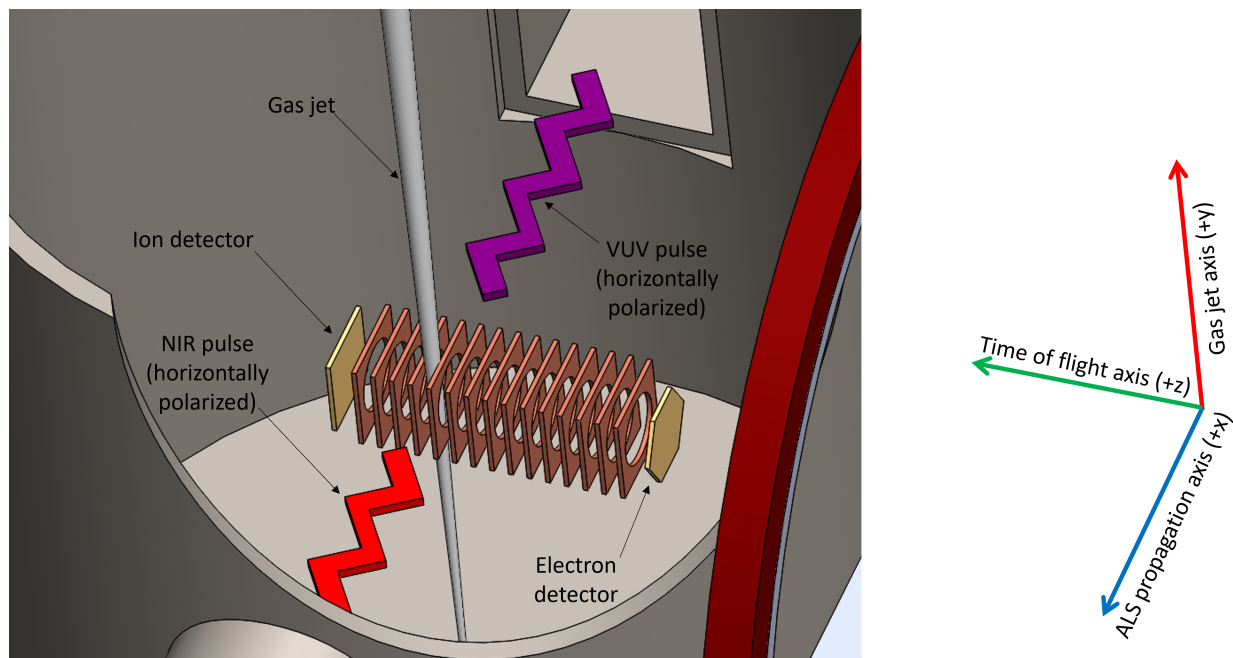


Figure 2.18: Experimental coordinate system.

Chapter 3

General COLTRIMS analysis using LMF2Root

3.1 LMF2Root 3.42 overview

RoentDek is the primary vendor for the detector systems used in COLTRIMS experiments. Their detectors systems are intended to be used with a data acquisition software package called COBOLD, which RoentDek also provides. Files recorded by COBOLD are saved using a list mode format (LMF). These .LMF files contain all the data recorded during a given run, and serve as the raw data that COLTRIMS analysis begins with. In order to analyze this data, a C++ based software package known as LMF2Root has been written by the COLTRIMS community. This software, built using the open-source Root data analysis framework from CERN, allows us to visualize and analyze important physical quantities extracted from the raw data.

3.2 Data flow

Raw data for each recorded event saved in .LMF files is imported into LMF2Root. LMF2Root analyzes each event and puts each fragment through a reconstruction algorithm that extracts time of flight and hit position on the detector. Presort conditions specified by the user to tag a desired reaction channel are then applied, and each event meeting these criteria is then saved in a .root file.

This presorted .root file can then be put through LMF2Root again for analysis. The COLTRIMS Helper Analysis Library, or ColAHell, is used to determine the initial momentum of each fragment, and can then do a variety of calculations based on the derived

momentum vectors. Quantities such as energy, kinetic energy release, and various angular relationships between fragments can all be found using these momentum vectors.

3.3 Installation

In order to run LMF2Root 3.42 in a Windows environment, CERN’s Root data analysis framework and Microsoft Visual Studio 2017 must first be installed.¹

To install the needed Microsoft Visual Studio 2017 Community packages, select “Desktop development with C++”, and add the option to add “Visual C++ MFC for x86 and x64” in the visual studio installer.

Next, Root must be installed. LMF2Root 3.42 is built on top of version 5 of Root, and is not compatible with later versions from CERN. Root 5.34.38 is the latest version that remains compatible with LMF2Root and can be downloaded for free from CERN². It can be installed using the provided executable using the default settings. An environment variable must then be created in Windows³ called “*rootsys*” with a value of “*C:\root_v5.34.38*”, and “*C:\root_v5.34.38\bin*” must be added to the “*Path*” system variable to allow LMF2Root to access Root 5.34.38.

Microsoft Visual Studio 2017 can then be used to edit and compile LMF2Root⁴. Once all these dependencies are installed, the LMF2Root zip file can be extracted.

3.4 Compiling

To compile LMF2Root, go to the folder that LMF2Root has been extracted into, and open the VC++ Project titled “*LMF2Root_VS2017.vcxproj*” in Visual Studio 2017. This is the main overall C++ project that must be compiled to create an LMF2Root executable. The

¹This software was written using VS 2017 and later versions of Visual Studio have compatibility issues that prevent compiling

²https://root.cern/download/root_v5.34.38.win32.vc12.exe

³This can be done in Windows 10 through the Power User Task Menu by clicking on System, then Advanced system settings, and then Environment Variables in the advanced tab

⁴Lines 198 to 202 in TVirtualX.h located in the include folder within Root 5.34.38 must be commented out in order to avoid errors when compiling LMF2Root 3.42

Visual Studio environment will highlight errors that prevent the program from compiling, and it allows the user to look at the definitions of various functions.

To compile, ensure that the debugger is in the *Release* and *WIN32* mode, then right click on *LMF2Root_V2017* in the Solution explorer and select *Build Solution*, as shown in Figure 3.1.

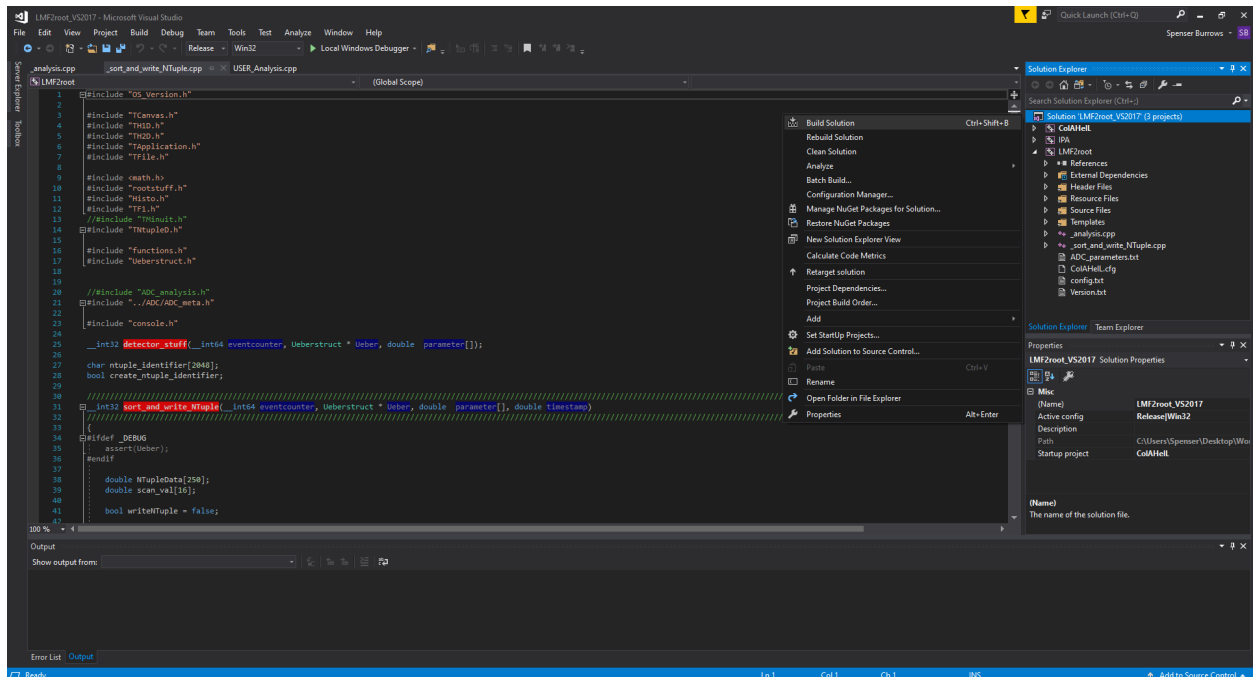


Figure 3.1: Compiling LMF2Root in Visual Studio 2017.

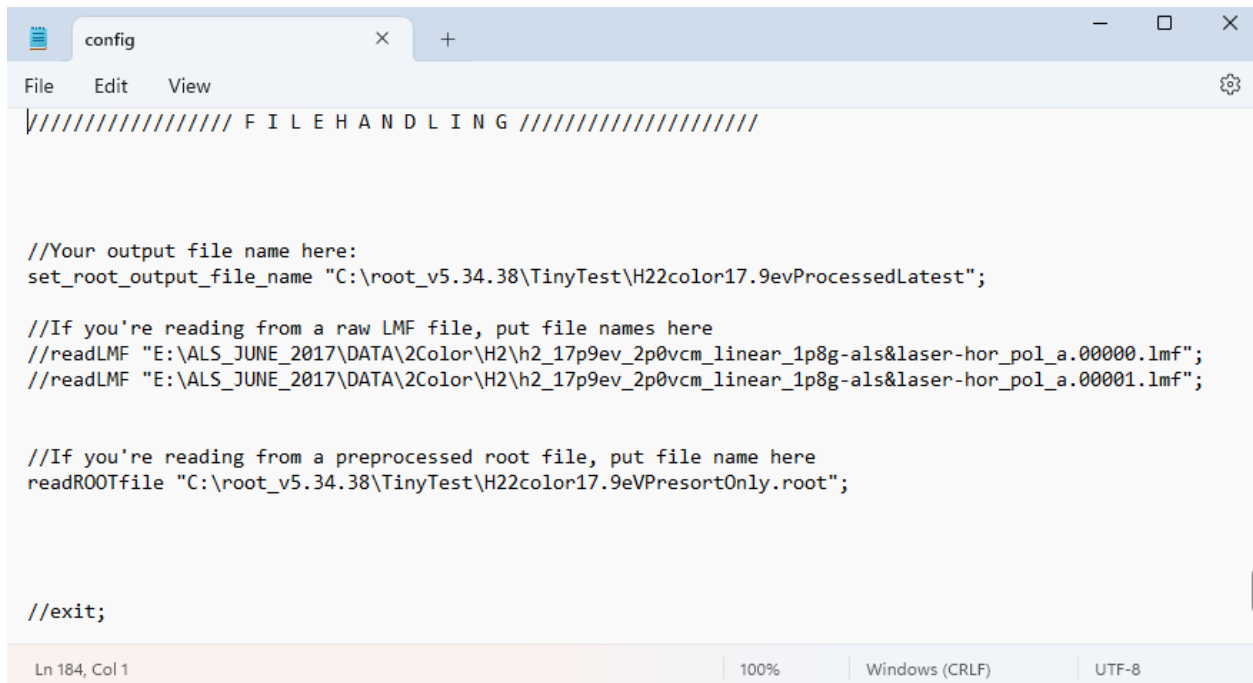
This must be done every time something is changed in the project, and will generate the *LMF2Root.exe* executable.

3.5 LMF2Root configuration file (Config.txt)

In order to analyze data, the user first must tell LMF2Root what files to load and where to save the results. File handling and information about the detector electronics is specified in an editable configuration file called *config.txt*, located in the LMF2Root folder.

File handling using *config.txt* is fairly straightforward. The user may specify an output .root file to save presorted data from specified raw .lmf input files, or they can specify a

.root file to output analyzed data about the events in a presorted .root input file, as shown in Figure 3.2.



```
config
File Edit View
//////////////////////////////// FILE HANDLING //////////////////////////////////

//Your output file name here:
set_root_output_file_name "C:\root_v5.34.38\TinyTest\H22color17.9evProcessedLatest";

//If you're reading from a raw LMF file, put file names here
//readLMF "E:\ALS_JUNE_2017\DATA\2Color\H2\h2_17p9ev_2p0vcm_linear_1p8g-als&laser-hor_pol_a.00000.lmf";
//readLMF "E:\ALS_JUNE_2017\DATA\2Color\H2\h2_17p9ev_2p0vcm_linear_1p8g-als&laser-hor_pol_a.00001.lmf";

//If you're reading from a preprocessed root file, put file name here
readROOTfile "C:\root_v5.34.38\TinyTest\H22color17.9eVPresortOnly.root";

//exit;
```

Ln 184, Col 1 | 100% | Windows (CRLF) | UTF-8

Figure 3.2: Filehandling in Config.txt.

Once file handling has been defined, the user must define the TDC channels for the detectors that were used. Which TDC channel is associated with what depends on the experiment, and is recorded in the experimental logbook. An example of a complete TDC set that can be used to assign channels is shown in Table 3.1, and is used to assign values for parameters 202-208 and 302-308 in configuration file.

TDC Channel	Signal Source
0	Ion-side MCP
1	Electron-side MCP
2	Hexanode Delay-Line Detector u1 layer
3	Quad Delay-Line Detector u1 layer
4	Hexanode Delay-Line Detector v1 layer
5	Quad Delay-Line Detector v1 layer
6	Hexanode Delay-Line Detector w1 layer
7	Laser Bunchmarker
9	Hexanode Delay-Line Detector u1 layer
10	Quad Delay-Line Detector u1 layer
11	Hexanode Delay-Line Detector v1 layer
12	Quad Delay-Line Detector v1 layer
13	Hexanode Delay-Line Detector w1 layer
16	Synchrotron Bunchmarker

Table 3.1: TDC channels and the source of their signals.

3.6 Detector electronics calibration

In order for the resort routine to reconstruct each event, the detectors must first be calibrated. This is needed to properly map the time signals recorded by the delay line anodes to a specific spacial position on the detector. LMF2Root3 has a built-in auto calibration routine to facilitate this.

The first part of this calibration procedure, laid out in an included manual known as LMF2Root3 in a Nutshell [34] by Till Jahnke, is to open *config.txt* and turn off the resort (parameter x29 for a given detector) and auto calibration (parameter x28 for a given detector) parameters.

Next, all scale factors (parameters x10-x12 for a given detector) are set to a value retrieved from a table of approximate factors, shown in Table 3.2.

Type	u-layer	v-layer	w-layer
DLD 40	0.61	0.58	-
DLD 80	0.55	0.52	-
DLD 120	0.42	0.4	-
HEX 40	0.53	0.53	0.51
HEX 80	0.55	0.53	0.52
HEX 90	0.49	0.48	0.48
HEX 90 (2/3)	0.35	0.35	0.35
HEX 120 (2/3)	0.38	0.38	0.38

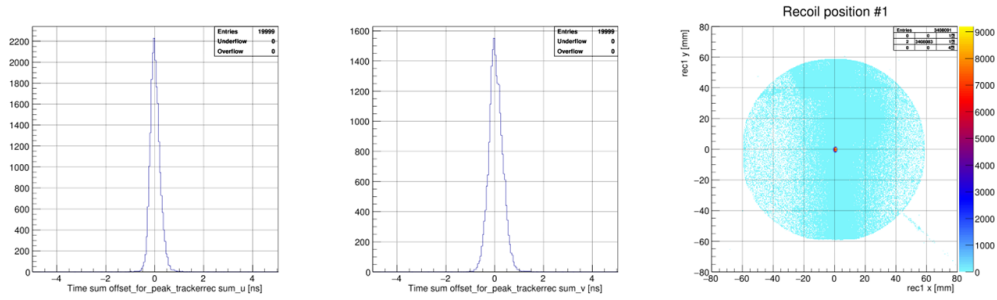
Table 3.2: Typical conversion factors.

Next, a number of offset and shift parameters are zeroed out. The w-layer position offset (parameter x16 for a given detector), time sum offsets (parameters x13-x15 for a given detector), and the position shifts (parameters x26 and x27 for a given detector) are all set to zero. The maximum runtimes for the detector layers are set to 300 (parameters x23-x25 for a given detector). Now, LMF2Root is run on the raw data in the LMF file.

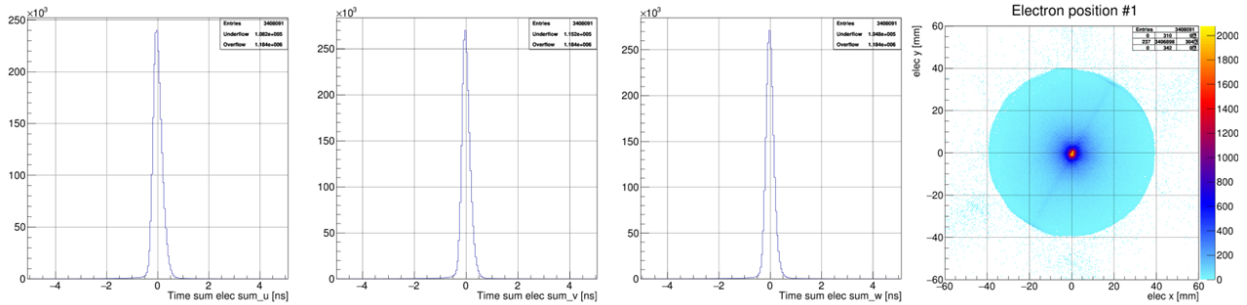
The resulting root output file can then be opened, and the integrated time sum value and width can be inspected. These plots are automatically generated, and can be found in the *rec* or *elec* sub-folders in the root file.

The time sum value and widths should then be used to set parameters x13-x15 and x17-x19 for a given detector. If the size of the detector is different from the actual size of the MCP in the detector, these scale parameters can be multiplied by a common factor to adjust the size.

Run LMF2Root again, and ensure that the time sums are now centered at zero and that the detector diameter is correct for the actual MCP, then use the center of the MCP to set parameters x26 and x27. Run LMF2Root again, and make sure that the MCP is centered, as seen in Figure 3.3.



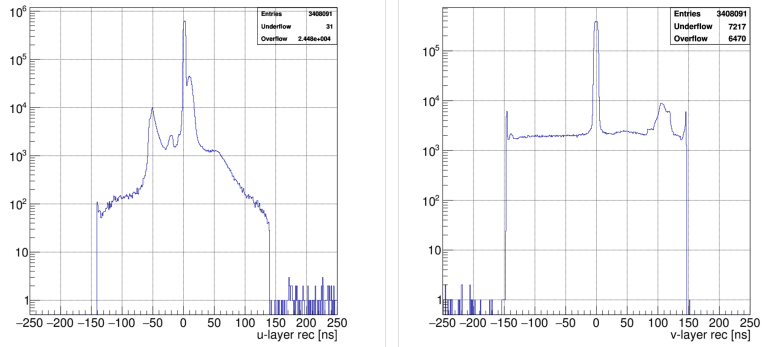
(a) Recoil ion time sums and hit positions.



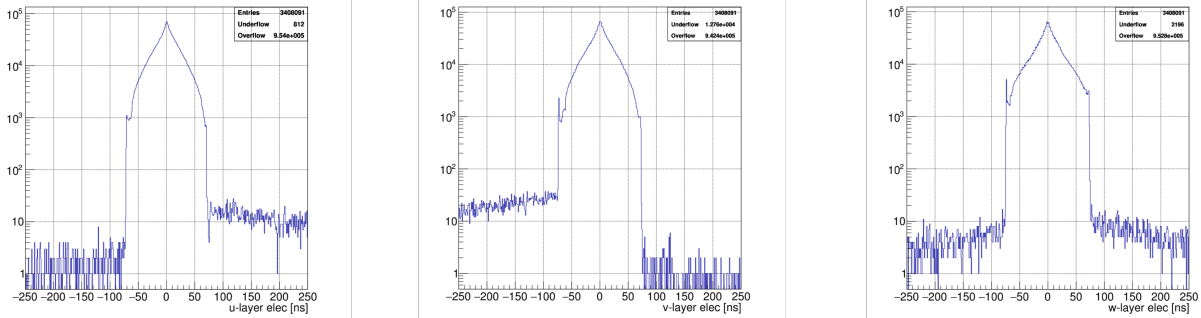
(b) Electron time sums and hit positions.

Figure 3.3: Zeroed recoil ion and electron time sums and centered position plots.

Next, examine the u1-u2, v1-v2, and w1-w2 histograms (for example, electron u1-u2 will be labeled elec_u_ns) with a logarithmic y-axis and determine the maximum run time for each layer by finding the maximum absolute value of the main distribution. Figure 3.4 shows these distributions, with maximum run times of approximately 75ns for the electron detector and 150ns for the recoil ion detector.



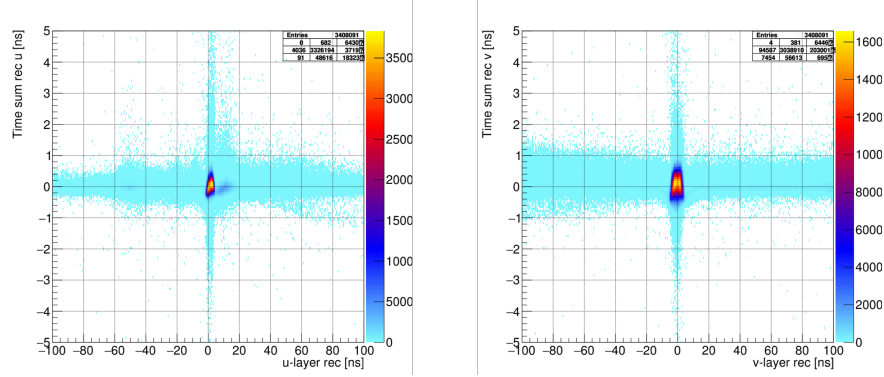
(a) Recoil ion run time.



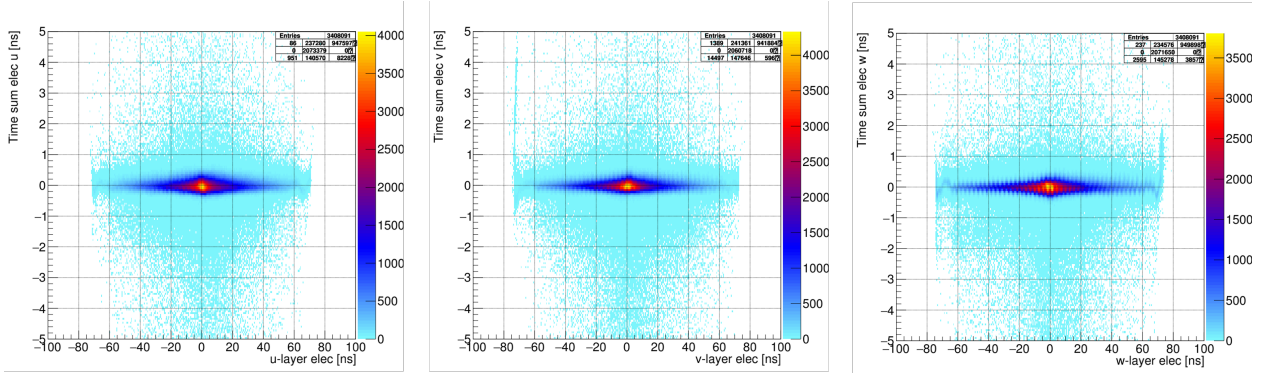
(b) Electron run time.

Figure 3.4: Recoil ion and electron run times.

Next, for each individual detector, switch on auto-calibration and run LMF2Root. As the program ends, it will provide new values for the scale factors and offsets on each layer. Repeat this process until the values stop changing. This should take 2-3 runs, and once complete, the time sums will be flattened out as seen in Figure 3.5.



(a) Recoil ion auto-calibrated time sum.



(b) Electron auto-calibrated time sum.

Figure 3.5: Recoil ion and electron auto-calibration.

The final step is to turn off the autocalibration, and then turn on resorting, sum correction, and position correction. Every subsequent time LMF2Root is run, the detectors will use this completed electronics calibration.

3.7 Hit reconstruction

With the detectors calibrated, LMF2Root can now loop through each recorded event saved in the list mode file to find the time of flight and hit position for each charged fragment. Raw information is saved from the TDCs in the form of time values. Each of these signals is stored as a number in nanoseconds.

The hit position is determined by running a reconstruction algorithm that is provided by RoentDek. This algorithm takes the available raw TDC time data and uses it to find hit position locations. This reconstruction algorithm can also produce a hit position if part of

the normal batch of signals was not recorded. While the ideal situation is for all channels to be recorded, the event can still be used if several are missing using different reconstruction methods, as seen in Table 3.3. This is most common on the electron detector, where there are 7 different channels to record. If one is lost, the rest can still be used to reconstruct the event. The reliability of the reconstruction methods decreases with fewer data channels, but even events where much of the data has been lost can be reconstructed.

Reconstruction Method	MCP	u layer	v layer	w layer
0	1	2	2	2
1	1	0	2	2
2	1	2	0	2
3	1	2	2	0
4	1	1	2	2
5	1	2	1	2
6	1	2	2	1
7	0	2	2	2
8	0	0	2	2
9	0	2	0	2
10	0	2	2	0
11	0	1	2	2
12	0	2	1	2
13	0	2	2	1
14	1	2	1	1
	1	1	2	1
	1	2	1	2
15	1	0	2	1
	1	1	0	2
	1	0	1	2
	1	0	1	2
	1	2	0	1
16	1	1	2	0
	1	1	1	1
	0	2	1	1
	0	1	2	1
	0	1	1	2
17	0	1	1	1
	0	2	1	0
	0	0	2	1
	0	1	0	2
	0	0	1	2
	0	2	0	1
18	0	1	2	0
	0	1	1	0
	0	2	0	1
	0	1	2	0
	0	1	1	0
	0	2	0	1
19	1	1	1	(Quad only)

Table 3.3: Reconstruction methods and number of input signals from each TDC source that are required for the method to be used.

These reconstruction methods provide X and Y hit position data, and electron and recoil ion clock hit times that are then used to extract particle time-of-flight information.

3.8 Time-of-flight using a bunchmarker signal

The time-of-flight of each particle is a key parameter measured in a COLTRIMS experiment. However, this is not directly recorded by the TDC and also needs to be reconstructed.

To do this with a bunchmarker signal, the electron time, a clock time that is returned from the resort routine, is needed. This electron time is then used to calculate the electron time of flight with the modulo operation shown below⁵:

$$e_{TOF} = \text{mod}(e_{time} + t_{shift} - t_{BM} - 1000 \cdot BM_{period}, BM_{period}) \quad (3.1)$$

where e_{time} is the time returned by the resort algorithm, t_{shift} is the time offset shift (that is determined using the procedure outlined in Section 3.12), t_{BM} is the bunchmarker time, and BM_{period} is the period between bunchmarkers. If the time of flight returned above is negative, the bunchmarker period is added to it. The electron time will always be less than a bunchmarker period, so this scheme ensures that we always find the difference in time between the electron hit and the bunchmarker that was immediately before it.

Once we have the electron time of flight, we can find the recoil ion time of flight by adding the electron time of flight to the difference between the recoil ion and electron times, as shown below:

$$r_{TOF} = r_{time} - e_{time} + e_{TOF} \quad (3.2)$$

3.9 Momentum calculation

The motion of charged particles moving in electric and magnetic fields is governed by the Lorentz force:

$$\vec{F} = q \left[\vec{E} + \vec{v} \times \vec{B} \right] \quad (3.3)$$

⁵see lines 134 to 155 and lines 70 to 78 in CH_Tof.cpp for implementation

In a COLTRIMS spectrometer, the electric field and magnetic field are set up so that both are parallel to the time of flight axis, leading to the following acceleration equation:

$$\vec{a} = \frac{q}{m} (B_z V_y \hat{x} - B_z V_x \hat{y} + E_z \hat{z}) \quad (3.4)$$

The PhD dissertation of Joshua Williams details integrating this expression [35], leading to the following momentum equations:

$$P_z = \left(\frac{qE_z}{2} t^2 + mz \right) / t \quad (3.5)$$

$$P_x = \frac{qB_z}{2} \left(x \cot \left(\frac{tqB_z}{2m} \right) - y \right) \quad (3.6)$$

$$P_y = -\frac{qB_z}{2} \left(y \cot \left(\frac{tqB_z}{2m} \right) + x \right) \quad (3.7)$$

where t is the time of flight, z is the length of the acceleration region, x is the x location of the hit on the detector, and y is the y location of the hit on the detector. The implementation for this is located in the “*CH_FUN_Lowlevel.cpp*” file inside of LMF2Root.

3.10 ColAHell configuration file (ColAHell.cfg)

Accurate time of flight calculations, and the momentum calculations that depend on the time of flight, require the user to specify information about the geometry of the spectrometer used in the experiment. This information is entered in a file called *ColAHell.cfg*, and can be updated without having to recompile the main program. An example *ColAHell.cfg* is shown in Figure 3.6.

```

ColAHell.cfg
1 <ColAHell_cfg Version="1.0">
2
3   <TOF_calc Type="BM" TDC_channel="16" BM_period="328.28" Shift="-2.476" /> <!--TOF calculation information-->
4
5   <Electron_det Size="80" Rotate="300" ProcessingOrder="RS"> <!--Detector information-->
6   </Electron_det>
7
8   <Ion_det Size="120" Rotate="-90" ProcessingOrder="RS">
9   </Ion_det>
10
11 <COLTRIMS> <!--Spectrometer information-->
12 <Electron_arm Type="Regions">
13   <Region L_mm="68.65" E_Vpcm="2.06" />
14   <Region L_mm="139.13" E_Vpcm="0" />
15 </Electron_arm>
16
17 <Ion_arm Type="Regions">
18   <Region L_mm="44.0" E_Vpcm="2.06" />
19   <Region L_mm="22.0" E_Vpcm="252" />
20 </Ion_arm>
21
22 <Bfield Strength="1.9" Unit="Gauss" Direction="Counterclock" />
23 <Jet Velocity="1400" Angle="0" Unit="mps" />
24 </COLTRIMS>
25
26 <Presorter Channel="11"> <!--Presorter to separate events into proper reaction channels-->
27 <Elec>
28   <TOF_range Min="98.53" Max="150.02" />
29 </Elec>
30 </Presorter>
31
32
33 <Reaction Channel="11" Name="H+p"> <!--Define reaction channel for ColAHell-->
34 <DIATOMIC>
35   <Ion_def Mass="1.00727647" Charge="1" />
36   <Ion_def Mass="1.007825" Charge="0" />
37 </DIATOMIC>
38 <ELECTRON>
39 </ELECTRON>
40
41 <Electron_momenta Rotate="0">
42   <Shift X="0.00475" Y=".011" Z="0.003" />
43   <Stretch X="1.0" Y="1.0" Z="1.05" Total="1" />
44 </Electron_momenta>
45
46 <Ion_momenta Rotate="0">
47   <Shift X="-.035" Y=".275" Z="0.001" />
48   <Stretch X="1" Y="1.0" Z="1.0" Total="1" />
49 </Ion_momenta>
50
51 </Reaction>
52
53 </ColAHell_cfg>

```

Figure 3.6: Example ColAHell.cfg file.

First, the user can define how to calculate TOF based on what kind of experiment is being analyzed. For synchrotron experiments, the bunchmarker signals are used to calculate the time of flight. The user can also define the TDC channel for the bunchmarker, the bunchmarker period, and the time shift in nanoseconds needed to account for the time the bunchmarker signal takes to be recorded and for light to reach the detector at the end of the beamline. The next section allows the user to define the electron detector size and rotation

for ColAHeLL. The *COLTRIMS* block allows the user to define the physical region length and field strength in the spectrometer. With the spectrometer defined, *ColAHeLL.cfg* allows the user to define presorter gates to tag desired events as part of a given reaction by separating them by time of flight. This is done using the *Presort* block. For each reaction tag, ColAHeLL calculates fragment momentum using reaction type and fragment mass information entered in the *Reaction* block. Specific minute momentum shifts and stretches to fine tune calibration can also be specified here. A variety of different example template files for different reactions, TOF calculation methods, and spectrometer definitions can be found in the *Templates* folder inside the main LMF2Root Visual Studio solution.

3.11 Excel COLTRIMS simulation

To find the electric field, magnetic field, and define the presorter time of flight gates for a given reaction in an experiment, a number of quantities need to be calculated. There is an Excel file called *COLTRIMS5d* that is set up to allow easy and rapid calculations for these quantities. Basic information about the geometry of the spectrometer such as the length of the acceleration regions, the size of the detectors, and energy of the desired reaction is entered. With this, the *Electrons* and *Recoils* tabs can calculate a variety of quantities such as the time of flight ranges at different field strengths, as seen in Figure 3.7.

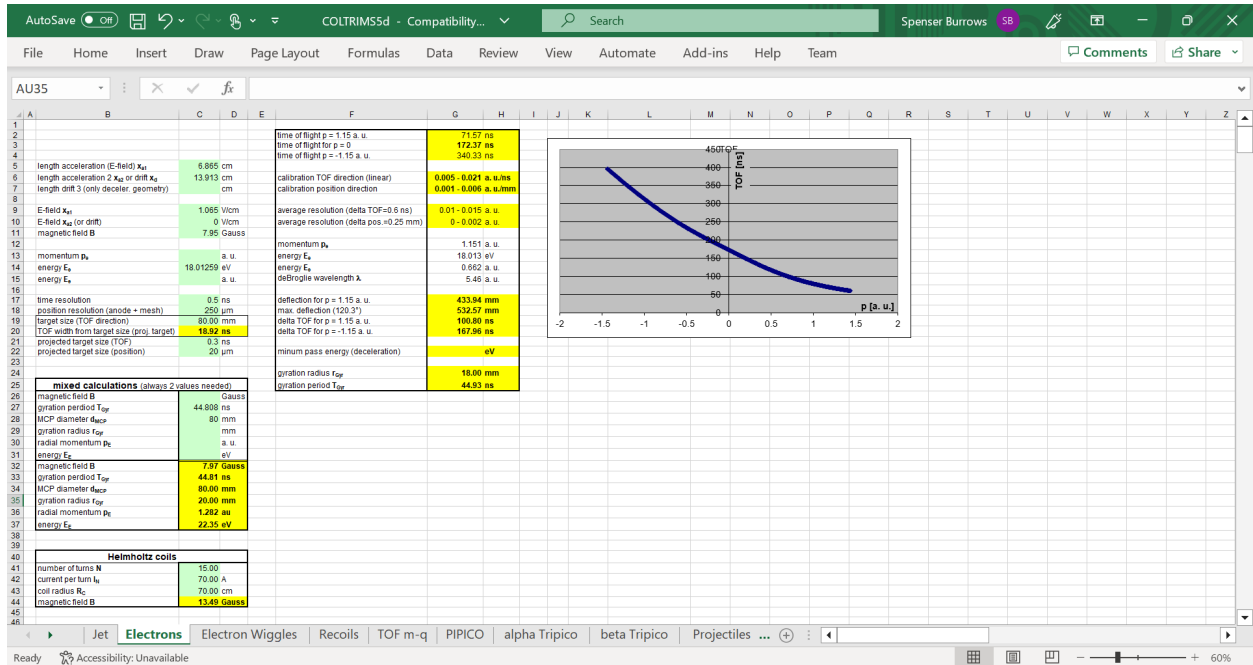


Figure 3.7: COLTRIMS5d Excel file.

A variety of other functions for determining calibration parameters, such as gas jet and electron wiggles calculations, are also available in their respective tabs.

3.12 Time offset calibration procedure

For a synchrotron experiment, light takes a finite amount of time to travel from its origin to the spectrometer at the end of the beamline, and signals take a finite time to travel through cables to be recorded. This constant offset needs to be accounted for to retrieve accurate times of flight. This is done by plotting electron detector radius vs time of flight, something known as a wiggles plot in the COLTRIMS community.

Fragments in a COLTRIMS spectrometer follow a helical trajectory towards the detectors, with a cyclotron period defined as:

$$T = \frac{2\pi m}{qB} \quad (3.8)$$

If the time of flight of the fragments is longer than the cyclotron period, there will be nodes on the wiggles plot at integer multiples of the cyclotron period. The Excel simulation can be used to help identify which nodes are which, and the time values of the nodes form a line with an intercept equal to the time offset. For example, the wiggles plot shown in Figure 3.8 has time of flight nodes at 115.5 ns, 160.8 ns, 204.8 ns, and 250.2 ns. A linear fit shows that these nodes fall on the line $y = 44.808x + 25.976$, indicating that the time offset is 25.976 ns.

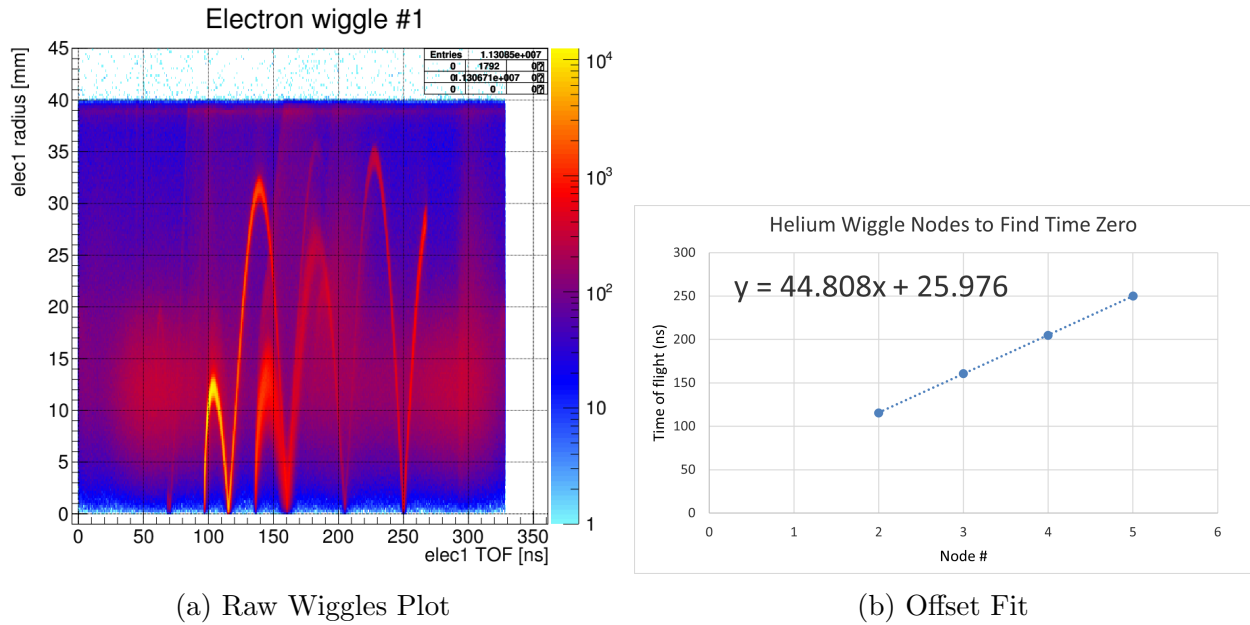


Figure 3.8: Raw wiggles plot and time offset fit.

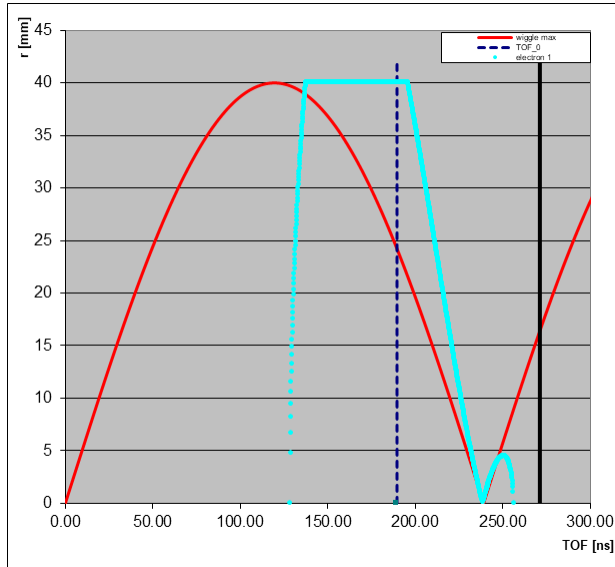
This time offset value is entered into *ColAHell.cfg* and is used to calculate accurate times of flight.

3.13 Magnetic and electric field calibration procedure

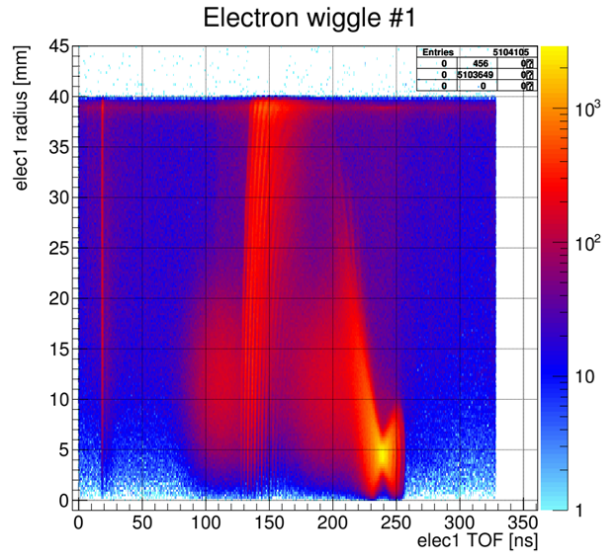
To produce accurate trajectories, ColAHell needs the strength of the electric and magnetic fields.

Ideally, there should be a separate wiggles run done at the desired magnetic field strength, controlled by the current through the Helmholtz coils. The separation between

nodes on the wiggles plot can be used to find the exact magnetic field, since the cyclotron frequency is a function of the magnetic field strength. Figure 3.9 shows a hydrogen breakup that was used to find the exact magnetic field by simply varying the simulated field until it matched the data.



(a) Excel simulation.



(b) Actual data.

Figure 3.9: Simulated and actual wiggles runs.

The time of flight is used to determine the electric fields. COLTRIMS spectrometers typically have 3 electric field regions: an acceleration region for the ions and electrons, a drift region for the electrons, and a booster region for the ions. The drift region will have an electrical field of zero. The electron time of flight can be used to calibrate the acceleration region. With the acceleration region defined by the electrons, the recoil time of flight can be used to determine the booster region.

For each of these fields, the field strengths in the Excel file can be fine-tuned until the simulation output matches the recorded data. Once this is done, the fine-tuned field strengths are used in *ColAHeLL.cfg*, and the resulting momentum spectra should be centered at zero.

3.14 Detector rotation procedure

The recoil ion and electron detectors each have multiple possible rotations and in order to get the correct position hit data, both need to be rotated properly to one another. This is again defined in *ColAHell.cfg*.

To do this, we can take advantage of the hot gas stripe seen on the hit position plots for each detector. For an experimental setup where the gas jet is traveling from the bottom of the chamber towards the top, the hot gas stripe needs to be horizontal. This limits the number of possible rotations to two. On the recoil detector, we can take advantage of the fact that the gas jet dot should be higher than the hot gas stripe because the heavier recoil ions take long enough to reach the detector that their initial lab frame momentum from the gas jet carries them higher on the detector. This allows us to clearly define the proper recoil ion detector orientation, as seen in Figure 3.10.

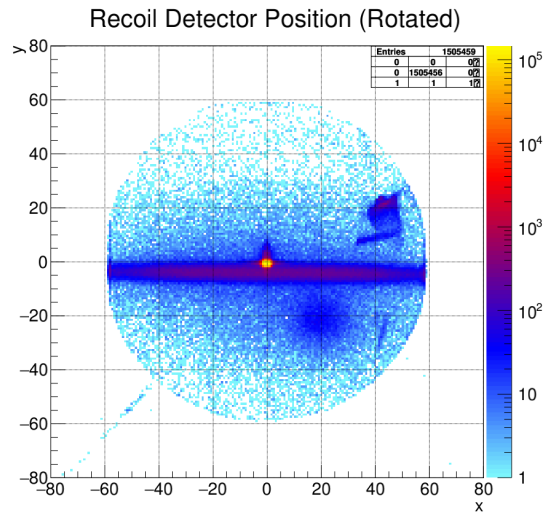


Figure 3.10: Properly rotated recoil detector hit position plot.

The electron side is slightly more difficult as the electrons are moving fast enough that there is not as clear of a spot on the detector. This can be seen in Figure 3.11.

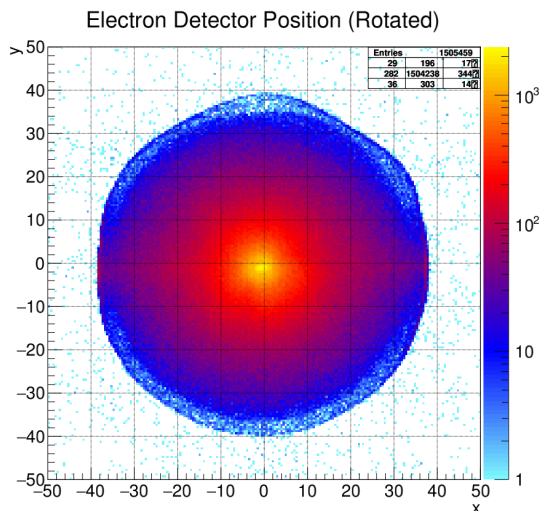


Figure 3.11: Properly rotated electron detector hit position plot.

To define the electron side, we can take advantage of momentum conservation in a 2-body breakup. If the rotation assignment is not correct (or incorrect by 180°), a blob will be observed in the electron vs recoil momenta. If we have an incorrect upside-down rotation with respect to the ion detector, a plot of the x and y components of the electron vs recoil momenta will have slopes of $+1$, while the z component plot will have the correct -1 slope, as can be seen in Figure 3.12.

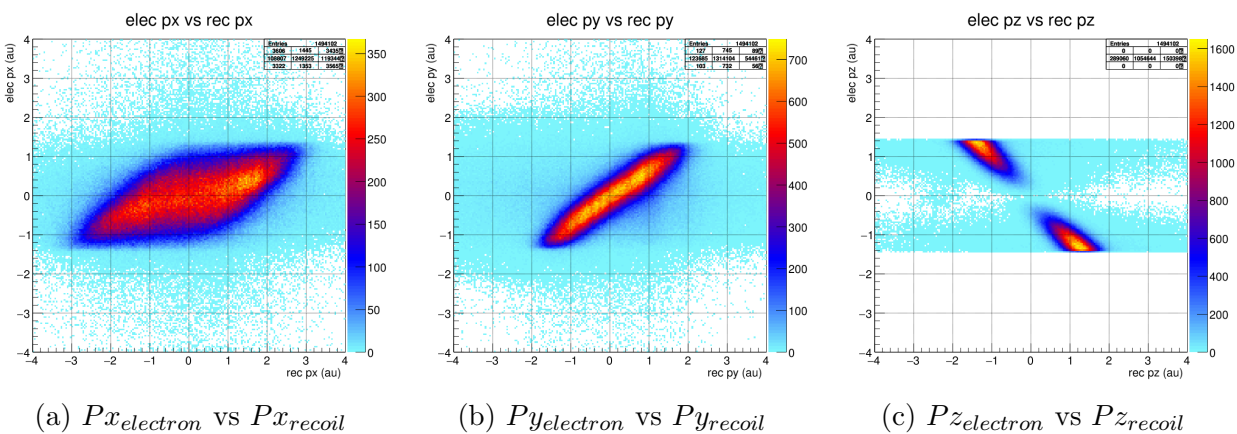


Figure 3.12: Electron momentum vs recoil ion momentum plots with incorrect upside-down detector rotation.

If the detector is properly rotated, a plot of $P_{electron}$ vs P_{recoil} will yield a slope of -1 , as can be seen in Figure 3.13.

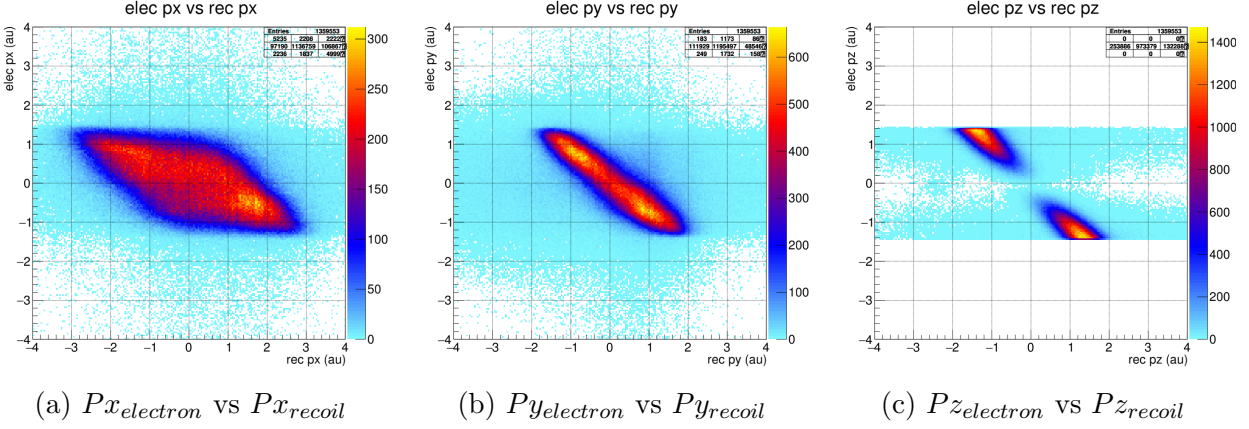


Figure 3.13: Electron momentum vs recoil ion momentum plots with correct detector rotation.

3.15 Determination of magnetic field direction

The direction of the magnetic field is needed to properly calculate momentum and is specified in *ColAHeL.cfg*. To determine the direction of the magnetic field from the Helmholtz coils, we can again look at the plot of $P_{electron}$ vs P_{recoil} we used to rotate the detectors. If the field is in the right direction, as it was in Figure 3.13, we will see clean -1 slopes. If the field is in the wrong direction, we see a swirling effect in the x and y components, as seen in Figure 3.14.

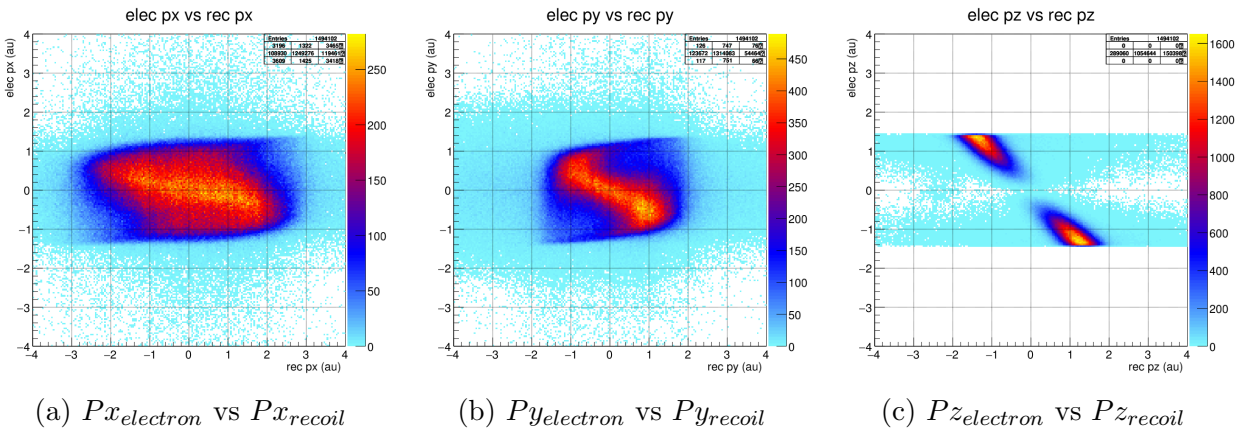


Figure 3.14: Electron momentum vs recoil ion momentum plots with incorrect B field direction.

3.16 Gas jet calibration procedure

Prior to the breakup, the molecules traveling in the gas jet carry an initial momentum that is dependent on the gas jet velocity. ColAHeLL corrects for this initial gas jet momentum using the velocity of the gas jet. This gas jet velocity can be determined by plotting the recoil x and y momentum components. We can use the difference between the gas jet dot and the hot gas stripe to find the momentum difference between the two in the y direction, then divide by the recoil ion mass to find the initial velocity of the gas jet. This velocity is defined in *ColAHeLL.cfg*, and will center the hot gas dot at zero when correctly defined.

The uncorrected momentum plot in Figure 3.15 has a hot gas dot that is approximately 2.3 atomic momentum units above zero.

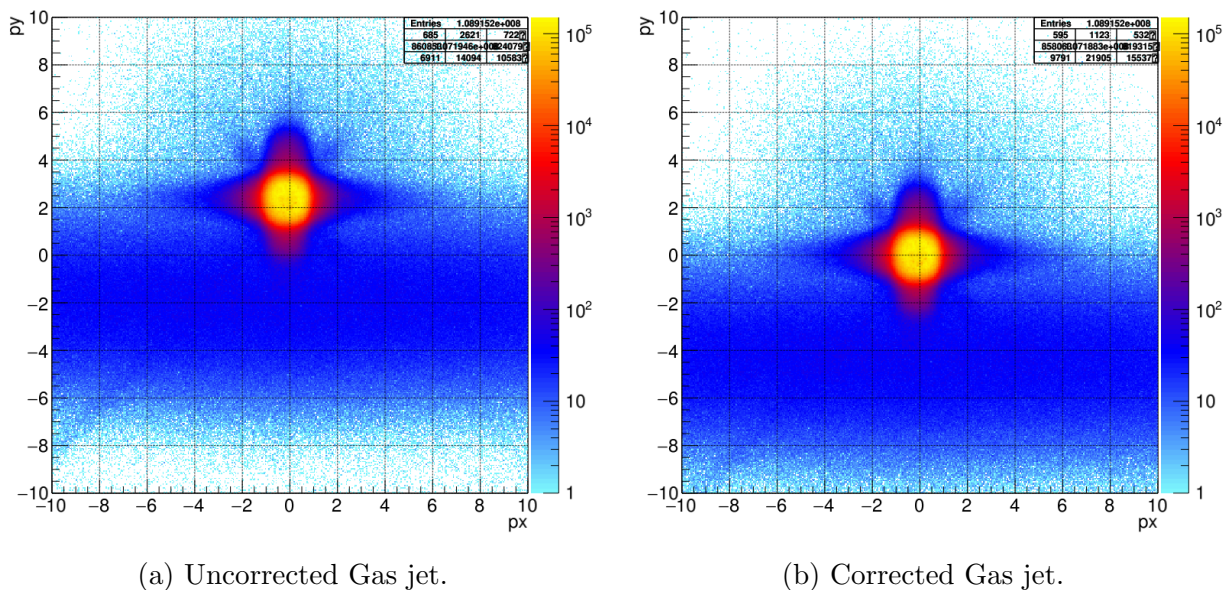


Figure 3.15: Recoil ion momentum plots before (a) and after (b) correction for gas jet velocity.

Dividing this by the mass of a hydrogen molecule yields a gas jet velocity of approximately 1400 m/s, which zeros the dot.

3.17 Generating custom plots in LMF2Root

With the basic calibration complete, the user can now examine the data. LMF2Root automatically generates a number of useful plots, but there are often specific and novel plots that are desired for a given experiment. To manipulate ColAHeLL data, the user can go to the *user_analysis.cpp* file and add their own analysis code.

Two of the most essential tools for writing analysis code are the histogram fill functions. These allow the user to create custom histograms to view their data. The general form for the 1 and 2 dimensional histogram fill commands is shown in Figure 3.16.

```
31 #undef AUTO
32 #define AUTO 1000 //returns the line number in the current file. Can be used to make life easier for histogram numbering.
33
34
35
36 char reaction_dir[360];
37
38 if (this->use_master_folder) {
39     strcpy(reaction_dir, this->CH_master_folder);
40     strcat(reaction_dir, reac->name);
41 }
42 else
43     strcpy(reaction_dir, reac->name);
44
45 int ID = reac->ID;
46 string dir = reaction_dir;
47 string old_dir = reaction_dir;
48
49 //Custom Plot
50 //H2 -> H + p + e-
51 if (ID == 7) { //Use tag from presort
52     dir = reaction_dir;
53     dir += "/TinyTestH2->Hp+e-"; //Name the directory for the reaction
54
55     //Hist->fill1(Plot #, "Plot Title", variable, 1.0, "Display Title", # of bins, Min value, Max value, "Axis label", dir.c_str());
56     Hist->fill1(AUTO, "Electron Energy", e[0]->energy(), 1.0, "Electron Energy", 100, 0, 5, "eV", dir.c_str());
57
58     //Hist->fill2(Plot #, "Plot Title", x variable, y variable, 1.0, "Display Title", # of x bins, Min x, Max x, "x axis label", # of y bins, Min y, Max y, "y axis label", dir.c_str());
59     Hist->fill2(AUTO, "EE vs RE", f[0]->energy(), e[0]->energy(), 1.0, "Electron energy vs Recoil energy", 400, 0, 10, "Recoil energy", 400, 0, 10, "Electron energy", dir.c_str());
60 }
61
62
63
64
```

Figure 3.16: Histograms in user_analysis.cpp.

The plot number is an identifier that tells LMF2Root where to put data. This can be defined specifically in order to overload a histogram, or can be left to the automatic line number. The histogram is given a title that will appear in the directory of the .root file. The variables are then defined, as is the display title, the axis labels, and the binning. These histograms can be set up to plot any of the different quantities recovered by ColAHeLL, or any combination of them. Table 3.4 shows how to access many of the most important values, and Table 3.5 shows how to execute a variety of common vector operations.

Particle	Quantity	Code Example
Electron 1	x hit position	<code>e[0]->raw.data.x</code>
	y hit position	<code>e[0]->raw.data.y</code>
	time of flight	<code>e[0]->raw.data.tof</code>
	momentum vector	<code>e[0]->mom</code>
	x momentum	<code>e[0]->mom.x</code>
	y momentum	<code>e[0]->mom.y</code>
	z momentum	<code>e[0]->mom.z</code>
	energy	<code>e[0]->energy()</code>
Electron 2	x hit position	<code>e[1]->raw.data.x</code>
	y hit position	<code>e[1]->raw.data.y</code>
	time of flight	<code>e[1]->raw.data.tof</code>
	momentum vector	<code>e[1]->mom</code>
	x momentum	<code>e[1]->mom.x</code>
	y momentum	<code>e[1]->mom.y</code>
	z momentum	<code>e[1]->mom.z</code>
	energy	<code>e[1]->energy()</code>
Recoil Ion 1	x hit position	<code>r[0]->raw.data.x</code>
	y hit position	<code>r[0]->raw.data.y</code>
	time of flight	<code>r[0]->raw.data.tof</code>
	mass	<code>r[0]->raw.m</code>
	charge	<code>r[0]->raw.q</code>
	momentum vector	<code>r[0]->mom</code>
	x momentum	<code>r[0]->mom.x</code>
	y momentum	<code>r[0]->mom.y</code>
z momentum	<code>r[0]->mom.z</code>	
energy	<code>r[0]->energy()</code>	
Recoil Ion 2	x hit position	<code>r[1]->raw.data.x</code>
	y hit position	<code>r[1]->raw.data.y</code>
	time of flight	<code>r[1]->raw.data.tof</code>
	mass	<code>r[1]->raw.m</code>
	charge	<code>r[1]->raw.q</code>
	momentum vector	<code>r[1]->mom</code>
	x momentum	<code>r[1]->mom.x</code>
	y momentum	<code>r[1]->mom.y</code>
z momentum	<code>r[1]->mom.z</code>	
energy	<code>r[1]->energy()</code>	

Table 3.4: Important ColAHeL commands.

Vector Operation	Code Example
Magnitude	<code>e[0]->mom.Mag()</code>
Unit Vector	<code>e[0]->mom.Norm()</code>
Cross Product	<code>r[0]->mom.Cross(e[0]->mom)</code>
Dot Product	<code>r[0]->mom.Dot(e[0]->mom)</code>
Angle Between Two Vectors	<code>r[0]->mom.Angle(e[0]->mom)</code>
Rodrigues' Vector Rotation	<code>r[0]->mom.rotate_about_k(e[0]->mom,PI())</code>
Polar θ_X Coordinate	<code>e[0]->mom.ThetaX()</code>
Polar θ_Y Coordinate	<code>e[0]->mom.ThetaY()</code>
Polar θ_Z Coordinate	<code>e[0]->mom.Theta()</code>
Polar ϕ_{XY} Coordinate	<code>e[0]->mom.Phi()</code>
Polar ϕ_{YZ} Coordinate	<code>e[0]->mom.PhiYZ()</code>
Polar ϕ_{XZ} Coordinate	<code>e[0]->mom.PhiZX()</code>

Table 3.5: Important vector operations.

With the histogram functions, vector operations, and the quantities retrieved by ColA-Hell, the user has a vast arsenal at their disposal to analyze COLTRIMS data.

Chapter 4

Detailed analysis of the two-color experiment

4.1 Fine momentum calibration procedure

The calibration procedure detailed in the previous chapter will yield generally centered momentum distributions. In the two-color ALS/laser data, many expected features are already identifiable, as seen in Figure 4.1.

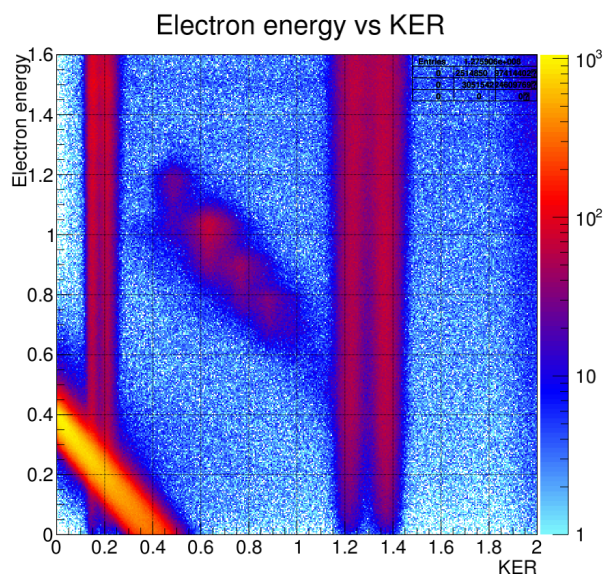


Figure 4.1: Electron energy vs KER with course calibration.

However, there are still imperfections in the way the data is being processed. Electric and magnetic fields are assumed to be constant in the various spectrometer field regions, and while this is a very good approximation of the actual fields, this is not entirely accurate. Small inhomogeneities in the electric and magnetic fields increase error in the momentum calculations, and this error can obscure important but subtle features. Thankfully, LMF2Root allows us to account for this by making small adjustments to the momentum vectors to correct for these errors.

4.1.1 Momentum sphere and calibration angles

A given molecular dissociation will occur at a unique energy, and the orientation of the molecules in the gas jet is random. This means that a molecule that dissociates parallel to the jet direction and a molecule that dissociates anti-parallel to the jet direction will have momentum vectors of the same magnitude. In the lab frame, each reaction fills out a momentum sphere as more randomly orientated events are recorded.

The fact that a uniform momentum sphere should be observed by a correctly calibrated measurement can be used to make the fine adjustments needed to correct for field inhomogeneities. If the momentum spheres recovered are not uniformly spherical in shape, then the calibration is not completely accurate.

It can be difficult to determine defects in the sphere by eye, as seen in Figure 4.2.

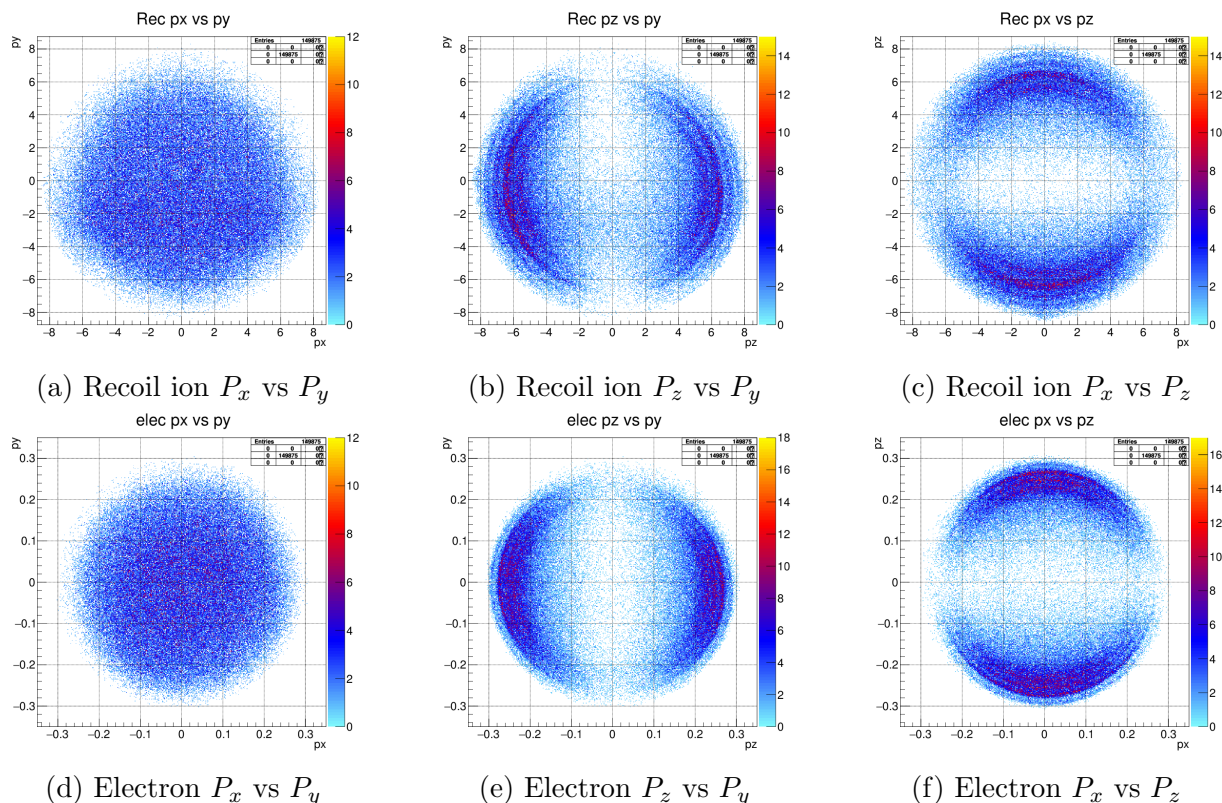


Figure 4.2: Uncorrected recoil ion and electron momentum sphere projections.

A more precise method is to calculate a series of azimuthal and polar momentum angles for both the recoil ion and electron momentum vectors, as shown below:

$$\theta_x = \arccos \left(\frac{p_x}{\sqrt{p_x^2 + p_y^2 + p_z^2}} \right) \quad (4.1)$$

$$\theta_y = \arccos \left(\frac{p_y}{\sqrt{p_x^2 + p_y^2 + p_z^2}} \right) \quad (4.2)$$

$$\theta_z = \arccos \left(\frac{p_z}{\sqrt{p_x^2 + p_y^2 + p_z^2}} \right) \quad (4.3)$$

$$\phi_{xy} = \arctan2 \left(\frac{p_x}{p_y} \right) \quad (4.4)$$

$$\phi_{xz} = \arctan2 \left(\frac{p_x}{p_z} \right) \quad (4.5)$$

$$\phi_{yz} = \arctan2 \left(\frac{p_y}{p_z} \right) \quad (4.6)$$

These angle plots, as seen in Figure 4.3, highlight the imperfections in the momentum sphere clearly.

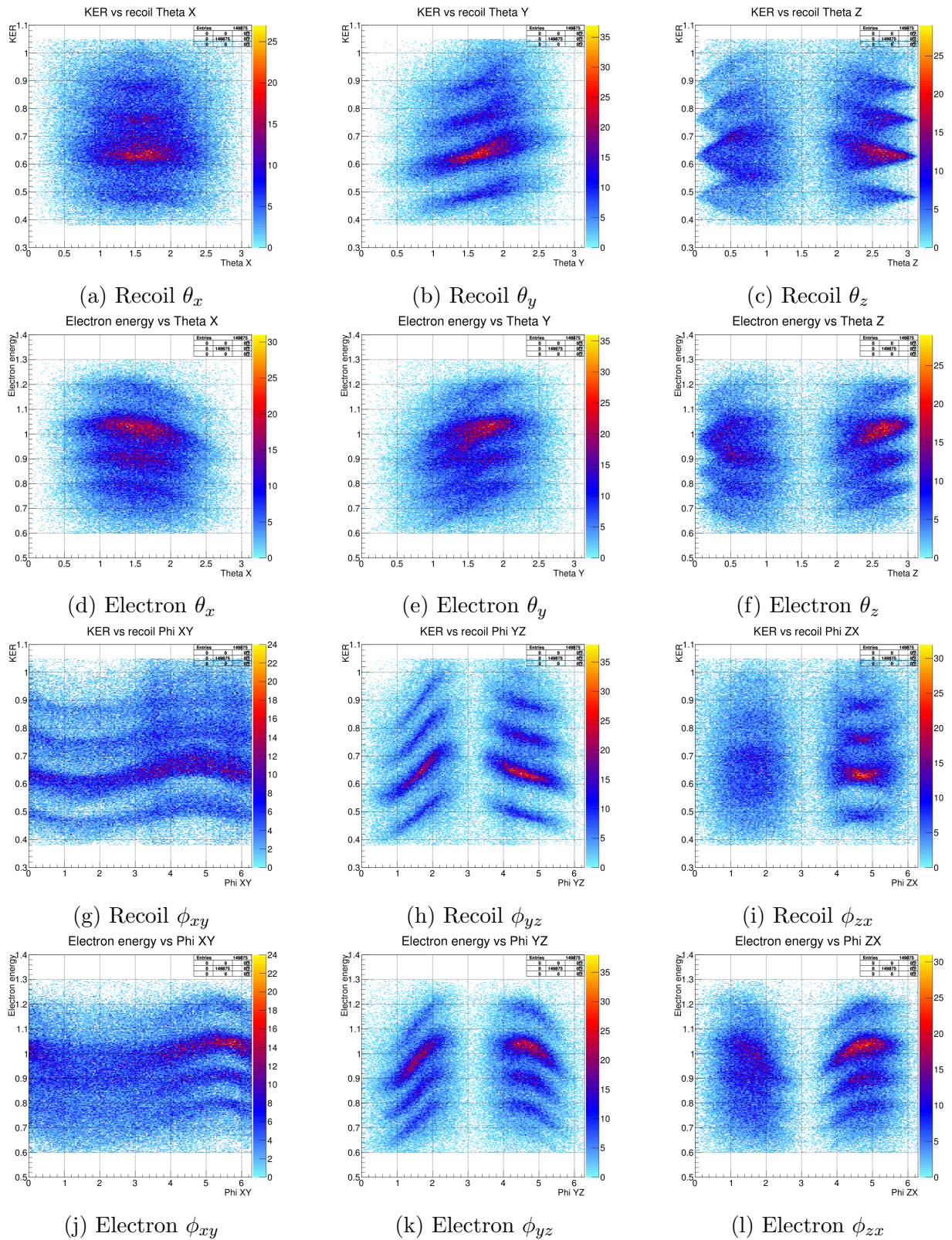


Figure 4.3: Uncorrected recoil ion and electron θ and ϕ angles.

4.1.2 Momentum shift and stretch operations

The *ColAHelL.cfg* reaction block allows users to stretch momentum in the x, y, and z directions by scaling the momentum components by multiplying the components by a user defined factor, or to shift momentum in the x, y, and z directions by adding a user defined correction factor. The shift and stretch corrections can be used to iteratively modify the momentum vectors to flatten the angle plots and to correct for defects in the momentum sphere.

The result of these corrections can be seen in Figure 4.4.

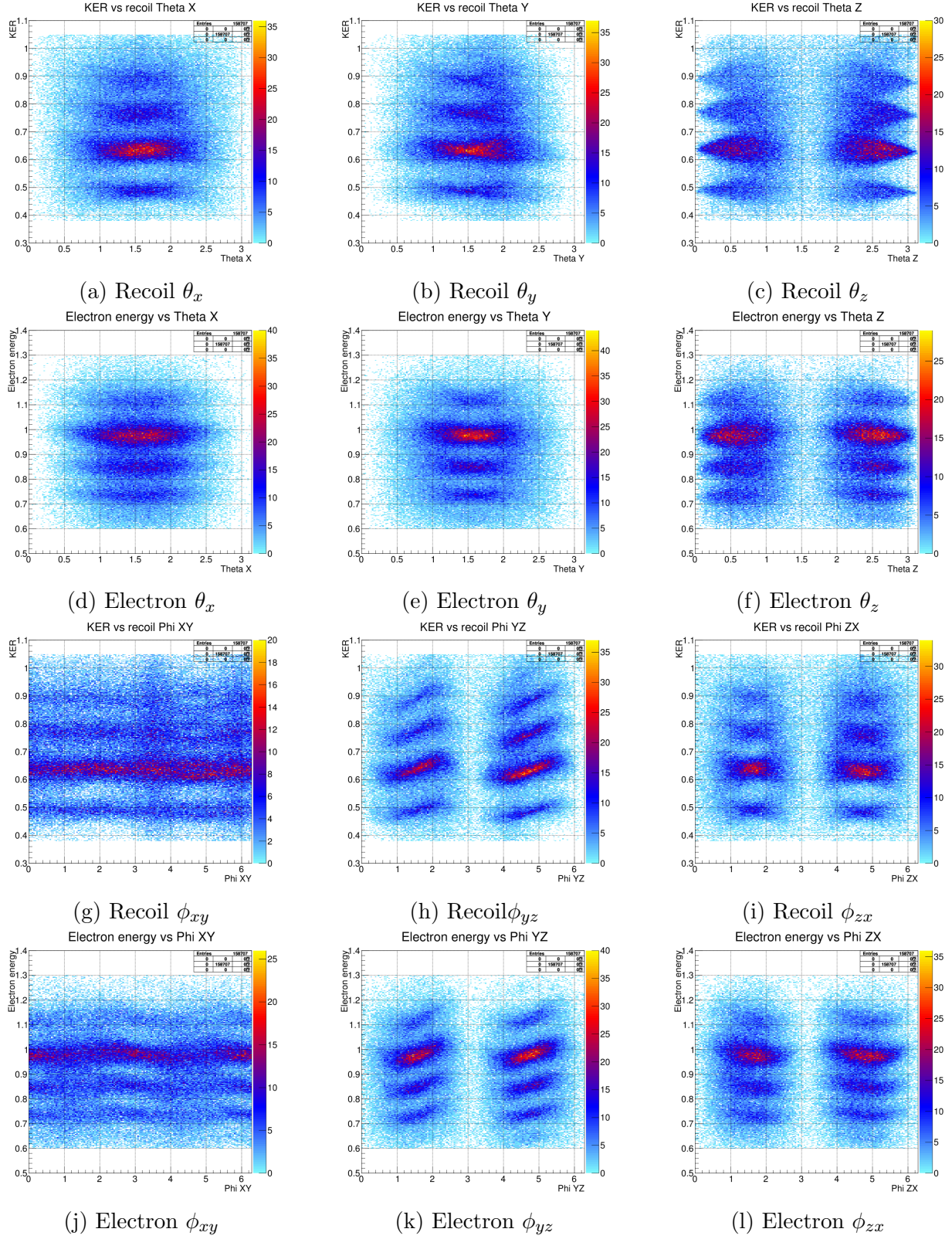


Figure 4.4: Shifted and stretched recoil ion and electron θ and ϕ angles.

These corrections, while minute, have a dramatic effect on the calibration. The electron energy vs KER map with the stretches and shifts, as seen in Figure 4.5, shows a dramatically sharper definition.

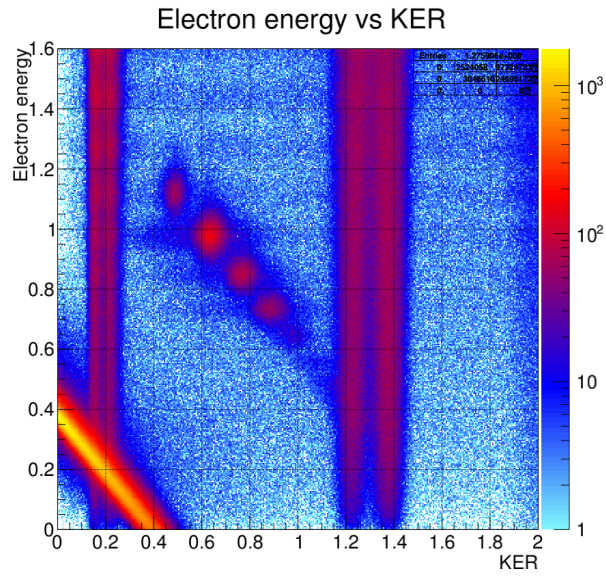
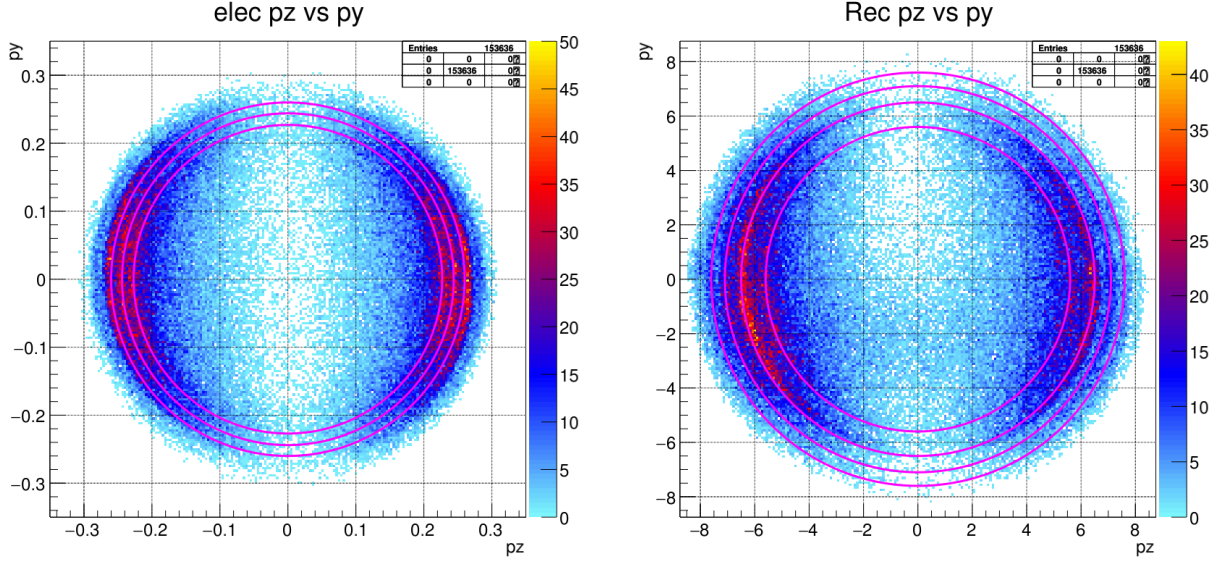


Figure 4.5: Electron energy vs KER with shifts and stretches.

However, while these improvements are dramatic, the ϕ plots show that there is still room for improvement.

4.1.3 Momentum skew operations

Careful inspection of the momentum plots reveals a slightly skewed elliptical distortion, as seen in Figure 4.6.



(a) Electron P_y vs P_z

(b) Recoil P_y vs P_z

Figure 4.6: Momentum plots showing skewed momentum sphere.

This skew distortion is likely due to a slight tilt between the spectrometer and the magnetic field. As the distortion is not along any of the three Cartesian axes defined in the experiment, a shear mapping correction is required to correct it, as shown below:

$$\begin{bmatrix} P'_x \\ P'_y \\ P'_z \end{bmatrix} = \begin{bmatrix} P_x + xySheerFactor \cdot P_y + xzSheerFactor \cdot P_z \\ P_y + yxSheerFactor \cdot P_x + yzSheerFactor \cdot P_z \\ P_z + +xzSheerFactor \cdot P_x + yzSheerFactor \cdot P_y \end{bmatrix} \quad (4.7)$$

This can be implemented in LMF2Root in *user_analysis.cpp*. Using an iterative process to determine the shear factors, the momentum vectors are updated with these small skew corrections, and can flatten the angle plots to give us our best possible calibration. The momentum angle results of this iterative process can be seen in Figure 4.7.

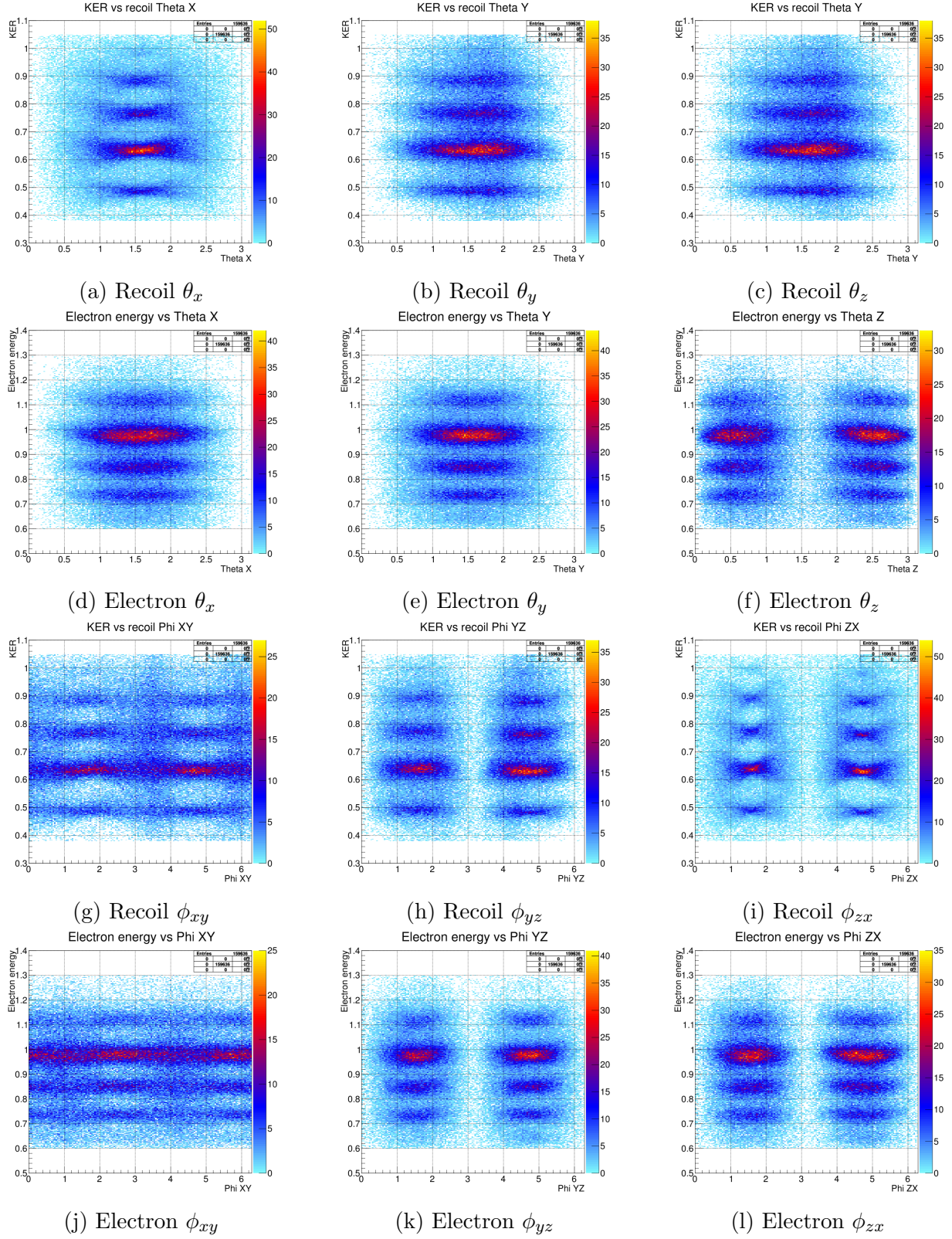


Figure 4.7: Skewed recoil ion and electron θ and ϕ angles.

With the momentum sphere optimally zeroed, the final tightest calibration can be achieved, as seen in Figure 4.8, showing improvements over preceding Figures 4.1 and 4.5.

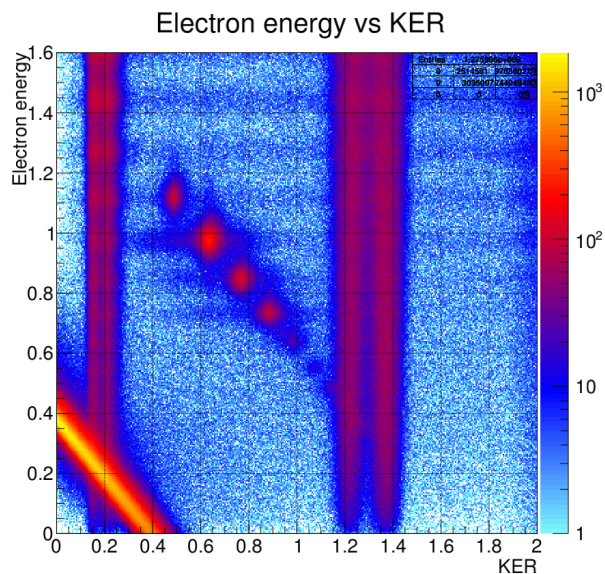


Figure 4.8: Electron energy vs KER with shear mapping operations.

4.2 Contamination removal

While the calibration is now at a level where the physically interesting features are sharply defined, there is a remaining problem of gas jet contamination. These contamination regions, seen as vertical stripes in the energy map plots, are due to ions being incorrectly associated with electrons and bunchmarkers from different breakup events.

Some contamination regions, such as the ones with higher than 1.1 eV KER in the 18.54 eV data, are fortunately positioned such that they could be ignored without obscuring the physically interesting regions of the energy map, but other contamination regions are positioned exactly where interesting physics would be expected, as seen in Figure 4.9.

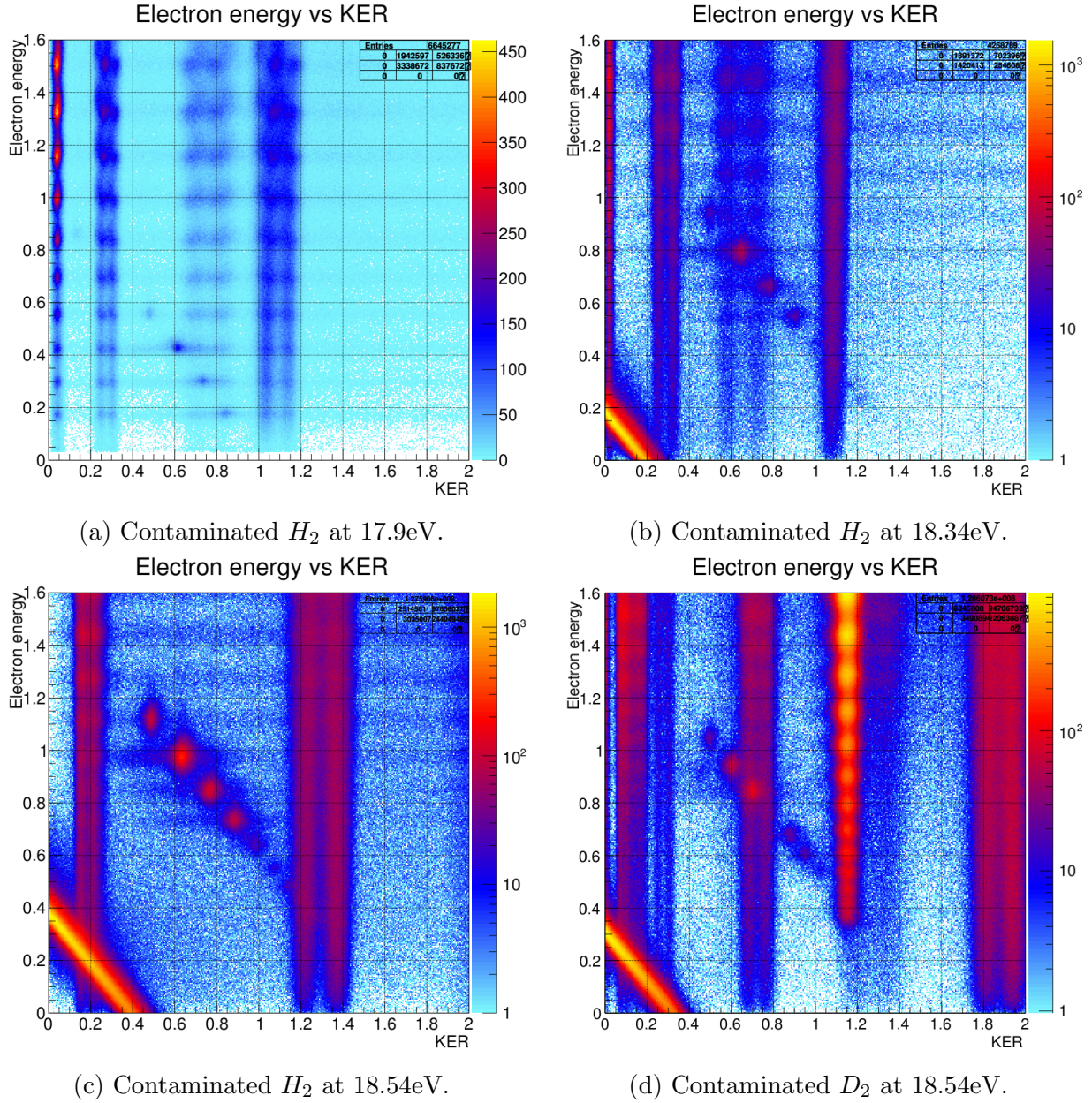
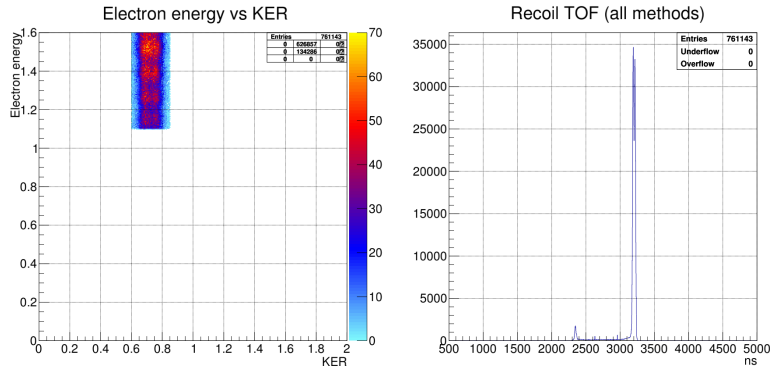


Figure 4.9: Jet dot contamination.

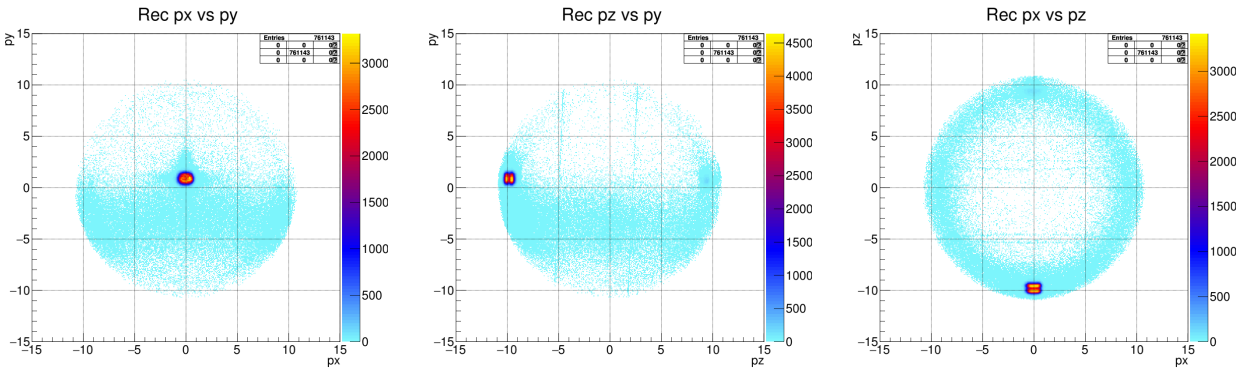
Proceeding any further in the analysis therefore requires determining a way of eliminating this contamination in such a way that the underlying events of interest can still be recovered. To do this, the contamination events need to first be isolated. There is a diverse parameter space that can be examined in order to find somewhere that localizes only the contaminated events.

A gate can be constructed using regions of the energy map to examine a region containing only the contaminated events and no other structures. Examination of this region shows that there is a specific signature in the recoil ion time of flight and momentum plots, as seen in Figure 4.10.



(a) Gated energy map.

(b) Gated recoil ion TOF.



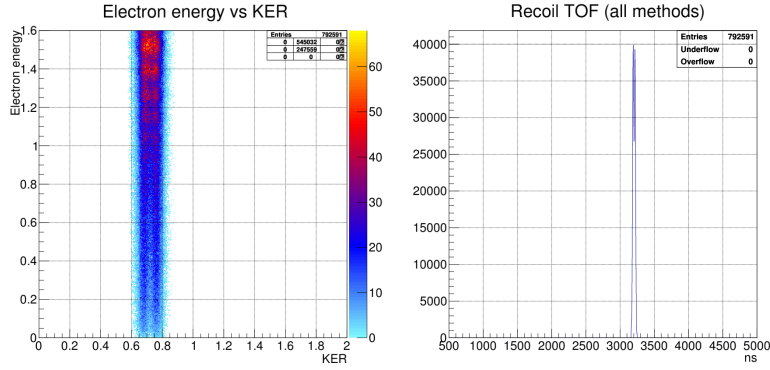
(c) Gated P_x vs P_y .

(d) Gated P_z vs P_y .

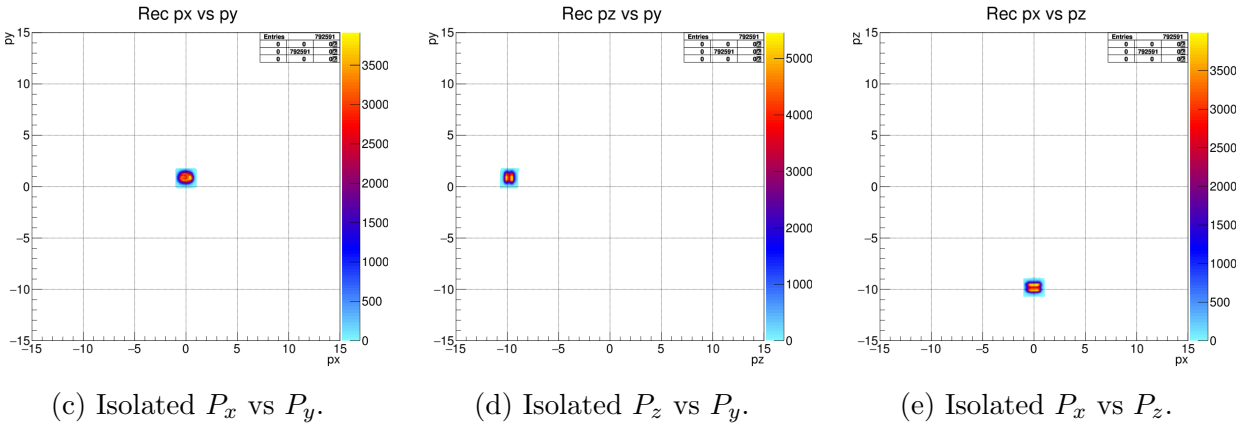
(e) Gated P_x vs P_z .

Figure 4.10: Contamination signature.

A gate selecting events that are located in the contaminated TOF region, and are in the contaminated P_x vs P_y region, and are in the contaminated P_y vs P_z region, AND are in the contaminated P_x vs P_z region, can be constructed. This gate can isolate the contamination, as seen in Figure 4.11.



(a) Isolated energy map. (b) Isolated recoil ion TOF.



(c) Isolated P_x vs P_y . (d) Isolated P_z vs P_y . (e) Isolated P_x vs P_z .

Figure 4.11: Contamination isolation.

Events isolated by this gate can be rejected. Since this method requires an event to be present in each signature contamination region to be rejected, background counts and real, physically important events are unaffected. The gated region shown in Figure 4.10 can be examined again with the contaminated stripe shown in Figure 4.11 removed. The resulting distribution in Figure 4.12 shows that the contamination stripe is cleanly removed.

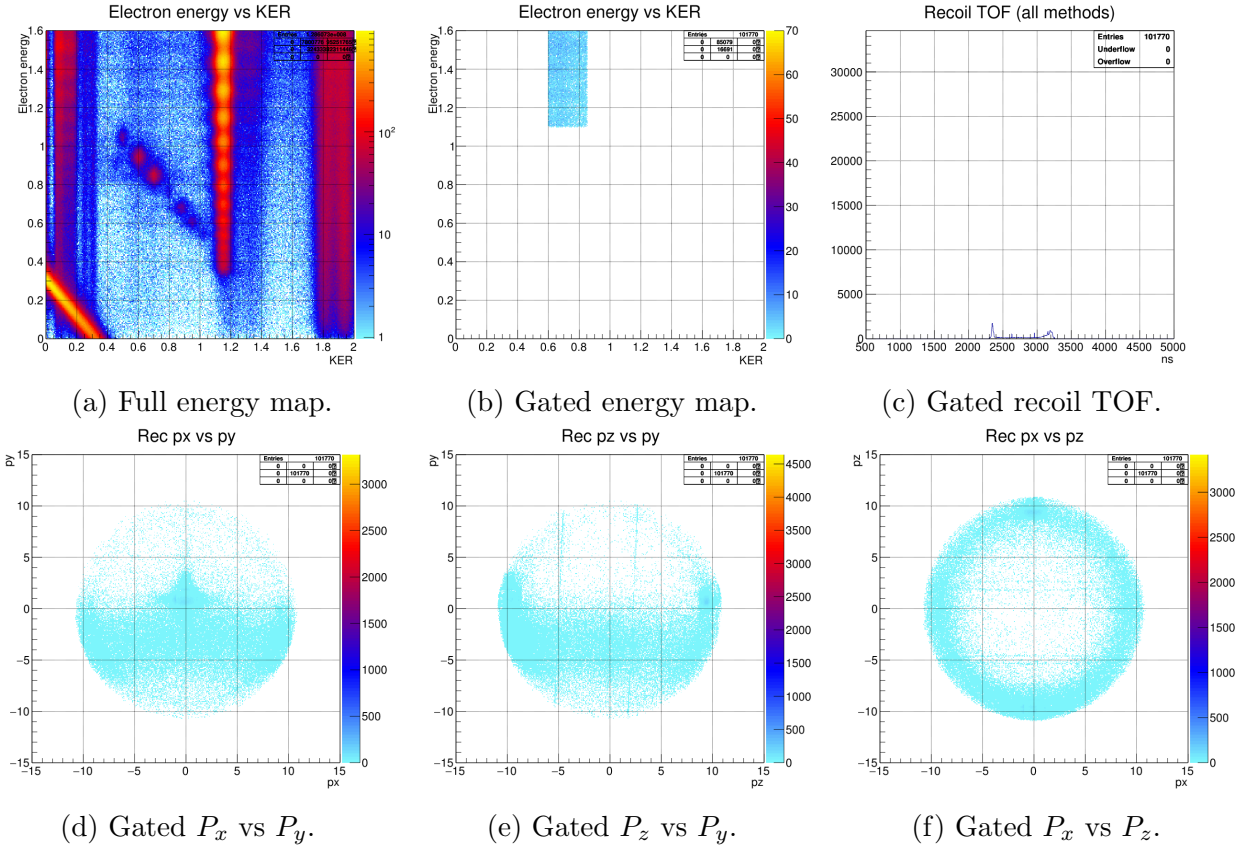
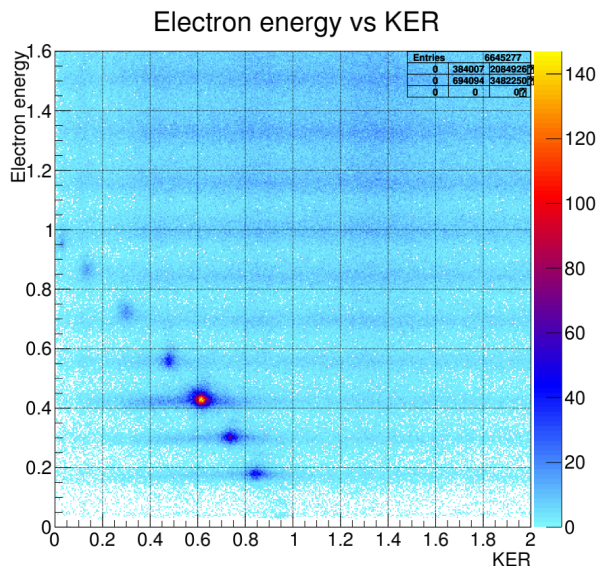
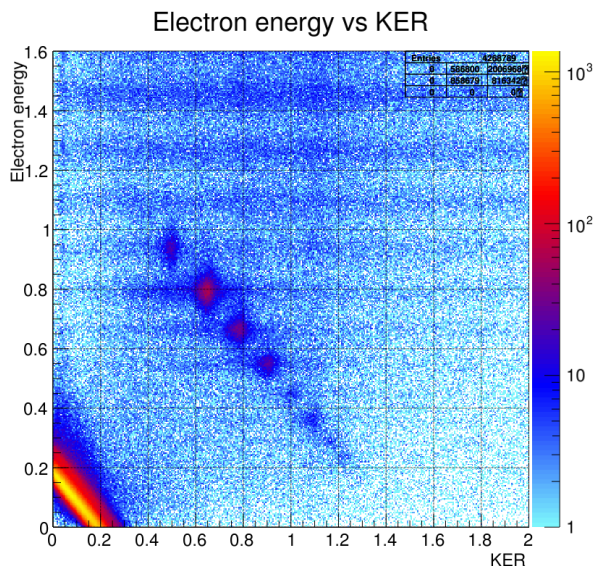


Figure 4.12: Removed contamination.

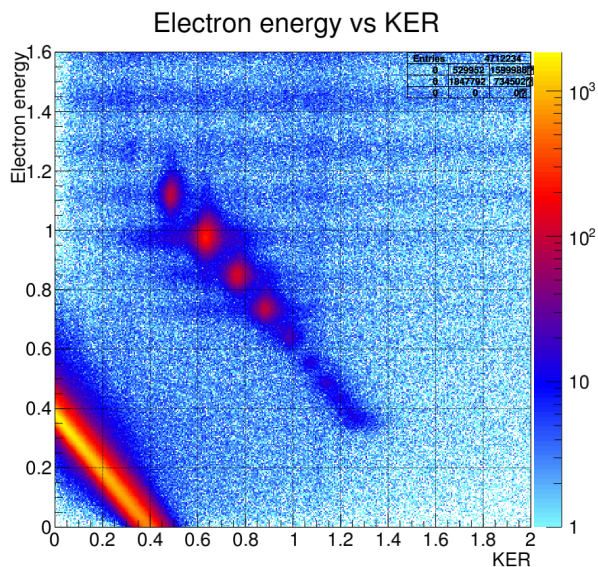
This process is repeated for each contamination stripe, until all have been excised. Cleaned energy maps are shown in Figure 4.13.



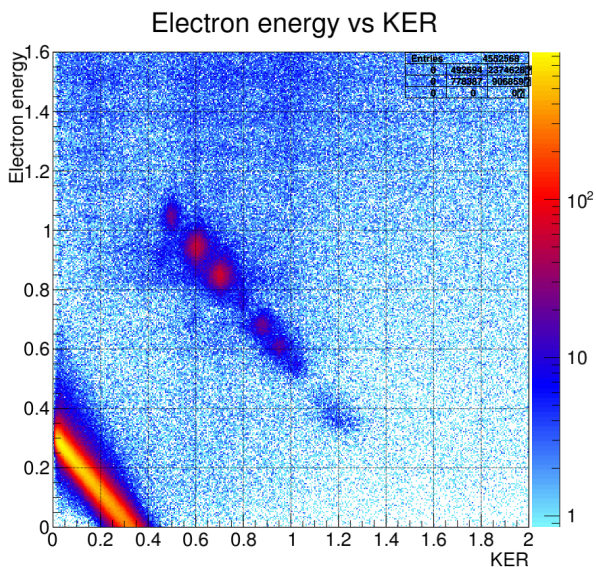
(a) Cleaned H_2 at 17.9eV.



(b) Cleaned H_2 at 18.34eV.



(c) Cleaned H_2 at 18.54eV.



(d) Cleaned D_2 at 18.54eV.

Figure 4.13: Energy maps after contamination removal.

4.3 Molecular Frame Photoelectron Angular Distribution (MFPAD)

In order to see the electron retroaction effect, the breakup must be examined in the molecular frame. The correction for the electron momentum vectors from lab frame to a center of momentum molecular frame is negligible, and the electron vectors can be used as

is. The recoil momentum vectors, however, receive a momentum kick from the electrons that is significant enough that it should be accounted for, as shown below:

$$\vec{p}_{rec}^{M.F.} = \vec{p}_{rec}^{L.F.} + 0.5\vec{p}_{elec}^{L.F.} \quad (4.8)$$

With the proper molecular frame momentum vectors now recovered, the details of the breakup can be examined. The angle between the molecular axis, defined by the molecular frame recoil ion momentum vector, and the molecular frame electron momentum vector, can be determined for every breakup. This molecular frame photoelectron angular distribution, which will subsequently be referred to as an **MFPAD**, shows the distributions of where electrons are ejected from the molecule in this experiment.

The MFPAD is an angular histogram. With only two vectors, the MFPAD is a polar angle without quadrant information. The histogram can be projected in a polar form that shows a $0 - \pi$ angular range, and then mirrored about the molecular axis to display the information in a convenient way, as shown in Figure 4.14

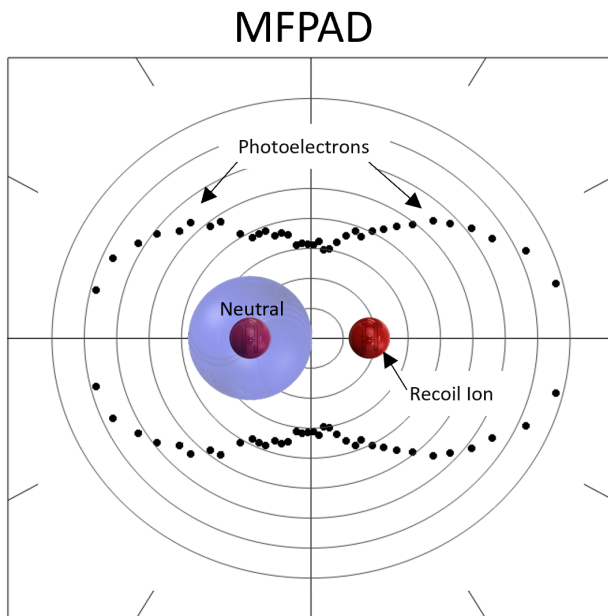


Figure 4.14: Polar representation of a Molecular Frame Photoelectron Angular Distribution.

4.4 Asymmetry parameter

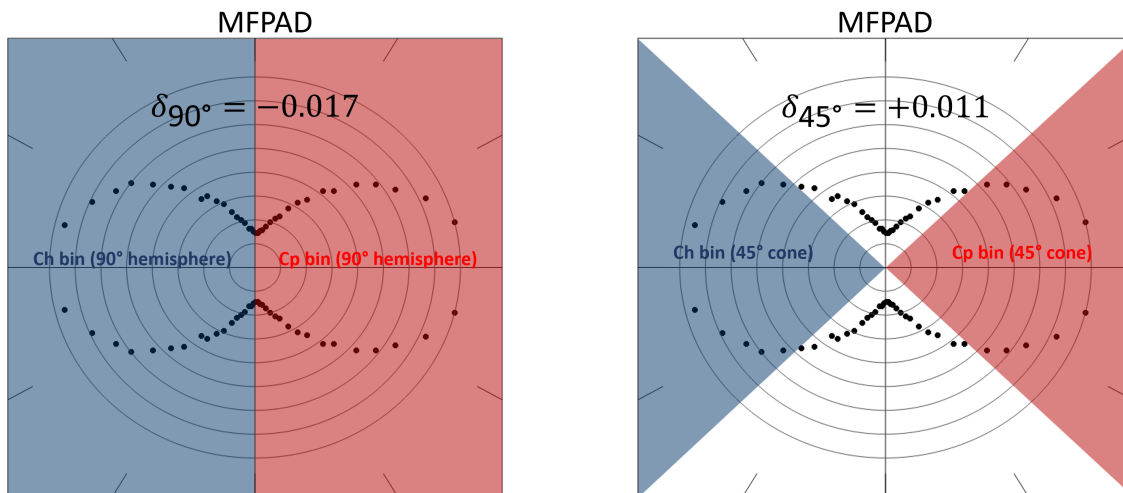
For a symmetrical breakup without any interesting physical phenomena, the MFPAD should be a symmetric dipole distribution. The breakups that this experiment is designed to examine, however, are not symmetrical.

The asymmetry of the photoelectron distribution is one of the key metrics of interest for this experiment. To that end, the asymmetry of the MFPAD must be quantified. Past electron retroaction experiments, conducted at Frankfurt[7] and Berkeley [8], have divided the MFPAD into a neutral side bin C_h and a recoil ion side bin C_p . These bins are then used to define an asymmetry parameter δ as such:

$$\delta = \frac{C_p - C_h}{C_p + C_h} \quad (4.9)$$

This asymmetry parameter will be zero for a symmetric distribution, positive for a distribution that is asymmetric favoring photoelectrons in the direction of the protons, and negative for a distribution that is asymmetric favoring photoelectrons in the direction of the neutral hydrogen.

The exact method of dividing the MFPAD bins also requires discussion. Past works have used a 45° cone to define the C_h and C_p bins. This focuses on the events with dissociation occurring parallel to the molecular axis, but can be misleading, especially with small asymmetries. Figure 4.15 shows an MFPAD that has a slight negative hemispherical asymmetry, and a slight positive 45° conical asymmetry.

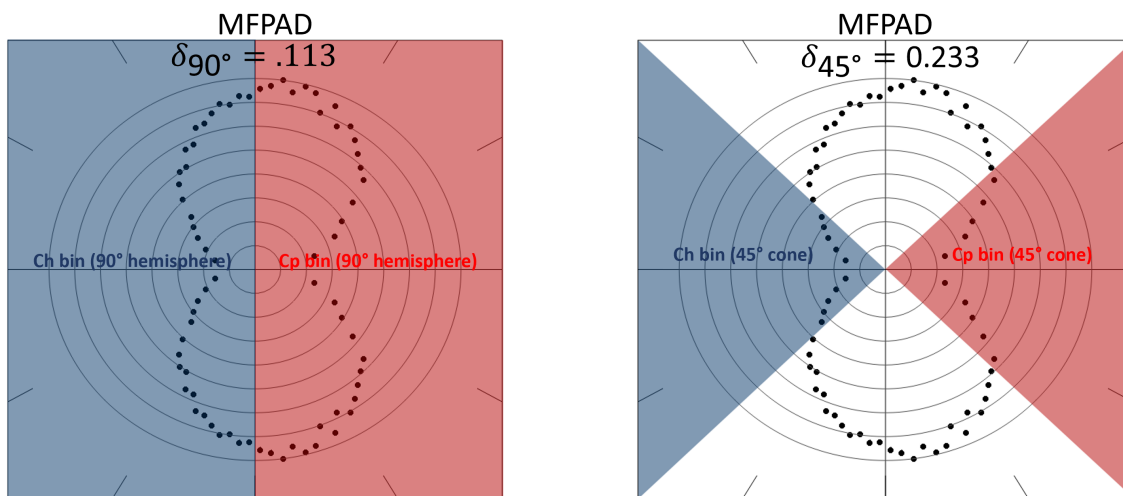


(a) 90° binning

(b) 45° binning

Figure 4.15: MFPADs of events dissociating with molecular axis parallel to polarization axis.

Narrower conical conditions also leave out significant portions of the distribution when looking at MFPADs with a molecular orientation perpendicular to the polarization axis, as seen in Figure 4.16.



(a) 90° binning

(b) 45° binning

Figure 4.16: MFPADs of events dissociating with molecular axis perpendicular to polarization axis.

Due to these factors, a 90° hemispherical bin will be used to compute the δ asymmetry parameters that are to follow.

4.4.1 Uncertainty in asymmetry parameter

The uncertainty in the asymmetry parameter δ can be found using the general formula for error propagation[36]. δ is a function of two variables:

$$\delta(C_p, C_h) = \frac{C_p - C_h}{C_p + C_h} \quad (4.10)$$

Using the general formula for error propagation, the uncertainty in δ can be expressed as:

$$\sigma[\delta(C_p, C_h)] = \sqrt{\left(\frac{\partial\delta(C_p, C_h)}{\partial C_p} \cdot \sigma_{C_p}\right)^2 + \left(\frac{\partial\delta(C_p, C_h)}{\partial C_h} \cdot \sigma_{C_h}\right)^2} \quad (4.11)$$

The uncertainty in each count can be expressed as the square root of that count:

$$\sigma_{C_p} = \sqrt{C_p} \quad \sigma_{C_h} = \sqrt{C_h} \quad (4.12)$$

Evaluating the partial derivatives gives us our final result:

$$\frac{\partial\delta(C_p, C_h)}{\partial C_p} = \frac{\partial}{\partial C_p} \left(\frac{C_p - C_h}{C_p + C_h} \right) = \frac{2 \cdot C_h}{(C_p + C_h)^2} \quad (4.13)$$

$$\frac{\partial\delta(C_p, C_h)}{\partial C_h} = \frac{\partial}{\partial C_h} \left(\frac{C_p - C_h}{C_p + C_h} \right) = \frac{-2 \cdot C_p}{(C_p + C_h)^2} \quad (4.14)$$

$$\sigma[\delta(C_p, C_h)] = \sqrt{\left(\frac{2 \cdot C_h}{(C_p + C_h)^2} \cdot \sqrt{C_p}\right)^2 + \left(\frac{-2 \cdot C_p}{(C_p + C_h)^2} \cdot \sqrt{C_h}\right)^2} \quad (4.15)$$

This result can be computed rapidly and is used for analysis of this data.

4.5 Legendre polynomial fit parameters

We can also approximate the MFPAD results as a function of $\cos(\theta)$ using a Legendre polynomial series. This series approximation, which we truncate at the 4th order Legendre polynomial to account for the absorption of two photons, can be seen below:

$$MFPAD(\cos(\theta)) = \frac{\sigma}{4\pi} (1 + \beta_2 P_2(\cos(\theta)) + \beta_4 P_4(\cos(\theta)) + \dots) \quad (4.16)$$

$$MFPAD(\cos(\theta)) = \frac{\sigma}{4\pi} (1 + \beta_2 P_2(\cos(\theta)) + \beta_4 P_4(\cos(\theta))) \quad (4.17)$$

$$MFPAD(\cos(\theta)) = \frac{\sigma}{4\pi} \left(1 + \beta_2 \frac{1}{2} (3(\cos(\theta))^2 - 1) + \beta_4 \frac{1}{8} (35(\cos(\theta))^4 - 30(\cos(\theta))^2 + 3) \right) \quad (4.18)$$

The free parameters in this series approximation function can be fit using a least squares method in Microsoft Excel [37]. To do this, first a table of experimental MFPAD data divided into bins is imported. Next, values for the approximation function $MFPAD(\sigma, \beta_2, \beta_4)$ are generated using equally spaced values of $\cos\theta$. We can then generate the sum of squared errors, as shown below:

$$SSE = \sum_{n=1}^{36} (MFPADdata_n - MFPAD(\sigma, \beta_2, \beta_4)_n)^2 \quad (4.19)$$

This can be minimized by using Excel's Solver add-in to change σ , β_2 , and β_4 . This solver uses a generalized reduced gradient method which can quickly find the minimum of the sum of squared errors. An option to use multiple starting guesses that are then iteratively solved using the GRG method can be used to ensure that the true minimum is found and that the solver algorithm avoids becoming "stuck" in a local minimum.

As before with bin count asymmetry parameters, we can cut the MFPAD into two regions. The C_h MFPAD and the C_p MFPAD can both be individually fit, as seen in Figure 4.17.

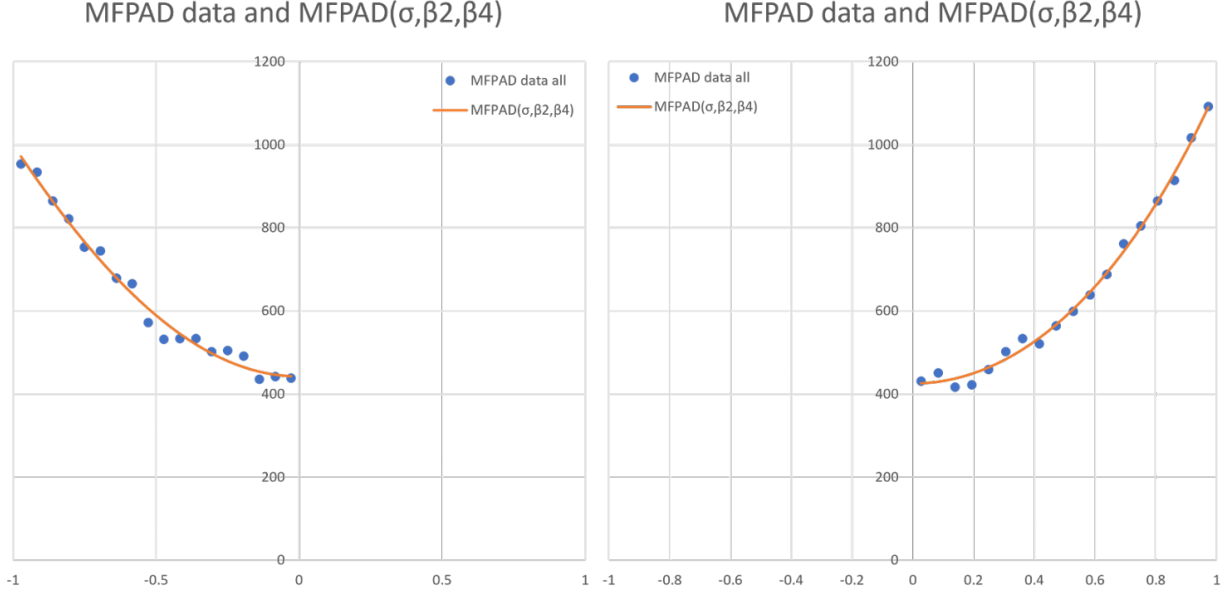


Figure 4.17: Legendre polynomial MFPAD C_h and C_p fits.

Once the fits are complete, we can define a new asymmetry parameter using the σ fit parameters for the two halves of the distribution:

$$\delta_\sigma(\sigma_{C_p}, \sigma_{C_h}) = \frac{\sigma_{C_p} - \sigma_{C_h}}{\sigma_{C_p} + \sigma_{C_h}} \quad (4.20)$$

4.6 Classical retroaction model

The previous work by Heck[8] introduces a classical retroaction model that assumes that since the Coulomb potential scales as $1/r_e$, the asymmetry due to electron retroaction can be modeled by a simple fit parameter. This is included in the paper[8] and discussed in detail in S. Heck's masters thesis[38].

First, the time required in the dissociation of H_2^+ to reach an internuclear distance of 5.5 au is calculated as a function of the kinetic energy release:

$$t(KER) = 5.5au\sqrt{\frac{m_H}{KER}} \quad (4.21)$$

where m_H is the mass of the hydrogen. A classical estimate for the distance from the electron to the bound molecular ion can then be expressed as a function of electron energy E_e and time as:

$$r_e(E_e, t) = \sqrt{\frac{2E_e}{m_e}} \cdot t(KER) \quad (4.22)$$

where m_e is the mass of the electron. This can be simplified to a final expression for r_e as a function of E_e and KER:

$$r_e(E_e, KER) = 5.5au\sqrt{\frac{2E_e \cdot m_H}{m_e \cdot KER}} \quad (4.23)$$

With this classical value for r_e , we can estimate the classical asymmetry parameter β as[8]:

$$\beta = \frac{1}{\pi(1 + b \cdot r_e(E_e, KER))} \quad (4.24)$$

where b is a fit parameter found by least squares fitting[37].

4.7 Lab-frame photoelectron angular distribution

When examining the molecular frame, a full 4π solid angle is flattened into a plane to display the photoelectron distribution. This is done by finding the angle between the recoil ion and electron momentum vectors in the plane that those two vectors define.

A planar slice of the lab frame can be used to find an azimuthal photoelectron angular distribution of the events that lie on that plane. For example, consider the lab frame XZ plane (defined as the horizontal plane parallel to both the polarization and propagation of

the VUV and NIR light). In this plane, the lab frame azimuthal ϕ_{xz} angle can be found as shown below:

$$\phi_{xz} = \arctan2\left(\frac{p_x}{p_z}\right) \quad (4.25)$$

A planar azimuthal PAD can be recovered by finding the difference between the lab frame azimuthal angle of the recoil ion momentum vector (the recoil ion ϕ_{xz} in the XZ plane example) and the lab frame azimuthal angle of the electron momentum vector (the electron ion ϕ_{xz} in the XZ plane example) for all events that reside on that plane.

Gates using the azimuthal angle between the molecular axis defined by the recoil ion momentum vector and the polarization axis (again, the recoil ion ϕ_{xz} in the XZ plane example) can then be easily created. These gated planar azimuthal PADs are a convenient tool to visualize the relationships between the molecular axis, the electron momentum vector, and the polarization axis.

Since the number of events that lie exactly on any one lab frame plane will be small, it is convenient to instead include all events that are within a small angle of that plane, and to recover the distribution using the projection of their azimuthal angle onto the plane. Such a gate using an acceptance angle of $\pm 15^\circ$ is shown in Figure 4.18.

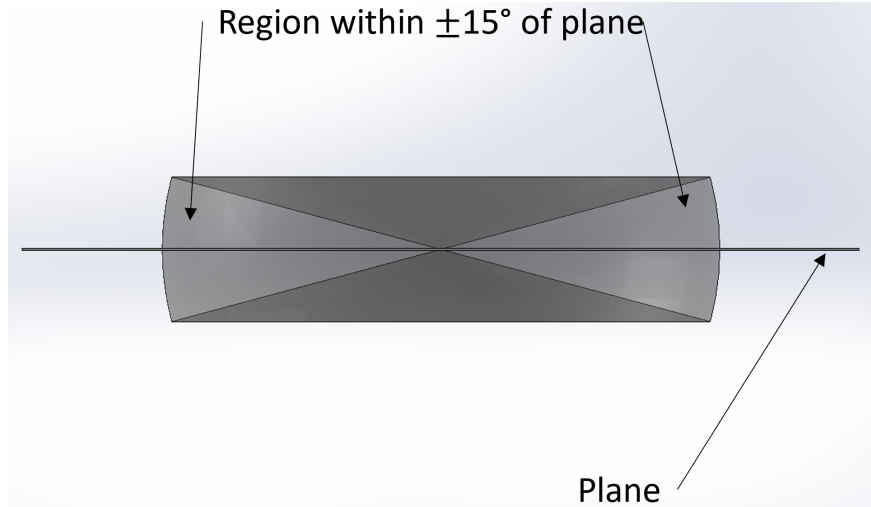


Figure 4.18: Angular slice for photoelectron azimuthal angular distribution in a lab frame plane. Events within $\pm 15^\circ$ are added to the distribution by finding their azimuthal angular projection upon the plane.

Statistics can be improved further by adding the distribution from another plane that shares an axis with the first. The YZ plane (defined by the gas jet axis and the polarization axis) distribution, for example, could be added to double the statistics of the XZ plane. Six planes that were all parallel with the Z axis would provide six times the statistics when added together to form a lab frame PAD.

To this end, the XZ plane, the YZ plane, and four other planes were defined in the lab frame. These are shown in Figure 4.19.

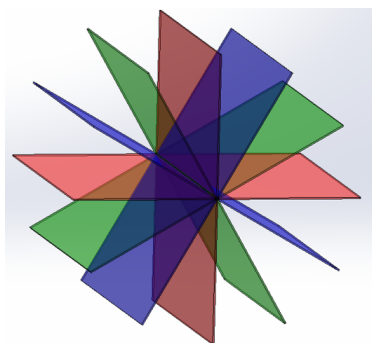


Figure 4.19: A set of planes that are all parallel to the lab frame Z axis. The red planes represent the YZ and XZ planes in the lab frame. The green planes are rotated 30° from the lab frame YZ and XZ planes. The blue planes are rotated 60° from the lab frame YZ and XZ planes.

To boost statistics further, all events within $\pm 15^\circ$ of one of the planes are projected onto it in order to form to that plane's PAD. These acceptance regions are shown in Figure 4.20.

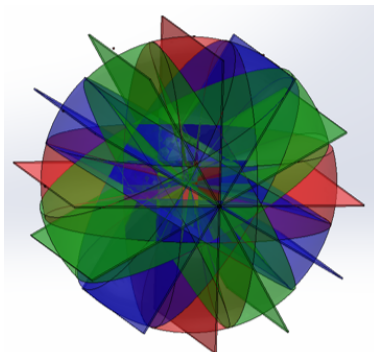


Figure 4.20: A set of acceptance regions that are all parallel to the lab frame Z axis. The red regions are within $\pm 15^\circ$ of the YZ and XZ planes in the lab frame. The green regions are within $\pm 15^\circ$ of planes that are rotated 30° from the lab frame YZ and XZ planes. The blue regions are within $\pm 15^\circ$ of planes that are rotated 60° from the lab frame YZ and XZ planes. All events inside those regions are projected onto the nearest plane to generate a planar lab frame PAD.

The planar distributions are added together to form the final lab frame azimuthal PAD.

This lab frame photoelectron azimuthal angular distribution can then be gated upon using the lab frame Z angle to select only events that dissociate with the molecular axis at a desired angle to the polarization. This allows for convenient visualization of how the photoelectron angular distribution changes as the angle with the polarization axis changes.

4.8 Detector homogeneity

A last consideration that should be accounted for in this experiment is the homogeneity of the MCP detector. An ideal, factory-new microchannel plate should have spatially uniform quantum efficiency. However, over time and use, regions of the MCP can be burned and start to suffer from reduced detector efficiency. The AMOS chamber at LBNL that this experiment was conducted with has such a region on the recoil ion detector. This region, visible in the hit position plot, affects the more tightly distributed trajectories of events where the recoil

ion's initial momentum is headed towards the recoil detector (events with positive recoil P_z). This notch area of reduced efficiency can be seen in the VUV-only channel in Figure 4.21.

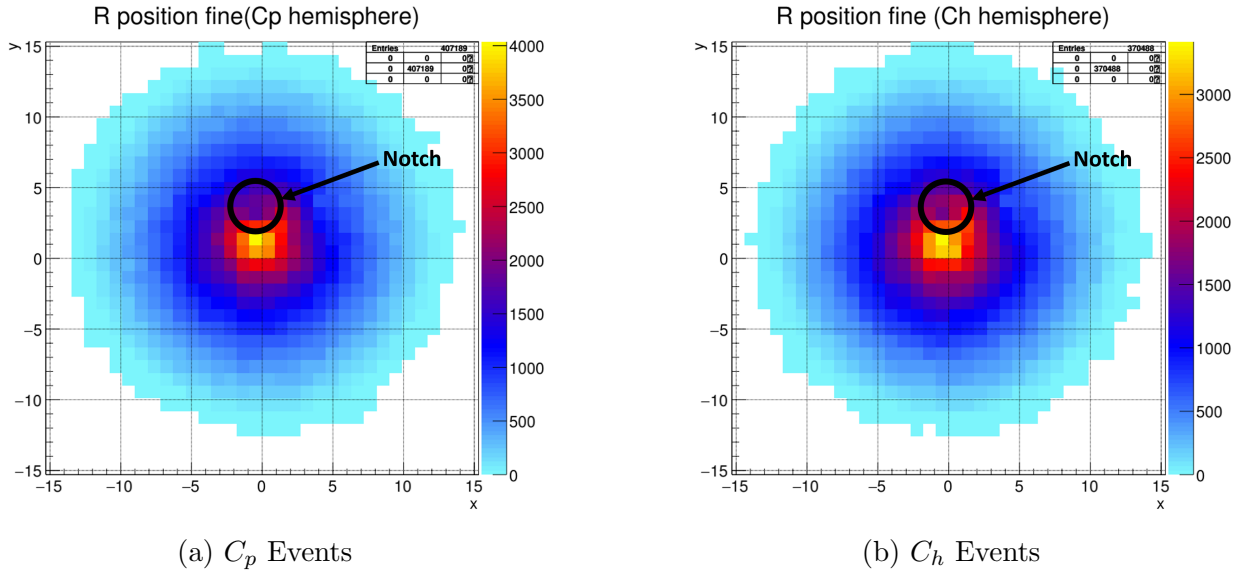


Figure 4.21: Hit positions of C_h and C_p events with positive recoil ion Z momentum.

The events where the recoil ion's initial momentum is headed away from the recoil ion detector (events with negative recoil P_z) have a more spread-out spatial distribution of trajectories, and the notch region of reduced efficiency is not prominent, as seen in the VUV-only channel in Figure 4.22.

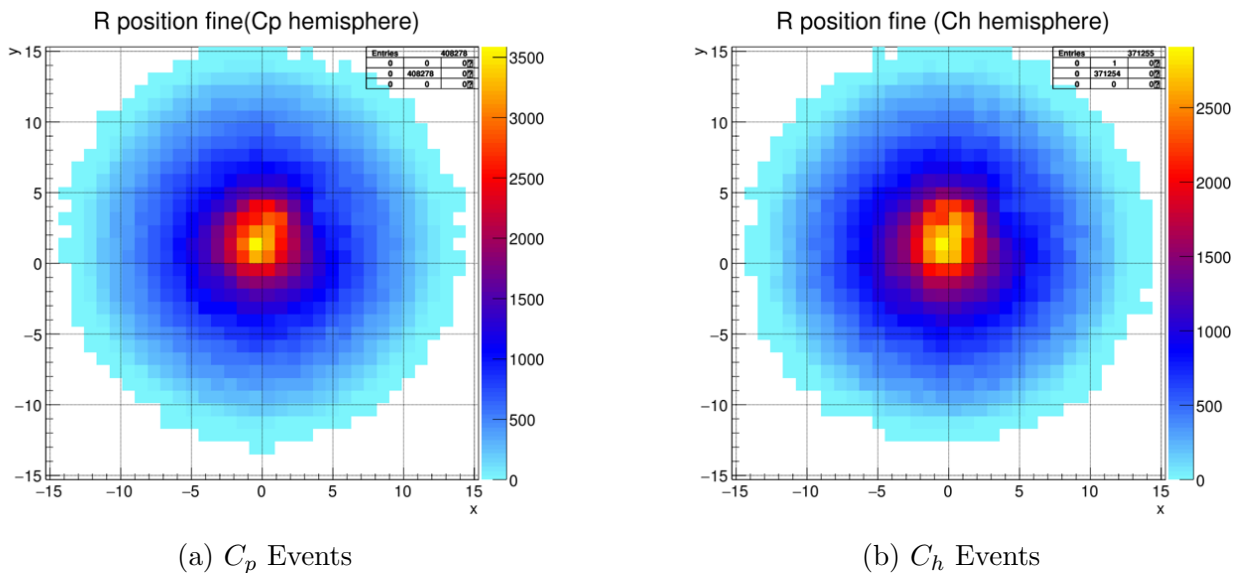


Figure 4.22: Hit positions of C_h and C_p events with negative recoil ion Z momentum.

This region presents a dilemma: Is it better to only use the negative recoil P_z events where the more spread-out spatial trajectory distribution dilutes the effect of the reduced detector efficiency, or is it better to use all the events possible for better statistics?

In light of the relatively paltry event counts that are inherent for key parts of this experiment, especially for the statistically rare two-color dissociation events, the judgement has been made that using all the events available is the best way to proceed.

Chapter 5

Experimental results

5.1 Data overview

This experiment was carried out during the Summer 2017 two-bunch beamtime at the ALS. A number of datasets were recorded during this beamtime. For some datasets, the laser synchrolock system was not functioning, and several were looking at different molecular systems to examine different reactions. The usable and relevant two-color data for this experiment is separated into six different datasets, which are divided by varying three different parameters.

First, two different isotopes of hydrogen were used: standard hydrogen (H_2) and heavier deuterium (D_2). The heavier deuterium fragments have longer times of flight than their hydrogen equivalent. Experiments using D_2 can therefore be somewhat cleaner as it is easier to separate them from background contamination. A major downside of deuterium, unfortunately, is the much higher cost of using it for experiments, especially for experiments that involve using as much gas as was needed for this experiment. Five H_2 datasets and a single D_2 dataset were recorded.

Second, the VUV radiation from the ALS beamline could be precisely controlled. Data was recorded at 3 different VUV energies, 17.9 eV, 18.34 eV, and 18.54 eV. All three energies allow the H_2^+ and D_2^+ single photoionization channel to take place, and since all datasets also feature NIR laser irradiation, the two-color dissociation channel should also be present. Since the dissociation threshold is 18.075 eV for H_2 and 18.158 eV for D_2 , any VUV energy greater than the threshold will also allow dissociation via the one-color channel to take place. The 17.9 eV channel will not feature this channel, as the VUV photons do not have enough energy to allow for it to take place.

Finally, the time delay between the VUV and NIR pulses can be controlled. The VUV pulses from the ALS are 80ps in length, and the NIR laser pulses are 12ps in length. As explained in Chapter 1, a delay of even a single picosecond gives the photoelectron ample time to leave the proximity of the remaining H_2^+ molecular ion. The photoionization of the neutral molecule can take place at any point during the 80 picosecond VUV pulse. NIR induced dissociation can take place at any point during the during the 12 picosecond NIR pulse. In order for NIR induced dissociation to occur while the photoelectron is still in the molecular ion's vicinity, which is necessary for electron retroaction effect to have a possibility of taking place, the VUV and NIR pulses must overlap. Therefore, the VUV-NIR time delays can be categorized into two general categories: overlapping short time delay, and non-overlapping long time delay. The dataset with the longest overlapping time delay is 33 ps, and the dataset with the shortest non-overlapping time delay is 160 ps, as seen in Figure 5.1.

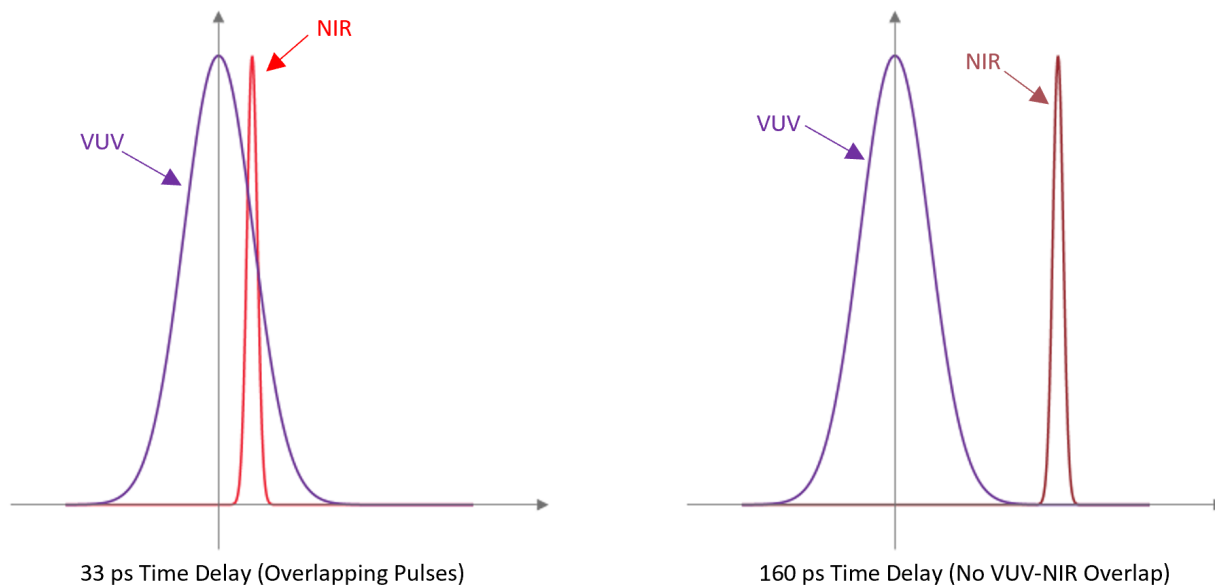


Figure 5.1: Overlapping and non-overlapping VUV and NIR pulses.

Using these parameters, the datasets that were recorded consist of a short-delay 18.54 eV D_2 dataset, a long delay 18.34 eV H_2 dataset, long and short 18.54 eV H_2 datasets, and long and short 17.9 eV H_2 datasets. All six datasets are shown in Figure 5.2.

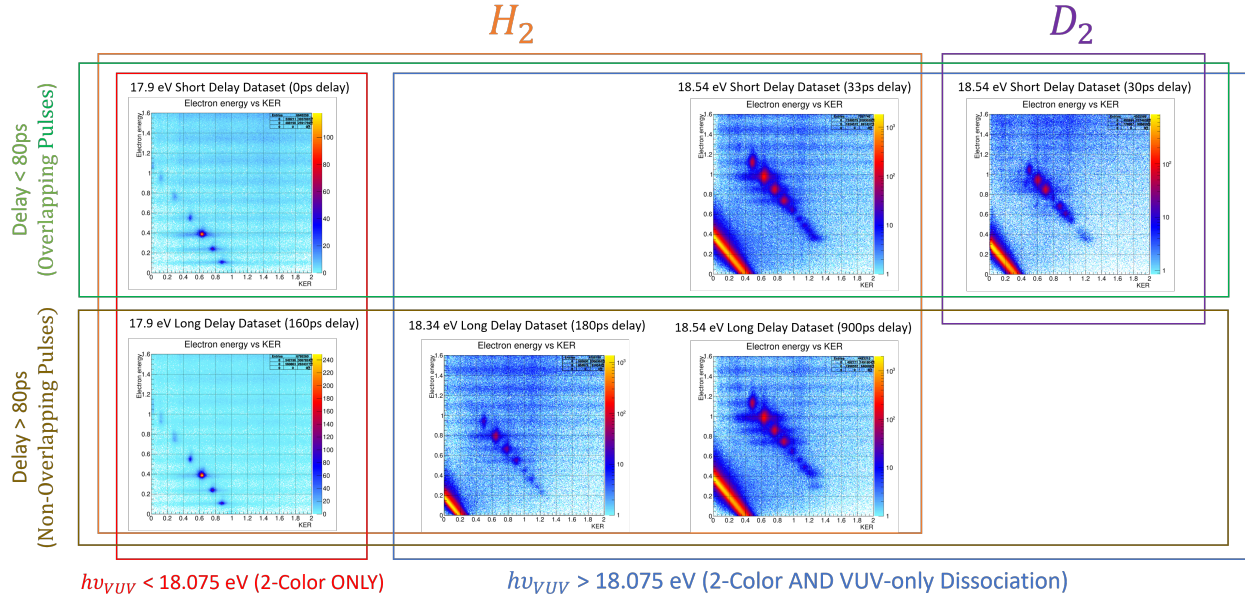


Figure 5.2: Two-color datasets taken during the 2017 two bunch beamtime at the ALS.

The spectrometer settings used to analyze each of these datasets, including time offset, acceleration region electric field, booster region electric field, magnetic field, and gas jet velocity are shown below in Table 5.1.

Datasets	18.54 eV D_2	18.54 eV H_2	18.34 eV H_2	17.9 eV H_2
Time offset (ns)	-2.476	-2.476	-2.476	-2.476
Acceleration Region E field (V/cm)	2.795	2.61	1.97	2.06
Booster Region E field (V/cm)	247	260	230	252
B field (Gauss)	2.128	2.128	2.128	1.900
Gas jet velocity (m/s)	875	1165	1400	1400

Table 5.1: COLTRIMS spectrometer settings for the two-color experiment.

5.2 One-color channel

The one-color channel is present in every dataset except for the H_2 data taken at 17.9 eV. The net reaction is shown below:



This channel can be isolated using the electron energy vs KER map using the following energy sum relation:

$$E_{sum} = KER + E_e = h\nu_{VUV} - E_{diss} \quad (5.2)$$

The electron energy vs KER relation for this reaction is a diagonal line with a slope of negative 1, that has intercepts at electron energy equal to $h\nu_{VUV} - E_{diss}$ and KER equal to $h\nu_{VUV} - E_{diss}$. This diagonal line in the electron energy vs KER plot can be used to isolate the one-color dissociative channel for analysis, as shown in Figure 5.3.

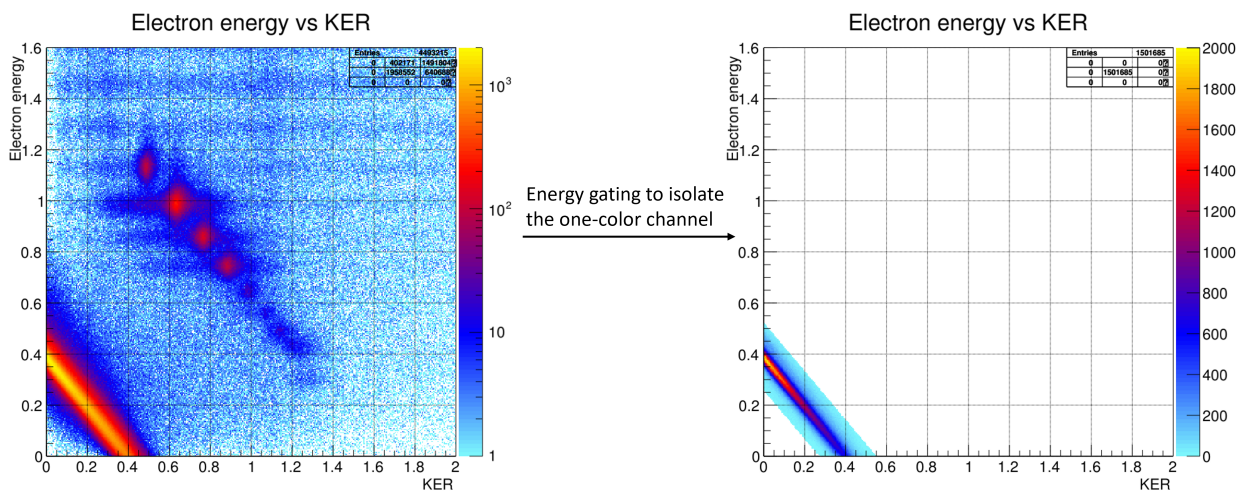


Figure 5.3: Isolation of the one-color dissociative channel in 18.54 eV H_2^+ .

As noted previously, the one-color channel has been examined prior to this experiment, by groups at both Frankfurt[7] and Berkeley[8]. However, there are still some novel observations that can be made about it.

5.2.1 Angular dependence on polarization for dissociation via the one-color channel

The previous works focused on the energy dependence of the electron retroaction effect, and did not examine the relationship between the molecular axis.

These works showed that the MFPAD has asymmetry due to preferential proton emission in the direction of the photoelectron. As the electron energy increases, the asymmetry decreases. Figure 5.4, taken from the Heck paper[8], shows these trends clearly, using bin count asymmetry parameters with a 45° acceptance angle (discussed in Section 4.4), and lines from the classical retroaction model (discussed in Section 4.6).

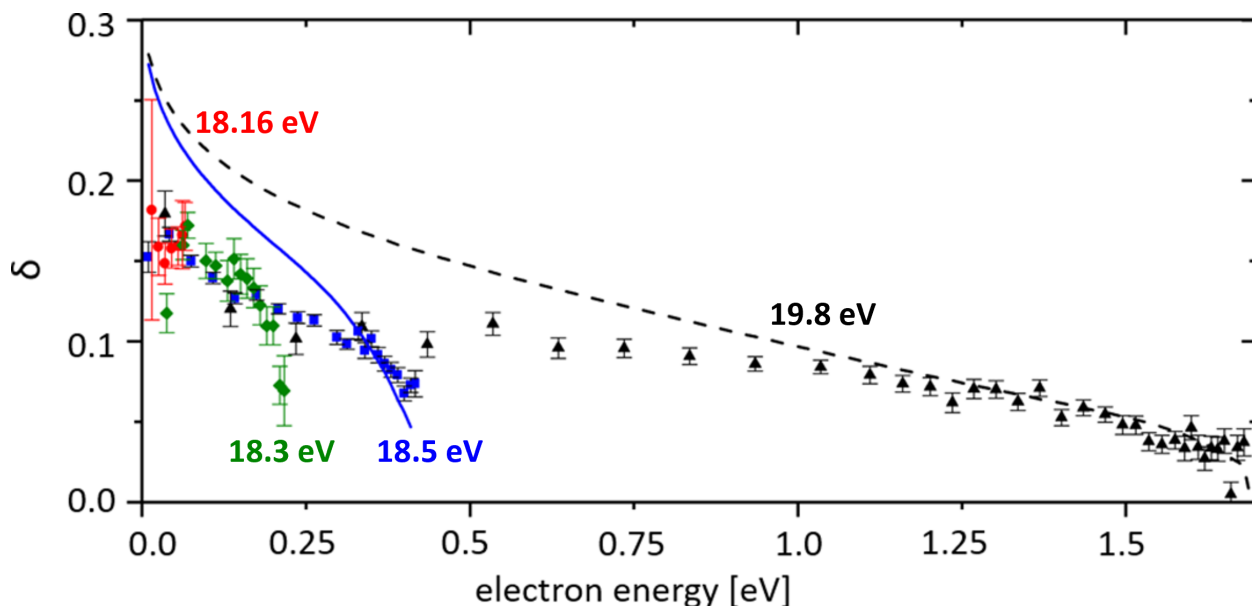
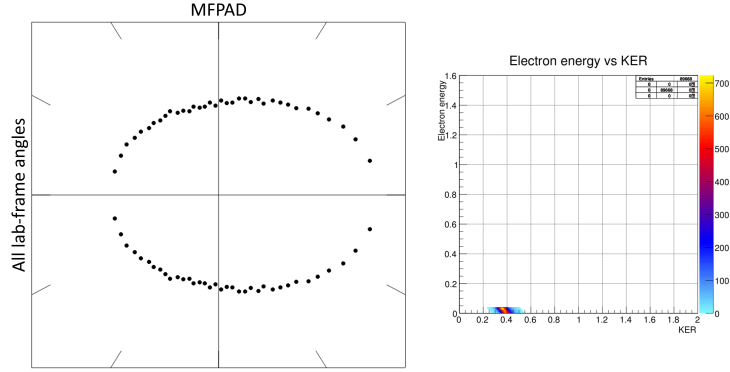
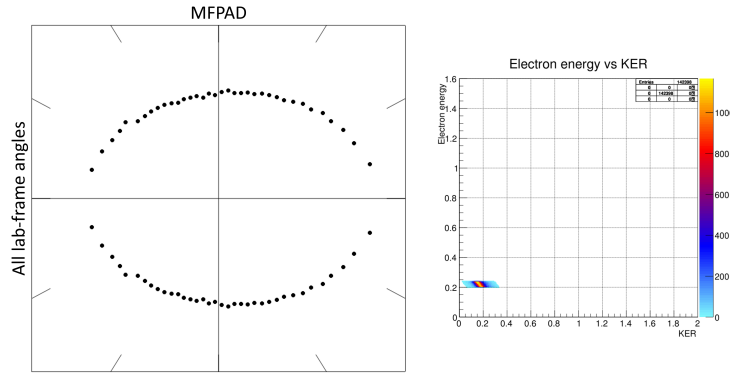


Figure 5.4: 45° Asymmetry parameter δ vs electron energy for the dissociation of H_2^+ via the one-color channel in a VUV-only experiment. Data points represent δ parameter values, and lines represent classical β parameter fits. VUV energies of 18.16 eV, 18.3 eV, 18.5 eV, and 19.8 eV are indicated in red, green, blue, and black respectively. Taken from [8].

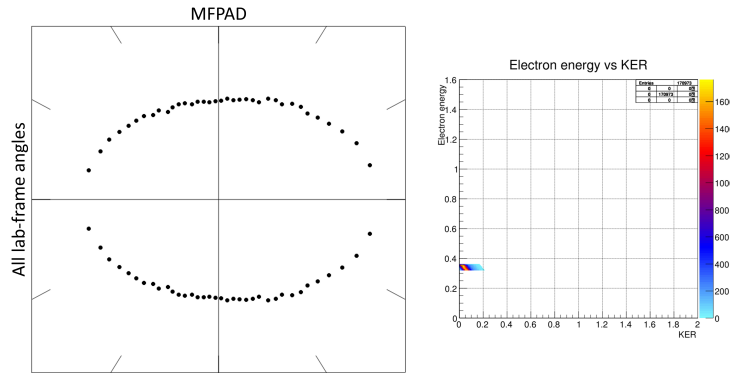
In this experiment, ignoring the relationship between polarization and molecular axis and gating along the one-color channel's signature diagonal line to subdivide the MFPAD into electron energy slices allows the electron energy dependence to be examined. The result is consistent with the results from Waitz[7] and Heck[8]. The MFPAD has an elliptical shape, and follows the same electron energy trends as before. These trends are shown in Figure 5.5.



(a) Events with electron energy between .00 eV and .04 eV, $\delta = 0.091 \pm 0.003$.



(b) Events with electron energy between .20 eV and .24 eV, $\delta = 0.048 \pm 0.003$.



(c) Events with electron energy between .32 eV and .36 eV, $\delta = 0.042 \pm 0.002$.

Figure 5.5: MFPAD energy dependence for events that dissociate via the one-color channel in 18.54 eV H_2^+ (short delay dataset) without any gating dependent on the angle between the molecular axis and the polarization axis.

This result assumes that there is no dependence on the angle between the molecular axis and the polarization axis of the ionizing VUV synchrotron radiation. However, in this experiment that assumption was not made. An angular dependence in the two-color channel might indicate the presence of a LICl. This fact led to an emphasis on examination of these angular relationships.

Section 4.7 describes in detail a scheme that can be used to generate lab-frame photoelectron angular distributions. The one-color channel data was used to generate a series of lab-frame PADs that scan through the angle between the molecular axis and the VUV polarization axis for events with low photoelectron energy, which are shown in Figure 5.6.

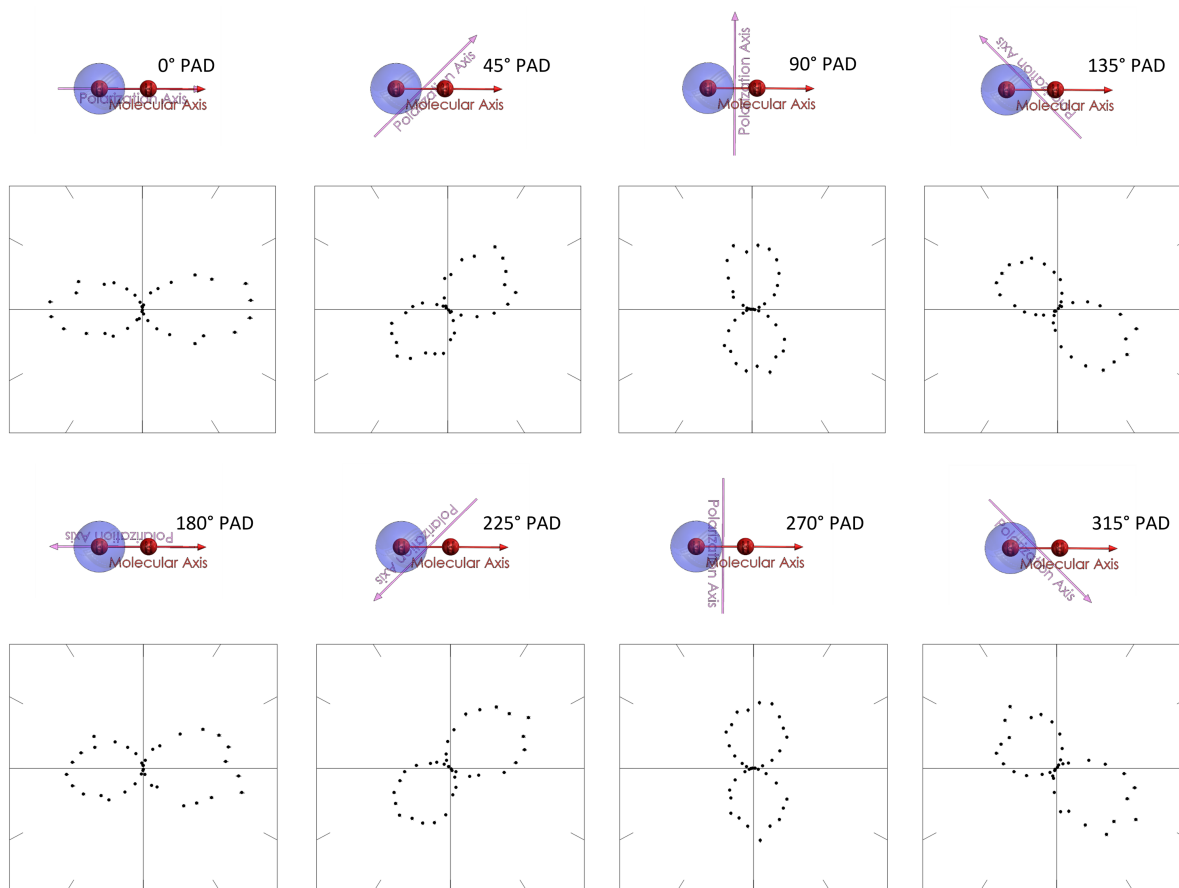


Figure 5.6: H_2^+ Lab-frame photoelectron angular distributions of events that dissociate via the one-color channel at a VUV energy of 18.54 eV and electron energy between .00 eV and .10 eV.

The lab frame PAD is a rotating P-shape that stays aligned with the polarization axis of the VUV radiation. The P shape is also asymmetric, with an asymmetry that is dependent on the angle between the molecular axis and polarization axis and indicates that proton and electron emission preferentially occurs in the same direction, consistent with the electron retroaction effect. This asymmetry decreases with increasing photoelectron energy, as seen in Figure 5.7.

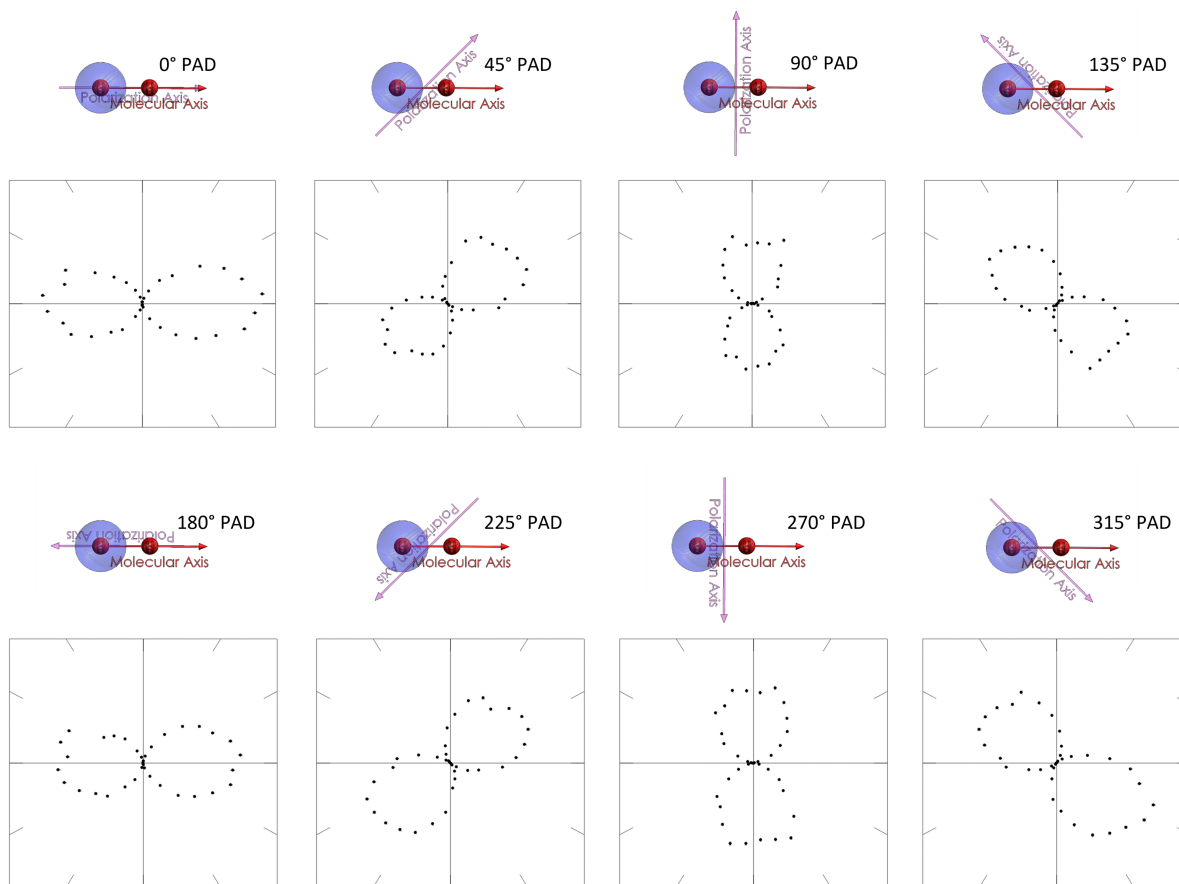


Figure 5.7: H_2^+ lab-frame photoelectron angular distributions of events that dissociate via the one-color channel at a VUV energy of 18.54 eV and electron energy between .30 eV and .40 eV.

The angular dependence that these lab-frame PADs reveal is buried in the all-angle MFPADs that were described previously. If these asymmetric P-shapes are all summed together, the asymmetric elliptical MFPAD seen in Figure 5.5 and reported on by Waitz[7] and Heck[8] is recovered.

5.2.2 Parallel and perpendicular one-color channel dissociation MFPADs at different electron energies

Returning to the molecular frame, azimuthal information about the photoelectron angular distribution is lost, and the structure of PADs that lack symmetry about the polarization axis is obscured. However, since events that dissociate parallel or perpendicular to the polarization axis do have this symmetry, they can be examined and their asymmetry about the molecular axis can be quantified in the molecular frame. The polar angle between the molecular axis and the polarization axis, recoil θ_z , can be plotted vs the MFPAD to see the angular dependence reflected in the structure of the MFPAD. This plot is shown in Figure 5.8.

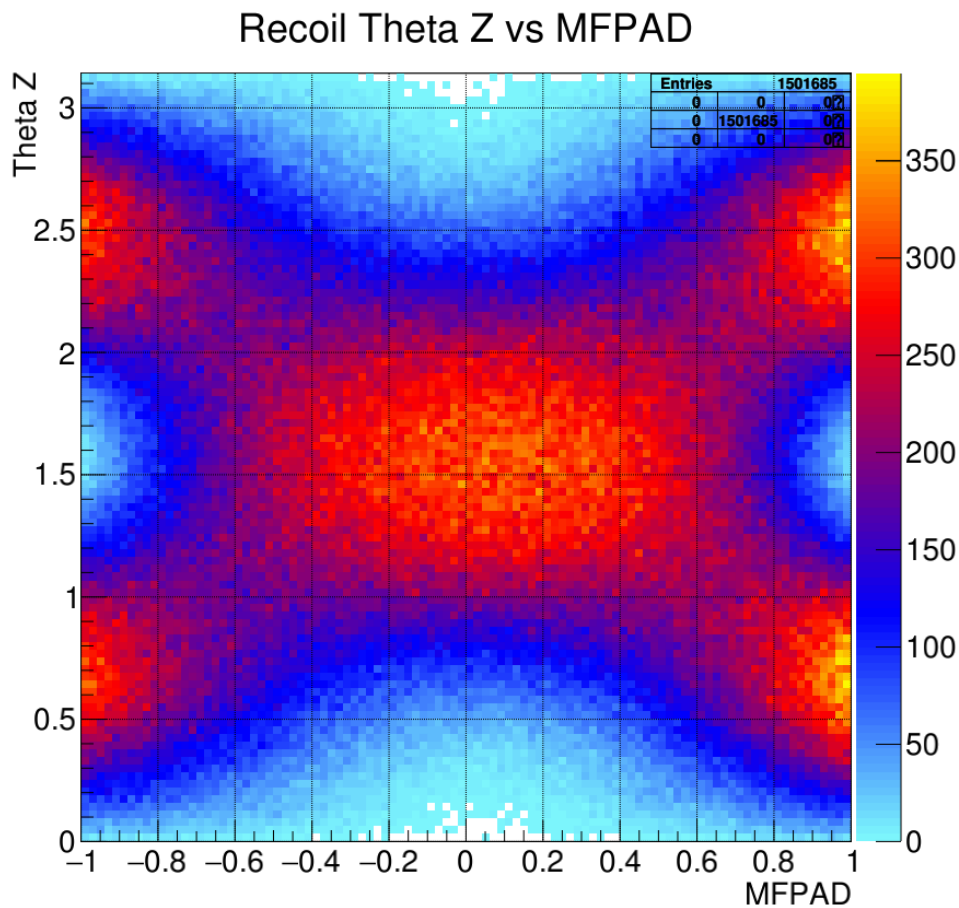
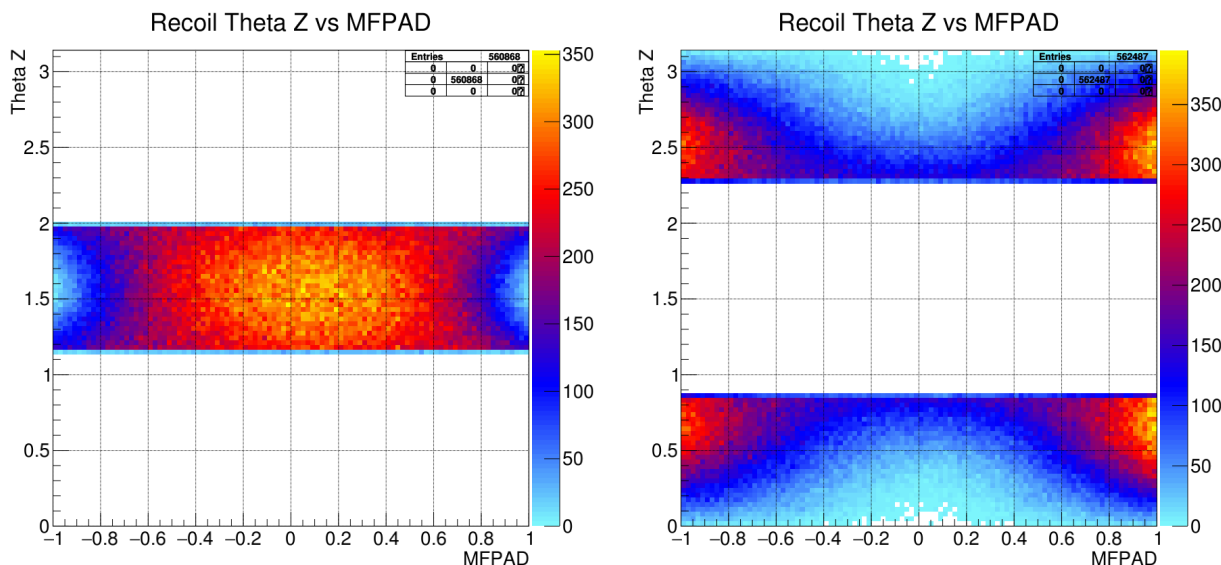


Figure 5.8: Recoil ion θ_z vs one-color dissociation MFPAD plot for 18.54 eV H_2^+ (long delay dataset).

Events where the molecular axis is parallel to the polarization axis are at the top and bottom of this plot, and events where the molecular axis is perpendicular to the polarization axis form an island in the center. This structure allows a gate to be easily constructed on the recoil ion lab frame θ_z angle to segregate the parallel and perpendicular dissociative events. Events with $\cos(\theta_z)$ values greater than 0.65 or less than -0.65 are classified as parallel dissociation, and events with $\cos(\theta_z)$ values between -0.4 and 0.4 are classified as perpendicular dissociation. This is shown in Figure 5.9

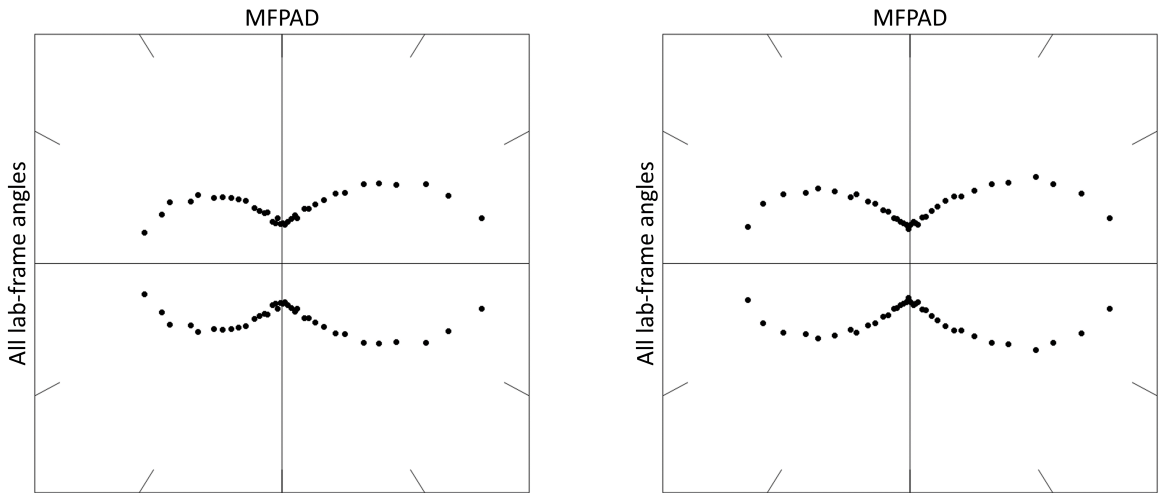


(a) Events that dissociate perpendicular to the polarization axis.

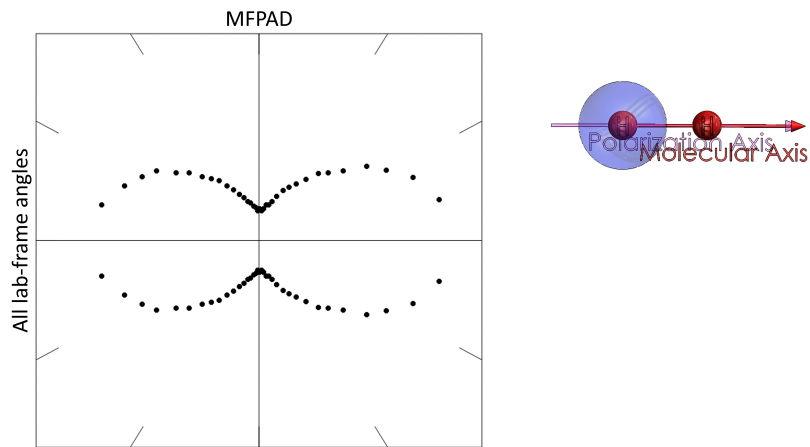
(b) Events that dissociate parallel to the polarization axis.

Figure 5.9: Parallel and perpendicular dissociation via the one-color channel gating shown using recoil θ_z vs MFPAD plot for 18.54 eV H_2^+ (long delay dataset).

The MFPAD for the events in this parallel dissociation gate (shown in Figure 5.9b) is the expected P-shape parallel to the molecular axis. The molecular axis asymmetry in the parallel dissociative events is inversely proportional to the photoelectron energy, and essentially dies off and goes towards zero at high photoelectron energy. This is shown in Figure 5.10.



(a) Events with electron energy between .00 eV and .04 eV, $\delta = 0.069 \pm 0.005$. (b) Events with electron energy between .20 eV and .24 eV, $\delta = 0.041 \pm 0.004$.



(c) Events with electron energy between .32 eV and .36 eV, $\delta = 0.017 \pm 0.004$.

Figure 5.10: Parallel one-color dissociation MFPAD energy dependence in 18.54 eV H_2^+ (short delay dataset).

Quantifying the asymmetry using the bin count asymmetry parameter described in Section 4.4, this trend is consistent throughout all four of the datasets where the one-color dissociative channel is energetically available. Parallel dissociation in the one-color channel trends to zero as photoelectron energy increases. The D_2 asymmetry has the same shape, but is lower than the H_2 , as would be expected given the higher nuclear mass. The classical

retroaction fit parameter β described in Section 4.6 also captures the general trend similar to Figure 5.4. This is shown in Figure 5.11.

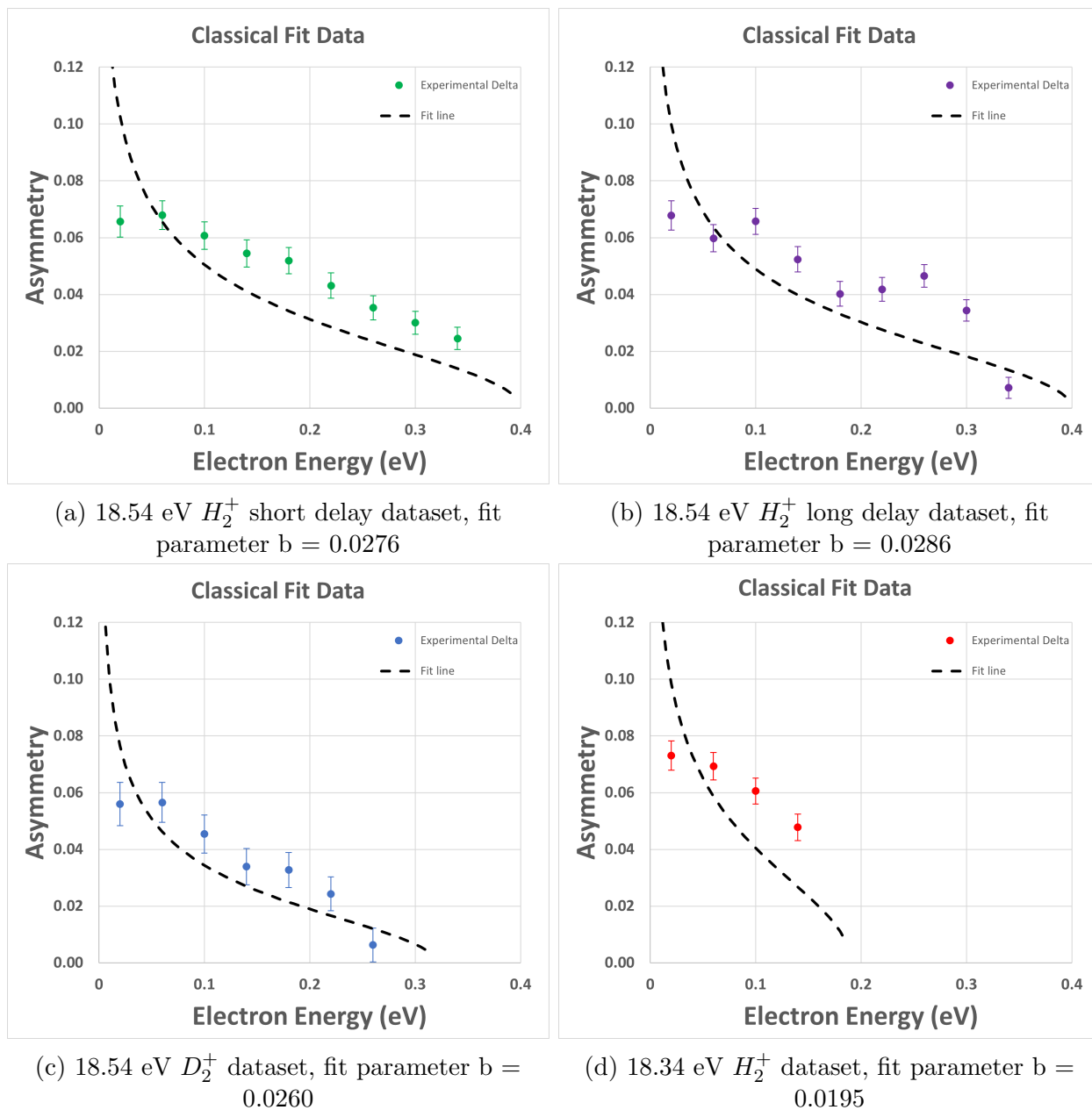


Figure 5.11: δ asymmetry parameters and β fit lines for events dissociating via the one-color channel while the molecular axis and polarization axis are parallel.

The asymmetry δ parameters for the H_2 and D_2 datasets where the one-color channel is accessible are shown below in Figure 5.12.

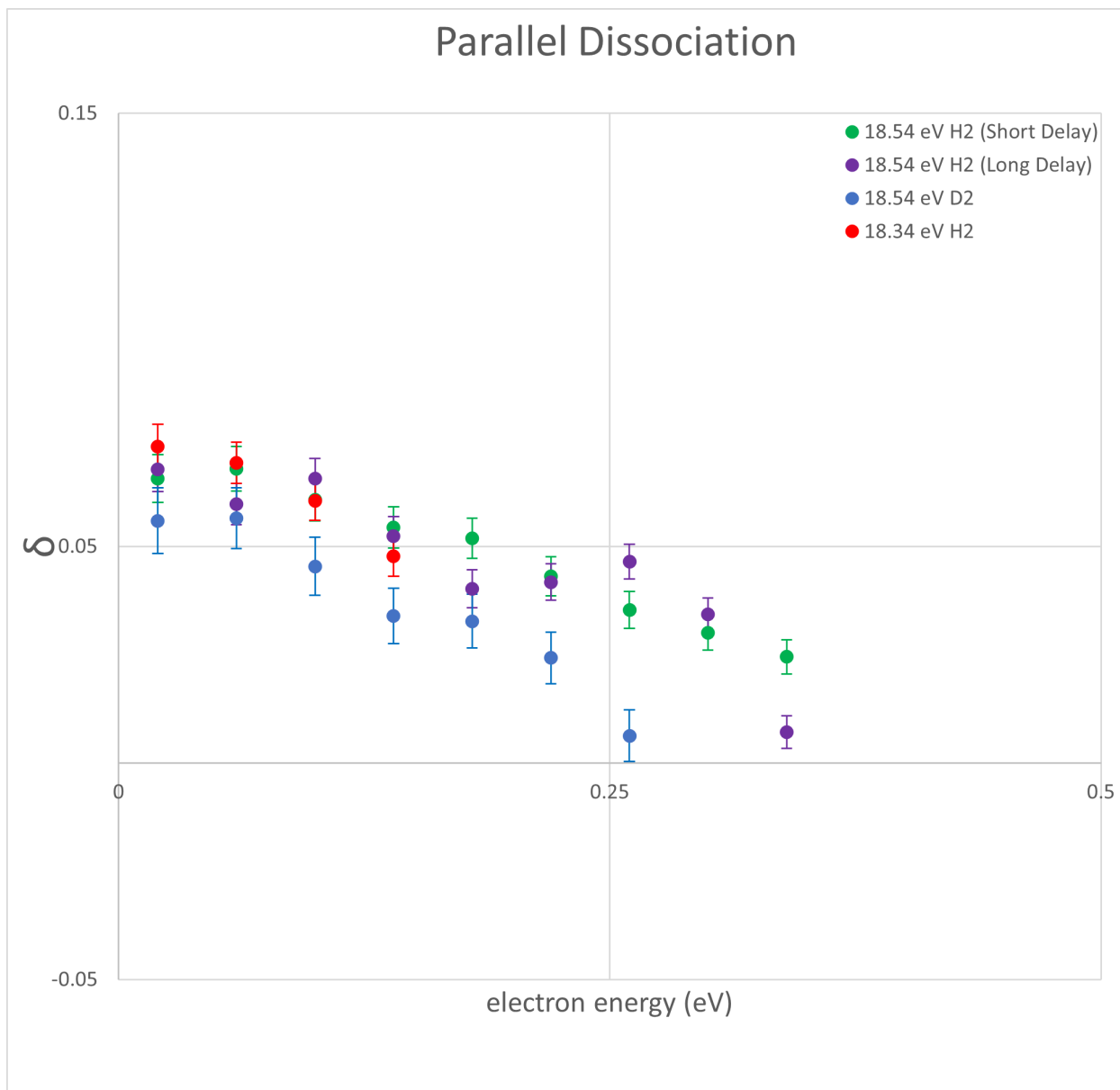


Figure 5.12: Asymmetry parameter δ (defined in section 4.4) vs electron energy for events dissociating via the one-color channel while the molecular axis and polarization axis are parallel.

The asymmetry can also be quantified using Legendre polynomial fits, as described in Section 4.5. For the one-color channel, the MFPAD approximation can be truncated to the second Legendre polynomial to account for the absorption of a single photon, as shown below:

$$MFPAD(\cos(\theta)) = \frac{\sigma}{4\pi} (1 + \beta_2 P_2(\cos(\theta))) \quad (5.3)$$

Using the $\delta\sigma$ asymmetry parameter recovered from Legendre polynomial fits yields essentially the same values as the δ parameter using the bin counts. These are shown below in Figure 5.13.

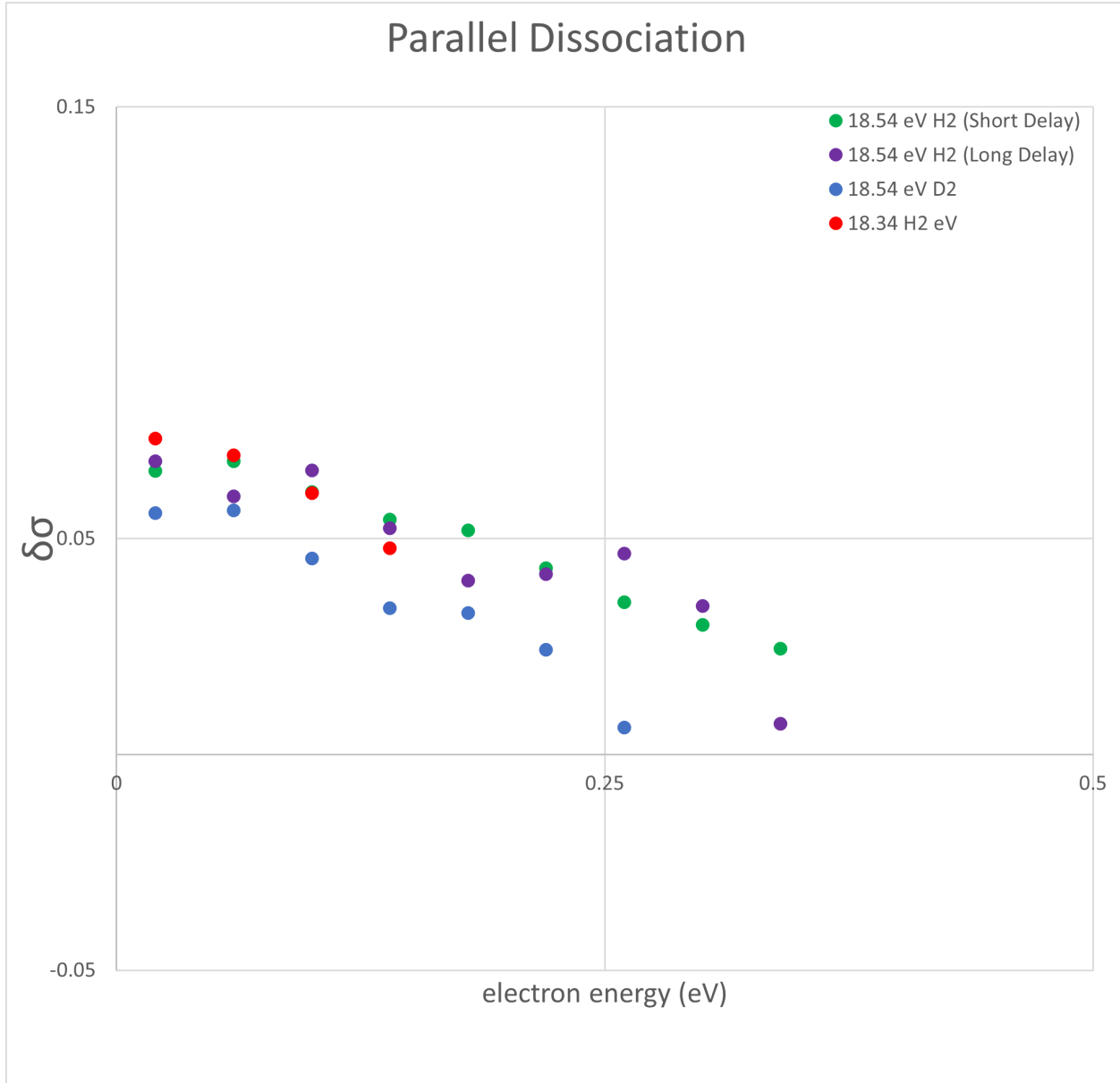
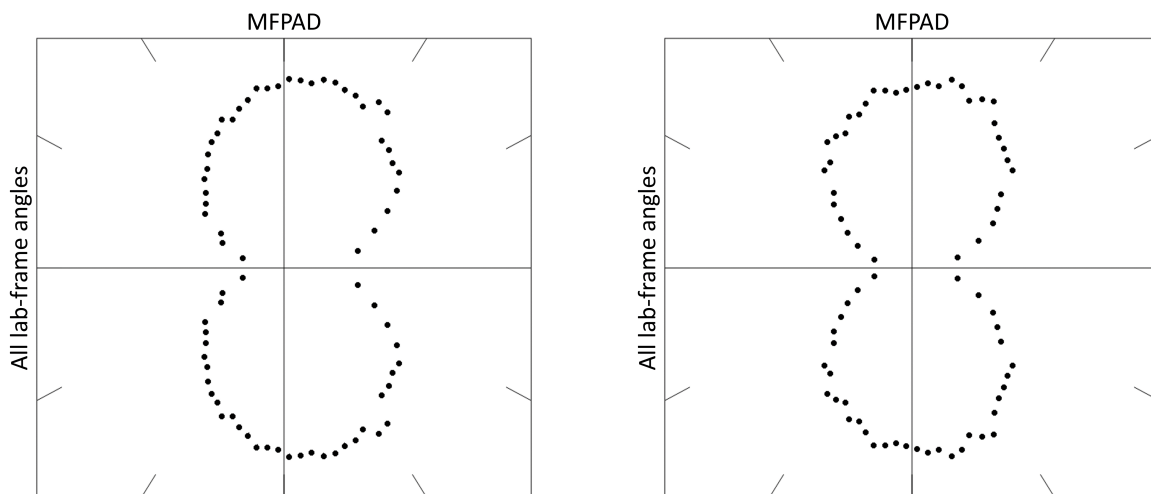
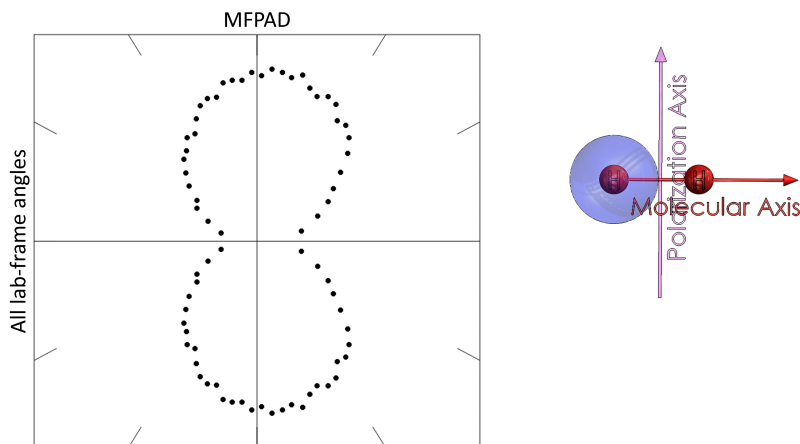


Figure 5.13: Legendre polynomial fit asymmetry parameter $\delta\sigma$ (defined in Section 4.4) vs electron energy for events dissociating via the one-color channel while the molecular axis and polarization axis are parallel.

The MFPAD for the events in the perpendicular dissociation gate (shown in Figure 5.9a) is the expected P-shape aligned perpendicular to the molecular axis. The molecular axis asymmetry in the perpendicular dissociative events has a dependence on the photoelectron energy that is very different from the parallel dissociation. The asymmetry decreases from the low photoelectron energy maximum, then increases again as the photoelectron energy increases. This behavior is shown in Figure 5.14.



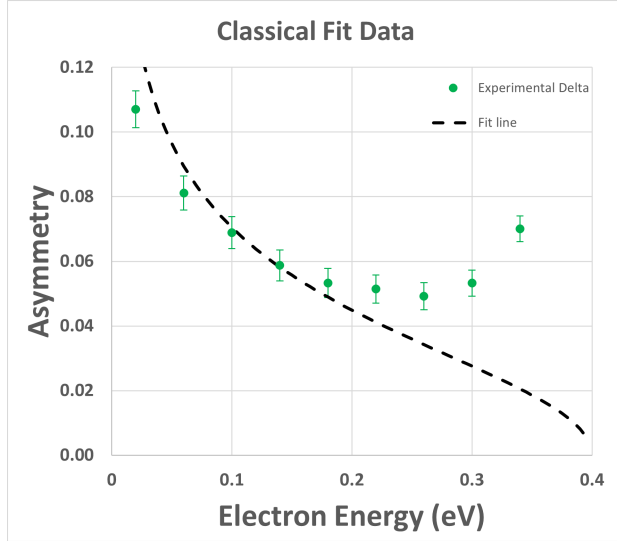
(a) Events with electron energy between .00 eV and .04 eV, $\delta = 0.107 \pm 0.006$. (b) Events with electron energy between .20 eV and .24 eV, $\delta = 0.051 \pm 0.004$.



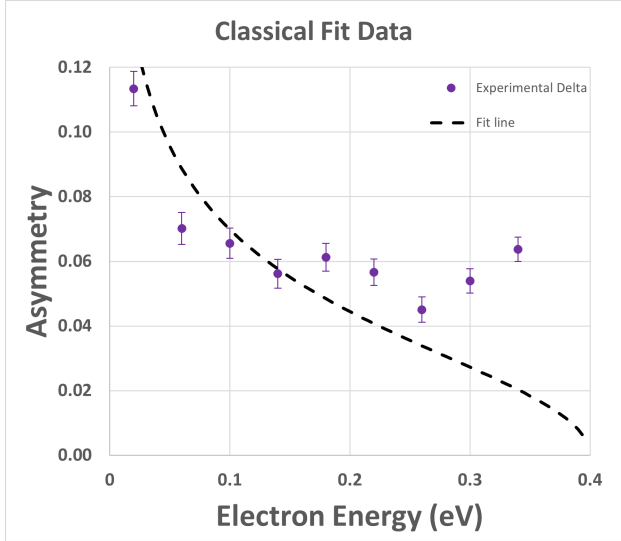
(c) Events with electron energy between .32 eV and .36 eV, $\delta = 0.068 \pm 0.005$.

Figure 5.14: Perpendicular one-color dissociation MFPAD energy dependence in 18.54 eV H_2^+ (short delay dataset).

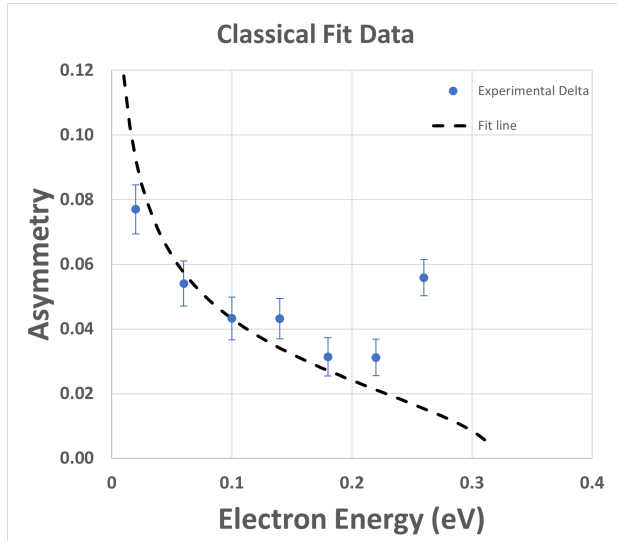
The perpendicular dissociation asymmetry can again be quantified using the bin count asymmetry parameter described in Section 4.4, and again, the observed trends are consistent throughout all four of the datasets where the one-color dissociative channel is energetically available. Perpendicular dissociation in the one-color channel all decreases to a minimum then begins to increase again. The D_2 asymmetry gain has the same shape, but is lower than the H_2 , as would be expected given the higher nuclear mass. The classical retroaction fit parameter β described in Section 4.6 diverges as energy increases and outright fails to account for the increase in asymmetry at high energy. This is shown in Figure 5.15.



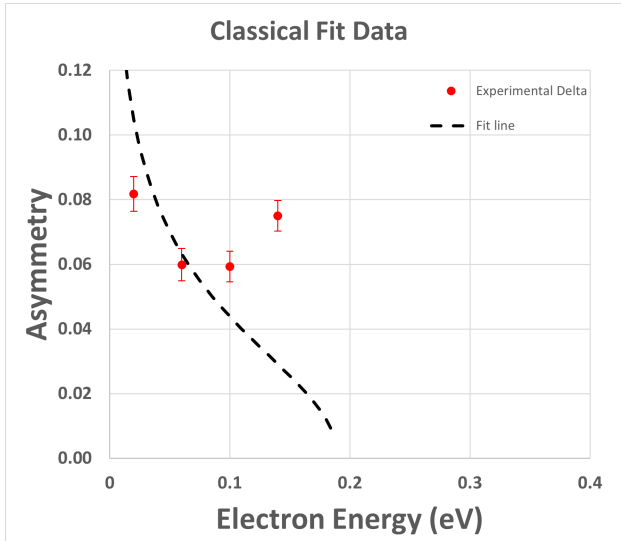
(a) 18.54 eV H_2^+ short delay dataset, fit parameter $b = 0.0183$



(b) 18.54 eV H_2^+ long delay dataset, fit parameter $b = 0.0185$



(c) 18.54 eV D_2^+ dataset, fit parameter $b = 0.0201$



(d) 18.34 eV H_2^+ dataset, fit parameter $b = 0.0178$

Figure 5.15: δ asymmetry parameters and β fit lines for events dissociating via the one-color channel while the molecular axis and polarization axis are perpendicular.

The asymmetry δ parameters for the H_2 and D_2 datasets where the one-color channel is accessible are shown below in Figure 5.16.

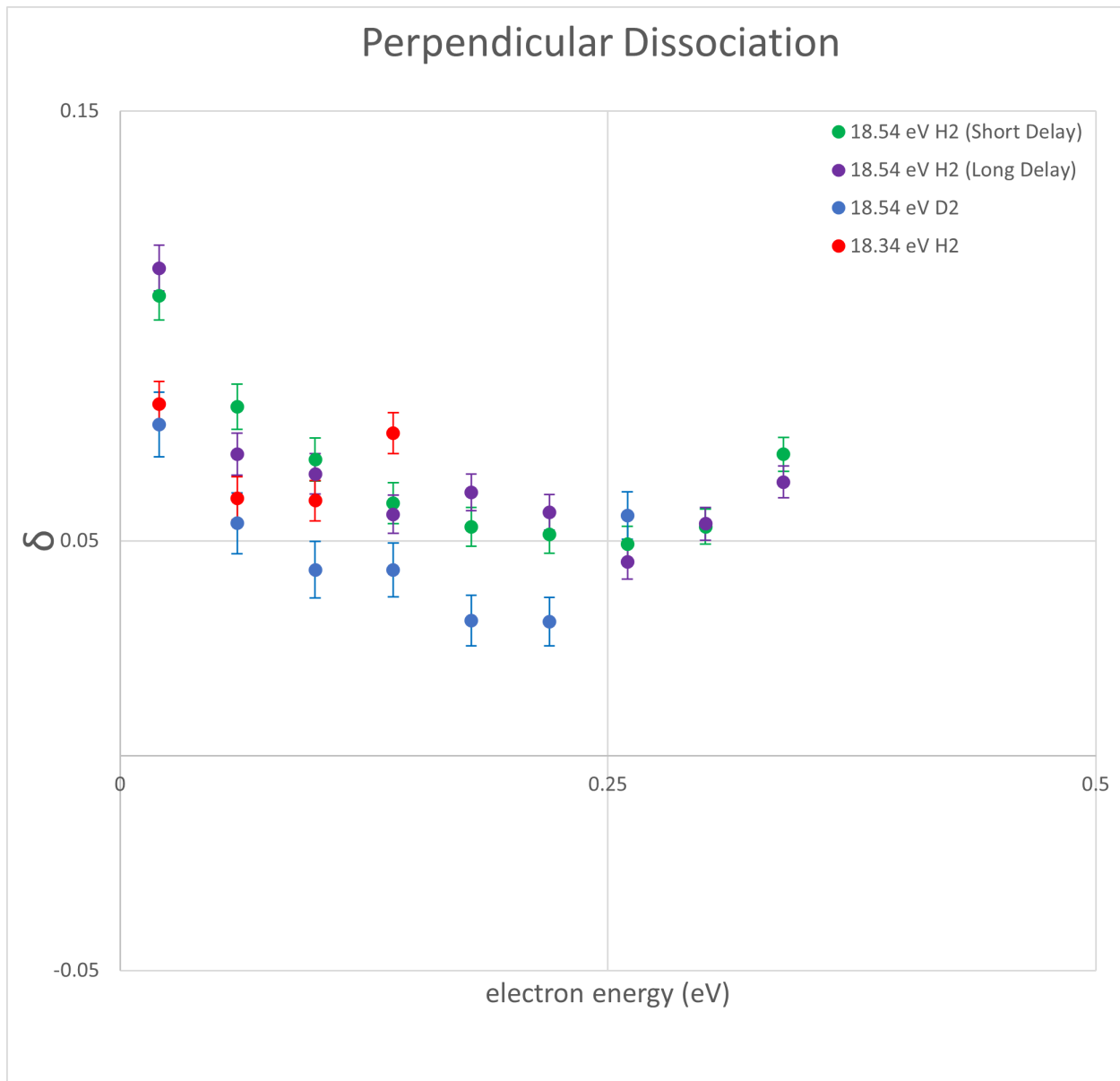


Figure 5.16: Asymmetry parameter δ vs electron energy for events with perpendicular dissociation via the one-color channel.

Again, the $\delta\sigma$ asymmetry parameter recovered from Legendre polynomial fits yields essentially the same values as the δ parameter using the bin counts. This is shown below in Figure 5.17.

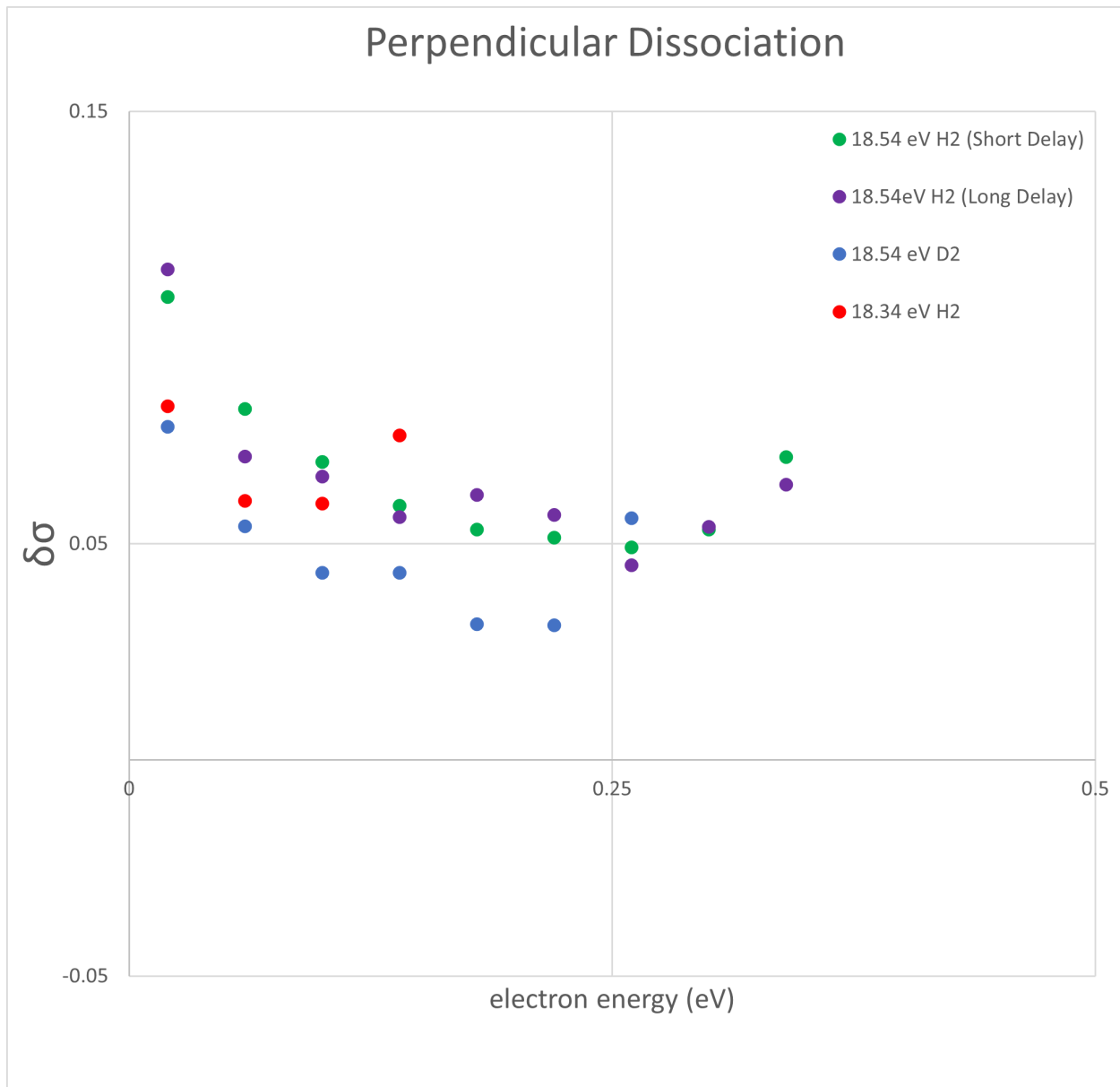


Figure 5.17: Legendre polynomial fit asymmetry parameter $\delta\sigma$ vs electron energy for events with perpendicular dissociation via the one-color channel.

The failure of the β fit parameter is indicative that something more complex than just a Coulomb $1/r$ dependent effect is involved in perpendicular dissociation.

5.2.3 Energy-dependent perpendicular side lobes

A final result of interest extracted from the one-color channel can be found by taking an extremely narrow angular slice of the perpendicular one-color dissociation data. This slice

restricts the analysis to events with a molecular axis that is at an angle of between 89° and 91° to the polarization vector, as shown in Figure 5.18.

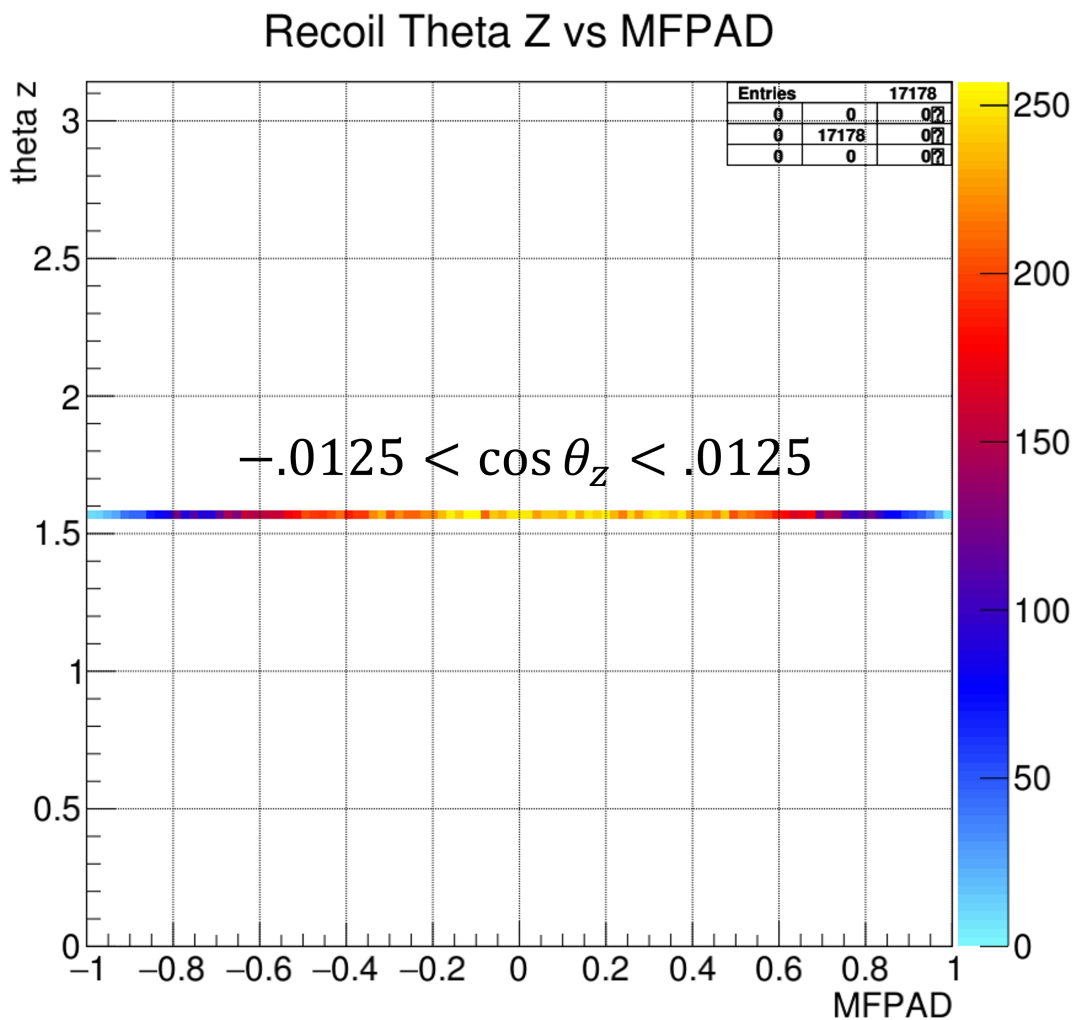


Figure 5.18: MFPAD vs recoil ion θ_z plot showing narrow acceptance window to select events with a molecular axis that is at an angle of between 89° and 91° to the polarization vector that dissociate via the one-color channel (18.54 eV H_2^+ short delay dataset).

When the MFPADs recovered from this narrow angular slice are scanned through in photoelectron energy, the expected P-shape varies in unexpected ways, beyond the simple molecular axis asymmetry. At some photoelectron energies, small side lobes in the P-shape can be observed. These side lobe features are subtle, and seem to be very sensitive to the photoelectron energy. A series of these narrow angular slice perpendicular dissociation MFPADs recovered at different photoelectron energies can be seen in Figure 5.19.

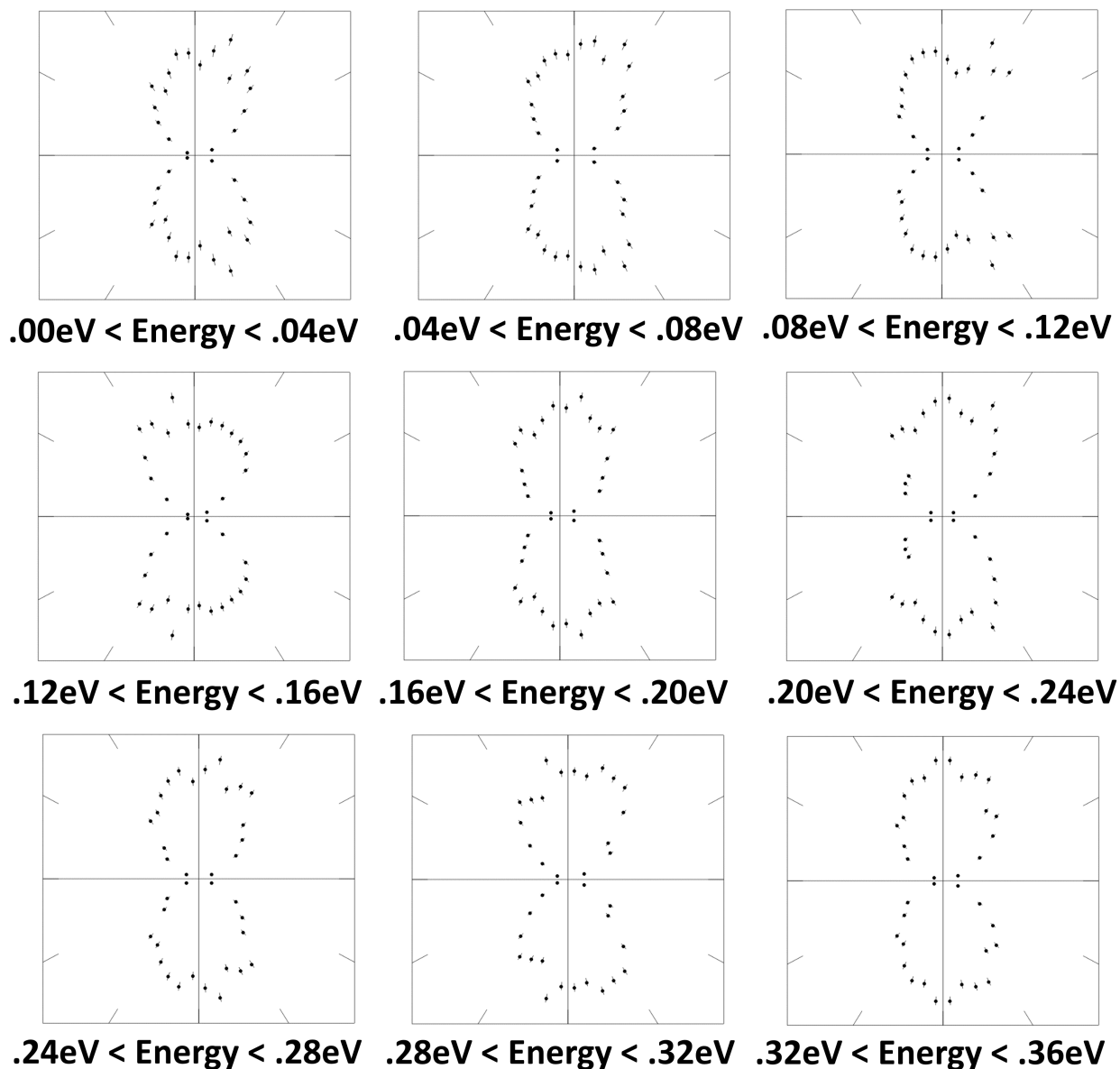


Figure 5.19: Perpendicular one-color dissociation MFPADs showing side lobes (18.54 eV H_2^+ short delay dataset).

The origins of these features is unknown. Similar energy dependent features were observed by Martin et. al. in [5]. In that experiment, a much higher VUV photon energy of 33 eV was used. This photon energy makes the Q_1 and Q_2 doubly excited states accessible in the Franck-Condon region of H_2 , as is shown in Figure 5.20.

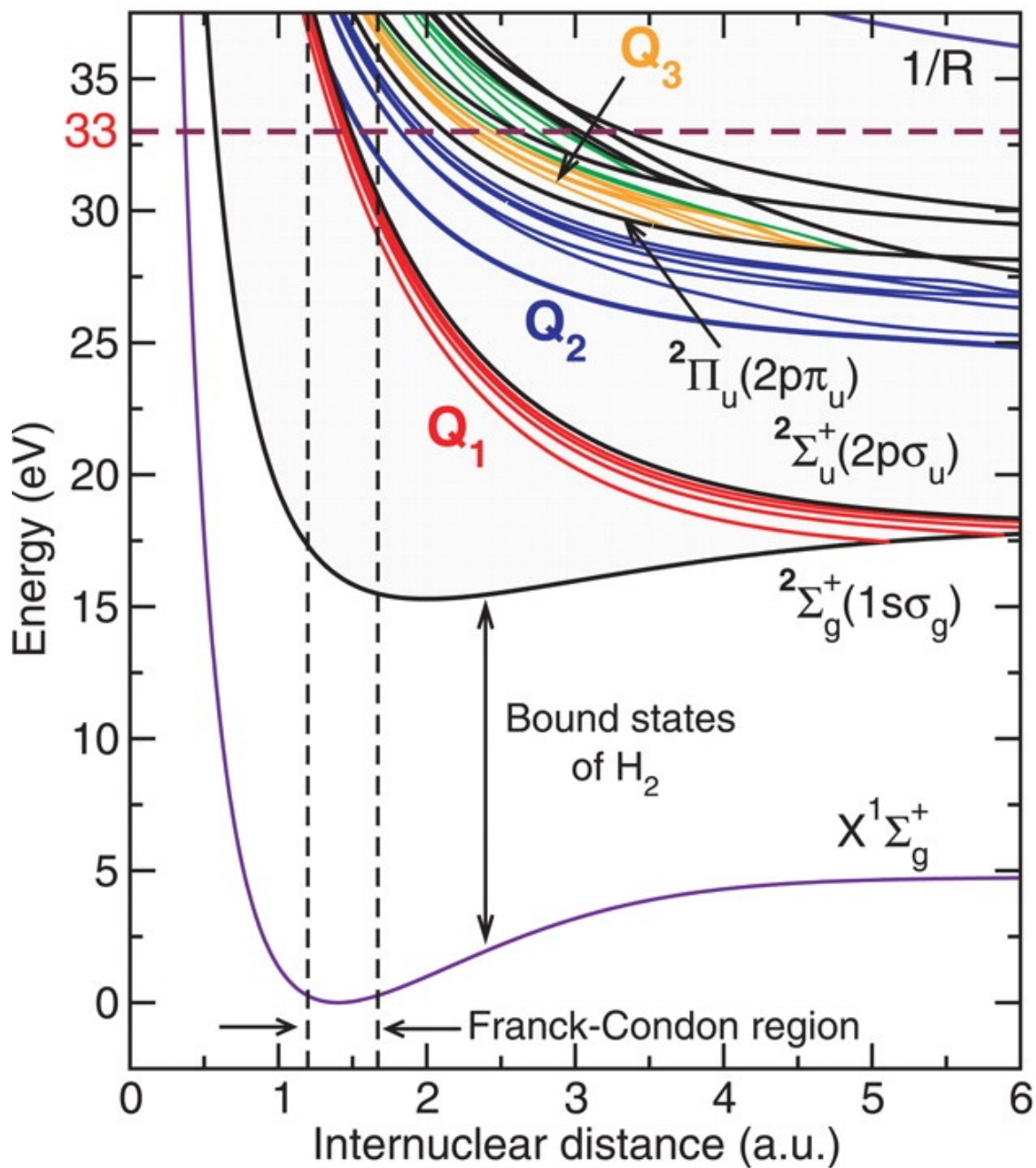


Figure 5.20: Energy diagram showing 33 eV experiment to access Q_1 and Q_2 states. The Q_1 energy curve is shown in red, and the Q_2 curve is shown in blue. Figure adapted from [5].

In that 33 eV experiment where the doubly excited states were energetically accessible in the Franck-Condon region, energy-dependent lobes appeared when the polarization and the molecular axis were perpendicular, and were attributed to interference between direct dissociation and dissociation proceeding via an autoionization decay process from the doubly

excited Q_1 and Q_2 states. An example of these energy dependent sidelobes from that 33 eV experiment is shown in Figure 5.21., taken from [5].

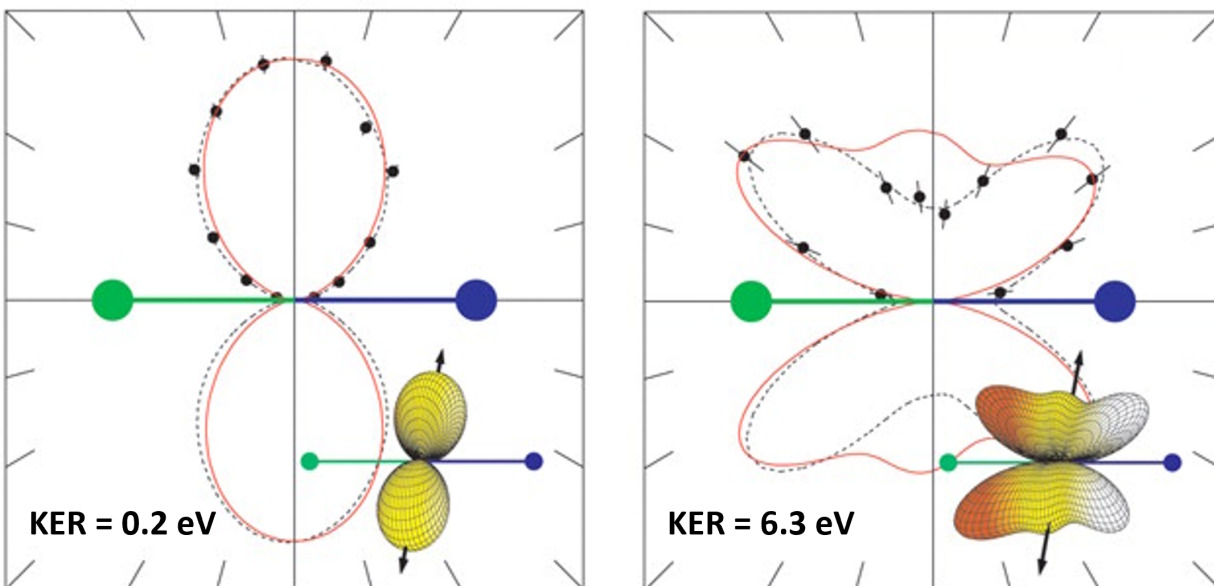


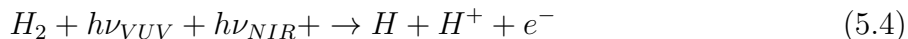
Figure 5.21: Calculated and experimental angular distributions showing sidelobes at KER values of .02 eV and 6.3 eV in the dissociative ionization of D_2 . The ion is shown in blue, and the neutral atom is shown in green. The polarization vector is shown as a black vertical arrow, and is perpendicular to the molecular axis. Figure adapted from [5].

For the current two-color experiment, the VUV energies where the one-color channel is observed range from 18.34 eV to 18.54 eV. At these energies, the Q_2 state is inaccessible, and the only way to get to the Q_1 state is by a transition VERY far from the Franck-Condon region of the neutral H_2 ground state, possibly involving the $1s\sigma_g$ state.

While there is not yet a definitive explanation for it, the observed perpendicular dissociation behavior seen in this experiment will hopefully prove to be a useful observation for future theoretical work.

5.3 Two-color channel

The two-color channel is present in every dataset. The net reaction is shown below:



Dissociation via the two-color channel proceeds from specific bound vibrational states. This means that, while dissociation via one-color channel leads to a continuous diagonal line on the electron energy vs KER map, dissociation via the two-color channel results in specific vibrational islands. The islands that make up this vibrational archipelago are located along a diagonal line defined following energy sum relation:

$$E_{sum} = KER + E_e = h\nu_{VUV} + h\nu_{NIR} - E_{diss} \quad (5.5)$$

This line runs parallel to the diagonal line that is the signature of the one-color dissociation, with intercepts that have been shifted 1.2 eV higher in energy. This line can be used to isolate the vibrational states for analysis. The event counts recorded for some states are so low that they prevent meaningful examination, and are excluded. A typical isolation of a vibrational archipelago to show events with good statistics is shown in Figure 5.22.

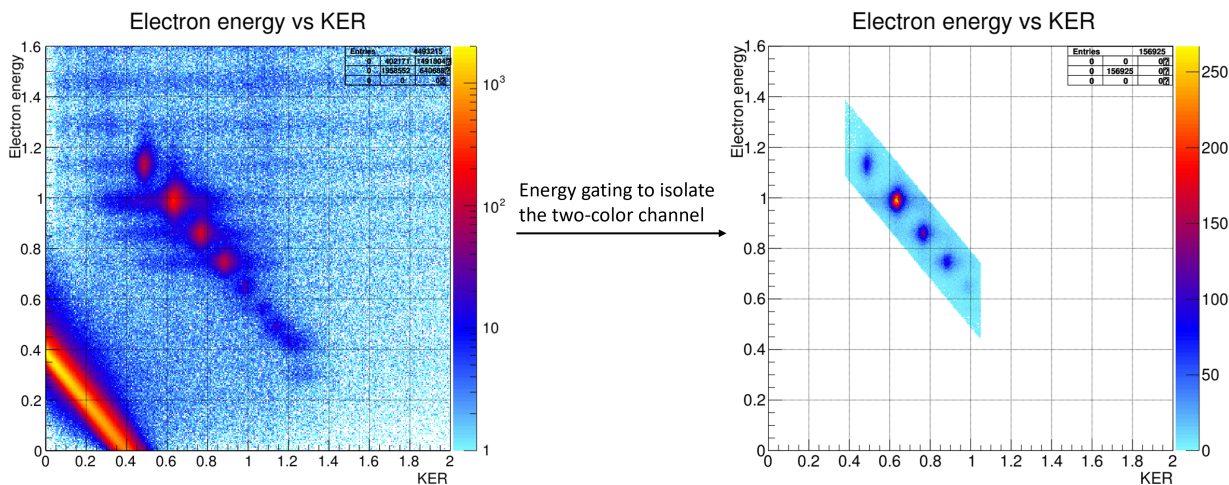


Figure 5.22: Isolation of the two-color dissociative channel in 18.54 eV H_2^+ .

The lab-frame photoelectron angular distributions, again recovered using the method described in Section 4.7, show that dissociation via the two-color channel has a very different angular dependence than the one observed via the one-color channel. The P-shape is observed while the molecular axis and the polarization axis are parallel, but decreases dramatically as the angle increases. Two-color dissociation does not occur when the molecular axis and polarization axis are perpendicular. Typical two-color lab frame PADs are shown in Figure 5.23.

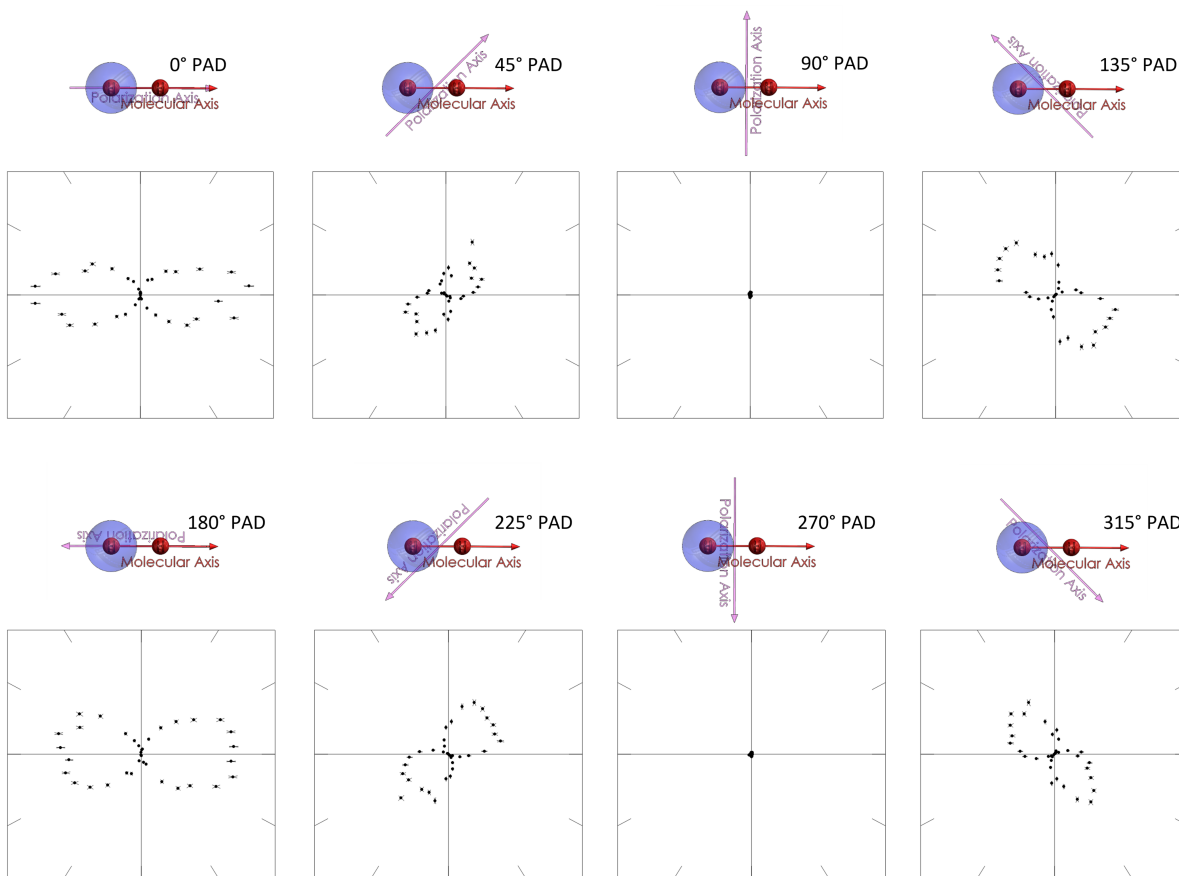


Figure 5.23: Lab-frame photoelectron angular distributions in the two-color channel ($\nu = 10\ 18.54\ \text{eV}\ H_2^+$, long delay dataset).

This behavior is also very visible when looking at the recoil θ_z vs MFPAD plots. The signature center island that represents perpendicular dissociation in the one-color channel is absent, while the parallel dissociation signature is still visible. This difference is demonstrated in Figure 5.24, and plots for each individual vibrational state are shown in Appendix E.

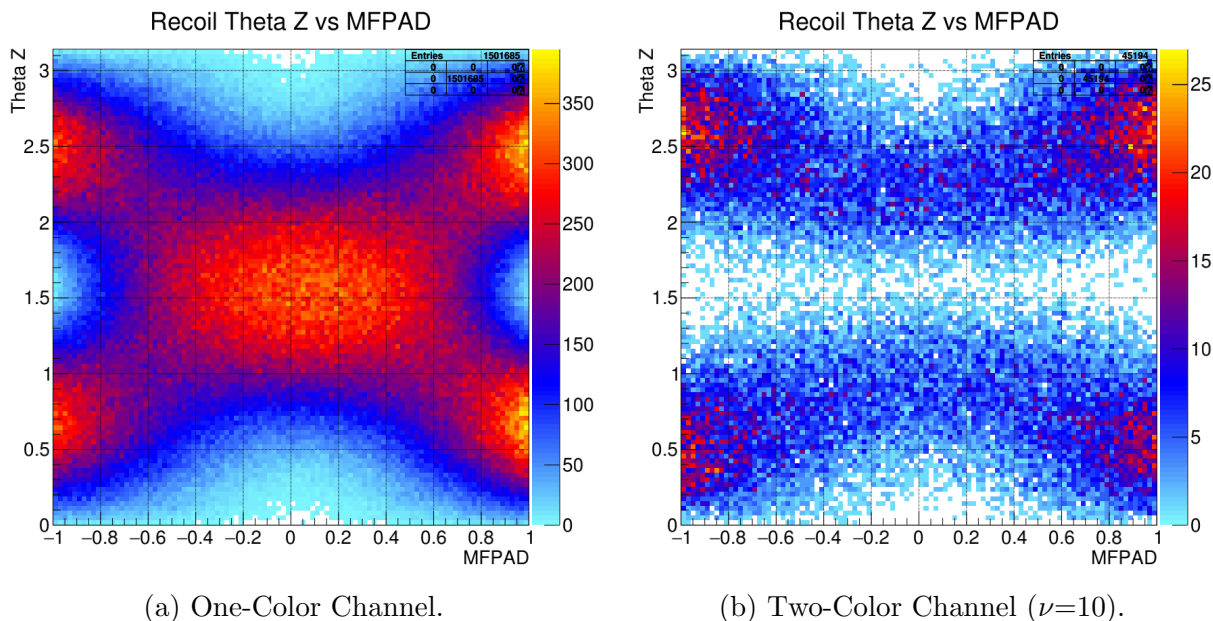


Figure 5.24: Recoil θ_z vs MFPAD plot for 18.54 eV H_2^+ long delay dataset.

The nodal line seen in Figure 5.24b indicating the inability of molecular ions oriented parallel to the polarization axis to dissociate can be explained by conservation of angular momentum.

A molecular ion with a single remaining electron and a molecular axis that is perpendicular to the polarization would not be able to accept the angular momentum of the incoming horizontally polarized NIR photon, preventing the NIR photon's absorption.

Armed with the ability to isolate individual vibrational states and the knowledge of the angular dependence of dissociation on the polarization axis, further exploration of the results of the two-color channel can be best done by looking at the various datasets at individual VUV photon energies.

5.3.1 18.54 eV D_2 dataset

The first dataset to be examined is the short-delay deuterium (D_2) dataset. Despite the advantages deuterium offers in TOF resolution, its high cost leads to deuterium being used sparingly. Nevertheless, analysis of the single deuterium two-color dataset yielded results that offer great insight into the processes taking place.

The first and most obvious feature that sets the D_2 data apart is the fact that there is a notable gap in the vibrational archipelago. Vibrational states $\nu = 13, 14, 15, 17,$ and 18 are clearly visible. States $\nu = 20$ and higher are very faint. Vibrational states $\nu = 16$ and $\nu = 19$, however, are noticeably absent. This is clear in the D_2 energy map shown in Figure 5.25, and isolation of the vibrational states that are present is shown in Figure 5.26.

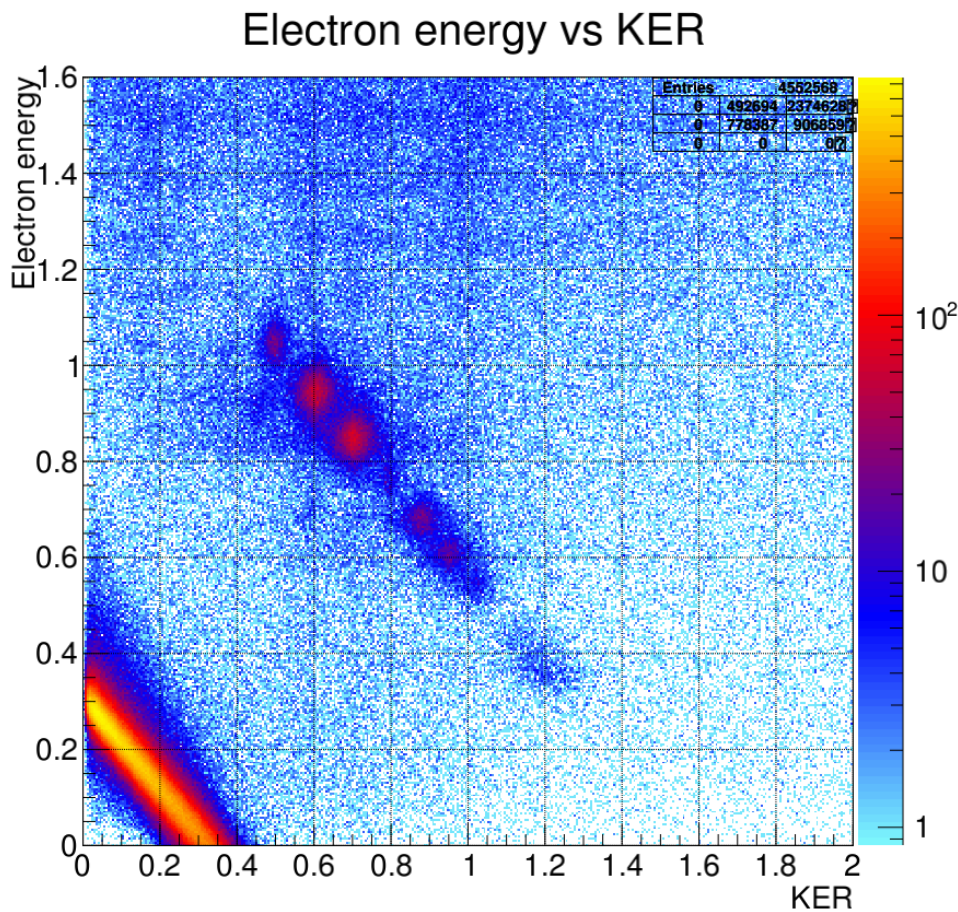


Figure 5.25: D_2^+ energy map.

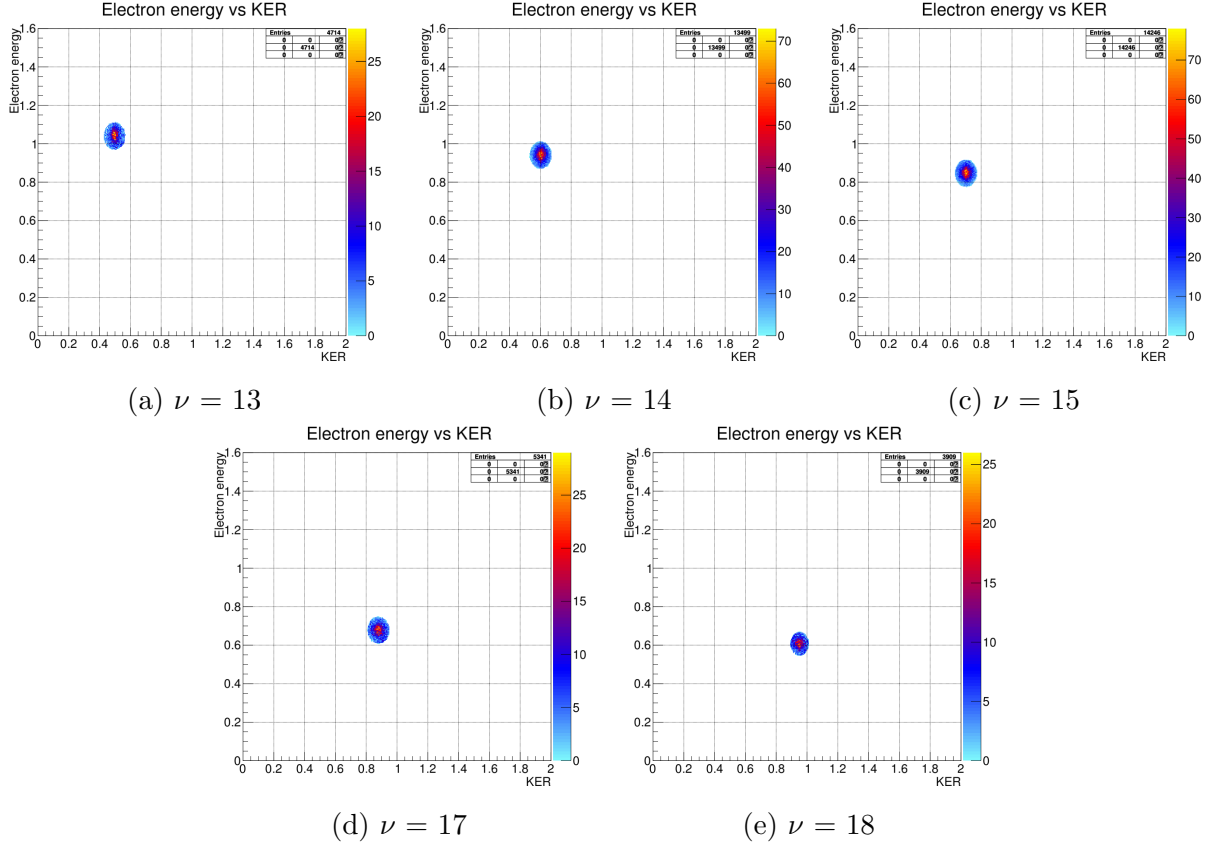


Figure 5.26: D_2^+ vibrational islands.

Initially, it was believed that the events with two-color dissociation of the $\nu = 16$ and $\nu = 19$ states had been lost in the contamination removal process described in Section 4.2. However, this process would not have eliminated the full momentum sphere of events. The absence of $\nu = 16$ and $\nu = 19$ could not be due to that process.

Gating on the whole vibrational archipelago allows for the relative heights of the vibrational peaks to be expressed as a function of electron energy. This electron energy vibrational spectrum also shows the absence of $\nu = 16$ and $\nu = 19$, as seen in Figure 5.27.

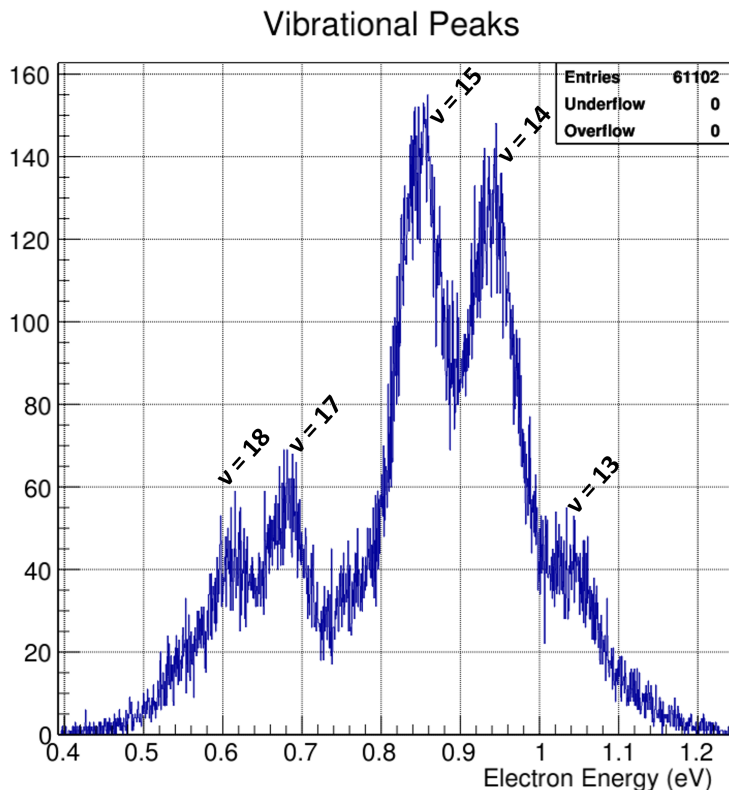


Figure 5.27: D_2^+ electron energy vibrational spectrum.

The solution to this mystery of the absent $\nu = 16$ and $\nu = 19$ vibrational states comes from theory discussed in Section 1.4, specifically the Franck–Condon factors.

Consider $\nu = 16$. For this vibrational state of D_2^+ to dissociate, it first needs to be populated from the neutral D_2 ground state during initial photoionization by the 18.54 eV VUV photon. This step can be approximated using the following Franck–Condon factor:

$$P_{16}^0 = |\langle \chi_{16} | \chi_0^0 \rangle|^2 \quad (5.6)$$

A transition then must take place from the bound $\nu = 16$ state of D_2^+ to a continuum state using a 1.2 eV NIR photon. This step can be approximated using the following Franck–Condon factor:

$$P_{16} = |\langle \chi_\epsilon | \mu | \chi_{16} \rangle|^2 \quad (5.7)$$

The product of the two Franck–Condon factors can be used to estimate the dissociation. Collaborators at Lawrence Berkeley National Laboratory, specifically Jan Dvořák from the Bill McCurdy group, carried out these calculations for this set of experimental conditions. The dissociation observed experimentally matches the results of these theoretical calculations strikingly well, including the absence of $\nu = 16$ and $\nu = 19$. This is shown in Figure 5.28.

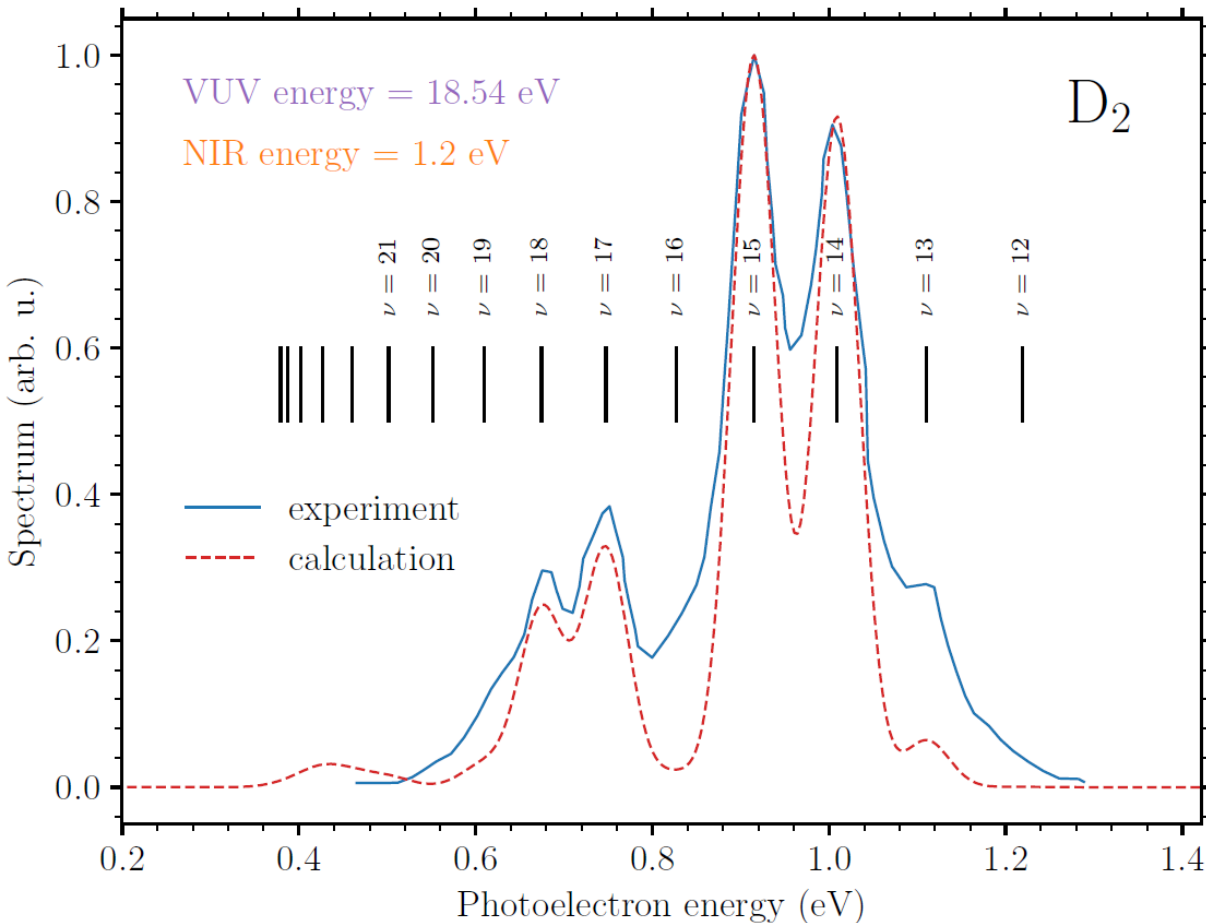


Figure 5.28: D_2^+ experimental vibrational peaks vs theoretical peaks calculated using Franck–Condon factors by Jan Dvořák.

The absence of $\nu = 16$ is starkly visible in the plot theory calculation. The dip for vibrational state $\nu = 19$ is more subtle and not as clear as it is in Figure 5.25, but is still visible in the theory calculation.

To understand the results of this calculation, consider a simple quantum harmonic oscillator with an angular frequency $\omega = \sqrt{k/m}$. The energy levels of a vibrational state ν in this system are:

$$E_\nu = \hbar\sqrt{\frac{k}{m}} \left(\nu + \frac{1}{2} \right) \quad (5.8)$$

The energy of a given vibrational state is inversely proportional to the square root of the mass, so the heavier mass of the deuterium nucleus compared to hydrogen nucleus means that the spacing of the D_2^+ vibration levels will be closer together.

It also means that the highest-in-energy bound vibrational states that are being dissociated by the 1.2 eV laser in this experiment have higher ν vibrational levels, with correspondingly more nodes in their wavefunctions.

If the 1.2 eV vertical transition between bound and continuum states happens to be located at a position where a node in the wavefunction is located, the overlap integral between the two wavefunctions will be very small. This could account for the lack of dissociation for a vibrational state in deuterium at 1.2eV that would dissociate at a slightly higher or lower NIR laser energy, with a vertical transition occurring at a slightly different internuclear distance coordinate where the Franck–Condon overlap is greater.

To demonstrate this, again consider vibrational state $\nu = 16$. Calculations show that the $\nu = 16$ vibrational wavefunction and the continuum wavefunction have an overlap integral that is vanishingly small for a 1.2 eV vertical transition. The two wavefunctions are shown in Figure 5.29, and this accounts for the absence of the $\nu = 16$ and $\nu = 19$ states in the D_2 data.

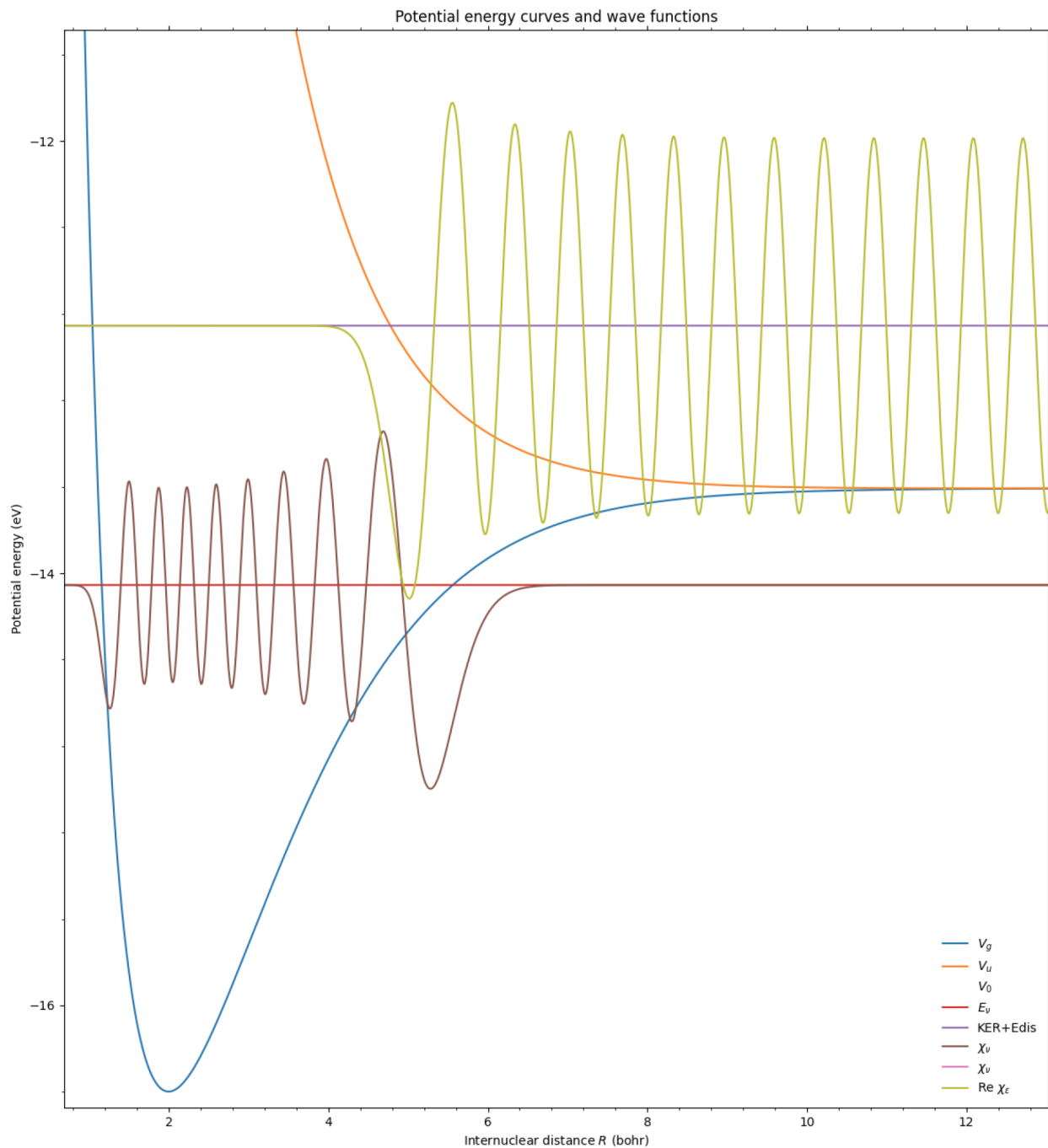


Figure 5.29: D_2^+ $\nu=16$ vibrational and continuum wavefunctions used to calculate the Franck–Condon factor for dissociation. Figure courtesy of Jan Dvořák.

D_2 data was only taken at a single time delay, 30 ps. This is short enough to allow overlap between the VUV and NIR pulses, as shown in Figure 5.30.

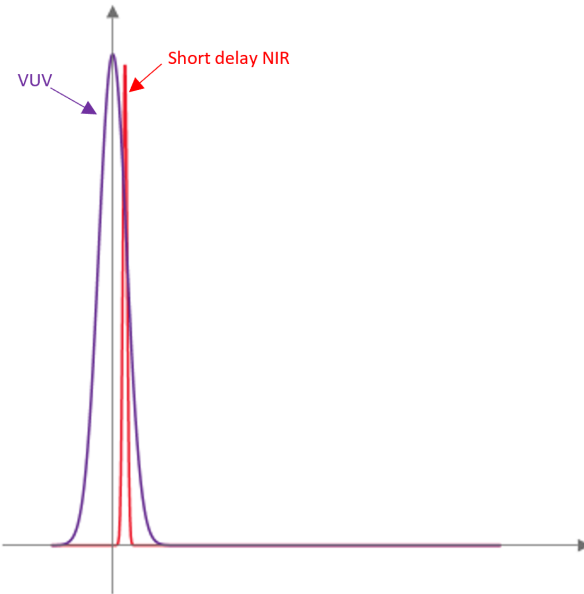


Figure 5.30: VUV/NIR time delay for D_2 dataset.

As with the one-color channel, a bin count asymmetry parameter δ was calculated as described in Section 4.4 for vibrational states $\nu = 13, 14, 15, 17,$ and 18 . These are shown in Figure 5.31.

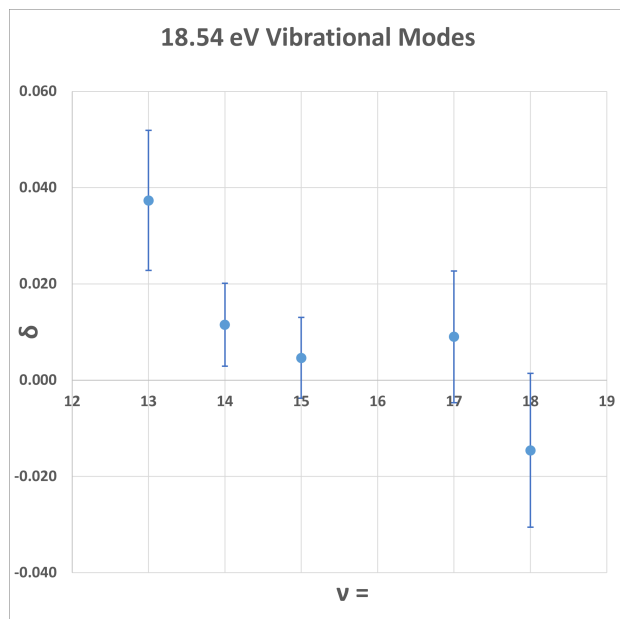


Figure 5.31: δ vs ν for 18.54 eV D_2^+ with 30 ps delay.

In addition, $\delta\sigma$ Legendre polynomial fit asymmetry parameters, as described in Section 4.5, were also found. These parameters are shown in Figure 5.32, and have essentially the same shape as the δ parameters.

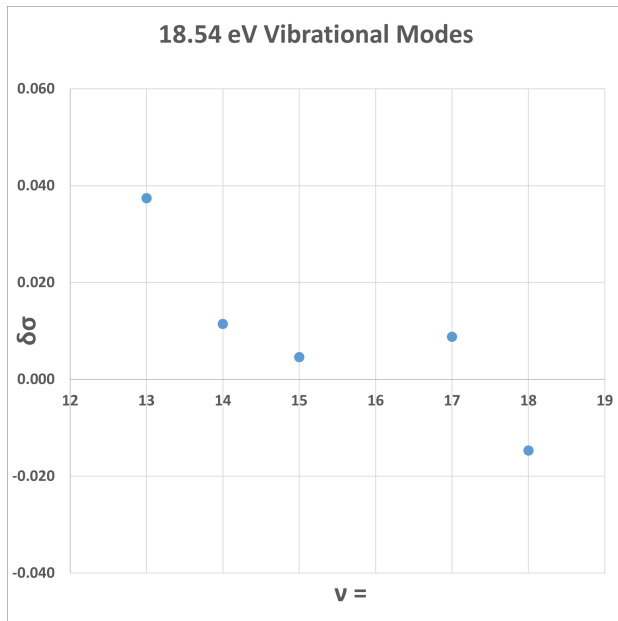


Figure 5.32: Legendre polynomial fit asymmetry Parameter $\delta\sigma$ vs ν for 18.54 eV D_2^+ with 30 ps delay.

A full summary of the numerical values in the above figures is shown in Table 5.2.

$\nu =$	13	14	15	17	18
EE	1.04	0.941	0.846	0.678	0.607
KER	0.497	0.602	0.701	0.879	0.952
C_p	2445	6827	7156	2694	1926
C_h	2269	6672	7090	2646	1983
δ	0.037 ± 0.015	0.011 ± 0.009	0.005 ± 0.008	0.009 ± 0.014	-0.015 ± 0.016
$\delta\sigma$	0.037	0.011	0.005	0.009	-0.015

Table 5.2: Summary of two-color D_2^+ data.

Using either methodology of quantifying asymmetry shows that there is a slight positive asymmetry for several of the vibrational states. The 30 ps time delay is short enough to allow for the VUV/NIR overlap that is needed for the electron retroaction effect described in Section 1.2 to contribute to the asymmetry. However, the expected dependence of asymmetry on photoelectron energy is not observed in this dataset. Higher vibrational states

are associated with lower energy photoelectrons, and should have correspondingly higher asymmetry.

However, since only a short-delay overlapping dataset was taken for D_2 , sadly it is not possible to compare the asymmetry at a long time delay to isolate the possible effect due to the presence of the photoelectron.

5.3.2 18.54 eV H_2 dataset

The H_2 data taken at a VUV energy 18.54 eV includes both a short (33 ps) and a long (900 ps) delay dataset. This allows us to examine the effect of VUV/NIR time delay in detail by looking at the differences between the two sets of results. The 33 ps time delay dataset is short enough to allow the 80 ps VUV and 12 ps NIR pulses to overlap, while the 900 ps time delay dataset is long enough to ensure that there is no overlap and that the photoelectron is not present by the time the NIR pulse arrives, as shown in Figure 5.33.

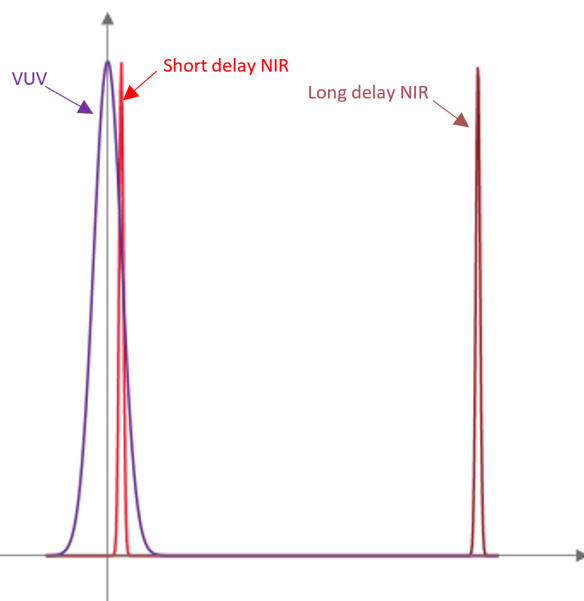


Figure 5.33: VUV/NIR time delays for 18.54 eV H_2 datasets.

The first thing to note is that the energy maps for the long and short delay datasets are essentially identical. Both feature well defined vibrational archipelagos that have essentially the same position. This is an indication that dissociation via the two-color channel is blind to the VUV/NIR time delay.

The energy maps for both long and short delay 18.54 eV H_2 data is shown in Figure 5.34, and isolation of the prominent vibrational states $\nu = 9$, $\nu = 10$, $\nu = 11$, and $\nu = 12$ is shown in Figure 5.35.

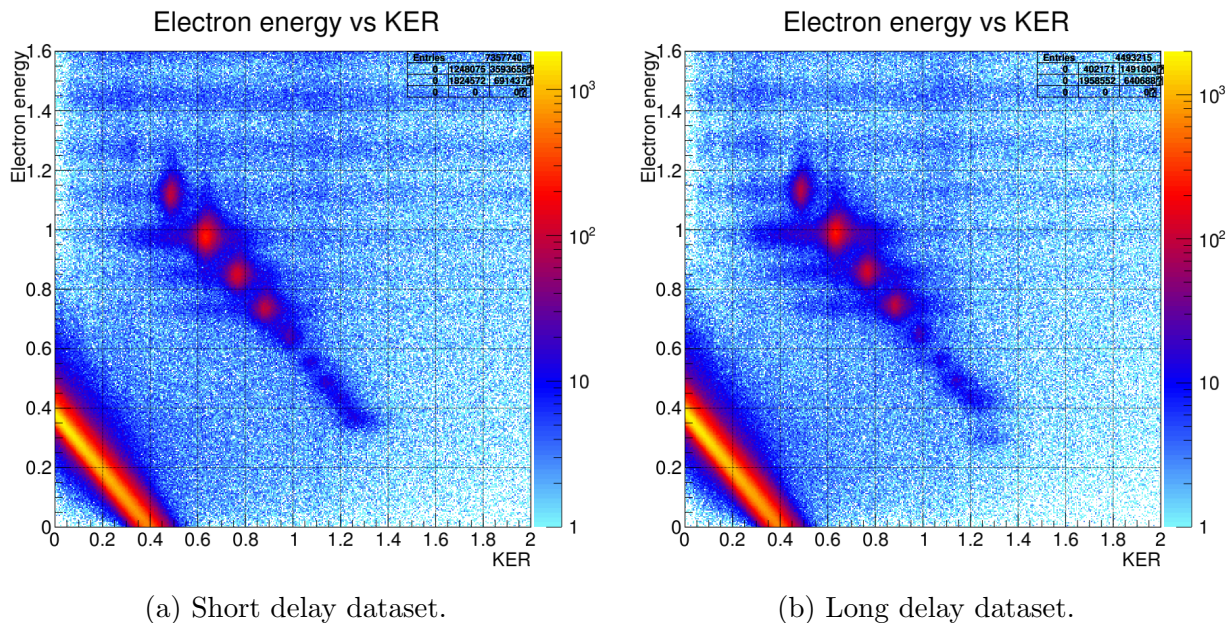


Figure 5.34: 18.54 eV H_2^+ energy maps.

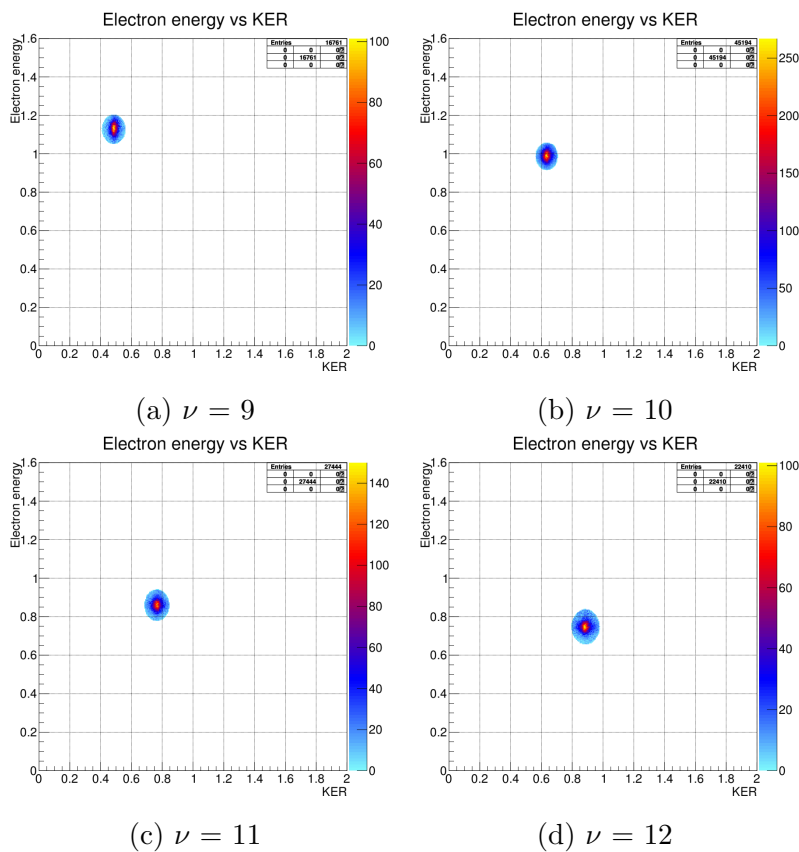


Figure 5.35: 18.54 eV H_2^+ vibrational islands.

Examining the vibrational peak electron energy spectrum for both the long and short datasets also shows that they are essentially identical in shape. A difference in relative heights of the vibrational peaks might indicate that dissociation of certain vibrational states is more or less dependent on the VUV/NIR time delay, but this does not appear to be the case, as is shown in Figure 5.36.

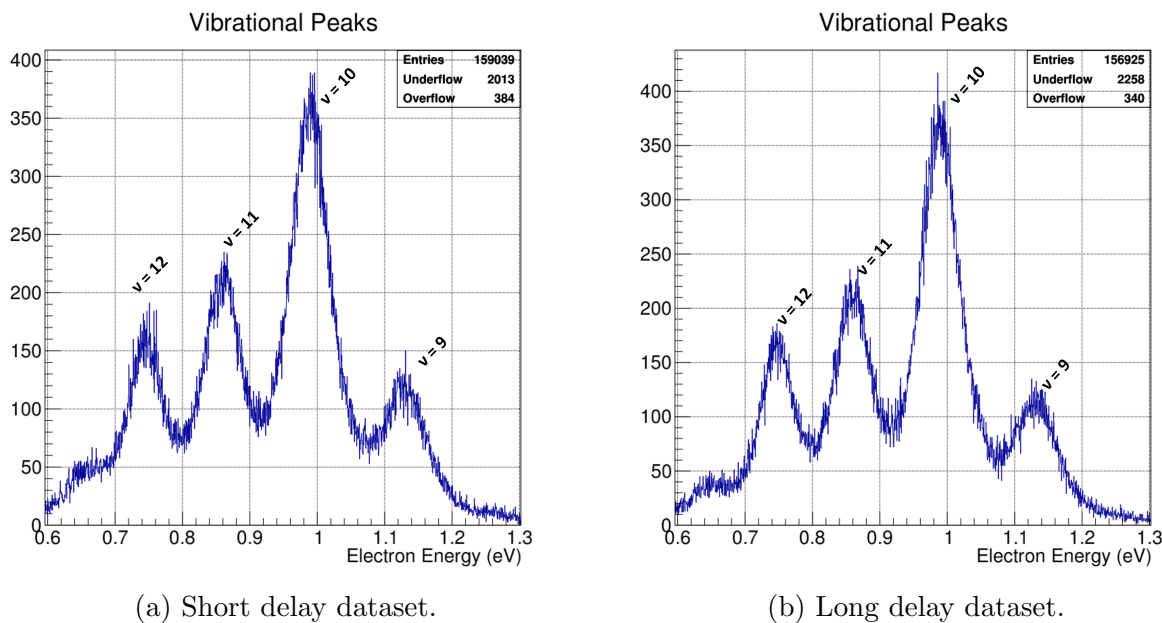


Figure 5.36: 18.54 eV H_2^+ electron energy vibrational spectrum.

As before, the observed vibrational peak electron energy can also be compared to the theoretical one recovered using Franck–Condon factors. These compare reasonably well for most vibrational states, but more dissociation of vibrational state $\nu = 9$ was observed than would be theoretically expected. This is shown in Figure 5.37.

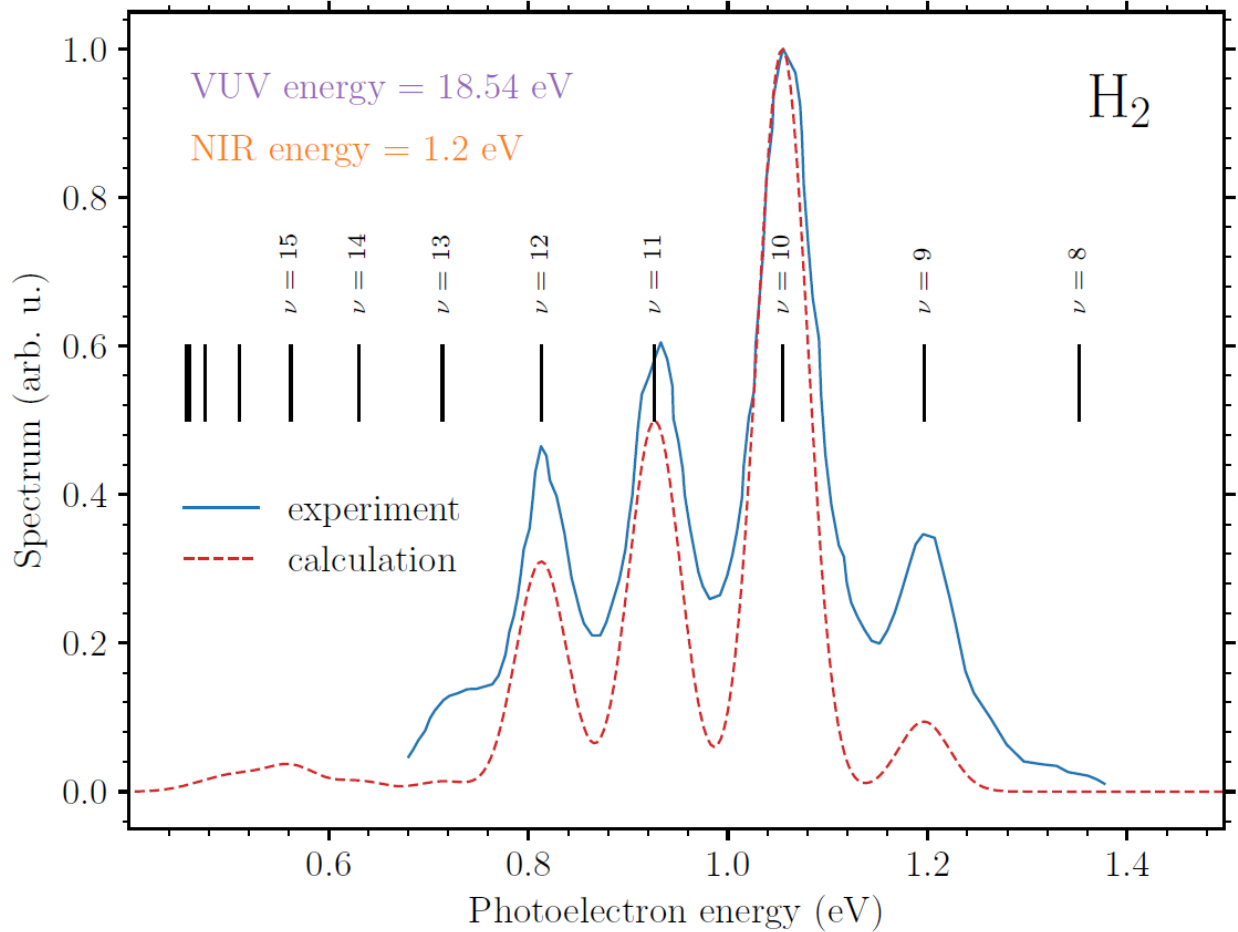
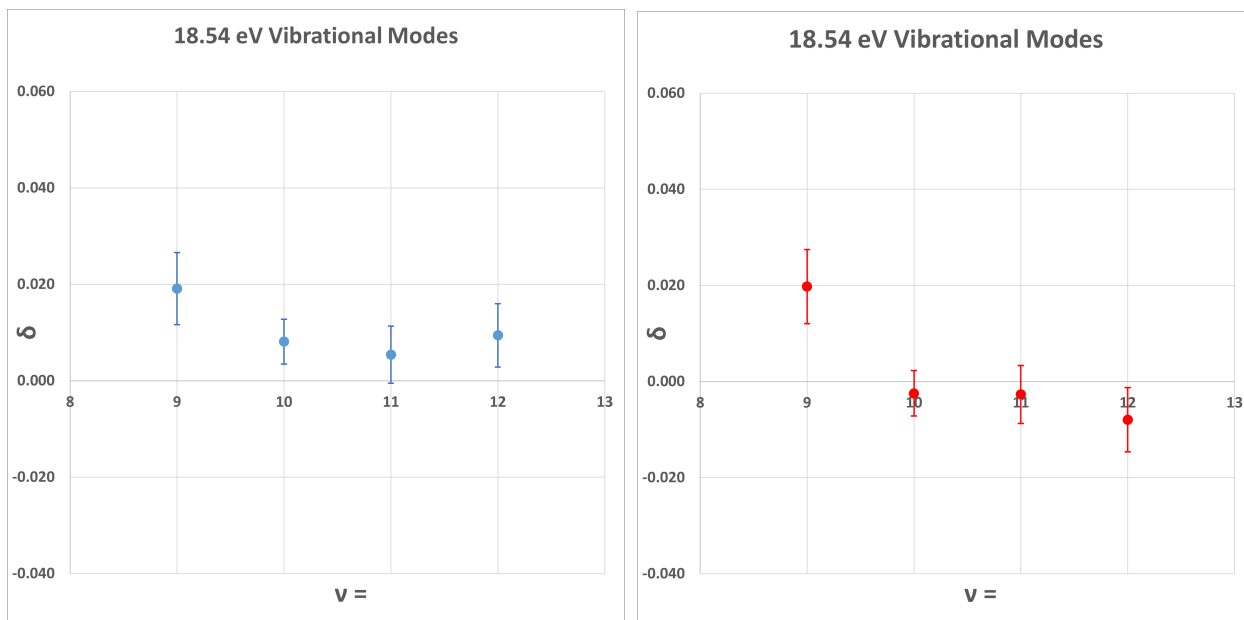


Figure 5.37: 18.54 eV H_2^+ experimental vibrational peaks vs theoretical peaks calculated using Franck–Condon factors. Figure courtesy of Jan Dvořák.

Without an energy signature to differentiate the two VUV/NIR time delays, we must examine the MFPADs to see if the asymmetry changes. When we look at the asymmetry parameters, we would expect to see an increased asymmetry at the shorter time delay if the electron retroaction effect is contributing. This is in fact observed. The asymmetry for dissociation via the two-color channel is small, but it is significantly larger in the short delay dataset than the long delay dataset for most vibrational states.

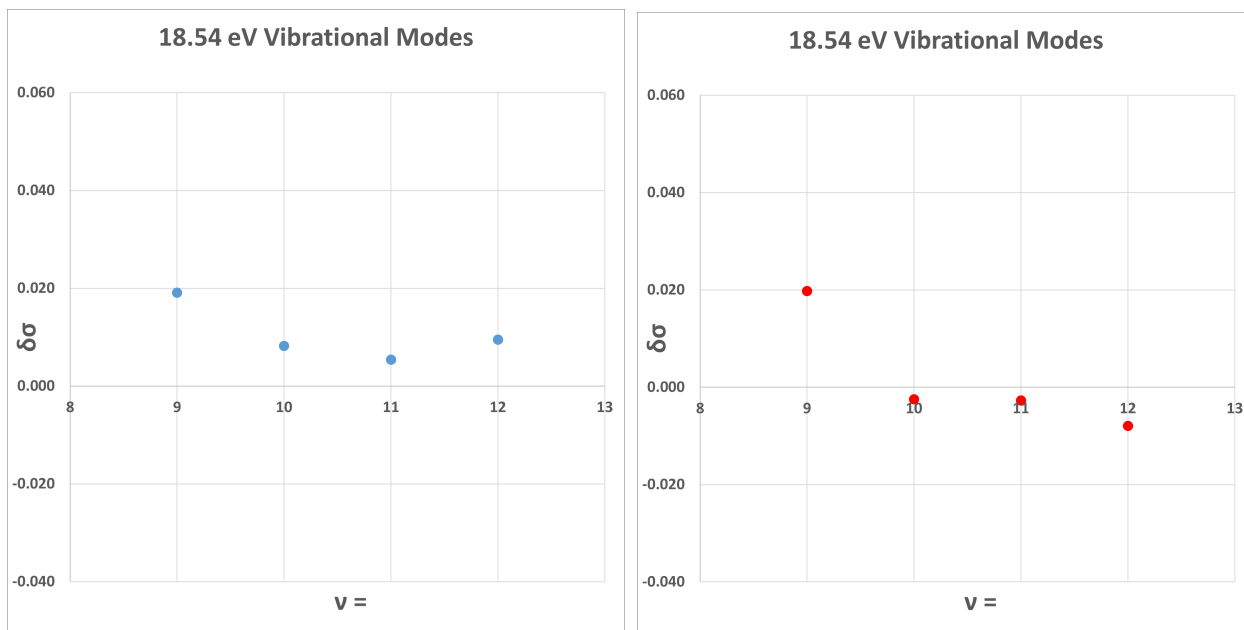
The bin count δ parameters for both long and short delay datasets are shown in Figure 5.38, and the $\delta\sigma$ Legendre polynomial fit asymmetry parameters are shown in Figure 5.39.



(a) 33 ps delay dataset.

(b) 900 ps delay dataset.

Figure 5.38: δ vs ν for 18.54 eV H_2^+



(a) 33 ps delay dataset.

(b) 900 ps delay dataset.

Figure 5.39: Legendre polynomial fit asymmetry parameter $\delta\sigma$ vs ν for 18.54 eV H_2^+ .

In the short delay data, $\nu = 10$ and $\nu = 11$ have approximately the same asymmetry, while $\nu = 12$, the state with the slowest photoelectron, has a higher asymmetry. In the

long delay dataset, these three vibrational states have negligible asymmetry. This time dependence is consistent with a small electron retroaction effect.

The asymmetry of dissociation from vibrational state $\nu = 9$, however, is almost exactly the same at both short and long time delays. This result, and the fact that there is more dissociation of $\nu = 9$ than was predicted by theory, indicates that there might be more complicated dynamics in play.

A full summary of the numerical values in the above figures is shown in Table 5.3 and Table 5.4.

$\nu =$	9	10	11	12
<i>EE</i>	1.128	0.987	0.860	0.747
<i>KER</i>	0.485	0.635	0.765	0.887
C_p	9103	23262	14286	11637
C_h	8762	22887	14133	11420
δ	0.019 ± 0.007	0.008 ± 0.005	0.005 ± 0.006	0.009 ± 0.007
$\delta\sigma$	0.019	0.008	0.005	0.009

Table 5.3: Summary of two-color 18.54 eV H_2^+ short delay data.

$\nu =$	9	10	11	12
<i>EE</i>	1.128	0.987	0.860	0.747
<i>KER</i>	0.485	0.635	0.765	0.887
C_p	8543	22540	13684	11116
C_h	8212	22651	13758	11294
δ	0.020 ± 0.008	-0.002 ± 0.005	-0.003 ± 0.006	-0.008 ± 0.007
$\delta\sigma$	0.020	-0.003	-0.003	-0.008

Table 5.4: Summary of two-color 18.54 eV H_2^+ long delay data.

5.3.3 18.34 eV H_2 dataset

Data at a VUV energy of 18.34 eV was only taken at a single time delay of 180 ps. This limits the data's utility in exploring the dependence of dissociation via the two-color channel on time delay, but still contains useful information that corroborates other observations. This time delay is long enough that there is no overlap between the VUV and NIR pulses, as shown in Figure 5.40.

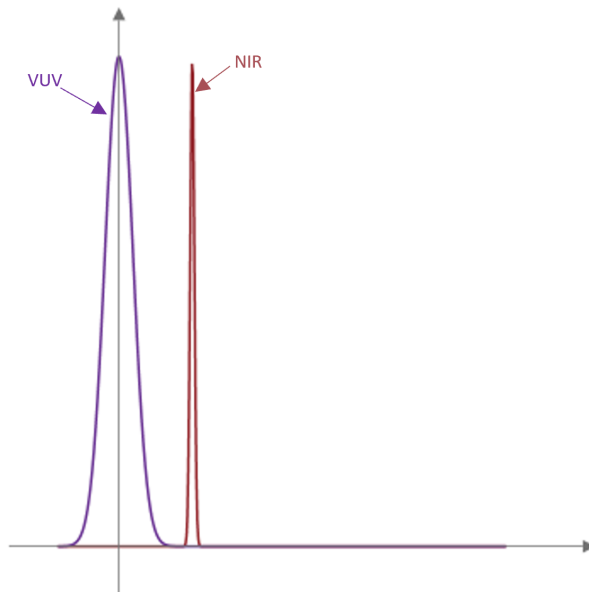


Figure 5.40: VUV/NIR time delay for 18.34 eV H_2 dataset.

The energy map is similar to the ones seen before, though shifted slightly lower due to the lower VUV energy, as shown in Figure 5.41.

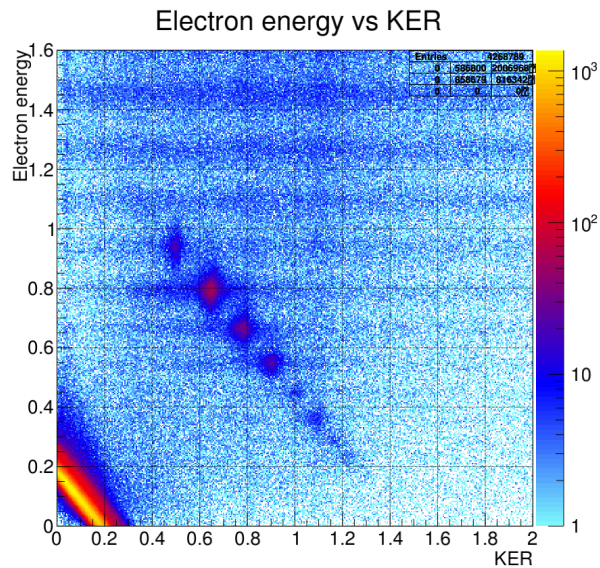


Figure 5.41: 18.34 eV H_2^+ energy map.

There is a well-defined vibrational archipelago, and states $\nu = 9$, $\nu = 10$, $\nu = 11$, and $\nu = 12$ are again prominent. Figure 5.42 shows the isolation of these states, and the resulting vibrational peak electron energy spectrum is shown in Figure 5.43.

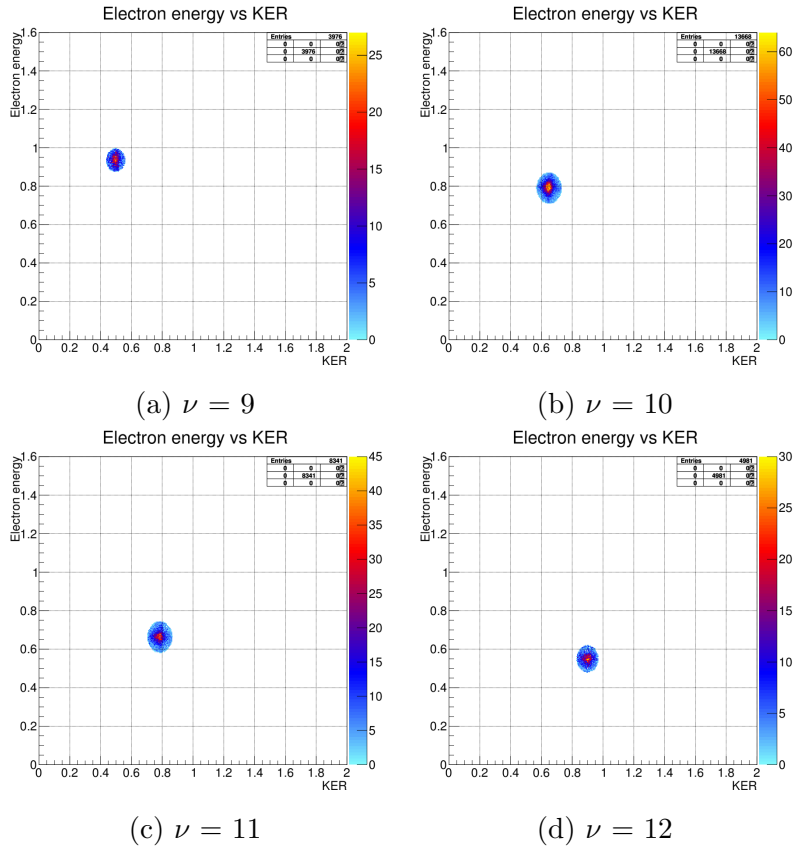


Figure 5.42: 18.34 eV H_2^+ vibrational islands.

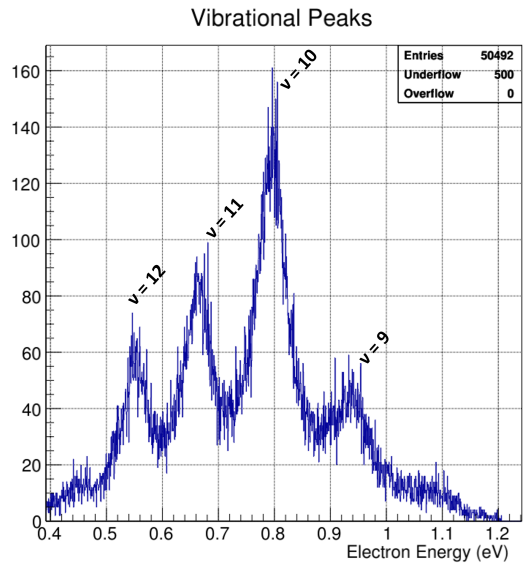


Figure 5.43: 18.34 eV H_2^+ electron energy vibrational spectrum.

As before, this observed energy spectrum and the theoretical one from Franck–Condon factors can be compared. It is notable that, again, observed dissociation of the $\nu = 9$ vibrational state is higher than theoretically anticipated. This is shown in Figure 5.44.

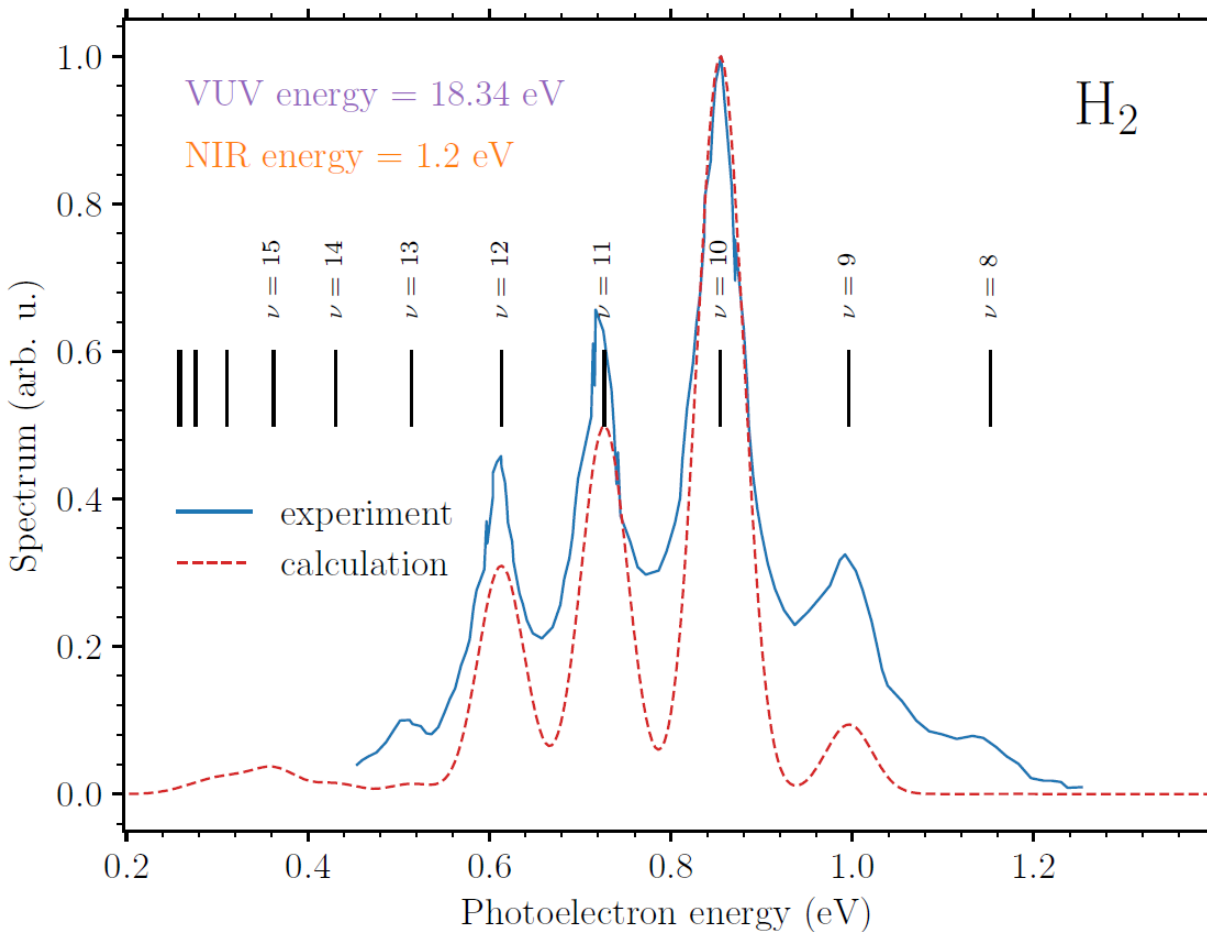


Figure 5.44: 18.34 eV H_2^+ experimental vibrational peaks vs theoretical peaks calculated using Franck–Condon factors. Figure courtesy of Jan Dvořák.

Examining the MFPADs shows that dissociation via the two-color channel in this dataset yields very little asymmetry, as shown in Figure 5.45 and Figure 5.46.

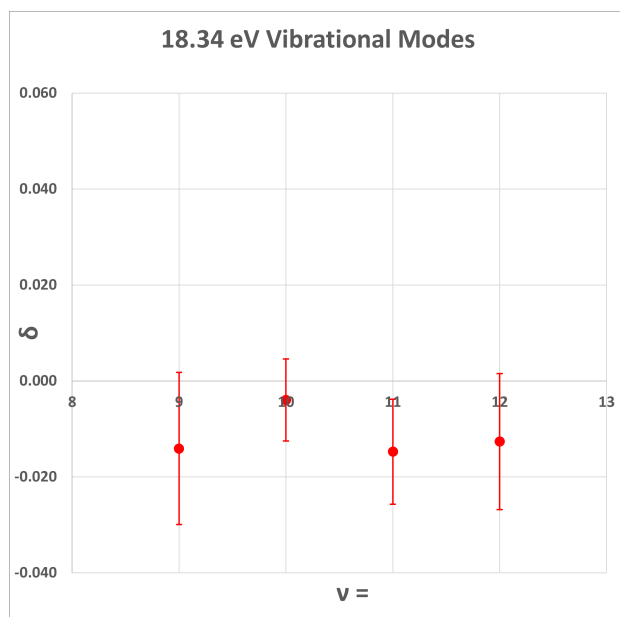


Figure 5.45: δ vs ν for 18.34 eV H_2^+ with 180 ps delay.

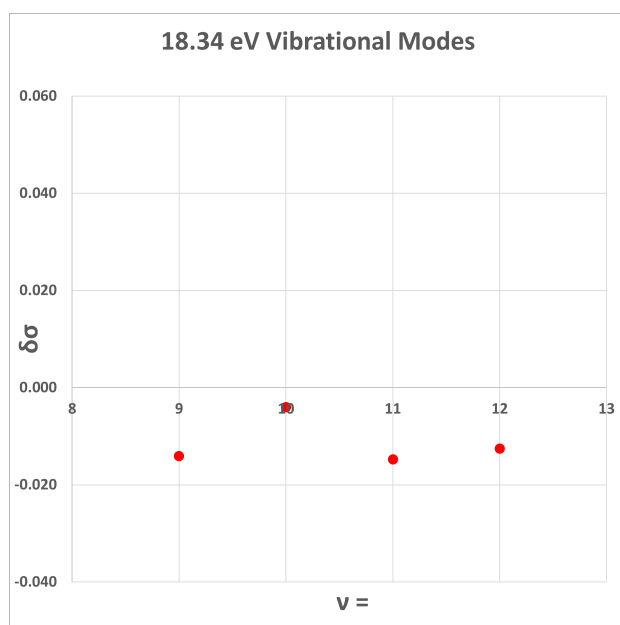


Figure 5.46: Legendre polynomial fit asymmetry parameter $\delta\sigma$ vs ν for 18.34 eV H_2^+ with 180 ps delay.

This negligible asymmetry is what would be expected in the electron retroaction picture. The long time delay gives the photoelectron ample time to leave before the NIR pulse arrives, and asymmetry due to this effect should be minimal.

A full summary of the numerical values in the above figures is shown in Table 5.5.

$\nu =$	9	10	11	12
EE	0.936	0.790	0.663	0.550
KER	0.498	0.650	0.785	0.900
C_p	1960	6807	4109	2459
C_h	2016	6861	4232	2522
δ	-0.014 ± 0.016	-0.004 ± 0.009	-0.015 ± 0.011	-0.013 ± 0.014
$\delta\sigma$	-0.014	-0.004	-0.015	-0.013

Table 5.5: Summary of two-color 18.34 eV H_2^+ data.

5.3.4 17.9 eV H_2 dataset

The final results to be examined are from the data taken at a VUV energy 17.9 eV. These datasets are unique in that the VUV energy is below the dissociation threshold of 18.075 eV, so dissociation can only proceed via the two-color channel. In addition, data was collected at two different VUV/NIR time delays, as shown in Figure 5.47.

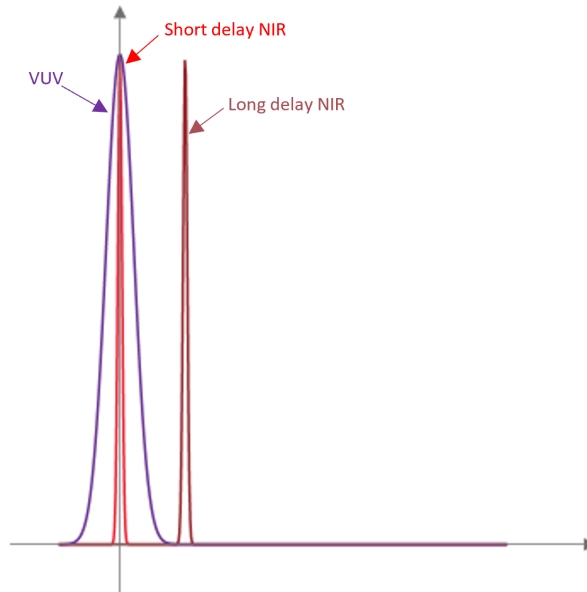


Figure 5.47: VUV/NIR time delays for 17.9 eV H_2 datasets.

The short delay dataset, with a delay of 0 ps, and the long delay dataset, with a delay of 160 ps, allow dissociation to be studied with both overlapping and non-overlapping pulses.

The first notable feature of the 17.9 eV energy maps is the absence of the one-color dissociation channel. Only the vibrational archipelago remains. In addition, the energy maps still seem to be the same regardless of VUV/NIR time delay, as is shown in Figure 5.48.

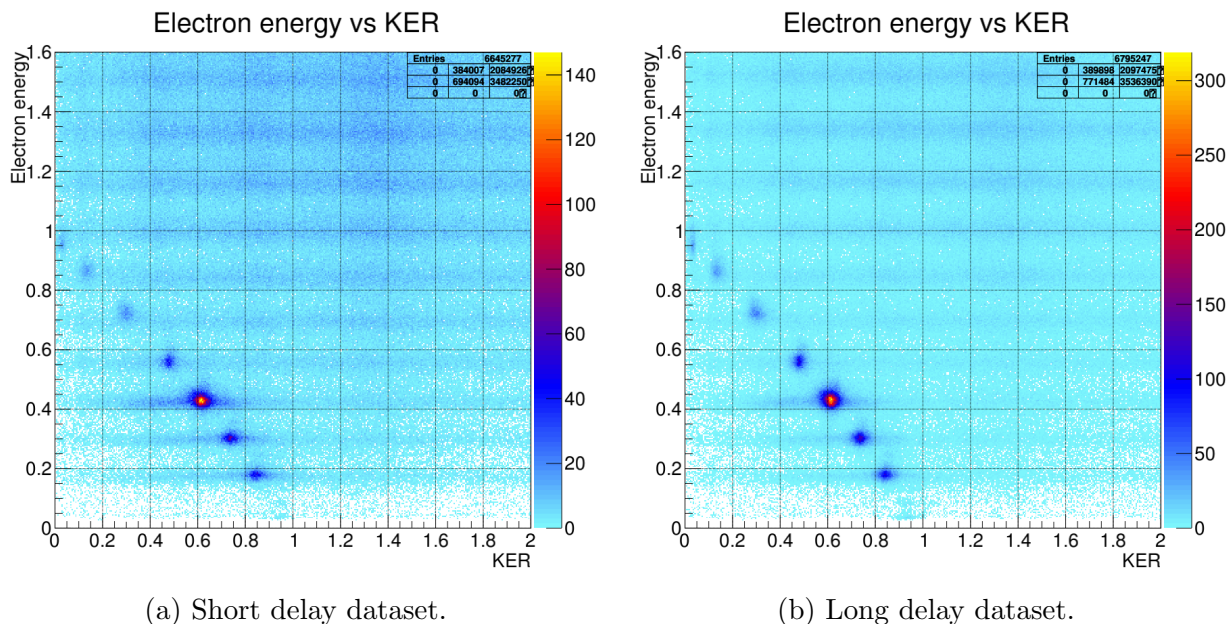


Figure 5.48: 17.9 eV H_2^+ energy maps.

Vibrational states $\nu = 9$, $\nu = 10$, $\nu = 11$, and $\nu = 12$ are very prominent. While faint, vibrational states $\nu = 7$ and $\nu = 8$ can also be seen clearly. There is also an extremely faint signature of vibrational state $\nu = 6$ that has almost no kinetic energy release. The isolation of states $\nu = 7$ through $\nu = 12$ is shown in Figure 5.49.

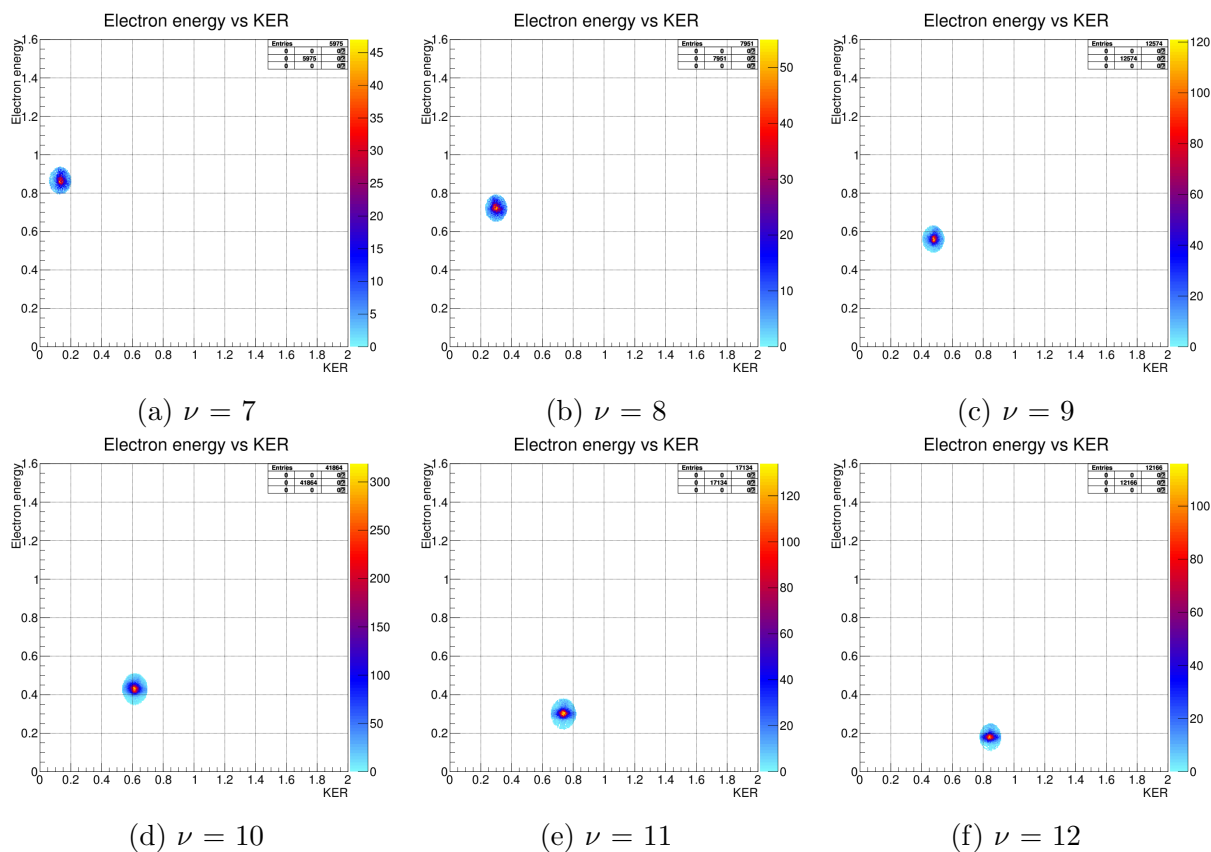


Figure 5.49: 17.9 eV H_2^+ vibrational islands.

As was seen with the 18.54 eV data, examination of vibrational peak electron energy spectrum for the long and short delay datasets at 17.9 eV shows little difference in shape, and suggests that the dissociation does not depend on the VUV/NIR time delay. The vibrational peak electron energy spectrum is shown in Figure 5.50.

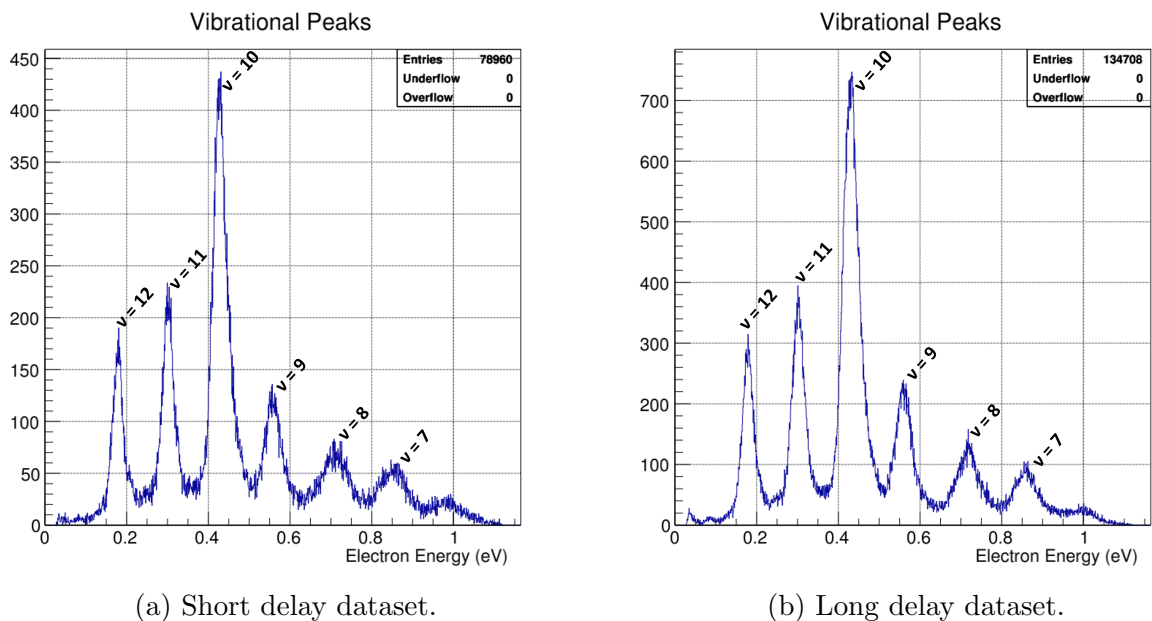


Figure 5.50: 17.9 eV H_2^+ electron energy vibrational spectrum.

A surprising result comes from the comparison of the observed energy spectrum and the theoretical one from Franck–Condon factors. Dissociation from vibrational states $\nu = 7$ and $\nu = 8$ can clearly be observed in the energy map and the electron energy vibrational spectrum at 17.9 eV. However, there should not be dissociation from these states according to the calculations using Franck–Condon factors. In addition, as has been seen previously, the observed $\nu = 9$ dissociation is higher than it should be. This discrepancy is shown in Figure 5.51.

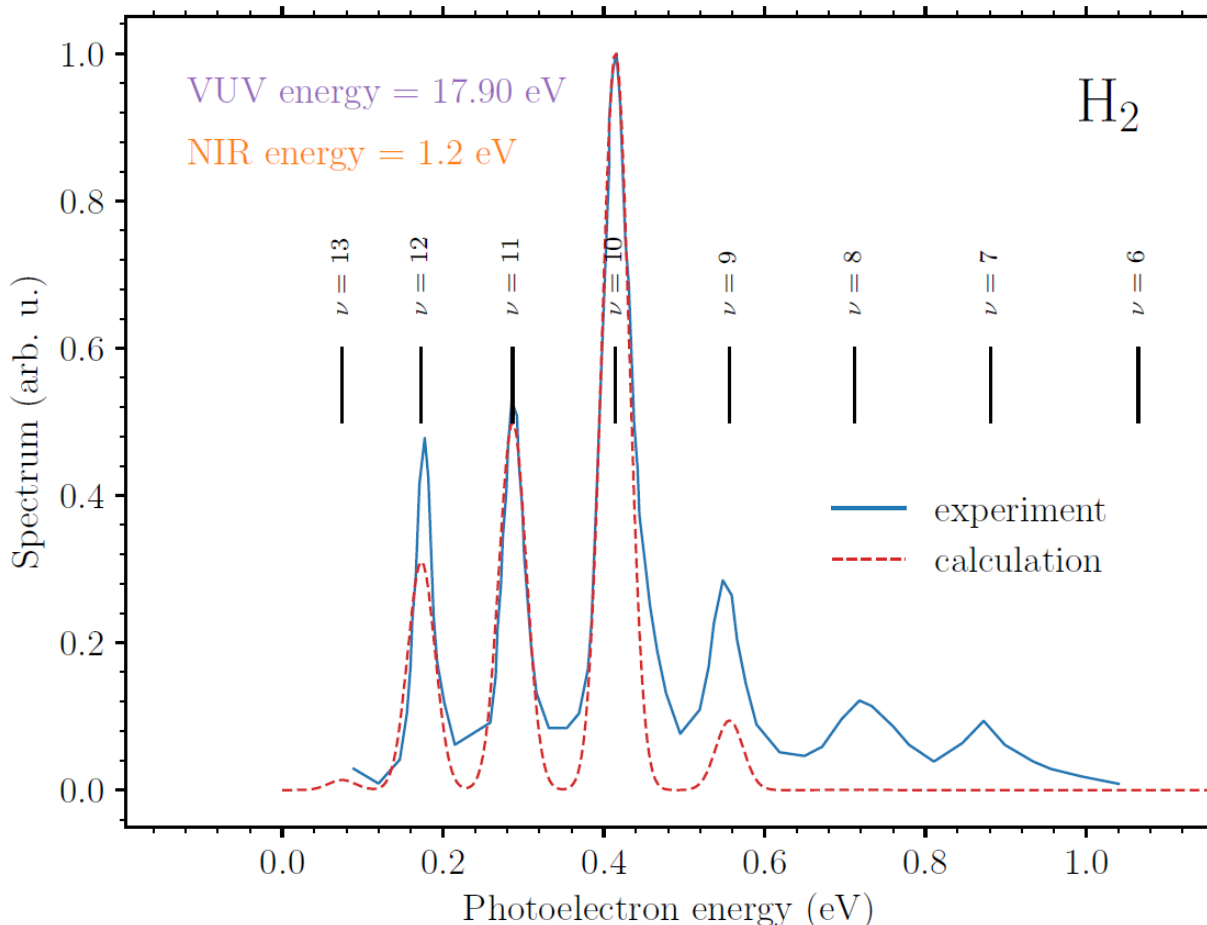
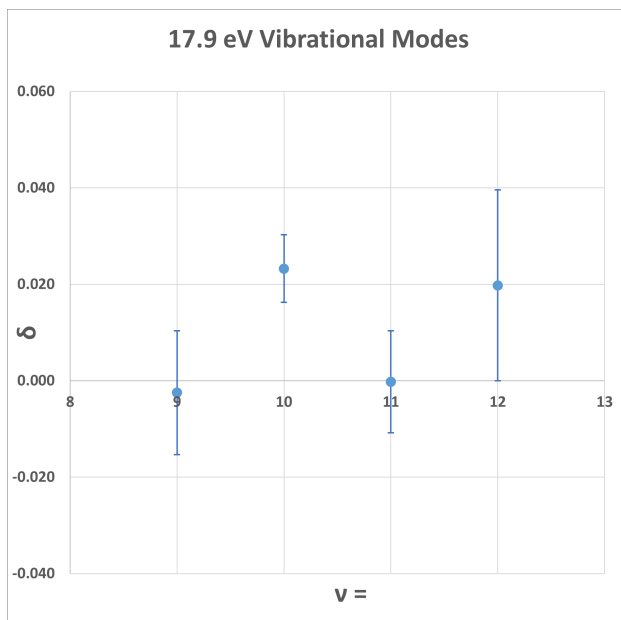
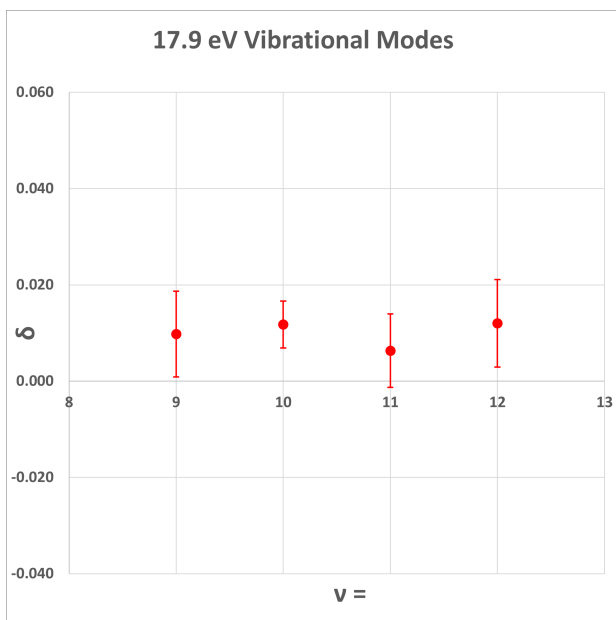


Figure 5.51: 17.9 eV H_2^+ experimental vibrational peaks vs theoretical peaks calculated using Franck–Condon factors. Figure courtesy of Jan Dvořák.

Examination of the MFPADs recovered at this VUV energy are also interesting. The short time delay dataset has generally higher asymmetry for vibrational states $\nu = 10$ and $\nu = 12$, as would be expected in the retroaction picture, but $\nu = 7, 8, 9$, and 11 seem to be less affected by the VUV/NIR time delay. In addition, the lower energy $\nu = 7$ and $\nu = 8$ states have very high and delay invariant asymmetry. Figure 5.52 shows the δ parameter asymmetry of states $\nu = 9, \nu = 10, \nu = 11$, and $\nu = 12$ at the same scale as used for previous similar figures in the two-color channel. Figure 5.53 and Figure 5.54 include the $\nu = 7$ and $\nu = 8$ states, and have re-scaled the vertical δ axis to show the abnormally high asymmetry in these states.

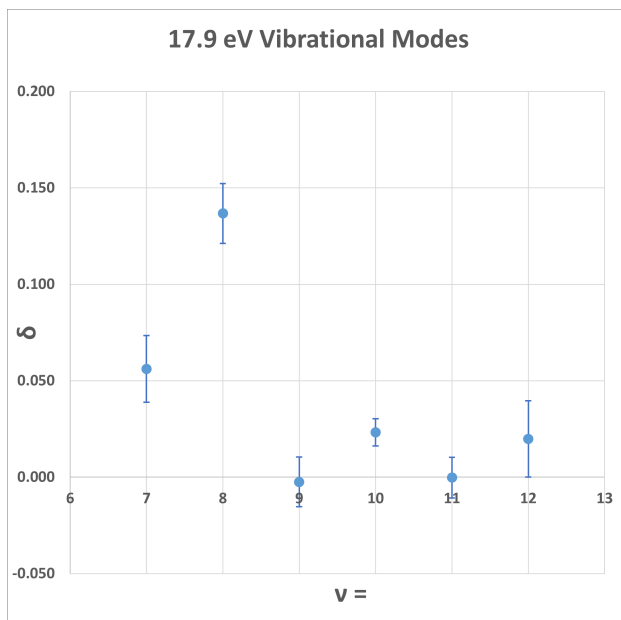


(a) 0 ps delay dataset.

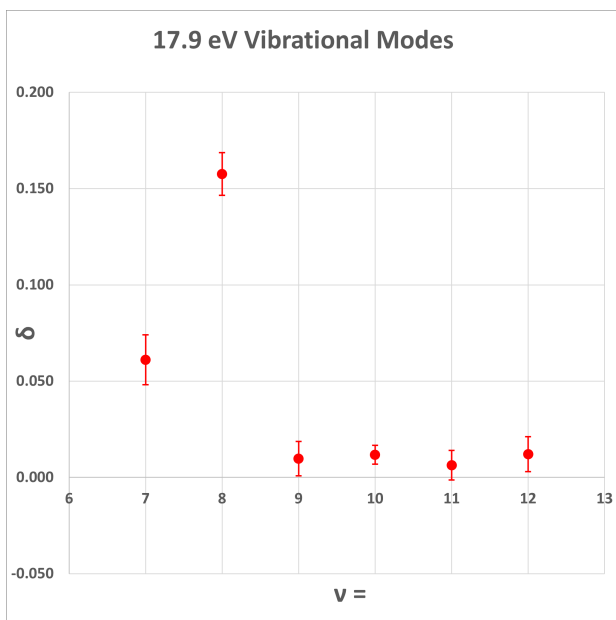


(b) 160 ps delay dataset.

Figure 5.52: δ vs ν for states $\nu = 9$, $\nu = 10$, $\nu = 11$, and $\nu = 12$ for 17.9 eV H_2^+ .

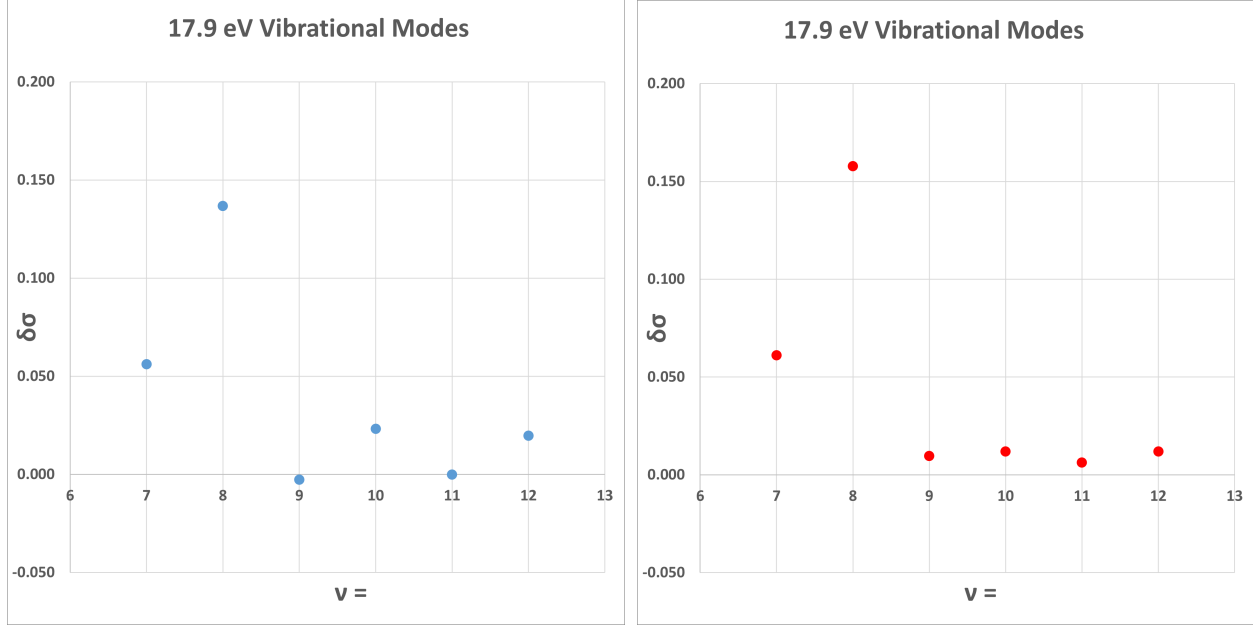


(a) 0 ps delay dataset.



(b) 160 ps delay dataset.

Figure 5.53: δ vs ν for all states for 17.9 eV H_2^+ .



(a) 0 ps delay dataset.

(b) 160 ps delay dataset.

Figure 5.54: Legendre polynomial fit asymmetry parameter $\delta\sigma$ vs ν for 17.9 eV H_2^+ .

A full summary of the numerical values in the above figures is shown in Table 5.6 and Table 5.7.

$\nu =$	7	8	9	10	11	12
EE	0.865	0.722	0.561	0.429	0.300	0.180
KER	0.131	0.30	0.476	0.616	0.737	0.847
C_p	1769	2303	3022	10387	4466	3118
C_h	1581	1749	3037	9915	4468	2997
δ	0.056 ± 0.017	0.137 ± 0.016	-0.002 ± 0.013	0.023 ± 0.007	0.000 ± 0.011	0.020 ± 0.013
$\delta\sigma$	0.056	0.137	-0.003	0.023	0.000	0.020

Table 5.6: Summary of two-color 17.9 eV H_2^+ short delay data.

$\nu =$	7	8	9	10	11	12
EE	0.865	0.722	0.561	0.429	0.300	0.180
KER	0.131	0.30	0.476	0.616	0.737	0.847
C_p	3170	4602	6348	21177	8621	6156
C_h	2805	3349	6225	20685	8513	6010
δ	0.061 ± 0.013	0.158 ± 0.011	0.010 ± 0.009	0.012 ± 0.005	0.006 ± 0.008	0.012 ± 0.009
$\delta\sigma$	0.061	0.158	0.010	0.012	0.006	0.012

Table 5.7: Summary of two-color 17.9 eV H_2^+ long delay data.

Dissociation from vibrational states $\nu = 7$ and $\nu = 8$ also has a different dependence on the angle between the polarization axis and the molecular axis. The recoil ion θ_z vs MFPAD plots for $\nu = 7$ and $\nu = 8$ feature faint center islands indicative of perpendicular dissociation, which is different from all the other observed vibrational states where only parallel dissociation is seen. This is shown in Figure 5.55.

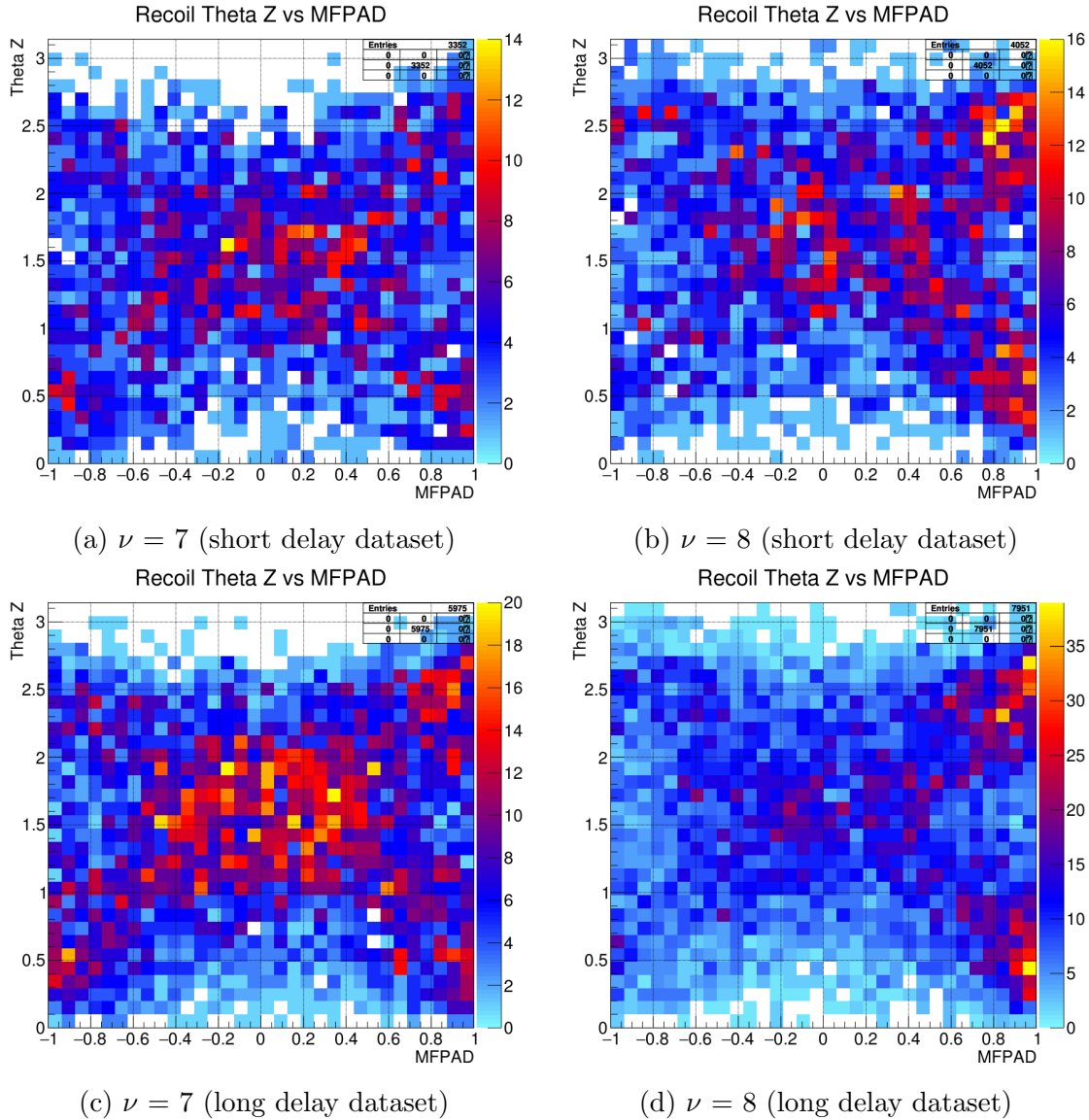


Figure 5.55: Recoil ion θ_z vs MFPAD plots for states $\nu = 7$ and $\nu = 8$ in 17.9 eV H_2^+ .

A dressed potential energy surface characterized by the presence of light induced conical intersections, discussed in Section 1.3, might explain the unexpected behavior of vibrational states $\nu = 7$, $\nu = 8$, and $\nu = 9$ in H_2^+ .

The laser-dressed potential energy curves are compressed together and bent. If an ion trapped in the dressed $1s\sigma_g$ state tunnels through the relatively narrower potential energy barrier, it can escape the bound well and the molecule can dissociate. Figure 5.56 shows the dressed potential energy curves at an intensity of $3 \times 10^{11} W/cm^2$, and the vibrational energy levels for H_2^+ .

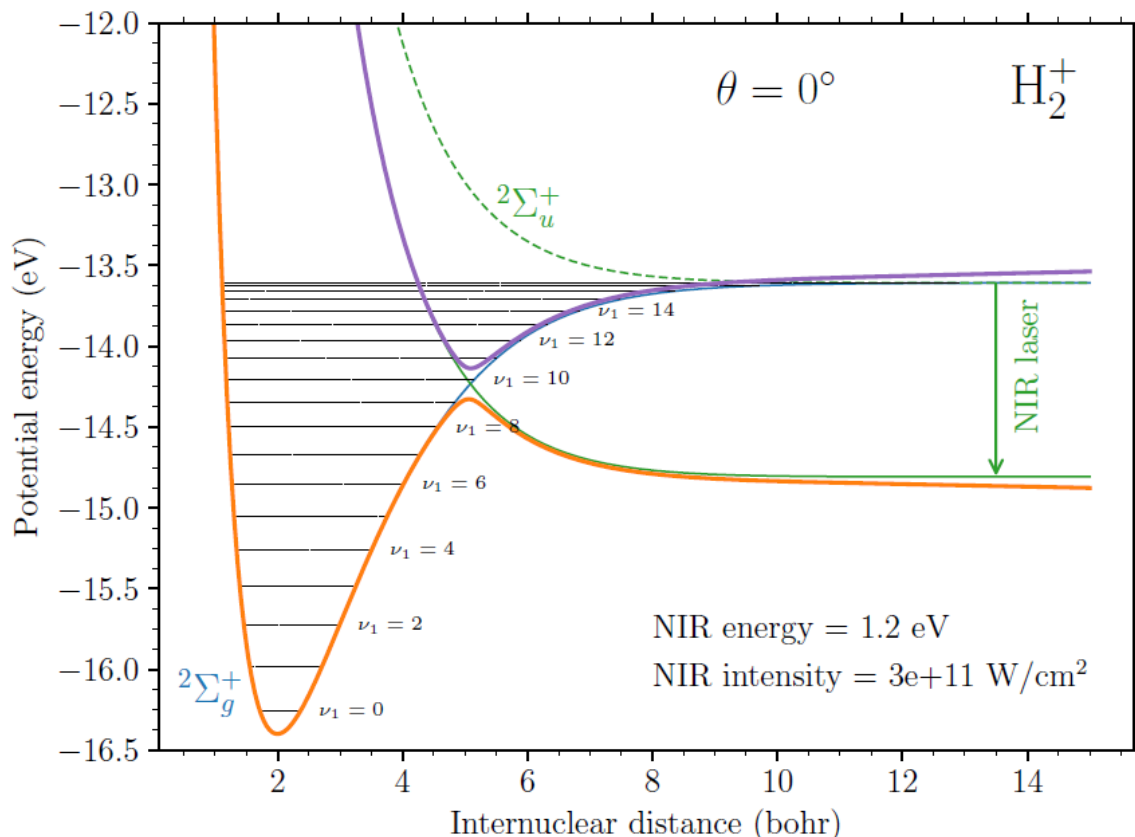


Figure 5.56: Potential energy curves of H_2^+ shown at $\theta = \pi/2$ (green and blue curves) and $\theta = 0$ (orange and violet curves). Figure courtesy of Jan Dvořák.

States $\nu = 7$ and $\nu = 8$, which would need to undergo a 1.2 eV vertical transition at an internuclear distance that lies in a classically forbidden region to reach the undressed dissociative ungerade state, can now reach the continuum by tunneling horizontally.

The $\nu = 9$ state could either undergo a vertical transition or tunnel out, allowing for more dissociation of that state as well.

This is speculative however, and a conclusive mechanism for the observed dissociative behavior of these vibrational states remains unknown.

Chapter 6

Conclusion

This experiment has successfully provided a great deal of novel insight into the dissociation of H_2 and D_2 molecules after photoionization.

For the one-color channel, the results of this experiment show clearly that the MFPAD is dependent on the angle between the molecular axis and the polarization axis, and that the MFPAD asymmetry changes with electron energy.

The energy dependence of the MFPAD asymmetry for events with perpendicular dissociation is different from the dependence that is seen for parallel dissociation events. The MFPAD asymmetry for events with a molecular axis parallel to the polarization dissociating via the one-color channel decreases as photoelectron energy increases, as expected via the classical retroaction model. The MFPAD asymmetry for events with a molecular axis perpendicular to the polarization dissociating via the one-color channel drops to a minimum, then increases again, diverging from the classical retroaction model.

In addition, subtle energy-dependent side lobes are observed in the one-color perpendicular dissociation MFPADs. Similar behavior has been observed at higher energies with dissociation via doubly excited Q_1 and Q_2 states, but this mechanism should not be energetically accessible at the VUV energies used in this experiment. A conclusive origin of the behavior in the perpendicular dissociation remains unknown.

For the two-color channel, the MFPAD asymmetry can change at different time delays. The fact that there is generally less asymmetry at longer time delays, where the photoelectron has had ample time to leave the vicinity of the molecular ion, may be evidence of a surviving electron retroaction effect.

Some vibrational states, particularly $\nu=16$ and $\nu=19$ in D_2^+ , do not dissociate because there is not enough overlap between bound and continuum wavefunctions.

The two-color channel results also raise questions for theorists. Some vibrational states have an MFPAD asymmetry that is unaffected by changing the VUV/NIR time delay. Some vibrational states that are NOT expected to dissociate DO still dissociate, and some states have higher than anticipated dissociation. These states with increased dissociation also seem to have larger MFPAD asymmetry.

The presence of a dressed potential energy surface with a light-induced conical intersection, which the laser intensity should be high enough to create, might offer a possible explanation for the observed dissociation of states that should remain bound using the unaltered potential curves. The modified potential energy curves might allow for dissociation via tunneling horizontally to the continuum, accounting for the observed dissociation in states where the vertical overlap leads to little dissociation ($\nu = 9$ in H_2^+) or no dissociation ($\nu = 7$ and $\nu = 8$ in the 17.9 eV H_2^+ data).

However, this is speculative. As with the perpendicular dissociation in the one-color channel, a conclusive origin of the two-color dissociative behavior observed in these states also remains unknown.

It is hoped that the results of both dissociation channels presented will prove useful to future theoretical explorations of these phenomena, and that this work can help contribute to greater understanding of the complexities in nature's simplest molecules.

References

- [1] De Broglie, Louis. “Recherches Sur La Theorie Des Quanta.” Mas-son, 1924. English Translation: https://fondationlouisdebroglie.org/LDB-oeuvres/De_Broglie_Kracklauer.pdf
- [2] Griffiths, David Jeffrey. Introduction to Quantum Mechanics. Pearson Prentice Hall, 2005.
- [3] Atkins, Peter, and Julio De Paula. Atkins’ Physical Chemistry. Oxford University Press, 2006.
- [4] Born, M., and R. Oppenheimer. “Zur Quantentheorie der Molekeln.” *Annalen Der Physik*, vol. 389, no. 20, 1927, pp. 457–484, <https://doi.org/10.1002/andp.19273892002>. English Translation: <https://www.theochem.ru.nl/files/dbase/born-oppenheimer-translated-s-m-blinder.pdf>
- [5] Martin, F., et al. “Single photon-induced symmetry breaking of H₂ dissociation.” *Science*, vol. 315, no. 5812, 2007, pp. 629–633, <https://doi.org/10.1126/science.1136598>.
- [6] Serov, Vladislav V., and A. S. Kheifets. “p-H symmetry breaking in dissociative photoionization of H₂ due to the molecular ion interacting with the ejected electron.” *Physical Review A*, vol. 89, no. 3, 2014, <https://doi.org/10.1103/physreva.89.031402>.
- [7] Waitz, M., et al. “Electron Localization in Dissociating H₂⁺ by Retroaction of a Photoelectron onto Its Source.” *Physical Review Letters*, vol. 116, no. 4, 2016, <https://doi.org/10.1103/physrevlett.116.043001>.
- [8] Heck, S., et al. “Symmetry breaking in the body-fixed electron emission pattern due to electron-retroaction in the photodissociation of H₂⁺ and D₂⁺ close to threshold.” *Physical Review Research*, vol. 1, no. 3, 2019, <https://doi.org/10.1103/physrevresearch.1.033140>.
- [9] Herzberg, G., and H. C. Longuet-Higgins. “Intersection of potential energy surfaces in polyatomic molecules.” *Discussions of the Faraday Society*, vol. 35, 1963, p. 77, <https://doi.org/10.1039/df9633500077>.
- [10] McFarland, B. K., et al. “Ultrafast X-ray auger probing of photoexcited molecular dynamics.” *Nature Communications*, vol. 5, no. 1, 2014, <https://doi.org/10.1038/ncomms5235>.

- [11] Natan, Adi, et al. “Observation of quantum interferences via light-induced conical intersections in diatomic molecules.” *Physical Review Letters*, vol. 116, no. 14, 2016, <https://doi.org/10.1103/physrevlett.116.143004>.
- [12] Introduction To Floquet Theory - Yale University, boulder-school.yale.edu/sites/default/files/files/floquetlecture_Konrad%20Viebahn.pdf. Accessed 22 Nov. 2023.
- [13] Schaad, L. J., and W. V. Hicks. “Equilibrium bond length in H₂+.” *The Journal of Chemical Physics*, vol. 53, no. 2, 1970, pp. 851–852, <https://doi.org/10.1063/1.1674078>.
- [14] Corkum, P. B. “Plasma perspective on strong field multiphoton ionization.” *Physical Review Letters*, vol. 71, no. 13, 1993, pp. 1994–1997, <https://doi.org/10.1103/physrevlett.71.1994>.
- [15] Vaughan, John. “Probing and Controlling Electron Dynamics at the Attosecond Timescale.” Auburn University, 2021. <https://etd.auburn.edu/handle/10415/7608>
- [16] Unzicker, B, et al. “Electron choreography at the attosecond time scale.” *New Journal of Physics*, vol. 23, no. 1, 2021, p. 013019, <https://doi.org/10.1088/1367-2630/abdbdf>.
- [17] Vaughan, John, et al. “Design of an optically-locked interferometer for attosecond pump-probe setups.” *Optics Express*, vol. 27, no. 21, 2019, p. 30989, <https://doi.org/10.1364/oe.27.030989>.
- [18] Goh, S.J., et al. “Fabrication and characterization of free-standing, high-line-density transmission gratings for the vacuum UV to soft X-ray range.” *Optics Express*, vol. 23, no. 4, 2015, p. 4421, <https://doi.org/10.1364/oe.23.004421>.
- [19] “Concave Blazed Holographic Gratings - for Flat-Field Polychromators.” SHIMADZU, www.shimadzu.com/opt/products/dif/o-k25cur0000007hxd.html. Accessed 21 Nov. 2023.
- [20] “Laminar-Type Replica Diffraction Gratings for VUV/Soft X-Ray Region.” SHIMADZU, www.shimadzu.com/opt/products/dif/o-k25cur0000006zd0.html. Accessed 21 Nov. 2023.
- [21] Newton SO Series - Oxford Instruments, andor.oxinst.com/assets/uploads/products/andor/documents/andor-newton-so-specifications.pdf. Accessed 22 Nov. 2023.
- [22] Zangwill, Andrew. *Modern Electrodynamics*. Cambridge University Press, 2016.
- [23] McMillan, Edwin M. “A history of the Synchrotron.” *Physics Today*, vol. 37, no. 2, 1984, pp. 31–37, <https://doi.org/10.1063/1.2916080>.
- [24] Advanced Light Source Quick Facts - Als, als.lbl.gov/wp-content/uploads/2018/11/QuickFacts2019.pdf. Accessed 22 Nov. 2023.
- [25] “Arpes at ALS - Beamline 10.” ARPES at ALS - Beamline 10, sites.google.com/lbl.gov/bl12-arpes-als/beamline-10. Accessed 21 Nov. 2023.

- [26] Gatton, Averell. “Electron Correlation in the Two-Color Photoionization and Laser Dissociation of H_2^+ .” Auburn University, 2018. <https://etd.auburn.edu/handle/10415/6244>
- [27] Eppink, André T., and David H. Parker. “Velocity map imaging of ions and electrons using electrostatic lenses: Application in photoelectron and Photofragment Ion Imaging of Molecular Oxygen.” *Review of Scientific Instruments*, vol. 68, no. 9, 1997, pp. 3477–3484, <https://doi.org/10.1063/1.1148310>.
- [28] Dörner, R., et al. “Cold target recoil ion momentum spectroscopy: A ‘momentum microscope’ to view Atomic Collision Dynamics.” *Physics Reports*, vol. 330, no. 2–3, 2000, pp. 95–192, [https://doi.org/10.1016/s0370-1573\(99\)00109-x](https://doi.org/10.1016/s0370-1573(99)00109-x).
- [29] Dörner, Reinhard. The Frankfurt Coltrims Movie. *Atomic Physics - COLTRIMS*, 2000, https://www.atom.uni-frankfurt.de/research/10_COLTRIMS/. Accessed 21 Nov. 2023.
- [30] Ladislav Wiza, Joseph. “Microchannel plate detectors.” *Nuclear Instruments and Methods*, vol. 162, no. 1–3, 1979, pp. 587–601, [https://doi.org/10.1016/0029-554x\(79\)90734-1](https://doi.org/10.1016/0029-554x(79)90734-1).
- [31] Beyond CCD - Roentdek.Com, www.roentdek.com/info/Beyond_CCD.pdf. Accessed 22 Nov. 2023.
- [32] Roentdek Handels GmbH - Time and Position Sensitive MCP Delay Line, www.roentdek.com/manuals/MCP%20Delay%20Line%20manual.pdf. Accessed 22 Nov. 2023.
- [33] Wiley, W. C., and I. H. McLaren. “Time-of-flight mass spectrometer with improved resolution.” *Review of Scientific Instruments*, vol. 26, no. 12, 1955, pp. 1150–1157, <https://doi.org/10.1063/1.1715212>.
- [34] Jahnke, Till. “LMF2Root3 in a Nutshell.” 8 June 2019.
- [35] Williams, Joshua. “Imaging Polyatomic Molecules in Three Dimensions Using Molecular Frame Photoelectron Angular Distributions.” Auburn University, 2012. <https://etd.auburn.edu/handle/10415/3127>
- [36] Taylor, John R. *An Introduction to Error Analysis: The Study of Uncertainties in Physical Measurements*. University Science Books, 1997.
- [37] Larsen, Ronald W. *Engineering with Excel*. Pearson Prentice Hall, 2009.
- [38] Heck, Saijoscha. “Photoelectrons in Molecular Fields: An Investigation of Shape Resonances and Electron Retroaction Using Coincident 3D Momentum Imaging Technique.” Max Planck Institut für Kernphysik, Heidelberg, 2017. <https://www.atom.uni-frankfurt.de/publications/files/Heck2017Master.pdf>

Appendices

A Isolation of the vibrational archipelago in the two-color channel

As described in Section 5.3, vibrational states dissociating via the two-color channel form islands that appear on a diagonal line with a slope of -1, obeying the following energy sum relation:

$$E_{sum} = KER + E_e = h\nu_{VUV} + h\nu_{NIR} - E_{diss}$$

The full vibrational archipelagos isolated by a diagonal cut with a -1 slope for for each dataset are shown below.

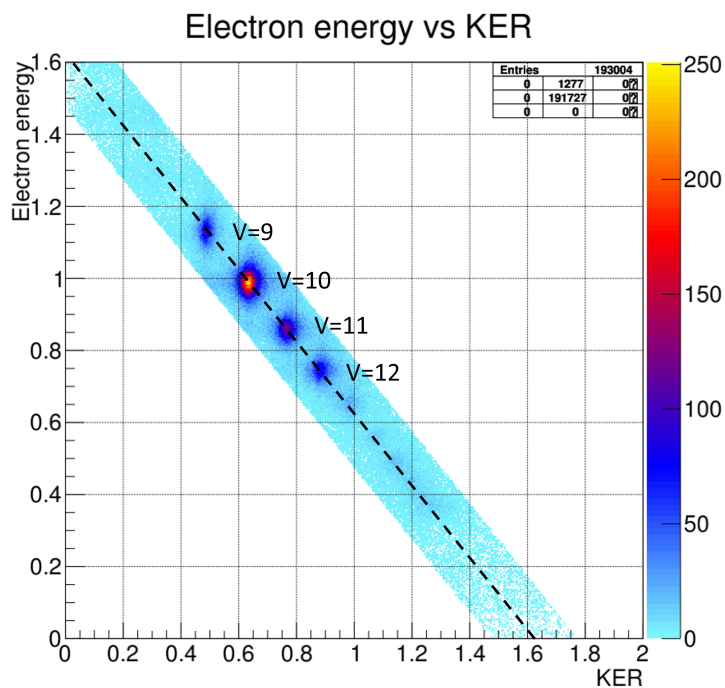


Figure A.1: Full vibrational archipelago of events dissociating via the two-color channel in the short-delay 18.54 eV H_2 dataset.

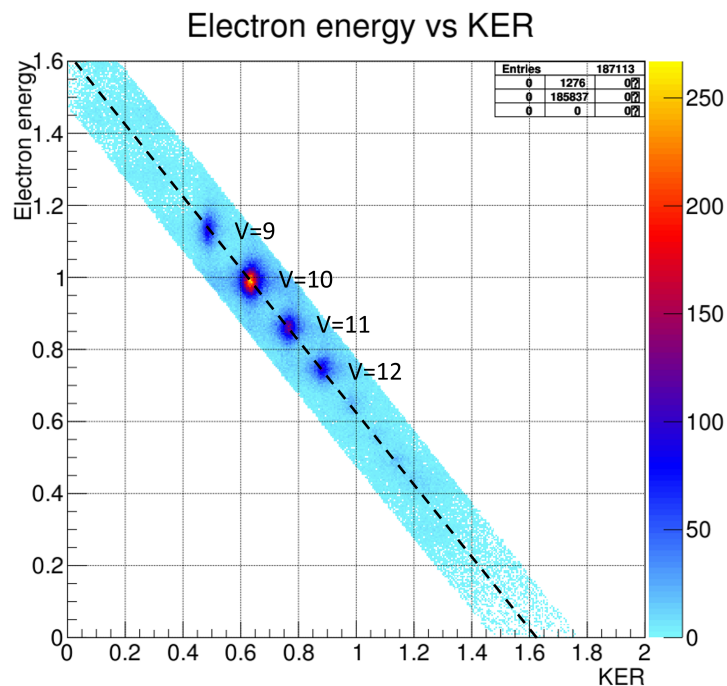


Figure A.2: Full vibrational archipelago of events dissociating via the two-color channel in the long-delay 18.54 eV H_2 dataset.

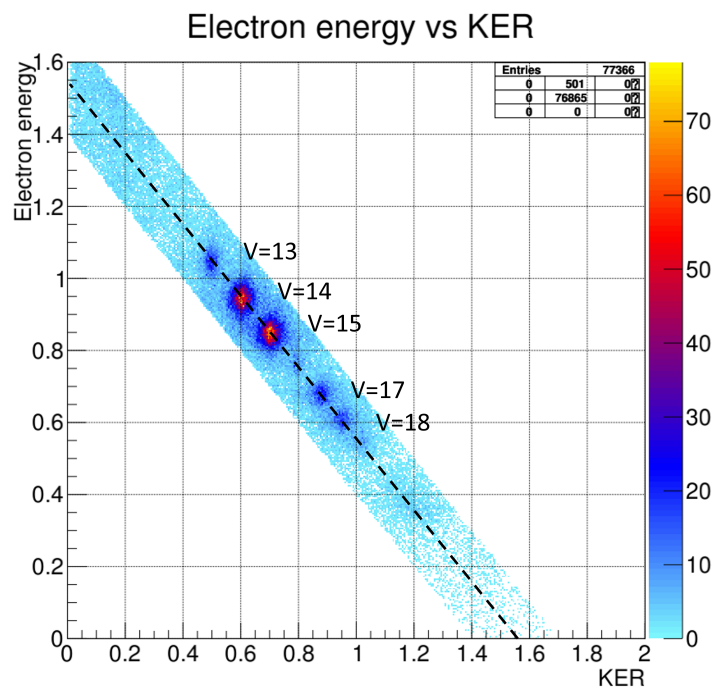


Figure A.3: Full vibrational archipelago of events dissociating via the two-color channel in the 18.54 eV D_2 dataset.

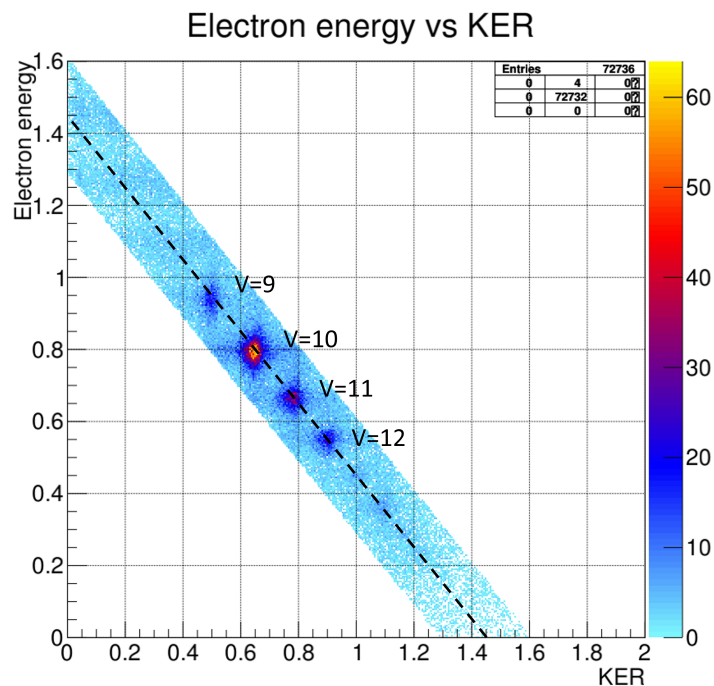


Figure A.4: Full vibrational archipelago of events dissociating via the two-color channel in the 18.34 eV H_2 dataset.

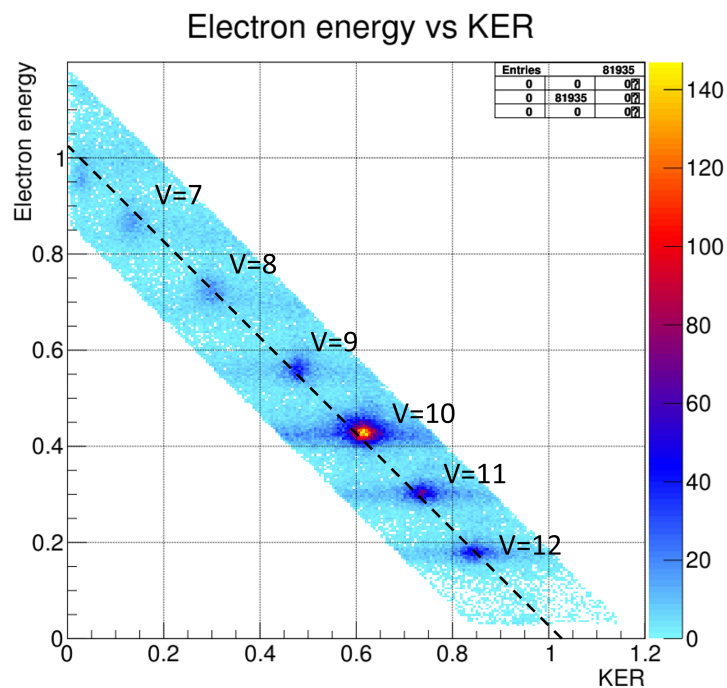


Figure A.5: Full vibrational archipelago of events dissociating via the two-color channel in the short-delay 17.9 eV H_2 dataset.

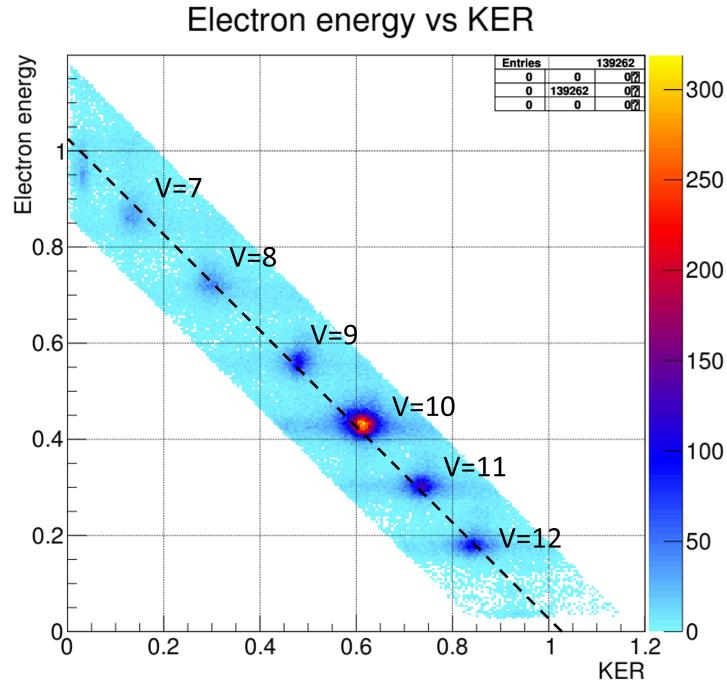


Figure A.6: Full vibrational archipelago of events dissociating via the two-color channel in the long-delay 17.9 eV H_2 dataset.

B Two-color calibration spectra

The calibration procedure described in Section 4.1 was repeated for each dataset. The calibration spectra for each dataset, showing the symmetry of the lab frame momentum sphere, is shown in the figures below.

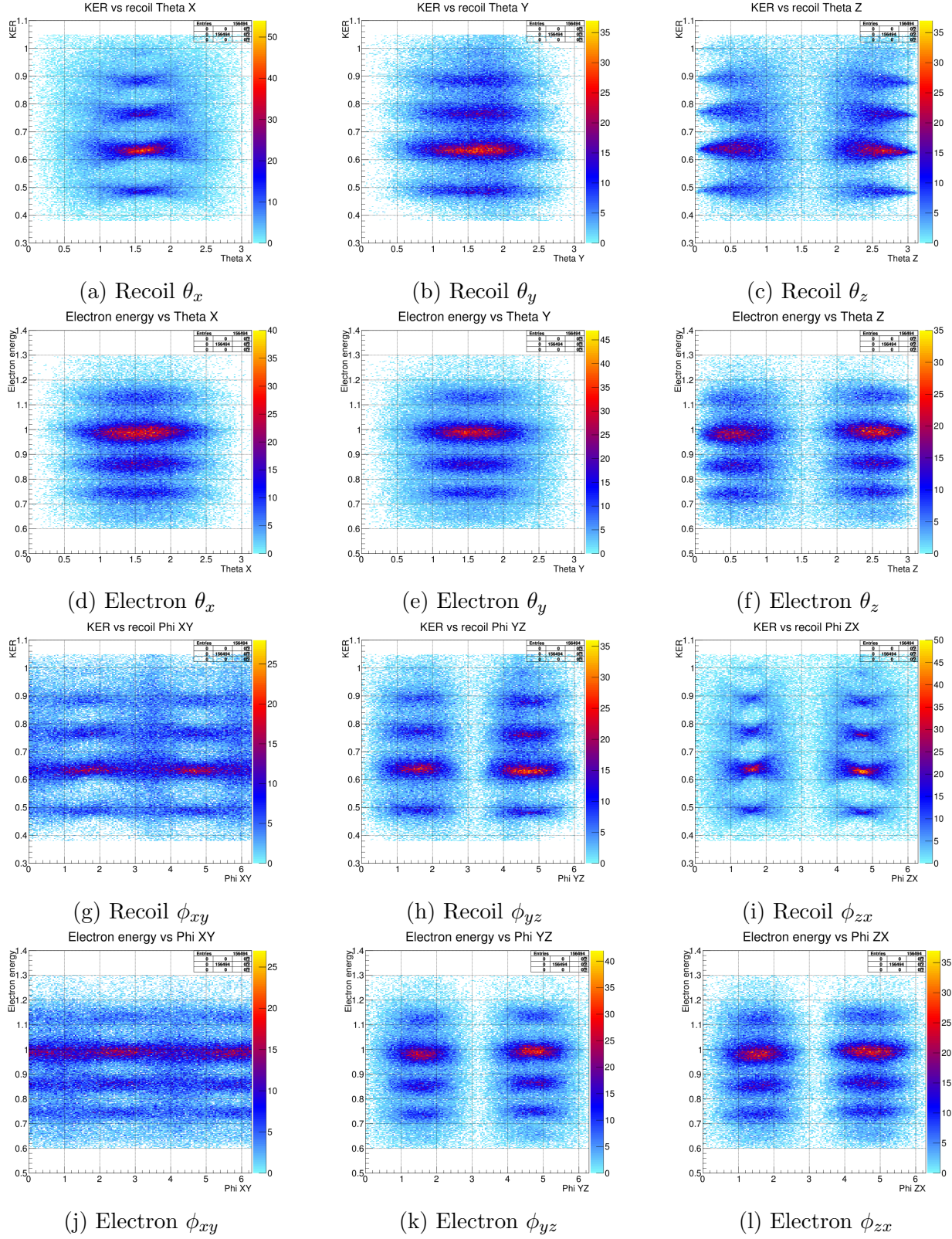


Figure B.1: Recoil ion and electron θ and ϕ calibration plots for the 18.54 eV short delay H_2 dataset.

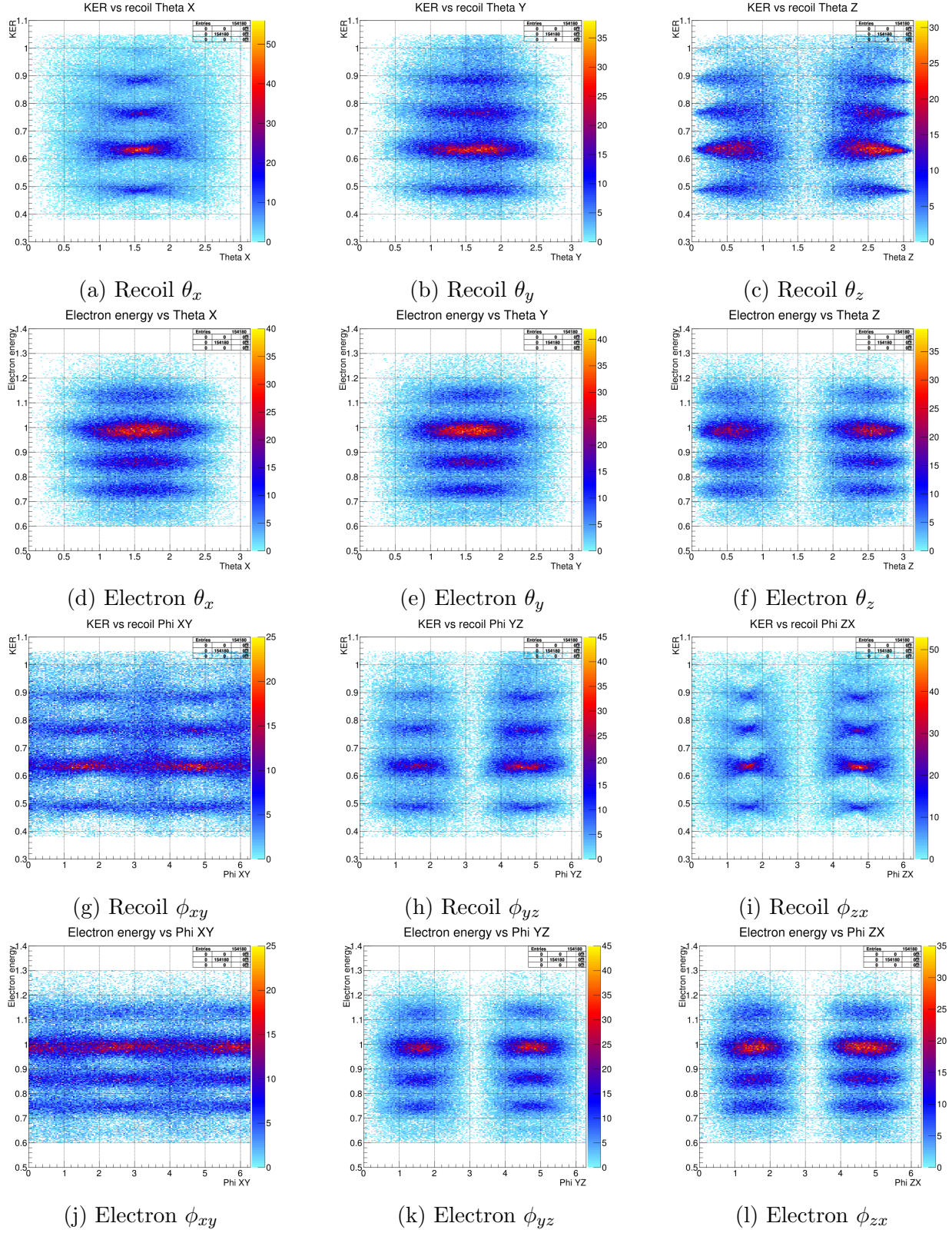


Figure B.2: Recoil ion and electron θ and ϕ calibration plots for the 18.54 eV long delay H_2 dataset.

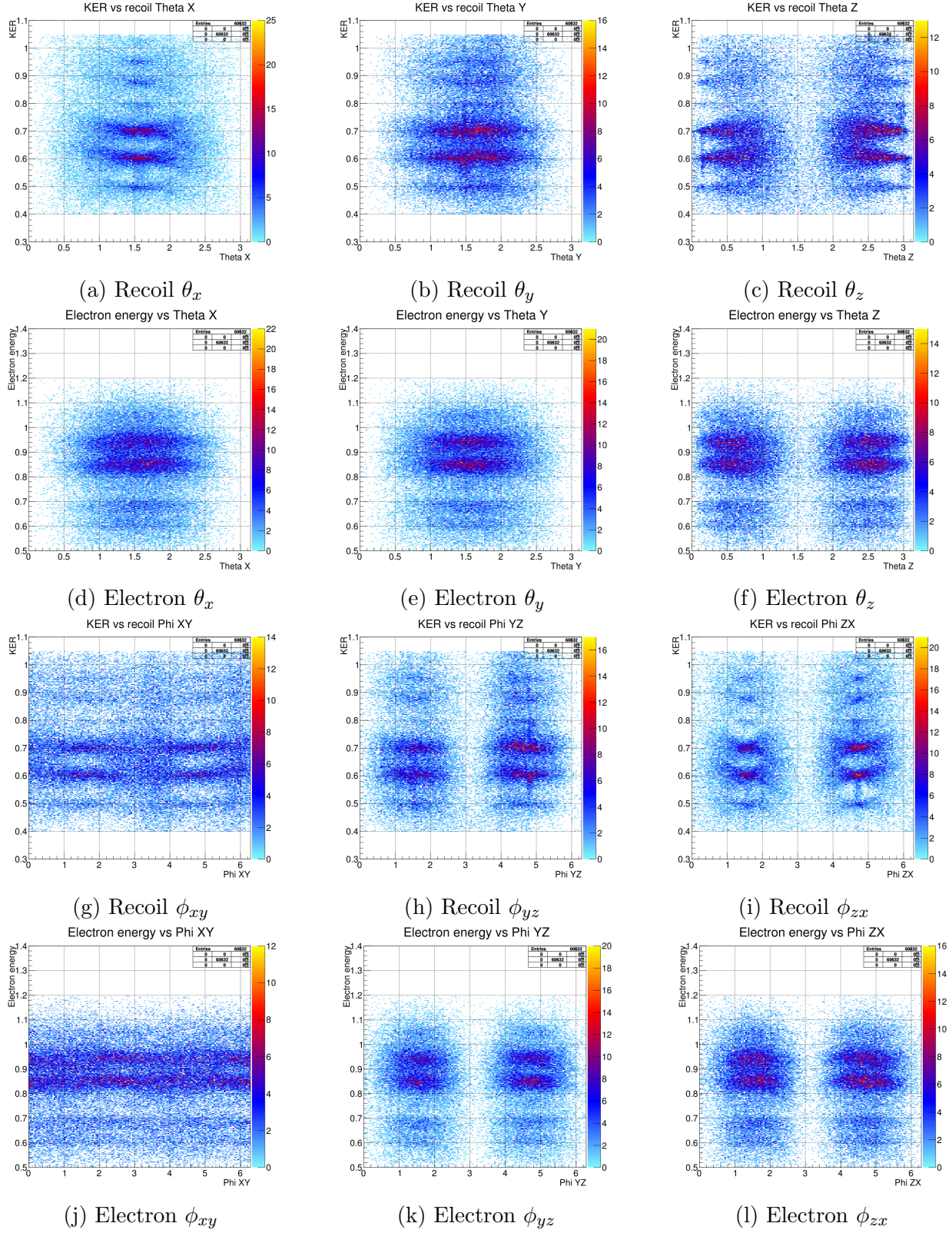


Figure B.3: Recoil ion and electron θ and ϕ calibration plots for the 18.54 eV D_2 dataset.

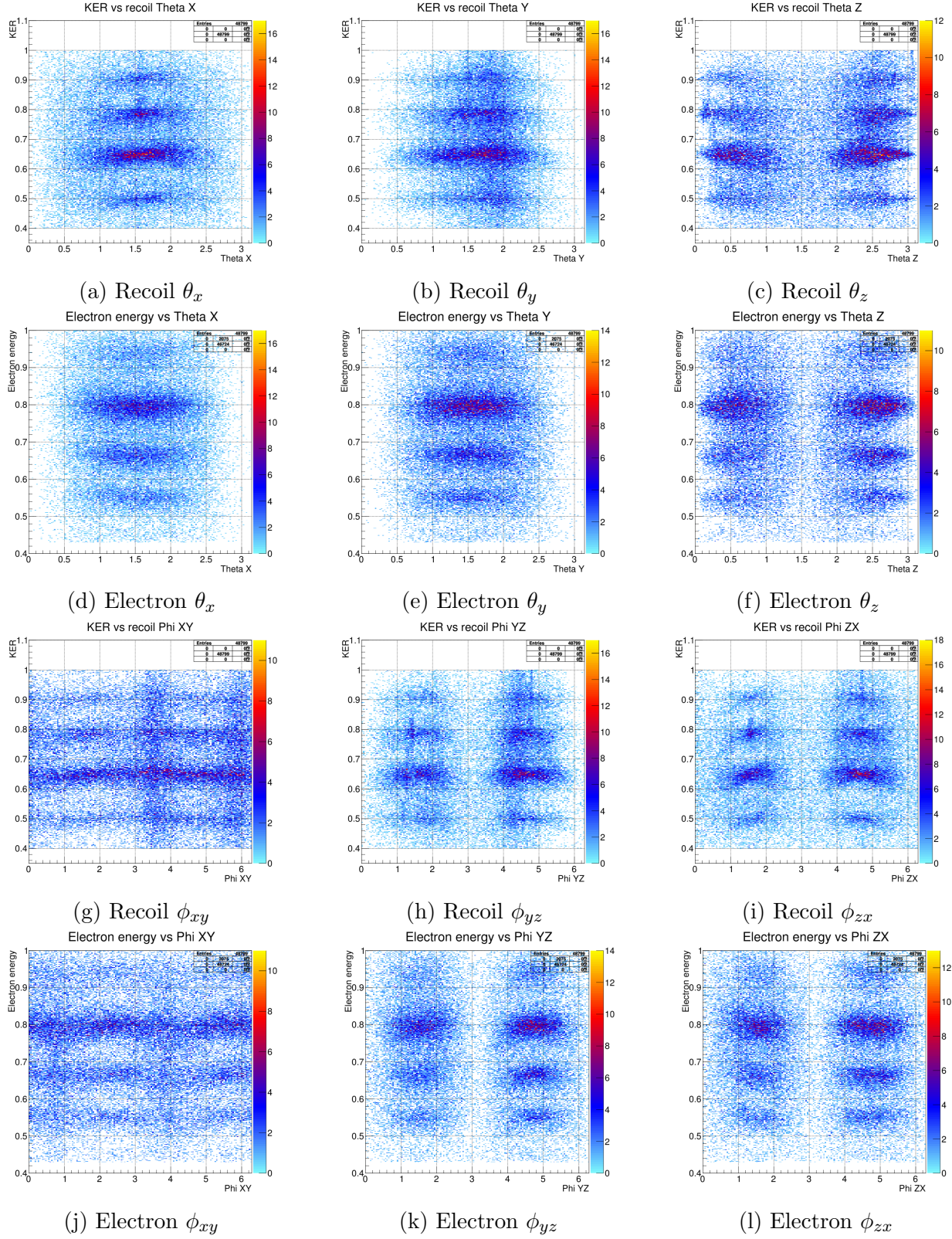


Figure B.4: Recoil ion and electron θ and ϕ calibration plots for the 18.34 eV H_2 dataset.

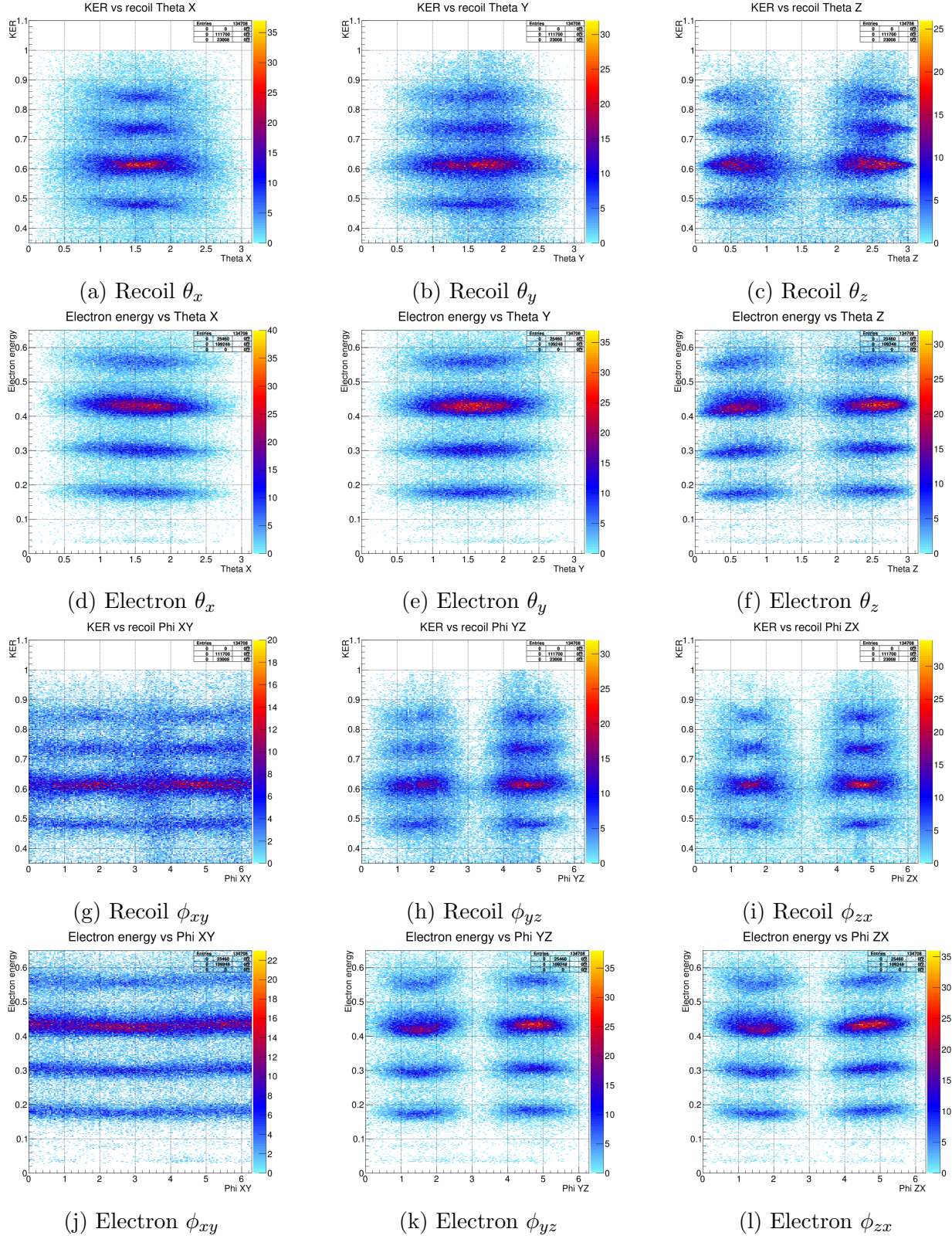


Figure B.5: Recoil ion and electron θ and ϕ calibration plots for the 17.9 eV long delay H_2 dataset.

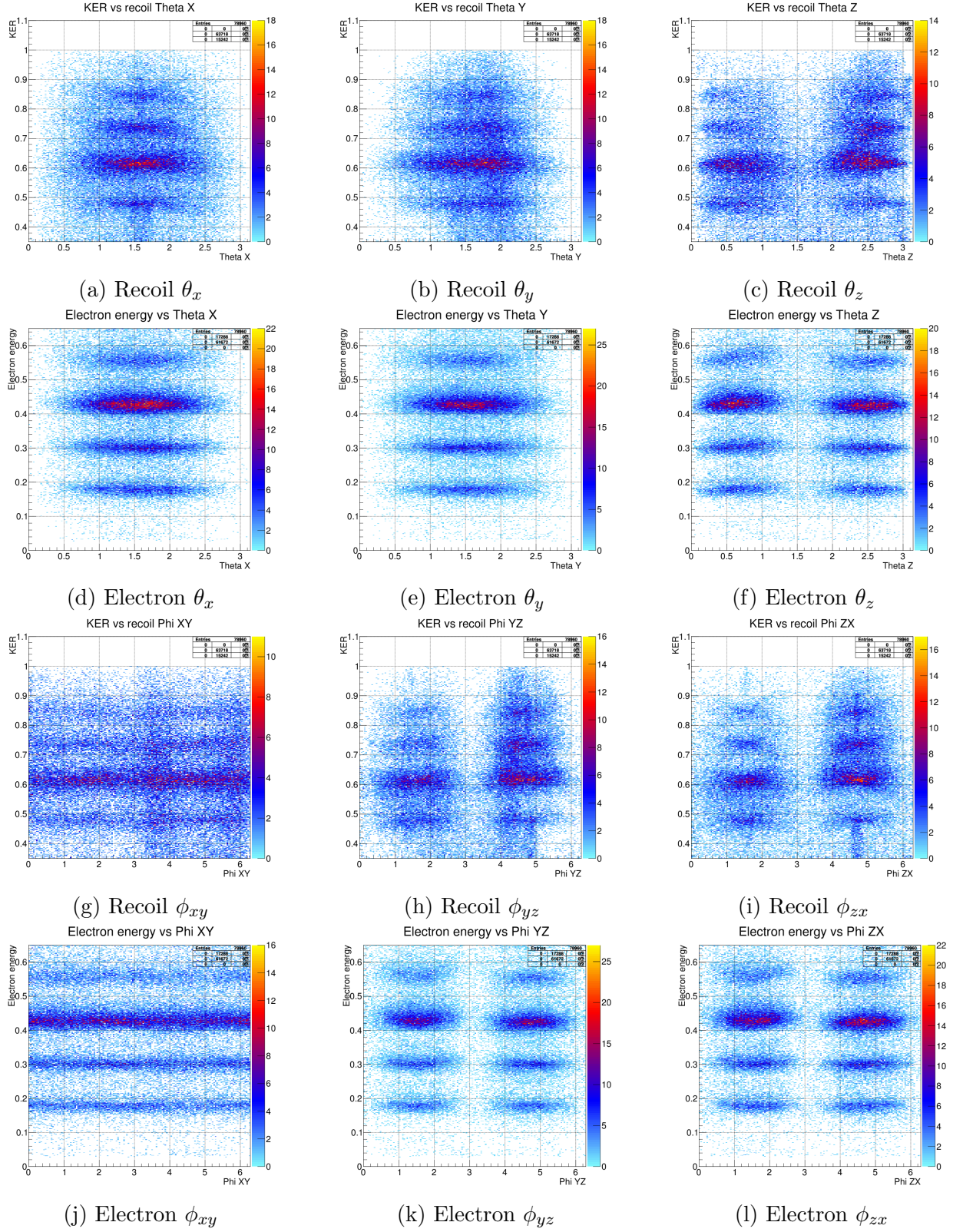


Figure B.6: Recoil ion and electron θ and ϕ calibration plots for the 17.9 eV short delay H_2 dataset.

C One-dimensional MFPADs

The MFPADs presented in this work have, for the most part, been projected in angular coordinates and mirrored about the horizontal axis for easier visualization. The MFPAD can also be plotted as a one-dimensional histogram of the cosine of the angle between the molecular axis and the electron momentum vector. These one-dimensional MFPADs are shown below.

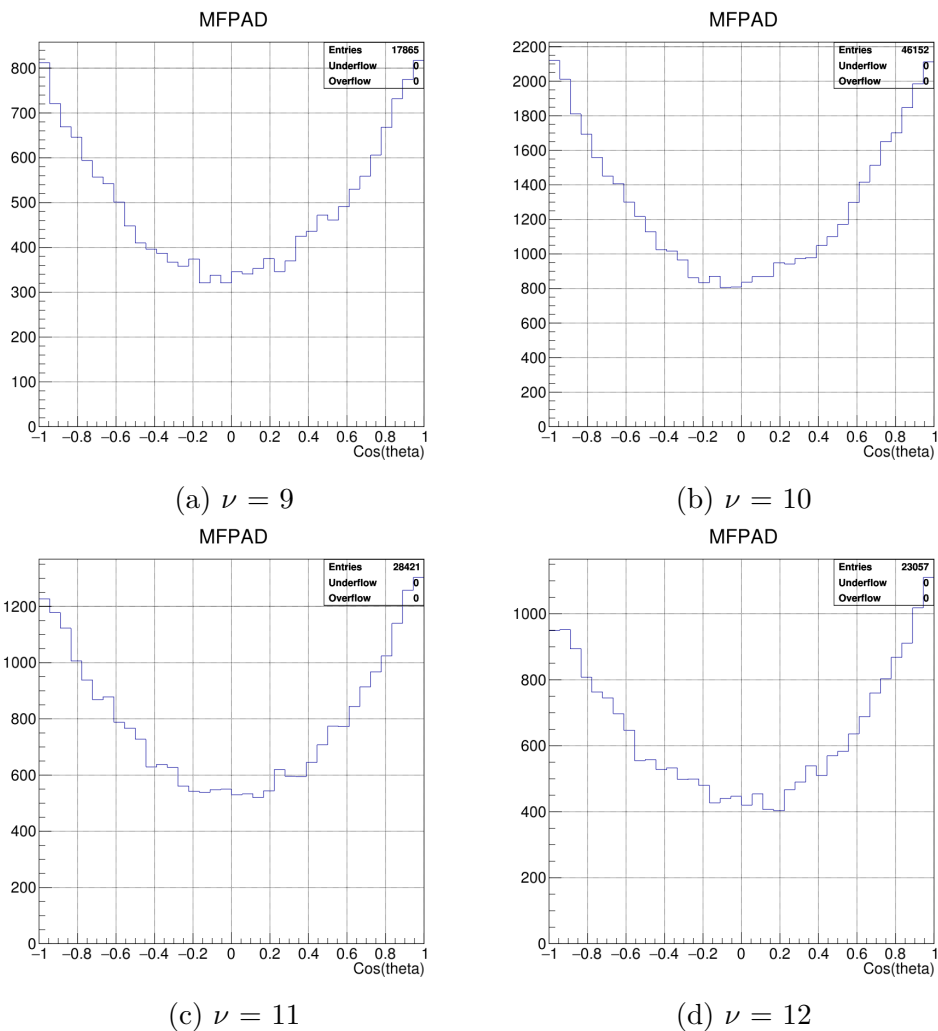
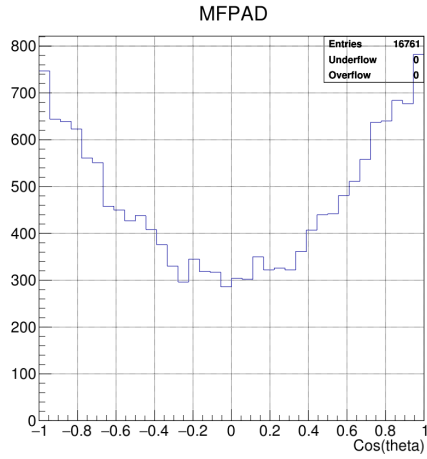
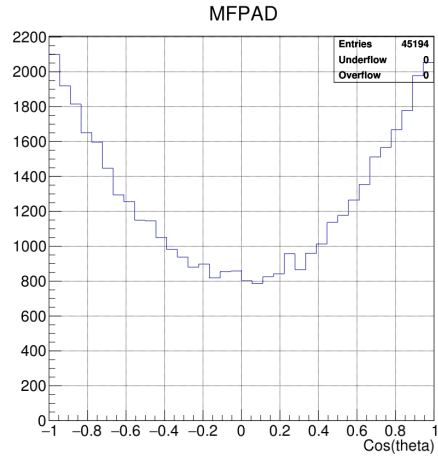


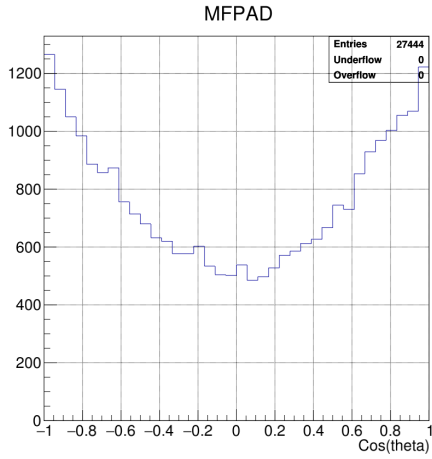
Figure C.1: One-dimensional MFPADs for states dissociating via the two-color channel for the short delay 18.54 eV H_2 dataset.



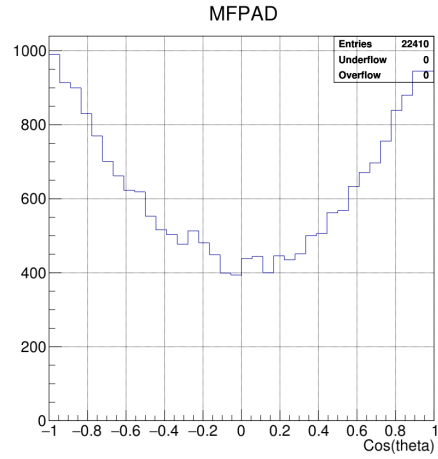
(a) $\nu = 9$



(b) $\nu = 10$

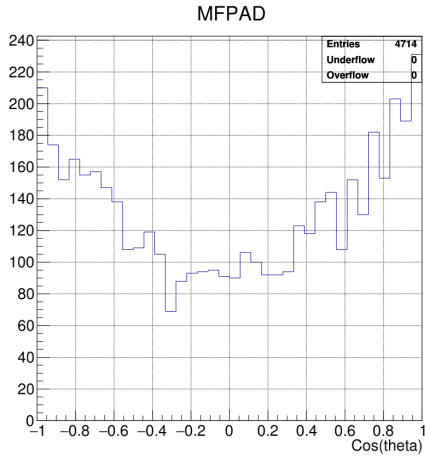


(c) $\nu = 11$

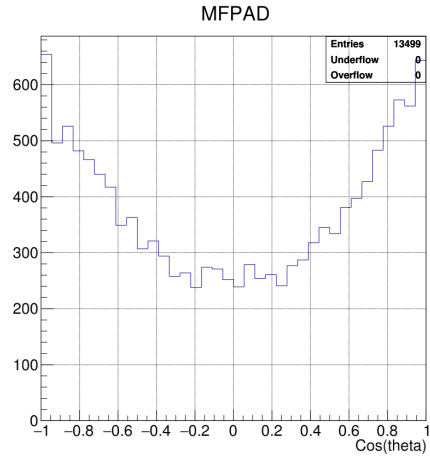


(d) $\nu = 12$

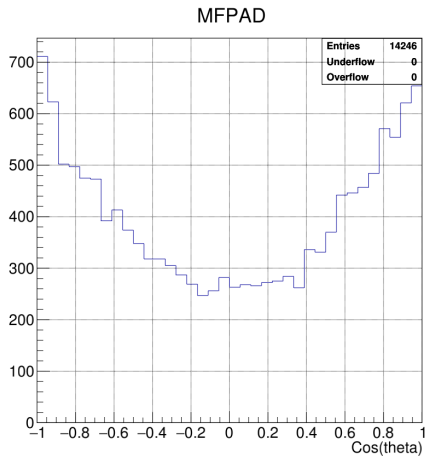
Figure C.2: One-dimensional MFPADs for states dissociating via the two-color channel for the long delay 18.54 eV H_2 dataset.



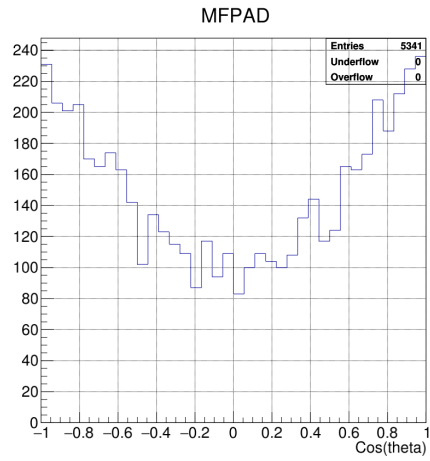
(a) $\nu = 13$



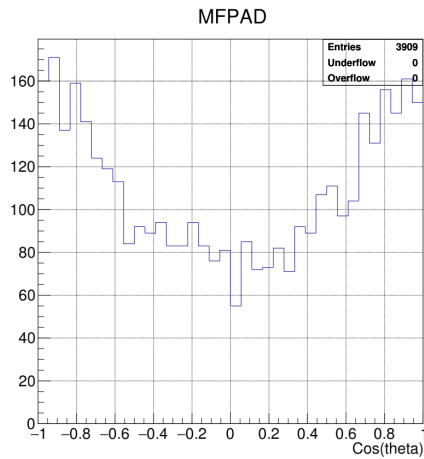
(b) $\nu = 14$



(c) $\nu = 15$

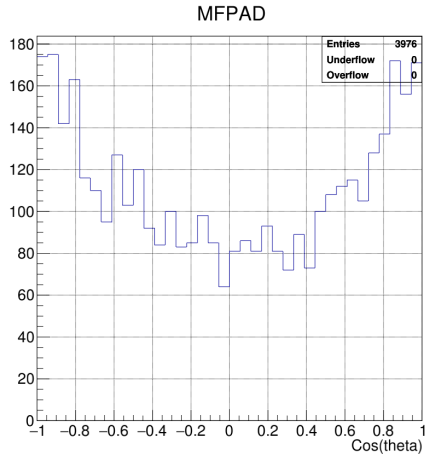


(d) $\nu = 17$

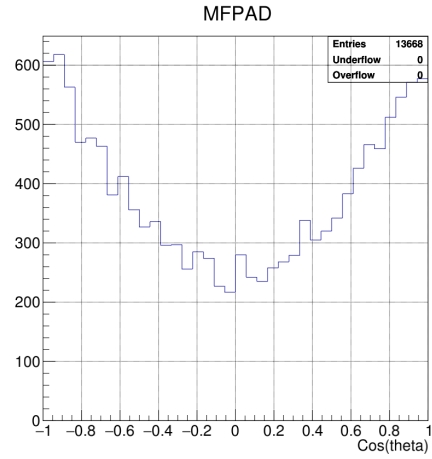


(e) $\nu = 18$

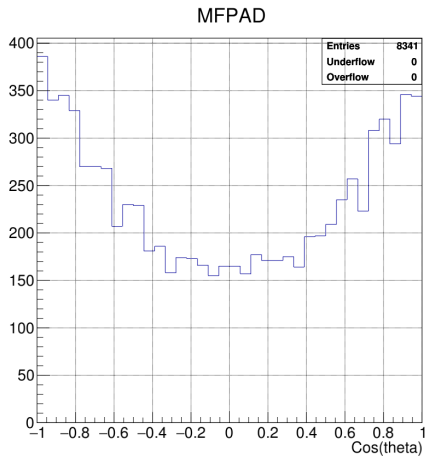
Figure C.3: One-dimensional MFPADs for states dissociating via the two-color channel for the 18.54 eV D_2 dataset.



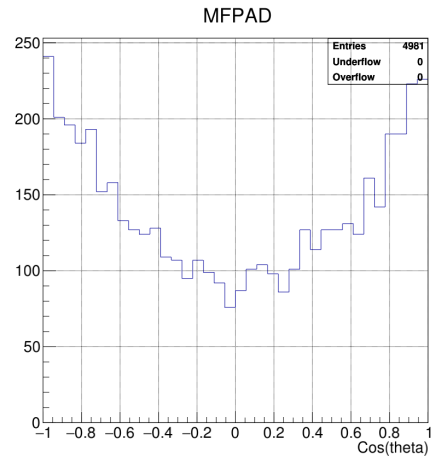
(a) $\nu = 9$



(b) $\nu = 10$

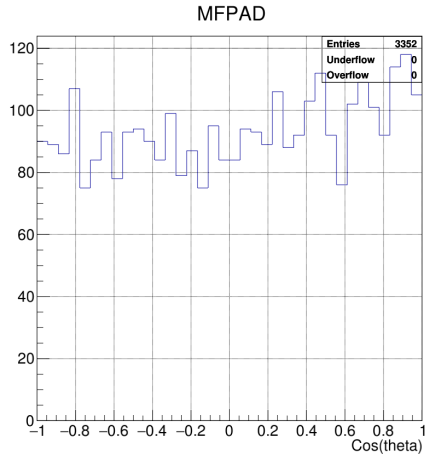


(c) $\nu = 11$

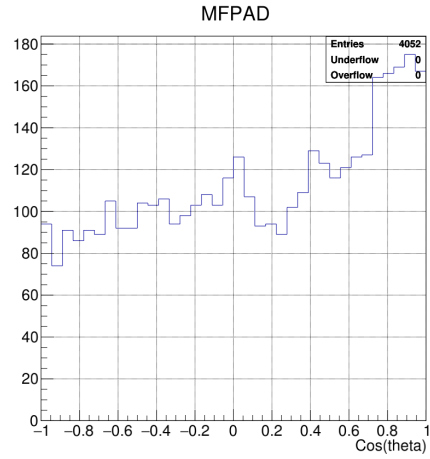


(d) $\nu = 12$

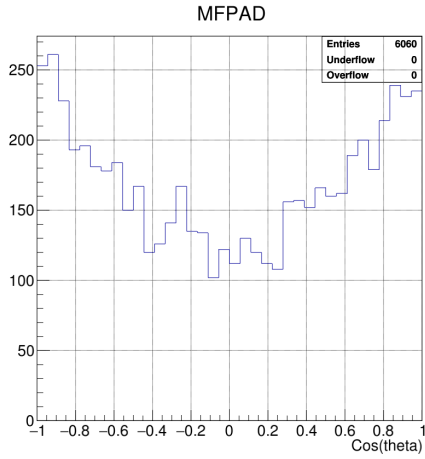
Figure C.4: One-dimensional MFPADs for states dissociating via the two-color channel for the 18.34 eV H_2 dataset.



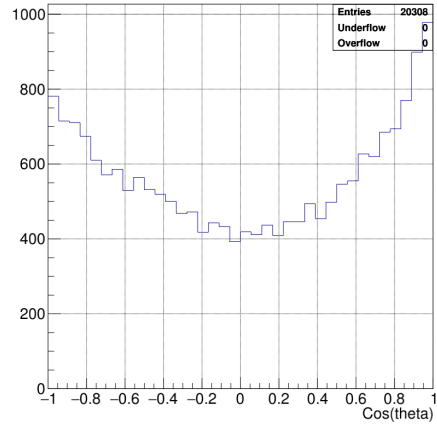
(a) $\nu = 7$



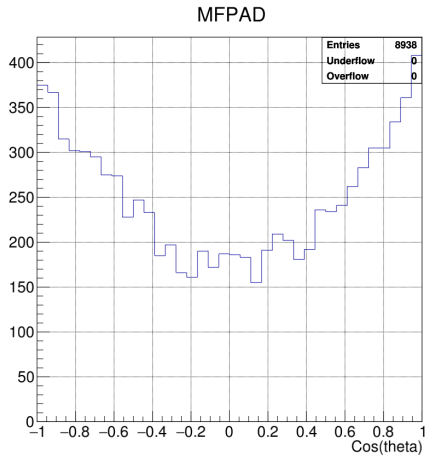
(b) $\nu = 8$



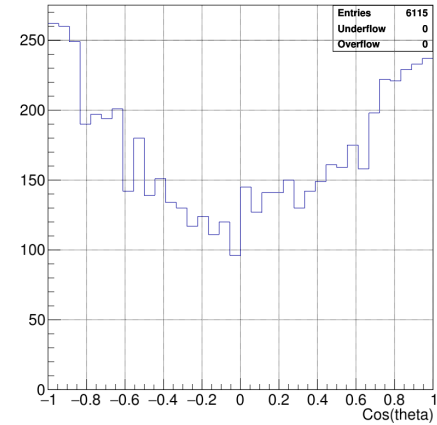
(c) $\nu = 9$



(d) $\nu = 10$

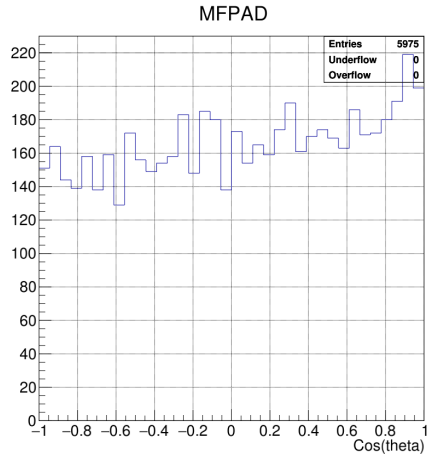


(e) $\nu = 11$

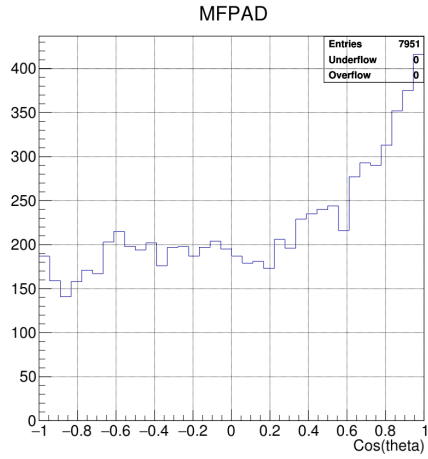


(f) $\nu = 12$

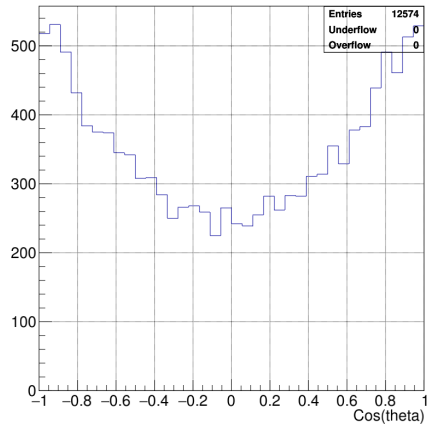
Figure C.5: One-dimensional MFPADs for states dissociating via the two-color channel for the short delay 17.9 eV H_2 dataset.



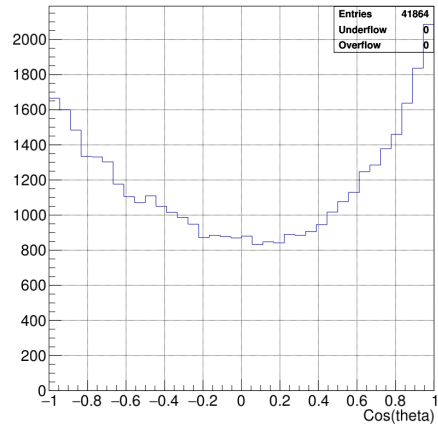
(a) $\nu = 7$
MFPAD



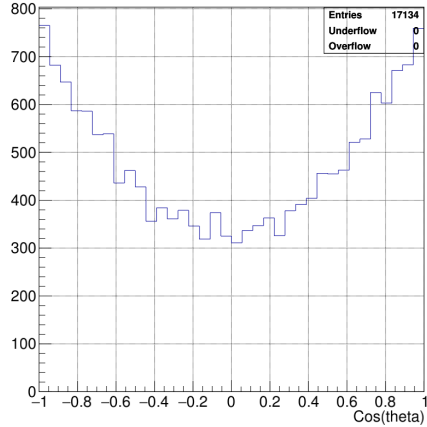
(b) $\nu = 8$
MFPAD



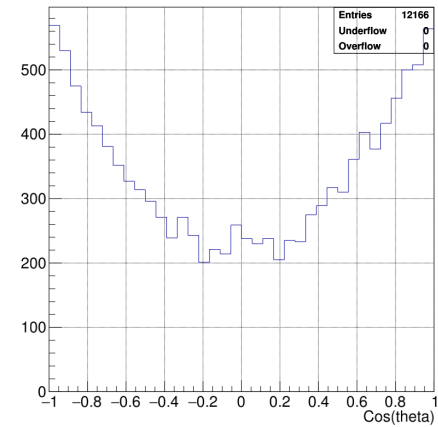
(c) $\nu = 9$
MFPAD



(d) $\nu = 10$
MFPAD



(e) $\nu = 11$
MFPAD



(f) $\nu = 12$
MFPAD

Figure C.6: One-dimensional MFPADs for states dissociating via the two-color channel for the long delay 17.9 eV H_2 dataset.

D Recoil ion θ_z distributions

The angle between the molecular axis (defined by the recoil ion momentum vector) and the polarization of the incident VUV and NIR radiation (horizontally polarized along the lab-frame z direction) is defined as the recoil ion θ_z angle. The distribution of these angles is shown below for two-color vibrational states.

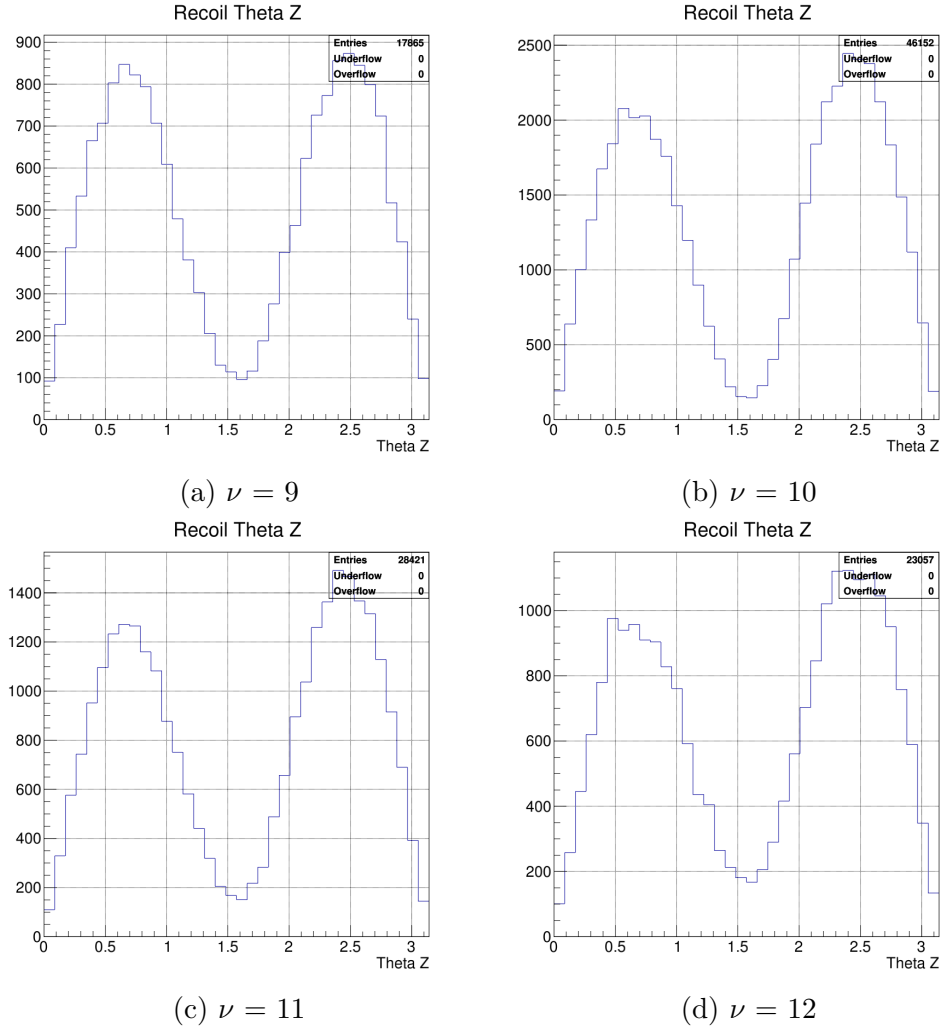
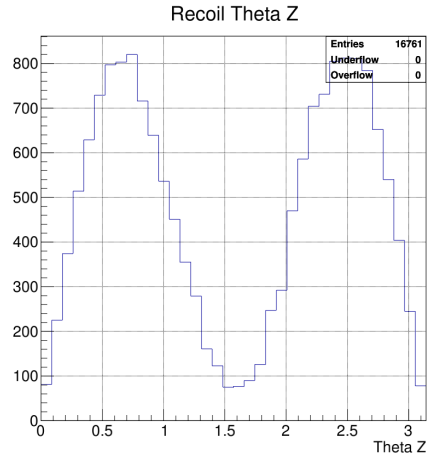
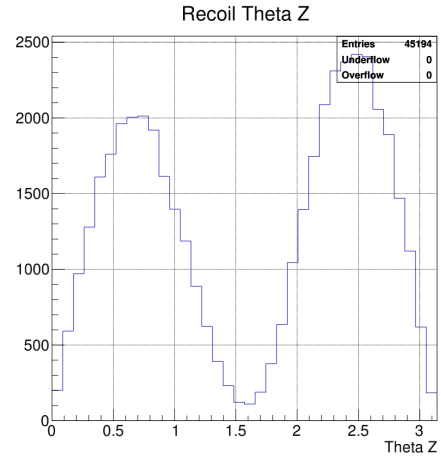


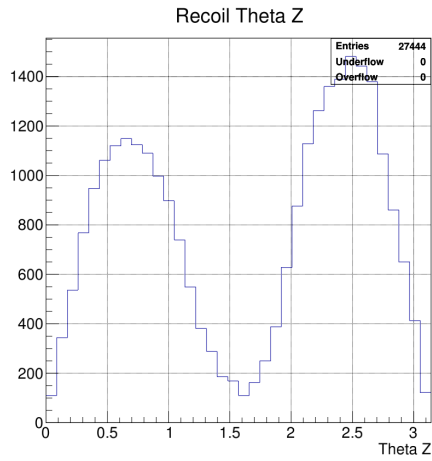
Figure D.1: Recoil ion θ_z distributions for states dissociating via the two-color channel for the short delay 18.54 eV H_2 dataset.



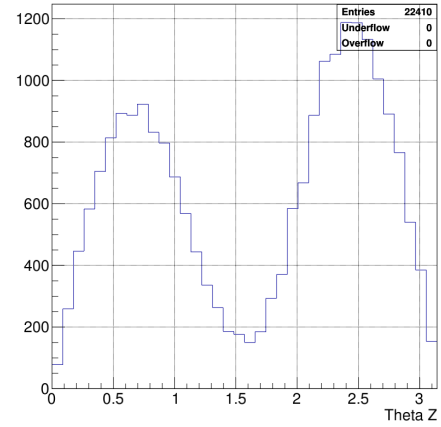
(a) $\nu = 9$



(b) $\nu = 10$

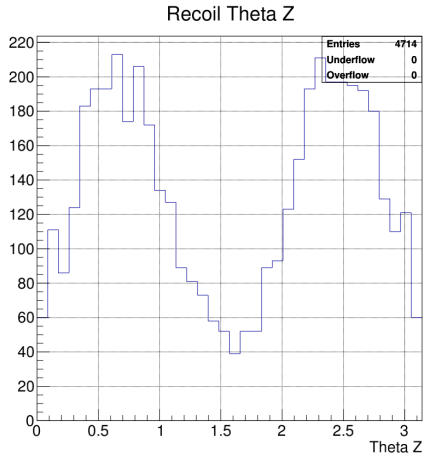


(c) $\nu = 11$

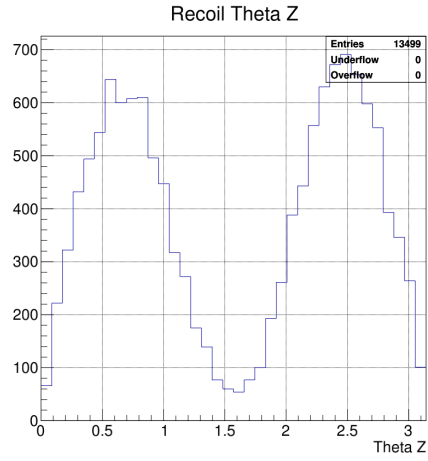


(d) $\nu = 12$

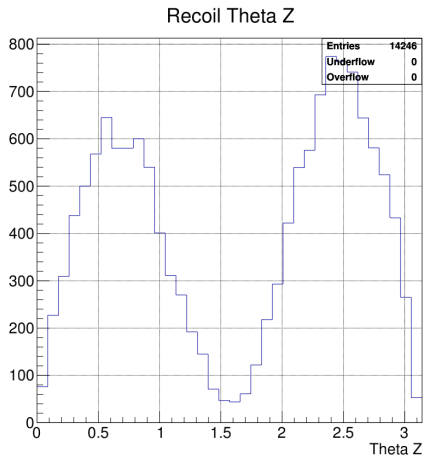
Figure D.2: Recoil ion θ_z distributions for states dissociating via the two-color channel for the long delay 18.54 eV H_2 dataset.



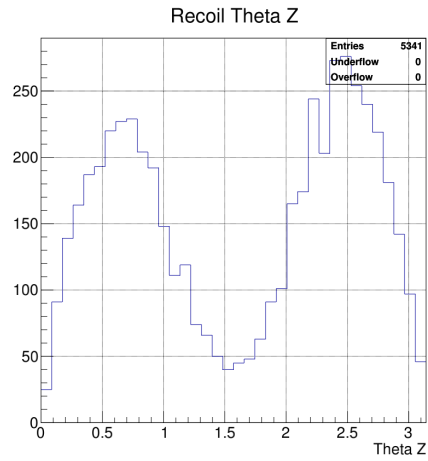
(a) $\nu = 13$



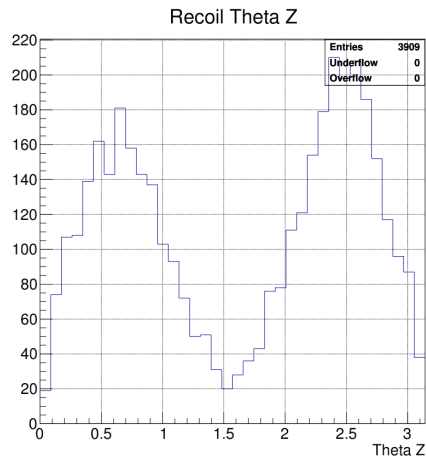
(b) $\nu = 14$



(c) $\nu = 15$

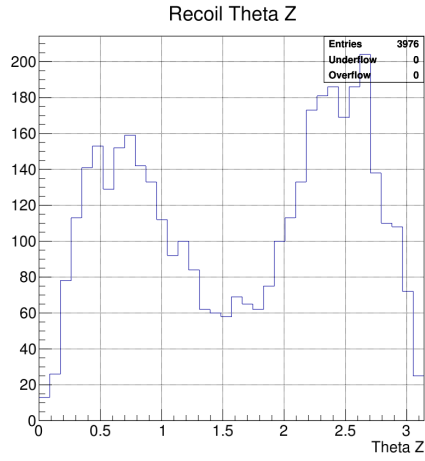


(d) $\nu = 17$

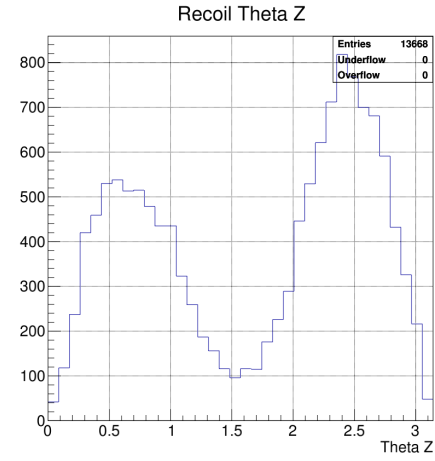


(e) $\nu = 18$

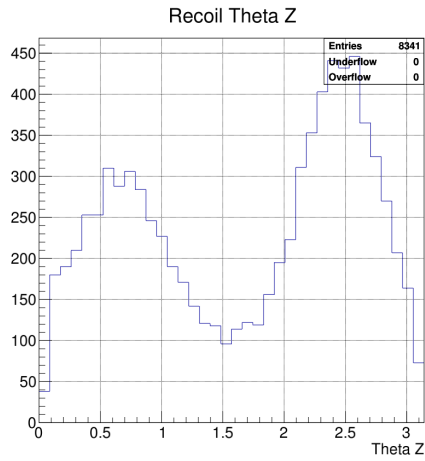
Figure D.3: Recoil ion θ_z distributions for states dissociating via the two-color channel for the 18.54 eV D_2 dataset.



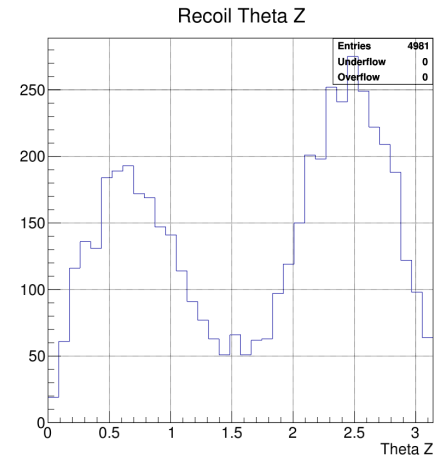
(a) $\nu = 9$



(b) $\nu = 10$

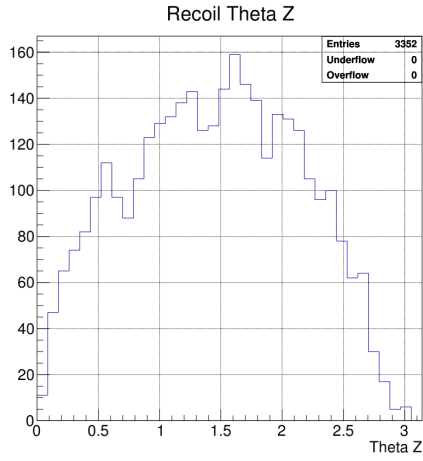


(c) $\nu = 11$

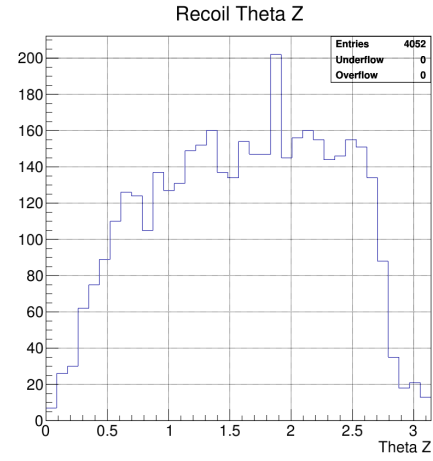


(d) $\nu = 12$

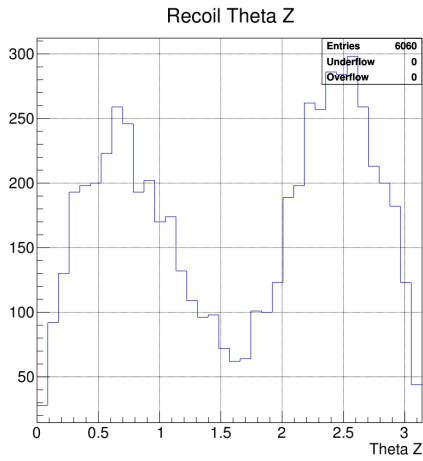
Figure D.4: Recoil ion θ_z distributions for states dissociating via the two-color channel for the 18.34 eV H_2 dataset.



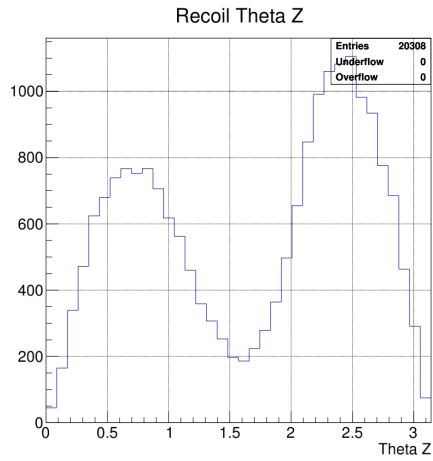
(a) $\nu = 7$



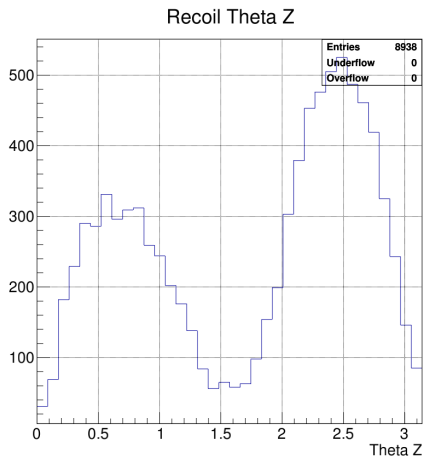
(b) $\nu = 8$



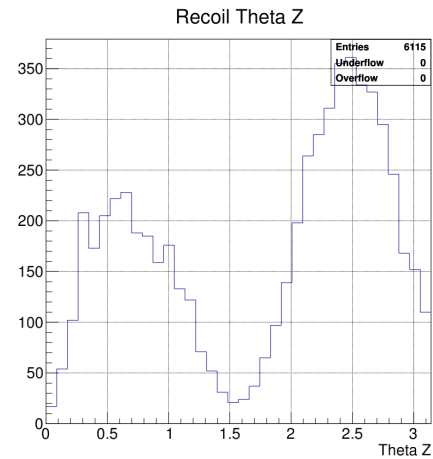
(c) $\nu = 9$



(d) $\nu = 10$

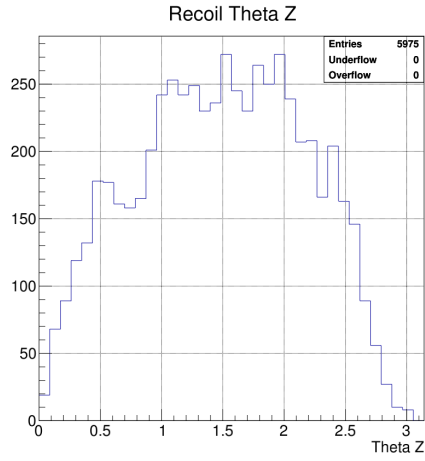


(e) $\nu = 11$

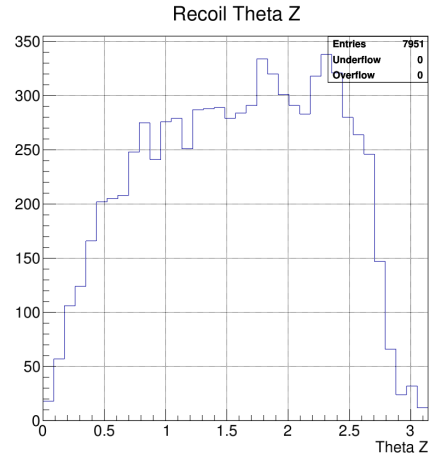


(f) $\nu = 12$

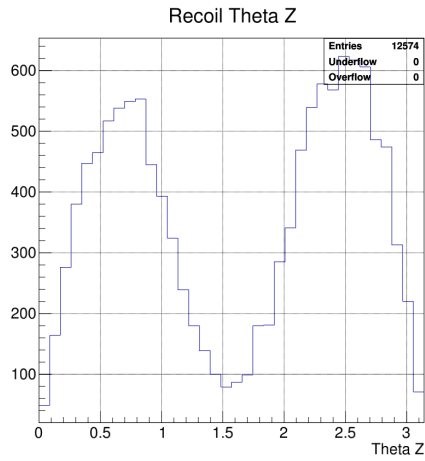
Figure D.5: Recoil ion θ_z distributions for states dissociating via the two-color channel for the short delay 17.9 eV H_2 dataset.



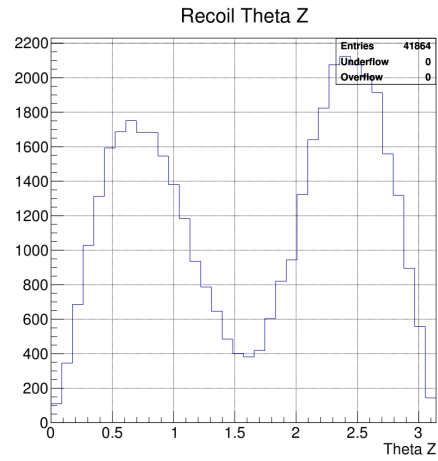
(a) $\nu = 7$



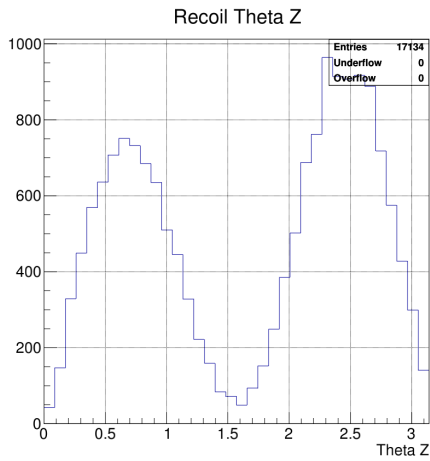
(b) $\nu = 8$



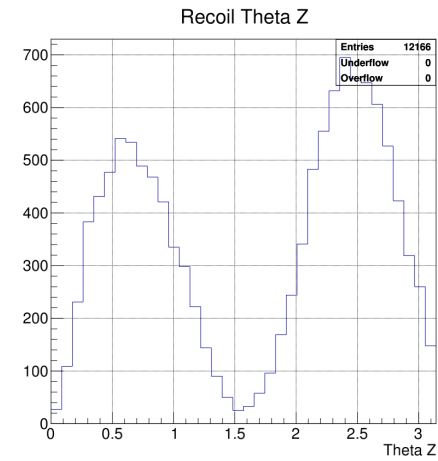
(c) $\nu = 9$



(d) $\nu = 10$



(e) $\nu = 11$



(f) $\nu = 12$

Figure D.6: Recoil ion θ_z distributions for states dissociating via the two-color channel for the long delay 17.9 eV H_2 dataset.

E Recoil ion θ_z vs MFPAD plots

The relationship between the MFPAD and the angle between the polarization axis and the molecular axis can be seen by plotting the recoil ion θ_z angle vs the MFPAD. These plots are shown below.

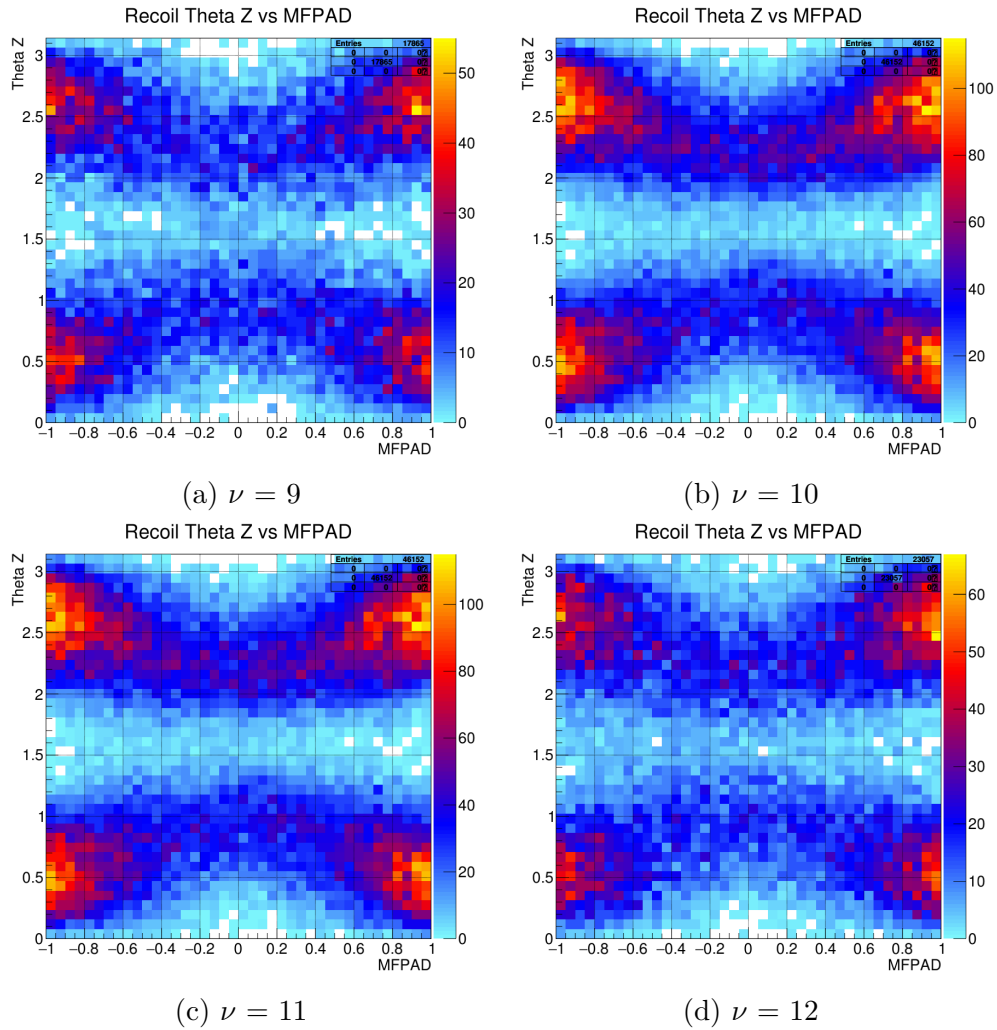


Figure E.1: Recoil ion θ_z vs MFPAD plots for states dissociating via the two-color channel for the short delay 18.54 eV H_2 dataset.

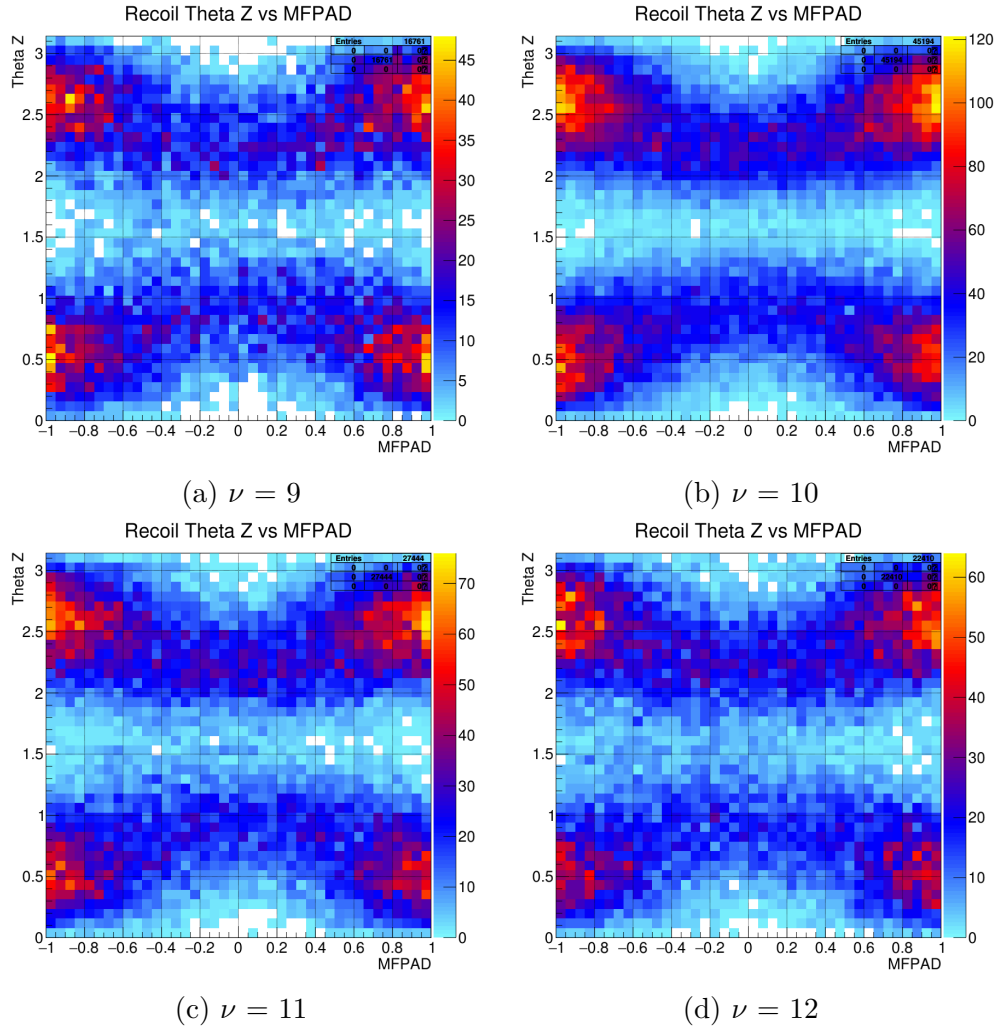


Figure E.2: Recoil ion θ_z vs MFPAD plots for states dissociating via the two-color channel for the long delay 18.54 eV H_2 dataset.

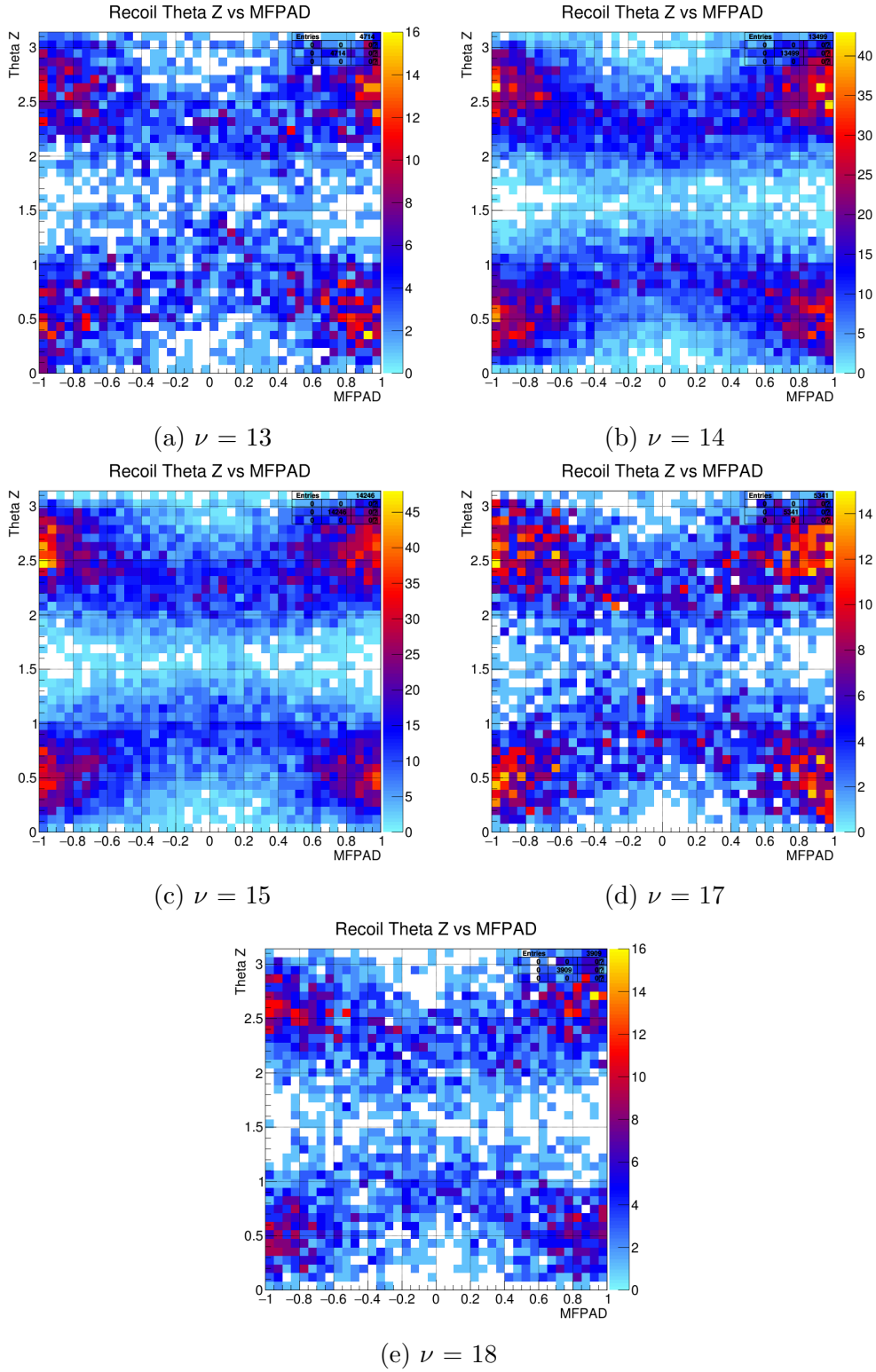


Figure E.3: Recoil ion θ_z vs MFPAD plots for states dissociating via the two-color channel for the 18.54 eV D_2 dataset.

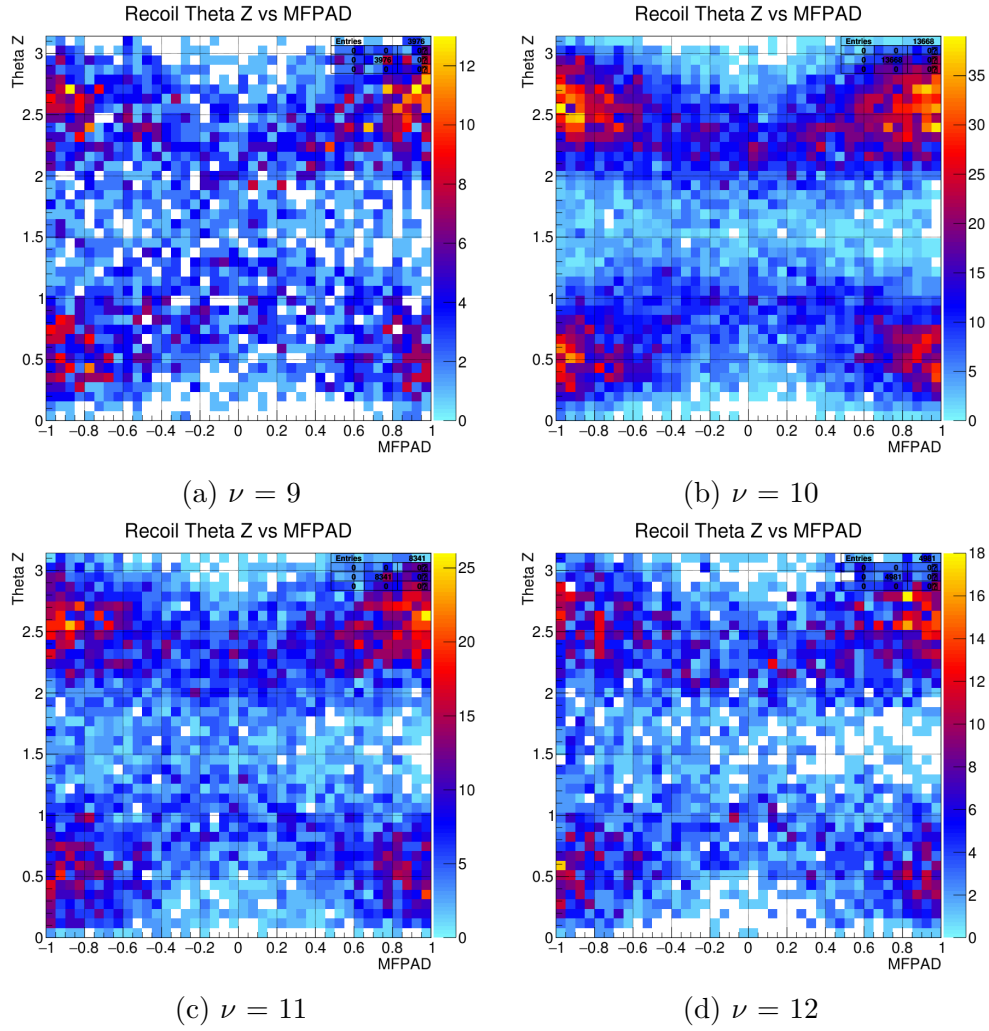


Figure E.4: Recoil ion θ_z vs MFPAD plots for states dissociating via the two-color channel for the 18.34 eV H_2 dataset.

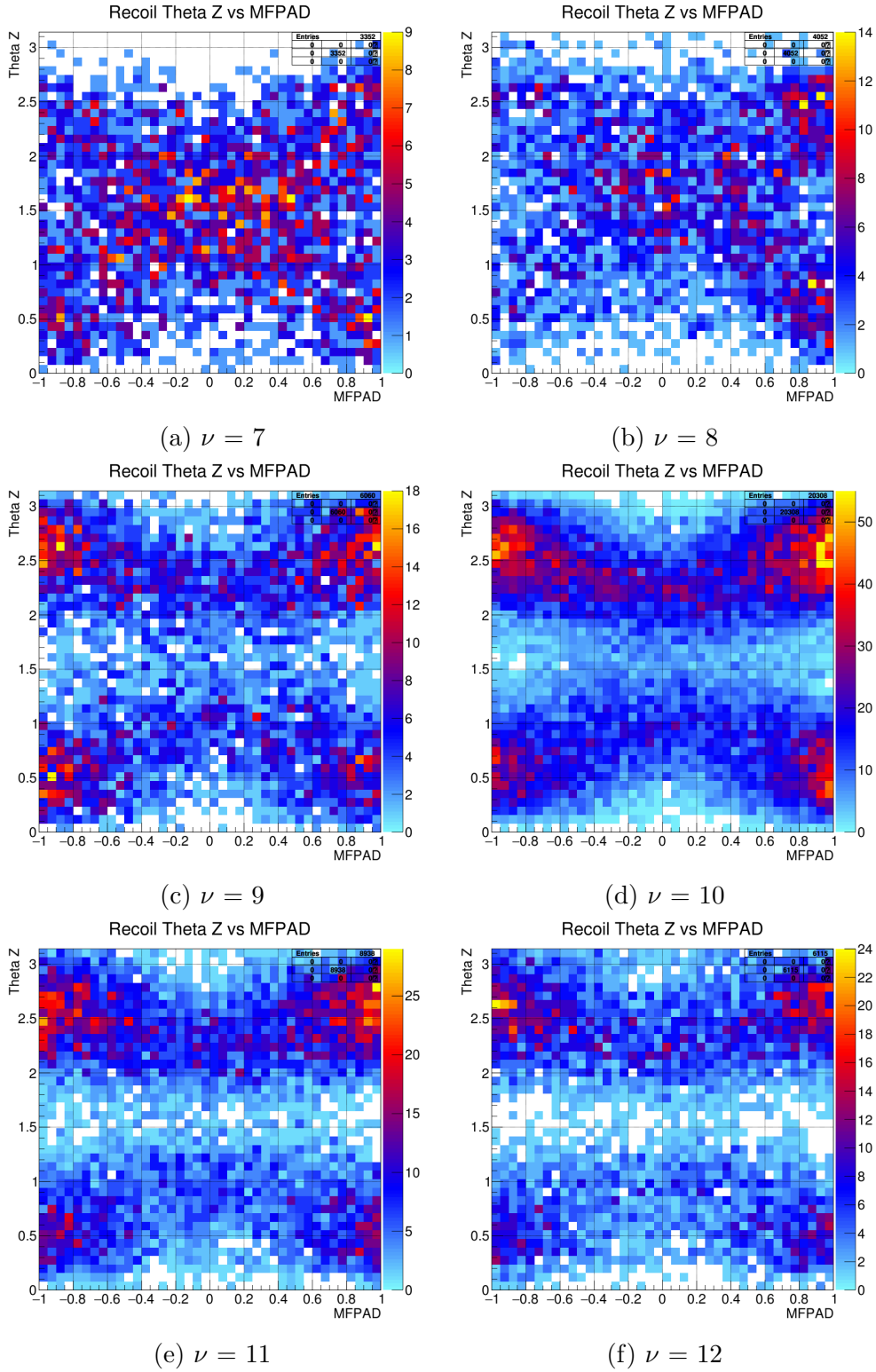


Figure E.5: Recoil ion θ_z vs MFPAD plots for states dissociating via the two-color channel for the short delay 17.9 eV H_2 dataset.

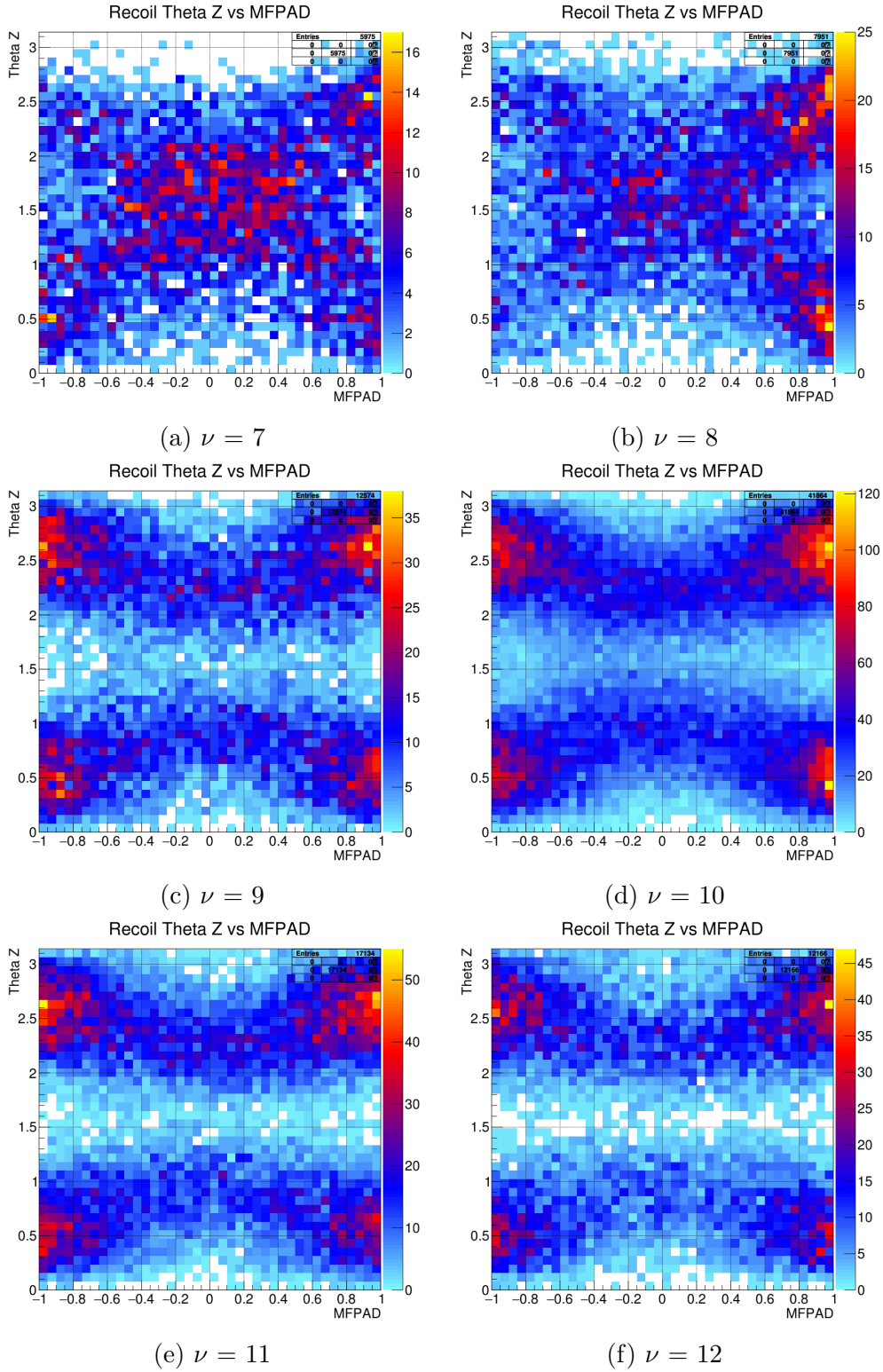


Figure E.6: Recoil ion θ_z vs MFPAD plots for states dissociating via the two-color channel for the long delay 17.9 eV H_2 dataset.

F 17.9 eV vibrational state $\nu=6$

The $\nu=6$ vibrational state is very faint and barely visible, but appears to be present in the 17.9 eV H_2^+ data. The statistics for this state are very low, and as such the analysis performed was limited. However, the presence of any dissociation from this state still may be of interest, and as such the following plots are included.

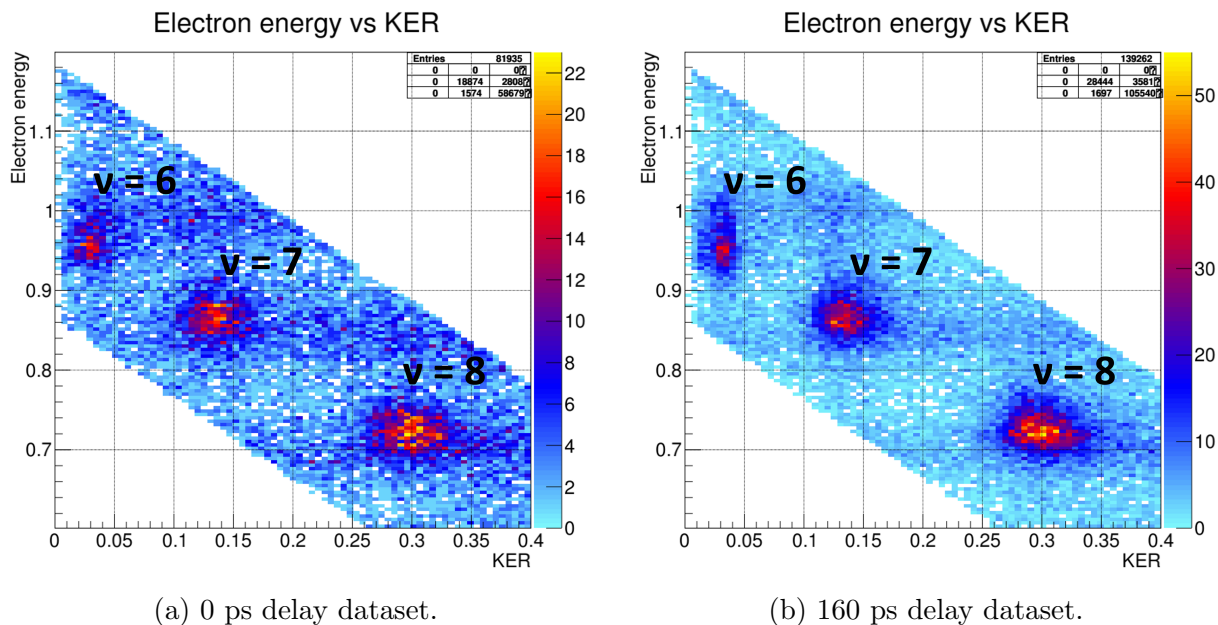
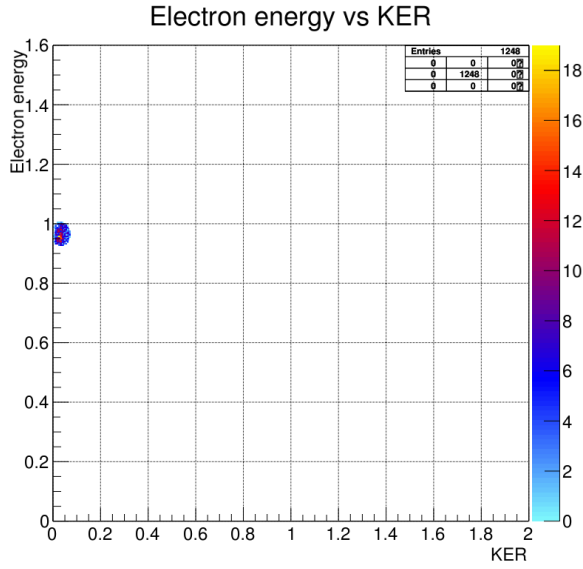
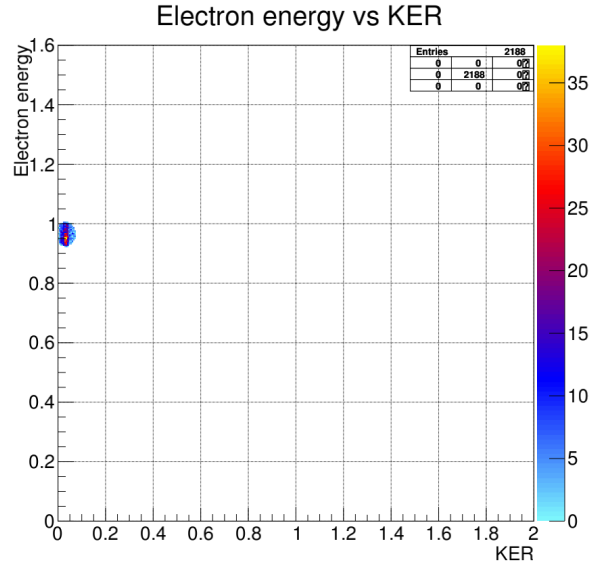


Figure F.1: Zoomed-in vibrational archipelago displaying states $\nu=6$, $\nu=7$, and $\nu=8$ for 17.9 eV H_2^+ .

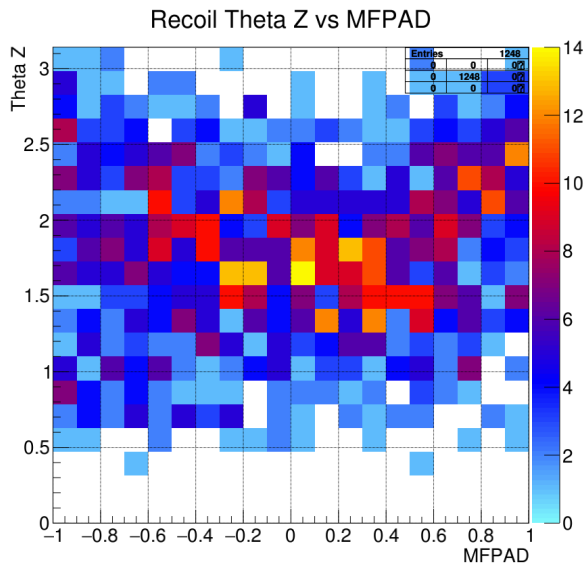


(a) 0 ps delay dataset.

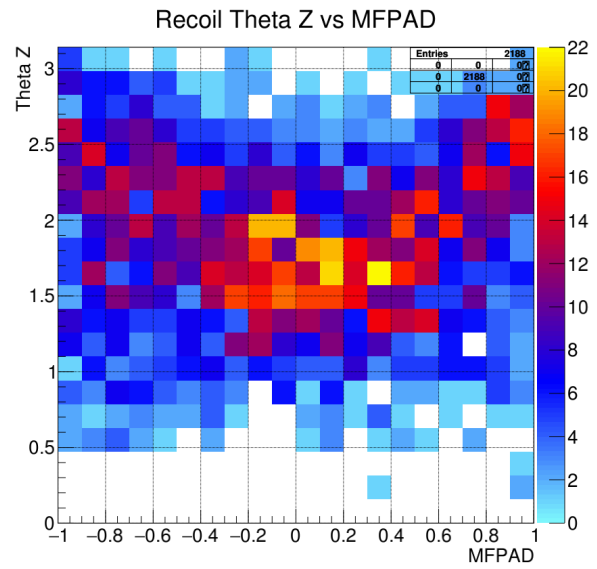


(b) 160 ps delay dataset.

Figure F.2: Isolation of vibrational state $\nu=6$ for 17.9 eV H_2^+ .

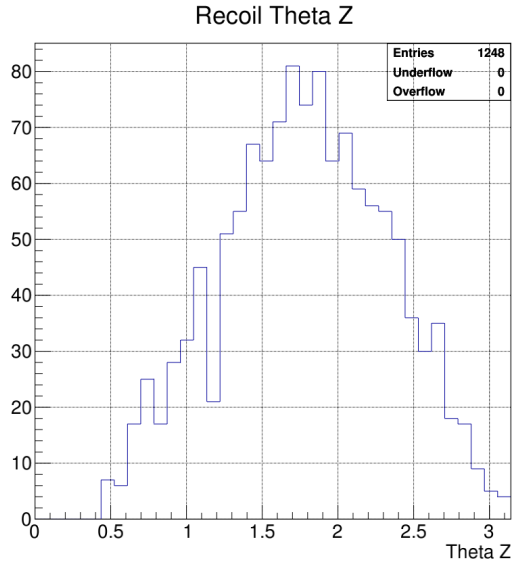


(a) 0 ps delay dataset.

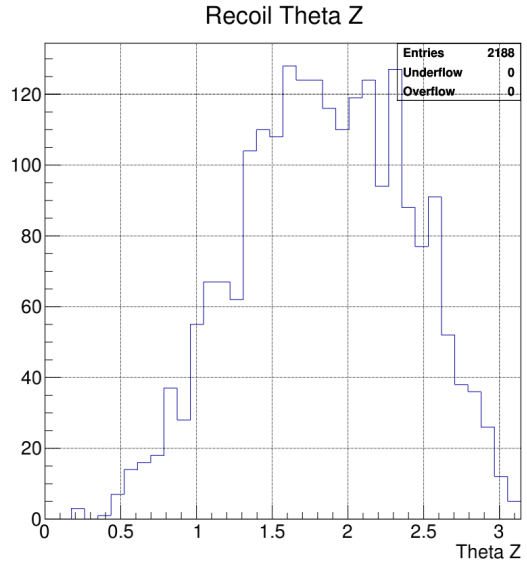


(b) 160 ps delay dataset.

Figure F.3: Recoil θ_z vs MFPAD plots for vibrational state $\nu=6$ for 17.9 eV H_2^+ .

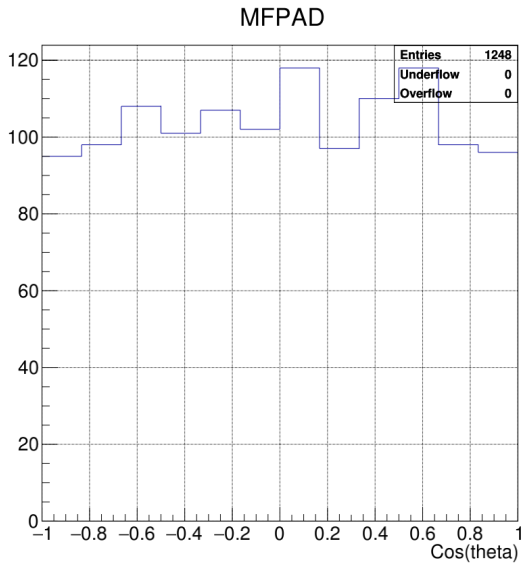


(a) 0 ps delay dataset.

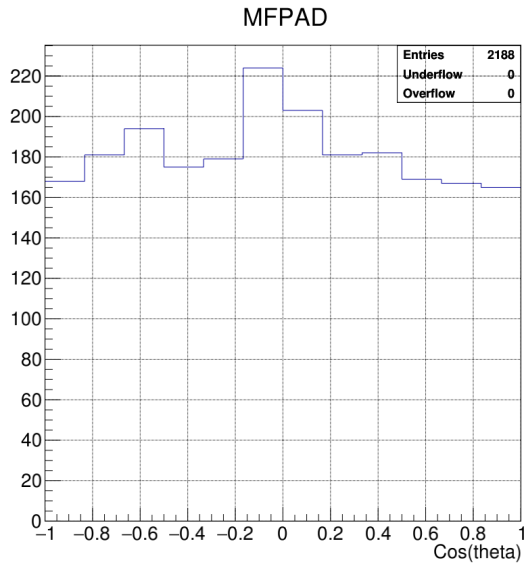


(b) 160 ps delay dataset.

Figure F.4: Recoil θ_z distributions for vibrational state $\nu=6$ for 17.9 eV H_2^+ .



(a) 0 ps delay dataset.



(b) 160 ps delay dataset.

Figure F.5: One-dimensional MFPADs for vibrational state $\nu=6$ for 17.9 eV H_2^+ .